CHEMICAL IONIZATION MASS SPECTROMETRY MEASUREMENTS OF PAN AND PAA IN THE REMOTE ATMOSPHERE

DISSERTATION
for Attaining the Academic Degree 'Doctor rerum naturalium'
(Dr. rer. nat.)

of the Departments
08 - Physics, Mathematics, and Computer Science,
09 - Chemistry, Pharmaceutics, and Geoscience,
10 - Biology,
University Medicine
of the Johannes Gutenberg University

by
ANNA CAROLINA NELSON

Max Planck Graduate Center
mit der Johannes Gutenberg-Universität

JG|U JOHANNES GUTENBERG UNIVERSITÄT MAINZ

MAX PLANCK INSTITUTE FOR CHEMISTRY

SUPERVISORS:
Prof. Dr. Jos Lelieveld
Prof. Dr. Joachim Curtius

MENTORS:
Prof. Dr. Holger Tost
Dr. John Crowley

Date of oral exam: 12.08.2025

Anna Carolina Nelson: *Chemical ionization mass spectrometry measurements of PAN and PAA in the remote atmosphere,*

ABSTRACT

This work presents a unique data set of simultaneous measurements of the two closely linked atmospheric trace gases peroxyacetyl nitrate (PAN) and peracetic acid (PAA) in the remote, tropical troposphere. The measurements were obtained using a Chemical Ionisation Mass Spectrometry (CIMS) instrument during the two Chemistry of the Atmosphere Field Experiments (CAFE) aircraft campaigns, CAFE Brazil and CAFE Pacific, aboard the High Altitude and Long Range Research aircraft (HALO) aircraft. The field experiments spanned a vertical range between a few hundred meters above the ground up to an altitude of almost 15 km.

The limit of detection (LOD) per flight for PAN varied between 20-60 parts per trillion (ppt) during CAFE Brazil and between 10-22 ppt during CAFE Pacific. The LOD of PAA was between 5-33 ppt and 4-11 ppt during the two campaigns. The measurement sensitivity for PAN was derived from in-flight calibrations in dry air at altitudes above 10 km to avoid matrix effects of by-products of the photochemical calibration source in humid air masses. A correction factor of around 0.86 was introduced to account for losses of the detecting acetate anion ($\frac{m}{z} = 59$) on formic acid. A total measurement uncertainty of around 30 % was assigned to the PAN measurements. Between the CAFE Brazil and CAFE Pacific the CIMS calibration was changed to produce isotopically labeled ^{13}PAN which removed the memory effects after an in-flight calibration.

The instrument's sensitivity to PAA was humidity corrected and calibrated in during- and post-campaign ground experiments. Due to the lack of in-situ calibrations and inconsistencies between different calibration methods, an uncertainty of around a factor of 2 must be taken into consideration when using the PAA data.

The CAFE Brazil campaign was conducted above the pristine Amazonian rainforest around the city of Manaus between December 2022 and January 2023, during the transition between the dry and wet season. Median PAN levels of the 12 analysed flights during CAFE Brazil were maximum in mid-tropospheric altitudes (6-10 km) around 100 ppt. In contrast, measured PAA was generally highest at low altitudes, with a median almost up to 500 ppt, except during flights explicitly targeting convective outflow, which led to PAA maxima in the mid- and upper troposphere. The sampled air masses were characterized by a low PAN-to-PAA ratio (median 0.3 at mid-troposphere), reflecting the dominance of biogenic volatile organic compounds (VOC)-driven hydrocarbon chemistry compared to higher-$NO + NO_2$ (NO_x) regions. The high mid-tropospheric PAN/(PAN+NOx)-ratio of 80 % highlighted the importance of PAN as a reservoir species of $NO + NO_2$ (NO_x) in tropical Amazonia and indicated a NO_x-limited PAN formation in this region. The comparison with the global chemical-transport model ECHAM/MESSy Atmospheric Chemistry (EMAC) revealed that methyl glyoxal (MGLY) was the most important (approx. 29 % of total model peroxyacetyl (PA)-production) single immediate PAN and PAA precursor during CAFE Brazil, compared to acetaldehyde (approx. 17 %) and acetone (approx. 9 %). Overall, isoprene oxidation products were responsible for almost three quarter of the total PA formation in the model.

The CAFE Pacific campaign was performed one year later, based in Cairns, Australia, and covered a large area between 130-165 °E and 0-45 °S above the Australian continent and the Southern Pacific. A special target region was the Indo-Pacific Warm Pool region in the north-east of Cairns, where PAN and PAA mixing ratios where close to or below the instrument's detection limit. In general, the CAFE Pacific campaign was characterized by low PAN and PAA levels, with medians of around 50 ppt and 100 ppt, respectively, during 12 analysed flights in the mid-troposphere. In comparison to the CAFE Brazil campaign, the relative contribution of the immediate biogenic PA-precursor MGLY was lower during CAFE Pacific (approx. 16 % of total model PA-production) based on EMAC model simulations. In contrast, the higher relative contributions of acetone (approx. 26 %) and acetaldehyde (approx. 22 %), which can have both biogenic and anthropogenic origins, indicated the mixture of different sources of PAN and PAA during CAFE Pacific. The presence of different air masses from different source regions was also confirmed by tracer-tracer correlations and back-trajectory calculations, which showed that sampled air masses originated from both maritime and continental regions. The influence of long-range transported pollution via the jet-stream, such as biomass burning emissions from southern Africa, on the sampled PAN and PAA mixing ratios appeared to be relatively small, as indicated by backward trajectory analysis.

Compared to the air masses sampled during the previous CAFE Africa campaign above the tropical Atlantic, the impact of fresh biomass burning plumes on the observed PAN and PAA levels during CAFE Brazil and CAFE Pacific was much less significant, based on the analysis of black carbon (BC) and satellite observations of open fires. In contrast to air masses during CAFE Brazil and CAFE Pacific, the PAN-toPAA ratio reached up to a factor of 6 during CAFE Africa, highlighting the seasonal and regional variability of PAN and PAA in the troposphere.

Calculated PA formation based on the measured precursors revealed that the high acetaldehyde levels (around 100 ppt in the mid-troposphere) measured with the gas chromatography-mass spectrometry (GC-MS) instrument during CAFE Brazil and CAFE Pacific are in contradiction to the observed low levels of PAN and PAA. The GC-MS acetaldehyde measurements exceeded the EMAC simulations up to a factor of 25, underscoring the gap between the current understanding of atmospheric sinks and sources of acetaldehyde and the observational data basis.

In addition, steady-state calculations of PAN and PAA based on model PA-radical concentrations resulted in much steeper gradients than in the modelled and measured vertical profiles of both species. That indicated that, in the model, convective mixing leads to significantly flatter vertical profiles in both regions, Amazonia and southern Pacific, than what would be expected in a chemical steady state.

In the case of the CAFE Brazil campaign, the EMAC model generally represented observed PAN well with a slight tendency of underestimation (by 20-50 %). In contrast, PAA was overestimated by EMAC (by 12-70 %). The overestimation of PAA was even larger with 300-500 % during CAFE Pacific, exceeding possible measurement uncertainties by far. These discrepancies may have several reasons in the model such as the incomplete or inaccurate loss and production processes of the PA-radical, insufficient parameterisation of lightning NO_x and convection or underestimation of cloud scavenging effects on organic peroxides.

The tropical aircraft measurements emphasized the need for comprehensive measurements of air composition in the troposphere in order to improve global model predictions with regard to PAN and PAA, notably in tropical remote areas, where sparce measurement data is available to date. In particular, this requires precise knowledge of the tropospheric distributions of the organic precursor species and the reactive trace gases $\mathrm{NO_x}$ and $\mathrm{OH + HO_2}$ ($\mathrm{HO_x}$).

KURZFASSUNG

Diese Arbeit präsentiert einen einzigartigen Datensatz simultaner Messungen der beiden eng miteinander verbundenen atmosphärischen Spurengase Peroxyacetylnitrat (PAN) und Peressigsäure (PAA) in der sauberen, tropischen Troposphäre abseits signifikanter anthropogenen Quellen. Die Messungen wurden mit einem chemischen Ionisations-Massenspektrometer (CIMS) durchgeführt an Bord des Forschungsflugzeugs HALO während der beiden Feldexperimente zur Chemie der Atmosphäre (CAFE) FlugzeugKampagnen CAFE Brazil und CAFE Pacific durchgeführt. Die Flugexperimente umfassten Messungen innerhalb eines vertikalen Bereichs von einigen hundert Metern über dem Boden bis hin zu einer Höhe von fast 15 km.

Die Nachweisgrenze für PAN variierte zwischen den Flügen zwischen 20-60 ppt während der CAFE Brazil Messkampagne und zwischen 10-22 ppt während der CAFE Pacific Messkampagne. Die Nachweisgrenze von PAA lag zwischen 5-33 ppt und 4-11 ppt in den jeweiligen Kampagnen. Die Messempfindlichkeit für PAN wurde aus Kalibrationsmessungen während des Flugs in trockener Luft in Höhen über 10 km abgeleitet, um Matrixeffekte von Nebenprodukten der photochemischen Kalibrationsquelle in feuchten Luftmassen zu vermeiden. Ein Korrekturfaktor von etwa 0,86 wurde eingeführt, um Verluste des detektierenden Acetat-Anions ($\frac{m}{z} = 59$) auf Ameisensäure zu berücksichtigen. Eine Gesamtmessunsicherheit von etwa 30% wurde auf die PAN-Messungen abgeschätzt. Die Messempfindlichkeit für PAA wurde in BodenExperimenten während und im Anschluss der Messkampagnen bestimmt und der Abfall der Messempfindlichkeit mit Feuchte auf Basis von Laborexperimenten korrigiert. Aufgrund des Mangels an In-situ-Kalibrierungen und der Inkonsistenz zwischen verschiedenen Kalibrierungsmethoden ist bei der Verwendung der PAA-Daten eine mögliche Unsicherheit von etwa einem Faktor 2 zu berücksichtigen.

Die CAFE Brazil-Kampagne wurde über dem intakten Amazonas-Regenwald rund um die Stadt Manaus zwischen Dezember 2022 und Januar 2023 durchgeführt, während des Übergangs zwischen der Trocken- und Regenzeit. Die mittleren PAN-Werte der 12 analysierten Messflüge aus CAFE Brazil waren in mittel-troposphärischen Höhen (6-10 km) mit etwa 100 ppt am höchsten. Im Gegensatz dazu war die gemessenen Mischungsverhältnisse von PAA im Allgemeinen in niedrigen Höhen am höchsten, mit einem Median von fast 500 ppt. Außnahmen bildeten die Flüge mit dem Ziel konvektiven Ausfluss zu messen und bei denen PAA-Maxima in der mittleren und oberen Troposphäre beobachtet wurden. Die beprobten Luftmassen in CAFE Brazil durch ein niedriges PAN-zu-PAA-Verhältnis (Median 0,3 in der mittleren Troposphäre) gekennzeichnet, was die größere Bedeutung der biogenen, flüchtigen organischen Verbindungen (VOC) auf die atmosphärische Kohlenwasserstoffchemie im Amazonasgebiet im Vergle-

ich zu NO_x-reicheren Regionen widerspiegelt. Das hohe PAN/(PAN+NOx)-Verhältnis von 80 % in der mittleren Troposphäre unterstreicht die Bedeutung von PAN als Reservoirspezies von NO_x über dem Amazonas-Regenwald und deutet auf eine Limitierung der PAN-Bildung durch NO_x in dieser Region hin. Der Vergleich mit dem globalen chemischen Transportmodell EMAC zeigte, dass Methylglyoxal (MGLY) der wichtigste (ca. 29 % der gesamten Modell-Peroxyacetyl (PA)-Produktion) der unmittelbaren Vorläufer von PAN und PAA während CAFE Brazil war, verglichen mit Acetaldehyd (ca. 17 %) und Aceton (ca. 9 %). Insgesamt waren Isopren-Oxidationsprodukte für fast drei Viertel der gesammten PA-Bildung im Modell verantwortlich.

Die CAFE Pacific-Kampagne wurde ein Jahr nach CAFE Brazil von Cairns, Australien, aus durchgeführt und umfasste ein großes Messgebiet zwischen 130-165°E und 0-45°S über dem australischen Kontinent und dem Südpazifik. Ziel war insbesonders die Beprobung der Warmwasserregion Region Indo-Pazifische Ozean nord-östlich von Cairns, wo Mischungsverhältnisse von PAN und PAA nahe oder unterhalb der Nachweisgrenze des Instruments beobachten wurden. Im Allgemeinen war die CAFE Pacific-Kampagne durch niedrige PAN- und PAA-Werte gekennzeichnet. Die Mediane der 12 analysierter Messflügen lagen für PAN und PAA bei etwa 50 ppt bzw. 100ppt in der mittleren Troposphäre. Im Vergleich zur CAFE Brazil-Kampagne war der relative Beitrag des unmittelbaren biogenen PA-Vorläufers Methylglyoxal (MGLY) während der CAFE Pacific niedriger (ca. 16 % der gesamten Modell-PA-Produktion), basierend auf EMAC-Modellsimulationen. Im Gegensatz dazu deutet die höheren relativen Beiträge von Aceton (ca. 26 %) und Acetaldehyd (ca. 22 %), die sowohl biogenen als auch anthropogenen Ursprungs sein können, auf eine Mischung verschiedener Quellen von PAN und PAA während CAFE Pacific hin. Das Zusammenspiel unterschiedlicher Luftmassen aus unterschiedlichen Quellregionen wurde durch Tracer-Tracer-Korrelationen und berechnete Rückwärts-Trajektorien untermauert. Die beproben Luftmassen stammten sowohl aus maritimen als auch kontinentalen Regionen. Der Einfluss weiträumig verfrachteter Verunreinigungen über den Jetstream, wie beispielsweiße Emissionen aus Biomasseverbrennung im südlichen Afrika, auf die gemessenen Mischungsverhältnisse von PAN und PAA erschien eher unerheblich, wie die Rückwärtsanalyse der Flugbahnen zeigte.

Im Vergleich zu den während der vorherigen CAFE Africa-Kampagne gemessenen Luftmassen über dem tropischen Atlantik war der Einfluss frisch verbrannter Biomasse auf die CAFE Brazil und CAFE Pacific PAN- und PAA-Messunge deutlich unbedeutender, basierend auf der Analyse von Ruß (BC) und Satellitenbeobachtungen offener Feuer. Im Gegensatz zu den von PAA gegenüber PAN dominierten Luftmassen während CAFE Brazil und CAFE Pacific, überstieg die median PAN Mischungsverhältnisse die von PAA während CAFE Africa im Median mehr also um den Faktor 6, was die saisonale und regionale Variabilität von PAN und PAA in der Troposphäre deutlich macht.

Steady-State-Berechnungen von PAN und PAA auf Basis gemessener Aceton und Acetaldehyd Daten zeigten, dass die während CAFE Brazil und CAFE Pacific mit dem GC-MS-Instrument gemesenen hohen Acetaldehyd-Werte (ca. 100 ppt in der mittleren Troposphäre) im Widerspruch zu den beobachteten niedrigen PAN- und PAA-Werten stehen. Die GC-MS-Acetaldehyd-Messungen überstiegen die EMAC-Simulationen um bis zu einen Faktor von 25, was die Lücke zwischen dem aktuellen Verständnis der atmosphärischen Senken und Quellen von Acetaldehyd und der Messdatenbasis unterstreicht. Darüber hinaus führten Steady-State-Berechnungen von PAN und PAA auf

Basis von Modell-PA-Radikalkonzentrationen zu viel steileren Gradienten als in den modellierten und gemessenen vertikalen Profilen beider Spezies. Das deutete darauf hin, dass im Modell konvektive Durchmischung zu deutlich flacheren vertikalen Profile in beiden Regionen, Amazonien und Südpazifik, führt, als von einem chemische stationären Zustand erwartet werden würde.

Im Fall der CAFE Brazil Messkampagne konnte das EMAC-Modell die beobachteten PAN-Mischungsverhältnisse im Allgemeinen gut simulieren mit nur einer leichten Unterschätzung (um 20-50 %). Im Gegensatz dazu überschätze das Model die gemessenen PAA Mischungsverhältnisses deutlich (um 12-70 %). Diese Überschätzung von PAA war während CAFE Pacific noch auffälliger, mit 300-500 %, was den Bereich möglicher Unterschiede durch Messunsicherheiten deutlich übersteigt. Diese Abweichungen der Modell-Ergebnisse kann viele mögliche Gründe habe, wie beispielsweiße unvollständige oder inakkurate Verlust- und Produktionsprozesse des PA-Radikals, unzureichende Parametrisierung von NO_x-Bildung durch Blitze und Konvektion oder Unterschätzung von Wolkenauswaschungseffekten auf organische Peroxide.

Die tropischen Flugzeugmessungen unterstreichen die Notwendigkeit umfassender Messungen der Luftzusammensetzung in der Troposphäre, um die globale Modell-Vorhersagen im Bezug auf PAN und PAA zu verbessern insbesondere in den von Menschen unbeeinflussten tropischen Gebieten, wo bisher nur wenige Messdaten verfügbar sind. Dazu ist insbesondere ein präzises Wissen über die troposphärische Verteilung der organischen Vorläufer sowie der reaktiven Spurengase NO_x und HO_x erforderlich.

CONTENTS

Part I

INTRODUCTION

1

CHARACTERISTICS OF THE TROPOSPHERE

Peroxyacetyl nitrate (PAN) ($CH_3C(O)O_2NO_2$) and peracetic acid (PAA) ($CH_3C(O)OOH$) are important tropospheric trace gases whose atmospheric distribution is governed by a complex interplay of chemical and physical processes. This chapter provides an introduction to the properties and characteristics of atmosphere, with a focus on the tropical, remote troposphere, where aircraft PAN and PAA measurements were conducted with a CIMS instrument.

The troposphere is the lowest layer of the Earth's atmosphere extending from the ground surface to an altitude of 10-15 km (Seinfeld and Pandis, 1998). In this layer, most weather phenomena occur, including the formation of clouds, precipitation, wind etc.. The height of the troposphere varies with latitude and time of year, generally increasing from the poles towards the equator.

The troposphere comprises approximately 80 % of the total atmospheric mass (Seinfeld and Pandis, 1998) and 99 % of the atmospheric water vapour[1]. The troposphere is characterised by a temperature profile that decreases with altitude due to a decrease in air pressure and rapid vertical, turbulent mixing driven by strong radiative heating at the surface.

However, exceptions to this decreasing temperature profile can occur in the boundary layer, the first few hundred meters to 2 km of the troposphere, which is directly affected by surface friction. Temperature inversions, where surface temperatures are lower than those aloft, frequently occur at night or in the vicinity of warm fronts.

Above the troposphere lies the stratosphere, where temperatures increase with altitude, hindering fast vertical mixing. The stratosphere is separated from the troposphere by the tropopause.

The temperature increase in the stratosphere is attributed to the excess heat released by the so called "Chapman cycle" (Reactions 1-4), which occurs above approx. 30 km altitude. In this cycle, ozone is formed by the photolysis of oxygen by ultra violet (UV)-radiation (Reaction 1). The stratospheric ozone is essential for life on Earth, as it strongly absorbs UV-light (Reaction 4). As a result of the stratospheric ozone layer, the actinic flux reaching the troposphere has wavelengths longer than 290 nm (Finlayson-Pitts and Pitts Jr., 2000).

$$O_2 + h\nu(\lambda \leqslant 242\,nm) \rightarrow 2O \tag{1}$$

$$O + O_2 + M \rightarrow O_3 + M \tag{2}$$

$$O + O_3 \rightarrow 2O_2 \tag{3}$$

$$O_3 + h\nu(\lambda \leqslant 1200\,nm) \rightarrow O + O_2 \tag{4}$$

M denotes a collision partner.

---

[1] https://scied.ucar.edu/learning-zone/atmosphere/layers-earths-atmosphere, last access: 22nd May 2025.

1.1 DYNAMICS IN THE TROPOSPHERE

While species emitted at the Earth's surface can ascend to the upper troposphere within hours to days, depending on meteorological conditions, vertical mixing in the stratosphere occurs on a time scale of months to years (Finlayson-Pitts and Pitts Jr., 2000; Holton et al., 1995). The chemical composition of air masses in the stratosphere is distinct from that in the troposphere, as the stratosphere contains significantly more ozone and only minimal water vapour. The upper troposphere (UT) and the lower stratosphere are not only strongly coupled by large-scale stratospheric circulations but also small-scale processes such as deep convective uplift in the tropics or stratospheric intrusions at tropopause folds in the extra-tropics (Holton et al., 1995). Transport between the stratosphere and troposphere is a critical process for atmospheric chemistry and can lead for example to stratospheric ozone depletion due to the intrusions of anthropogenic emissions from the troposphere. Inversely, stratospheric intrusions can serve as a source of tropospheric ozone.

In addition to vertical transport, the troposphere is also impacted by large-scale horizontal transport. The global circulation patterns are driven by thermal equalisation of the radiative forcing imbalance between the polar regions and the Equator. The three circulations cells - Hadley cell, Ferrell cell, and Polar cell - as well as the subtropical and polar jet streams, are a result of the movement of warm air towards the cool polar regions and the Coriolis force induced by Earth's rotation. The Intertropical Convergence Zone (ITCZ), where large-scale upward motion of tropospheric air occurs, acts as a barrier between the northern and southern hemispheres, meandering around the equator. While mixing within a hemisphere occurs on a timescale of about 1-2 months (Seinfeld and Pandis, 1998), inter-hemispheric exchange is in the order of 15 months and is primarily controlled by mid- and upper tropospheric mixing (Finlayson-Pitts and Pitts Jr., 2000).

1.2 AIR COMPOSITION AND TRACE GASES IN THE TROPOSPHERE

The air we breathe is a vital resource, and the understanding of its chemical composition is a fundamental aspect of atmospheric science. Trace gases play a crucial role in the chemical composition of the atmosphere as they impact Earth's radiative budget, the oxidative capacity, particle formation, air quality, and human health. Consequently, the comprehension of their present and future distribution as well as their impact on climate, is a central objective of atmospheric research (Schlager, Grewe, and Roiger, 2012). In contrast to the major components of air (nitrogen (N_2), oxygen (O_2) and noble gases like predominately Argon) which have maintained relatively stable concentrations over time, the amount of trace gases varies widely, ranging from a few ppt to part per million (ppm) (Schlager, Grewe, and Roiger, 2012; Seinfeld and Pandis, 1998). The regional and global distribution of trace gases is influenced by many factors, including transport and mixing dynamics, as outlined in Section 1.1, as well as the interplay between their sources and sinks, chemical reactions, interactions with radiation, aerosols, and clouds. Major sources of trace gases arise from anthropogenic industrial processes like fossil fuel combustion, biomass burning, agriculture, vegetation, volcanoes, and oceans (Schlager, Grewe, and Roiger, 2012). The atmospheric lifetime of trace gases spans a wide range, from seconds to thousands of years, and depends on their removal processes, including chemical reactions, biological activity, interactions with radiation, aerosols and particles, wet and dry deposition, and uptake by ocean and the Earth's surface. Long-lived trace gases, like carbon dioxide (CO_2), methane (CH_4), nitrous oxide N_2O, and halocarbons, act as greenhouse gases, strongly impacting the radiative budget of the atmosphere (Schlager, Grewe, and Roiger, 2012). This work focuses on shorter-lived reactive trace gases which control the oxidative capacity of the atmosphere, i.e., its "cleansing efficiency" of atmospheric pollutants and trace gases.

1.3 OXIDATION IN THE TROPOSPHERE

The majority of species emitted into the atmosphere undergo a process of oxidation, whereby they are converted into substances with higher chemical oxidation states and increased water-solubility until they are removed from the atmosphere by wet and dry deposition (Seinfeld and Pandis, 1998). The key oxidative species in the troposphere are the hydroxyl radical (OH) and ozone (O_3), and their catalytic cycles dominate the atmospheric chemistry (Schlager, Grewe, and Roiger, 2012).

OH reacts with most trace species in the atmosphere, and despite its relatively low daytime concentrations, typically in the order of $10^6 \mathrm{molec.cm^{-3}}$ (Seinfeld and Pandis, 1998), it is the major oxidant in the atmosphere. For example, OH can abstract hydrogen from organic compounds, forming thermodynamically stable water (Finlayson-Pitts and Pitts Jr., 2000), or attack the double bonds of alkenes. Although the reaction rates of O_3 with organics are orders of magnitude smaller than those of OH, the removal process of alkenes forming ozonoids and Criegee intermediates remains significant due to the much higher abundance of O_3, with typical concentrations in the order of $10^{12} \mathrm{molec.cm^{-3}}$ (Finlayson-Pitts and Pitts Jr., 2000; Seinfeld and Pandis, 1998). During nighttime hours, oxidation reactions via photolytically unstable NO_3 can also become relevant (Brown and Stutz, 2012).

While approximately 90 % of atmospheric ozone is found in the stratosphere, where it serves as a protective shield against UV-radiation, 10 % of total ozone are present in the troposphere (Lelieveld and Dentener, 2000; Seinfeld and Pandis, 1998). Since ozone absorbs both, ultraviolet and infrared radiation, tropospheric ozone can act as greenhouse gas. Furthermore, ozone is a toxic air component with harmful effects on both plants and human beings (Haagen-Smit, 1952). In the troposphere, O_3 is primarily formed through the photolysis of NO_2. Additionally, stratospheric intrusions can serve as a source of tropospheric ozone, transporting ozone-rich air from the stratosphere into the troposphere.

$$NO_2 + h\nu(\lambda \leqslant 420\,\mathrm{nm}) \rightarrow NO + O(^3P) \qquad (5)$$

$$O(^3P) + O_2 + M \rightarrow O_3 + M \qquad (6)$$

At typical tropospheric ozone concentrations, NO reacts within minutes with ozone reforming NO_2 (Reaction 7) which photolyses quickly back into ozone during daytime, hence leading to the recycling of ozone. As a result of this cycle, a photo-stationary steady-state is established between NOx and ozone during daytime, which is often described as the Leighton relationship (Leighton, 2012).

$$NO + O_3 \rightarrow NO_2 + O_2 \tag{7}$$

The most important sink of O_3 in the troposphere is photolysis which results in the formation of OH by the reaction of water with the fraction of excited $O(^1D)$ (Reaction 10) which is not quenched back to O in the ground state immediately reforming ozone (Seinfeld and Pandis, 1998).
In remote regions, where NOx levels are low compared to anthropogenically influenced regions, both HO_2 and OH can react with ozone (Reactions 8 and 9), serving as sink of ozone while recycling HOx.

$$HO_2 + O_3 \rightarrow OH + 2O_2 \tag{8}$$
$$OH + O_3 \rightarrow HO_2 + O_2 \tag{9}$$

Due to the higher solar radiation in tropical regions, both production and loss rates of ozone are greatest in these areas and, and result in a relatively short lifetime for tropical ozone (Schlager, Grewe, and Roiger, 2012).

OH in the troposphere can result from primary and secondary sources. The photolysis of ozone is the major primary source of OH in the troposphere (Lelieveld et al., 2016). Zonal OH is highest in the tropics at low latitudes, due to the high water vapour concentrations combined with the high incoming UV radiation (Crutzen and Zimmermann, 1991; Lelieveld et al., 2016).

$$O_3 + h\nu(\lambda \leqslant 336\,nm) \rightarrow O(^1D) + O_2 \tag{10}$$
$$O(^1D) + H_2O \rightarrow 2OH \tag{11}$$

In addition to the photolysis of ozone, other sources of OH in the troposphere are the photolysis of nitrious acid (HONO) and hydrogen peroxide (H_2O_2), the ozonolysis of alkenes, and the reaction of HO_2 with NO (Reaction 12) (Seinfeld and Pandis, 1998). Recent model simulations suggested that the recycling of OH in radical reaction chains can be twice as large as the the primary production in the free troposphere (Lelieveld et al., 2016).

$$HO_2 + NO \rightarrow OH + NO_2 \tag{12}$$

For example, in remote marine regions or high-altitude areas, where no significant sources of VOC are present, OH is lost through reactions with CO (Reaction 13) and CH_4 (Reaction 15) (Finlayson-Pitts and Pitts Jr., 2000).

$$OH + CO \longrightarrow H + CO_2 \tag{13}$$
$$H + O_2 + M \longrightarrow HO_2 + M \tag{14}$$
$$OH + CH_4 \xrightarrow{O_2} CH_3O_2 + H_2O \tag{15}$$

HO_2 is formed through various reactions in the troposphere that produce H or HCO, most importantly the photolysis of formaldehyde (HCHO), see Reactions 16-18, but also via higher aldehydes. HO_2 is essentially a product of the oxidation of organic compounds in the troposphere (Finlayson-Pitts and Pitts Jr., 2000).

$$HCHO + h\nu \rightarrow H + HCO \tag{16}$$

$$H + O_2 + M \rightarrow HO_2 + M \tag{17}$$

$$HCO + O_2 \rightarrow HO_2 + CO \tag{18}$$

1.4 ATMOSPHERIC FUEL: NOX-VOC CHEMISTRY

Nitrogen oxides, comprising $NO + NO_2$ (NO_x), are pivotal species in tropospheric chemistry as they significantly impact the oxidative capacity of the atmosphere and drive the formation of ground-level O_3 (Crutzen, 2016; Lelieveld and Dentener, 2000). The major global source of NO_x is anthropogenic fossil fuel combustion (Ehhalt et al., 2001). Other sources are soil release, followed by biomass burning, lightning, aircraft emissions, and the photo-dissociation of transported N_2O from the stratosphere (Seinfeld and Pandis, 1998). The majority of reactive nitrogen emissions occur as nitric oxide (Singh, 1987). In the troposphere, NO is oxidized to NO_2 by reactions with O_3 (Reaction 7) and HO_2 (Reaction 12), as well as with various organic peroxy radicals (RO_2). Notably, reactions like 19-21, where NO is catalytically oxidised to NO_2 without depleting ozone, are primarily responsible for the accumulation of ozone in the boundary layer during photochemical smog events (Singh, 1987).

$$RH + OH \xrightarrow{O_2} RO_2 + H_2O \tag{19}$$

$$RO_2 + NO \xrightarrow{O_2} aldehydes\,and\,ketones + NO_2 + HO_2 \tag{20}$$

$$NO_2 + h\nu \xrightarrow{O_2} NO + O_3 \tag{21}$$

The RO_2 radicals, which serve as "fuel" for the production of O_3, are a result of the oxidation of alkyl radicals (R) produced via the oxidation or photolysis of VOCs (Atkinson and Arey, 2003). VOCs encompass a wide range of carbon-containing compounds such as alkanes, alkenes, aromatic hydrocarbons, and oxygenated compounds (Atkinson and Arey, 2003; Williams and Koppmann, 2007). Typical biogenic VOCs, such as those emitted from tropical rain forests, include isoprene (C_5H_8), monoterpenes ($C_{10}H_{16}$) like alpha-pinene, and sesquiterpenes (Ringsdorf et al., 2024). However, VOCs are also emitted by anthropogenic industrial activities and fossil fuel combustion.

OH reacts readily with VOCs such as alkanes, as shown in Reactions 19. In the presence of NO_x, this reaction can initiate a cycle that not only oxidises VOCs but also NO to NO_2 leading to ozone enhancement. A typical sequence of OH initiated oxidation of an alkane is depicted in Figure 1.4.1, highlighting the interplay between HO_x, NO_x, and VOC chemistry. This sequence produces aldehydes (HC(O)R) and ketones, while OH is recycled and NO is oxidised to NO_2. The further breakdown of the chain products can lead to the formation of PAN and PAA, as will be discussed in Chapter 2.

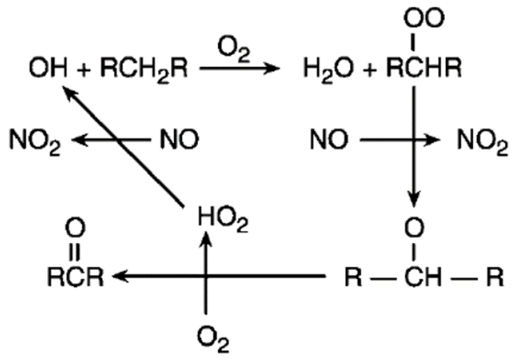

Figure 1.4.1: Typical oxidation sequence of hydrocarbons high-NO_x conditions in the troposphere initiated by OH and recycling OH. The cycle also leads to the oxidation of NO to NO_2 and hence impacts O_3 production. Figure taken from Finlayson-Pitts and Pitts Jr. (2000).

The chain reaction can be terminated by the formation of acids or the self reaction of the hydroperoxyl radical (Reactions 22 -24) (Finlayson-Pitts and Pitts Jr., 2000).

$$OH + NO_2 + M \rightarrow HNO_3 + M \tag{22}$$

$$HO_2 + HO_2 + M \rightarrow H_2O_2 + O_2 + M \tag{23}$$

$$RO_2 + HO_2 \rightarrow ROOH + O_2 \tag{24}$$

In summary, the sequence of reactions in the atmosphere can be described as follows: alkyl radicals R are converted into alkylperoxy radicals RO_2, which in turn lead to the formation of NO_2 and hence ozone in the presence of NO. However, in remote atmospheres, where NO levels are low, typically in the order of 40 ppt, the reaction of RO_2 with HO_2 or other RO_2 can occur (Finlayson-Pitts and Pitts Jr., 2000).

1.5 REACTIVE NITROGEN IN THE ATMOSPHERE

Nitrogen is an essential nutrient for all living organisms, but its chemical stability necessitates conversion to a more reactive state to be utilized by organisms. In nature, this can be achieved by the actions of certain bacteria and microorganisms, as well as lightning. However, the majority of reactive nitrogen is released through anthropogenic activities in the form of $NO + NO_2$ (NO_x) (Galloway et al., 2004). Globally, emissions from the combustion of fossil fuels are the largest source of NO_x in the troposphere, exceeding natural sources resulting from soil emissions, lightning, biomass burning, and intrusions from the stratosphere (Lamarque et al., 1996). In the atmosphere, NO_x are quickly transformed into a variety of oxidised reactive nitrogen species. The lifetime of NO_x with respect to OH is typically less than one day in summer and a few days in winter, limiting its transport to a few hundred kilometers (Singh, 1987). Total reactive nitrogen is defined as the sum of NO_x and all its oxidation products, and is usually denoted as $NO_x + HONO + N_2O_5 + PAN + RONO_2 + ROONO_2 + NO_3 + HNO_4 + ...$ (NO_y).

Wei et al. (2024) combined measurements from various aircraft missions, including the National Aeronautics and Space Administration (NASA) DC-8 aircraft during the ARCTAS, SEAC^{4}RS (Toon et al., 2016), KORUS-A1 (Crawford et al., 2021), and the four

Atmospheric Tomography mission (ATom) (Thompson et al., 2022) missions, as well as IAGOS commercial aircraft measurements. They found that PAN globally dominates NO_y in the upper troposphere (UT) with a fraction of 30-64, %, followed by NO_x (7-11 %), HNO_4 (6-13 %), and HNO_3 (7-11 %). Since measured NO_y levels frequently exceed the sum of individually measured NO_y species, the contribution of PANs in the nitrogen budget and a potential missing source of NO_y had been suggested (Fahey et al., 1986; Singh, 1987).

Given the relatively short lifetime of NO_x, longer-lived reactive nitrogen species such as PAN play a crucial role in the global distribution of NO_x (Moxim, Levy, and Kasibhatla, 1996). Nitrogen species which can exist in equilibrium with NO_x are referred to as reservoir species.

The rapid reaction of NO_2 with OH leads to the formation of nitric acid (HNO_3), which is typically removed from the atmosphere through dry and wet deposition within 1-10 days and is considered as a sink of NO_x (Singh, 1987). However, in the UT, where HNO_3 does not undergo strong wet and dry deposition, HNO_3 can also serve as a reservoir species, releasing NO_x through photolysis with a lifetime in the order of months in the UT.

The oxidation of non-methane volatile organic compound (NMVOC) in the presence of NO_x can also lead to the formation of longer-lived reactive nitrogen species, most importantly PAN (Crutzen, 2016; Huey, 2007). In contrast to most other reservoir species, peroxyacetyl nitrate species can be very long-lived (up to several month) in certain atmospheric conditions, allowing for long-range transport of NO_x and making PAN-type species crucial for the global NO_x-budget (Singh, 1987). In the mid-troposphere, the fraction of PAN to the sum of PAN and NO_x can be 50 to 100 %, underscoring its importance as NO_x-reservoir species (Crowley et al., 2025; Roberts, 1990; Singh, 1981a).

2

THE ROLE OF PAN AND PAA IN THE ATMOSPHERE

PAN and PAA are secondary pollutants, which are not (or not significantly) directly emitted but are formed in the atmosphere from the same precursor, the PA-radical ($CH_3C(O)O_2$), as depicted in Figure 2.0.1. PA results from the oxidation of aldehydes with OH or the photolysis of ketones and dicarbonyls (Roberts, 2007). The precursor species of PA can either be emitted directly or be the result of the oxidation of NMVOC, as described in Section 1.4.

Even though the formation of PAN and PAA is closely linked, as both species are formed from the same organic peroxy-radical precursor, PAN and PAA play different roles in the chemistry of the atmosphere and global climate. This chapter provides an introduction to the significance of PAN and PAA in the atmosphere, their origin, and their global impact.

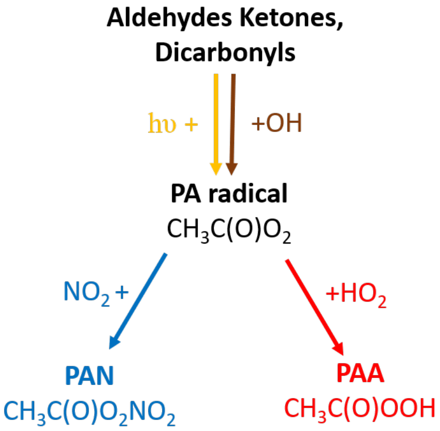

Figure 2.0.1: Simplified chemical scheme of PAN and PAA formation in the troposphere. NMVOC species are either photolysed (yellow) or oxidised (brown) to form the precursor peroxyacetyl (PA)-radical.

2.1 SIGNIFICANCE OF PAN IN THE ATMOSPHERE

The significance of PAN in the atmosphere and its impact on human health has been recognized for decades (Lovelock, 1977; Singh, 1987; Singh, 1981b). PAN plays a central role in the chemistry of the troposphere on local to global scales (Finlayson-Pitts and Pitts Jr., 1997). Its importance extends beyond highly polluted urban areas, where it was first discovered, to remote regions due to its link to the VOC-NO_x cycle (Singh, 1981a).

PAN, $CH_3C(O)O_2NO_2$, is the simplest and most abundant member of the class of peroxycarboxylic nitric anhydrides (PANs, $RC(O)OONO_2$) with R=CH_3. PANs are predominantly formed in the complex VOC-NO_x photochemistry by the photo-oxidation of

NMVOC, as depicted in Figure 2.1.1. PANs are therefore considered an important tracer of photochemistry. The chemical key features of PANs are the carbonyl group (C=O) and the nitrate group (−ONO2) (Roberts, 2007). Like many organic nitrates, PANs have explosive potential (Brauer et al., 1989). The fraction of PAN to total PANs is typically 75-90 % (Fischer et al., 2014; Roberts et al., 2002; Wolfe et al., 2007). The next most prevalent PAN compound is peroxy propionyl nitrate (PPN) with R = C_2H_5 which can be 8-20 % of the abundance of PAN in urban areas (Gaffney and Marley, 2021; Roberts, 2007). PPN is considered a marker of anthropogenic activity because it is exclusively formed from anthropogenic hydrocarbons (Roberts, 2007). Another important PAN compound is peroxymethacrylic nitric anhydride (MPAN) with R=$CH_2C(CH_3)$ which is formed from the isoprene oxidation product methacrolein (MACR) and is hence a marker for biogenic activity. In isoprene-rich areas, MPAN/PAN ratios are typically 5-10 % (Gaffney and Marley, 2021) but can even reach up to 25 % in urban areas % (Roberts, 2007).

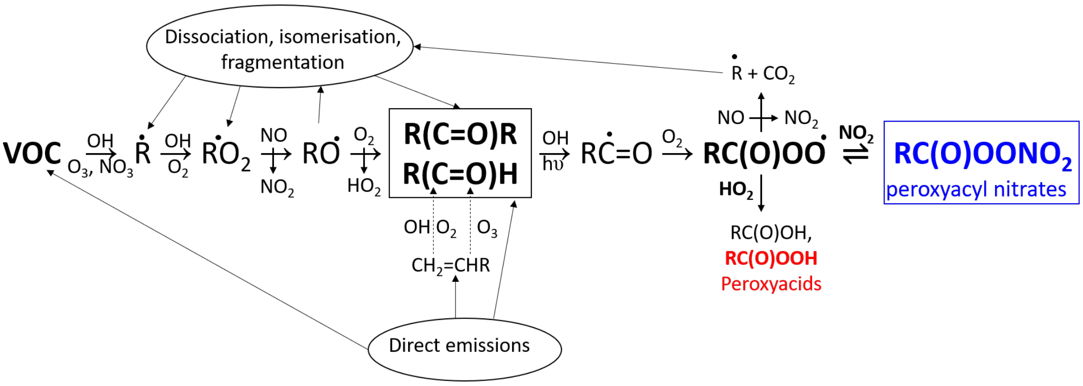

Figure 2.1.1: Formation of PANs ($RC(O)OONO_2$, blue) in the atmosphere from primary and secondary emissions (ellipses) of non-methane VOC via aldehydes and ketones (black box) involving HO_x and NO_x chemistry. The same pathway can also lead to the formation of peroxyacids (red), for example PAA. Based on Roberts (2007) and Seinfeld and Pandis (1998).

The relative abundance of PAN-type compounds formed in the VOC-NO_x chemistry depends on the mixture of NMVOC precursors. Hence, the mixture of PANs in an air mass can be used as a an indication of the mixture of VOCs involved in the photochemical production process of ozone (Roberts, 2007). The majority of NMVOC can form PAN precursors even though their efficiency is highly variable (Roberts, 2007). Since the formation of PANs is closely linked to the non-methane hydrocarbon cycle, changes in NMVOC emissions, such as those induced by a change of organic fuel use, can impact the distribution of PAN and other secondary pollutants in the atmosphere (Brauer et al., 1989; Grosjean, 1992).

The compound peroxyacetyl nitrate (PAN) was first discovered by infrared spectroscopy as a toxic constituent of photochemical smog in Los Angeles in the 1950 s, causing eye irritation and crop damage (Haagen-Smit, 1952; Stephens, 1987). Even though PAN levels in polluted atmospheres are roughly a factor of ten lower than ozone, PAN is more toxic than ozone on a molecular basis due to its oxidative effect and the ability to interact with lipid membranes (Brauer et al., 1989). PAN is a potent lachrymator and the long-term exposure to PAN can even lead to skin cancer[2]. PAN not only impacts air quality and human health (Lovelock, 1977) but is also responsible for serious plant injury in polluted areas, as it is phytotoxic and causes bronzing of the leaves (Taylor, 1969). PAN has helped to characterize the photochemical smog chemistry, as it is a direct indicator of organic peroxy radical levels (Brauer et al., 1989; Gaffney and Marley, 2021). The formation of PAN requires the same precursor peroxy radicals that produce tropospheric ozone.

PAN plays a central role in the chemistry of the troposphere on local to global scales, as it is the principal tropospheric reservoir species of NO_x in many regions, especially above the boundary layer (Finlayson-Pitts and Pitts Jr., 1997; Finlayson-Pitts and Pitts Jr., 2000; Singh, 1981b). Singh et al. (2007) analysed aircraft measurements over North America and found that PAN is the major carrier of reactive nitrogen in the UT, in contrast to the lower troposphere, where HNO_3 is the dominant NO_x reservoir. In contrast to inorganic NO_x reservoir species, like NO_3, HNO_3, and N_2O_5, the total atmospheric lifetime of PAN can be in the order of months in the upper troposphere.

The lifetime of PAN is highly temperature dependent, as PAN is in thermal equilibrium with the PA-radical and NO_2 (Equation 25).

$$CH_3C(O)O_2NO_2 \rightleftharpoons CH_3C(O)O_2 + NO_2 \tag{25}$$

For example, in the middle troposphere, where temperatures typically range from -10 to -50 °C, PAN has a lifetime of weeks with respect to thermal dissociation (around 14 days at -10 °C) to months. In contrast, its lifetime in the boundary layer is significantly shorter with 1.7 h at 20 °C[3]. The stability of PAN in cold conditions allows it to store uplifted NO_2 from polluted areas, transport it over long distances around the globe, and release it to pristine regions when air masses sink down and warm up. The lifetime of NO_x was estimated in summertime, continental US-American field-experiments to be around 4-8 hours which limits its transport to a few hundred kilometers while it can be stored and transported in the form of PAN, over more than 10000 km in the upper troposphere (Singh, 1987). Moxim, Levy, and Kasibhatla (1996) reported an enhancement of NO_x in remote areas by a factor of 2-5 through PAN transport which impacts the global ozone and OH formation. The long-range transport of NO_x in form of PAN can lead to significant enhancements of ozone, especially in remote areas (Jiang et al., 2016; Schultz et al., 1999). On a regional scale, PAN chemistry can reduce ozone production in highly polluted NO_x source regions as PAN formation becomes more efficient than ozone production (Roberts et al., 1995). PAN levels can be highly variable in space and time (Payne et al., 2017): In urban areas, measured PAN mixing ratios reached over 10 parts per billion (ppb), while PAN mixing ratios in pristine regions can be as low as a few ppt. The knowledge and understanding of the seasonal, regional, and global distribution of PAN is necessary for the understanding and modeling of the global oxidant distribution.

---

[2] `https://www.dwd.de/EN/research/observing_atmosphere/composition_atmosphere/trace_gases/cont_nav/pan_node.html`, last access: 31st March 2025.

[3] see reference in footnote [2] on page 13.

2.1.1 *Atmospheric sources of PAN*

PAN has no important source in the stratosphere (Singh, 1987). Instead, it is quasi uniquely formed in the photochemistry of hydrocarbons and NO_x in the troposphere, as shown in Figure 2.1.1. The most dominant immediate organic PAN precursors are the oxidation of acetaldehyde (CH_3CHO) and the photolysis of acetone ($CH_3C(O)CH_3$) and methyl glyoxal (MGLY) ($CH_3C(O)CHO$) (Fischer et al., 2014) forming the PA-radical. To a smaller degree, other NMVOC precursors, like the isoprene oxidation products methylvinyl ketone (MVK) and MACR also contribute to the PA formation (Fischer et al., 2014; LaFranchi et al., 2009). Fischer et al. (2014) simulated PAN observations from aircraft campaigns with global 3-D chemical transport modeling (GEOS-Chem) with improved NMVOC representation and estimated that acetaldehyde represents 44 % of the global source of immediate PA-radical precursors, followed by MGLY (30 %) and acetone (7 %). The residual 19 % resulted from diverse isoprene and terpene oxidation products. The origin of these precursor species can be direct emission as well as secondary formation. With respect to primary emissions, the most important NMVOCs responsible for global PAN formation are isoprene (37 %) and alkanes (14 %) (Fischer et al., 2014).

The sources of the immediate and indirect precursors of PAN are manifold and can originate form both biogenic (vegetation, plants, etc.) and anthropogenic activities (fossil fuel combustion, industry, perfumes, etc.). Biogenic emissions of VOC are dominated by isoprene, with tropical vegetation being the major global source (Guenther, 2013). According to the simulations of Fischer et al. (2014), in the northern hemisphere, anthropogenic sources are dominant outside the growing season, while in the Australian free troposphere, the convective updraft of biogenic NMVOC together with lightning NO_x leads to PAN formation. In addition to fossil fuel burning and natural VOC emissions, mid-infrared satellite observations revealed that biomass burning significantly contributes to the global PAN distribution and is responsible for the upper tropospheric spring maximum of PAN in the southern hemisphere (Moore and Remedios, 2010). The link between precursor emissions and secondary pollutant formation is non-linear and is additionally dependent on meteorology (Stavrakou et al., 2021). For example, drastic changes in NO_x emissions observed in four worldwide mega-cities during COVID lockdown led to changes in PAN in both directions, increases and decreases (Shogrin et al., 2024). Fischer et al. (2014) found that PAN concentrations in general were more sensitive to NMVOC emissions than NO_x emissions, except in fire-dominated regions.

2.1.2 *Sinks of PAN*

In contrast to the complex production mechanisms of PAN, its atmospheric sinks are much better defined. The loss of PAN -and PANs in general- in the atmosphere is a combination of thermal decomposition, photolysis, deposition to vegetation and natural surfaces, and oxidation by atmospheric by OH (and NO_3). The relative contribution of the loss terms significantly depends on altitude (Roberts, 2007).

In the lower and mid-troposphere, thermal dissociation is the most important sink of PAN (Roberts, 2007), leading to the release of NO_x and organic precursors, as shown in Reaction Equation 35.

$$CH_3C(O)O_2NO_2 + M \rightarrow CH_3C(O)O_2 + NO_2 + M \qquad (35)$$

In contrast, in the upper troposphere (UT), where PAN is thermally very stable, e.g. 42 years at 230 K (Singh, 1987), photolysis in the ultra violet/visible (UV/VIS) spectrum becomes relevant, even if it is a slow process. With respect to photolysis the lifetime of PAN in the UT is approximately 3 months (Talukdar et al., 1995).
The loss of PAN via the reaction with OH is considered a minor loss process (rate coefficient $< 3 \times 10^{-14} cm^3 molec.^{-1} s^{-1}$ at 298 K[4].), since photolysis exceeds the loss of PAN via the reaction with OH throughout the entire troposphere by almost an order of magnitude. The reaction of PAN with chlorine atoms (Cl) is similarly slow as the one with OH but is even about 10^3 less important in the UT and the stratosphere with respect to estimated relative abundances of Cl and OH (Roberts, 1990). Similarly, PAN does not significantly react with other typical tropospheric species, like CO, SO_2, NO_2, water, and ozone (Brauer et al., 1989).

Loss of PAN in the troposphere due to wet deposition are considered negligible due to the low Henry's law coefficient of approx. 4.1 mol/l per atmospheric pressure (Brauer et al., 1989; Kames and Schurath, 1995; Roberts, 1990). The solubility of PAN in water is orders of magnitude less compared to nitric acid under normal atmospheric pH conditions of 4-5 (Brauer et al., 1989). In contrast, PAN is highly soluble in nonpolar organic solvents, like tridecane, which is used for its aqueous synthetic chemical production.

Leaf-level studies have observed the uptake of PAN into leaf stomata, suggesting that PAN is a provider of nitrogen for vegetation (Sparks, Roberts, and Monson, 2003). Daytime dry deposition velocities of around 10 mm/s have been measured in forest areas by eddy covariance NO_y flux experiments (Turnipseed et al., 2006). However, when compared to thermal decomposition rates, the deposition rates resulting from these deposition velocities are minor for typical daytime boundary layer heights in the tropics, which range from 1-3 km (Engeln and Teixeira, 2013). The deposition rates could become relatively more significant in the nocturnal boundary layer (Andersen et al., 2025), especially at high latitudes during winter (Turnipseed et al., 2006).

2.2 SIGNIFICANCE OF PAA IN THE ATMOSPHERE

Organic hydroperoxides (ROOHs) play an important role in atmospheric chemistry as they serve as a reservoir of HO_2, which in turn impact gas-phase oxidation rates and the radical budget (Crounse et al., 2006; Wennberg et al., 1998). Peroxycarobxylic acids (RC(O)OOH), like peracetic acid (PAA) ($CH_3C(O)OOH$), account for nearly half of total global ROOH budget (Khan et al., 2015). PAA is ubiquitous in the atmosphere with mixing ratios reaching up to 1 ppb in urban and rural areas (Crowley et al., 2018; Phillips et al., 2013; Zhang et al., 2010) and tens to hundreds ppt in the UT (Crowley

---

[4] `https://iupac-aeris.ipsl.fr/datasheets/pdf/HOx_VOC44.pdf`, last access: 1st July 2025

et al., 2025; Travis et al., 2020). However, measurements of PAA are sparse.

Due to their high solubility, ROOHs can by taken up by aerosol or cloud droplets, promoting the formation and aging of secondary organic aerosol (SOA). Docherty et al. (2005) found in chamber experiments that organic peroxides contributed 47-85 % of total mass of SOA formed from monoterpenes α-pinene and β-pinene. PAA may play a potentially important role in SOA formation, as it undergoes aqueous phase oxidation on HSO_3^- at atmospheric pH levels (Lind, Lazrus, and Kok, 1987). PAA was found to make up around 10 % of the total ROOH observed at a rural mountain site Germany (Fels and Junkermann, 1994).

PAA is also an organic acid, and as such, it contributes to the acidity of the atmosphere which has impacts, among others, on aerosol formation, air quality, and acid deposition (Baker et al., 2021; Finlayson-Pitts and Pitts Jr., 2000). The most abundant organic acids in the gas phase are formic acid (HCOOH) and acetic acid (CH3COOH). Together, they make up the largest part of the total gas-phase acidity in the atmosphere (Grosjean, 1992).

Due to its oxidative and antimicrobial properties, PAA is widely used in industry as disinfectant and sterilant in various applications, including food, medical, and wastewater treatment (Henneken et al., 2006). However, PAA has also been shown to have toxic effects on human beings, for example causing skin and eye irritations.

PAA have also garnered research interest as its presence in the atmosphere is closely linked to PAN due to their common peroxy-radical precursor $CH_3C(O)O_2$ (see Figure 2.0.1). Both PAN and PAA are formed competitively from the chain reactions with VOCs, depending on the abundance of NO_2 or HO_2, respectively. PA reacts with HO_2 in three pathways (Reactions 32a- 32c) but only in Reaction 32a PAA is formed. However, the dominant pathway is Reaction 32c as classified by the International union of pure and applied chemistry (IUPAC)[5].

$$\begin{aligned} CH_3C(O)O_2 + HO_2 &\longrightarrow CH_3C(O)OOH + O_2 && \text{(32a)} \\ &\longrightarrow CH_3C(O)OH + O_3 && \text{(32b)} \\ &\longrightarrow CH_3C(O)O + OH + O_2 && \text{(32c)} \end{aligned}$$

PAA is often used as an indicator of photochemical activity. The relative abundance of PAN to PAA can provide an indication of the relative ratio of NO_2 and HO_2 (Crowley et al., 2018; Crowley et al., 2025). Furthermore, PAA represents not only a sink of HO_2, but also a sink for the PA-radical, which impacts the PAN formation.

2.2.1 *Atmospheric sources of PAA*

In contrast to other organic acids, no significant direct sources of PAA ($CH_3C(O)OOH$) are known. However, minor releases from industrial uses cannot be fully avoided (Henneken et al., 2006).

Having the same organic precursors like PAN, the origin of PAA can also be linked to both biogenic and anthropogenic sources. In the lowermost troposphere at atmospheric

---

[5] `https://iupac-aeris.ipsl.fr/datasheets/pdf/HOx_VOC54.pdf`, last access: 27th May 2025.

pressure and moderate temperatures, the reaction rate coefficients of PAN and PAA from the PA-radical are comparable, according to IUPAC recommendations. Generally, due to the presence of pollution by NO_x, the production of PAN is usually favoured over PAA. However, in clean environments or aged air pollution, HO_2-levels can compete with NO_2 levels (Crowley et al., 2018). For example, in the lower troposphere in remote, tropical regions, PAA formation can significantly exceed PAN formation because low-NO_2 conditions are combined with relative high temperatures (Crowley et al., 2018). Warm conditions lead to the rapid dissociation of PAN, releasing the PA-radical, which can be a source of PAA in this region. In contrast to PAN, PAA is thermally stable in the tropical, warm boundary layer, and its lifetime with respect to photolysis is in the order of 1-2 weeks. In rural, mountainous sites in China, the measured PAA levels of 0.2-0.1 ppb on sunny days were majorly attributed to local photochemical production (Zhang et al., 2010).

Biomass burning is an additional source of many trace gases (Andreae, 2019; Andreae and Merlet, 2001) and was found to be not only a source of PAN but also of PAA in young and aged air masses. (Crowley et al., 2025; Phillips et al., 2013; Wang et al., 2016; Wolfe et al., 2021; Yokelson et al., 2009).

2.2.2 *Sinks of PAA*

Like other acids, PAA can be removed from the atmosphere by reactions with OH as well as through wet or dry deposition (Finlayson-Pitts and Pitts Jr., 2000).

Recent kinetic experiments have shown that the reaction of PAA with OH is very slow, with a rate constant of around $4 \times 10^{-14} \mathrm{cm}^3 \mathrm{molec.}^{-1} \mathrm{s}^{-1}$ (Berasategui et al., 2020). This results in a lifetime of PAA with respect to typical OH concentrations of about one year (Crowley et al., 2025). Compared to the losses of photolysis, which have frequencies of around $1 \times 10^{-6} 1/\mathrm{s}$) and lead to lifetimes in the order of weeks, the reaction with OH is hence a minor sink.

While in the upper troposphere, the major sink of PAA is photolysis, in the planetary boundary layer, deposition becomes important (Berasategui et al., 2020).

The solubility of PAA is around 670-840 M/atm at 298 K (Sander, 1999), wherefore wet and dry deposition can become an important sink when photolysis rates are low. In forested regions, at high humidity nighttime conditions, the efficient deposition of PAA onto moist surface has been observed (Phillips et al., 2013).

2.3 REGIONAL AND GLOBAL DISTRIBUTIONS OF PAN AND PAA

The distributions of PAN and PAA can exhibit significant spatial and temporal variability. To understand and quantify their global and regional distributions, a range of measurement strategies have been employed, including remote sensing from space as well as airborne and ground-based in-situ measurements. These measurement strategies are briefly introduced in this section. Additionally, the current state of the art in simulating PAN and PAN in global chemical-transport models is outlined.

2.3.1 *Global remote-sensing observations of PAN*

The observation of PAN from space allows for the monitoring of its large-scale distribution and temporal evolution in the atmosphere. This is achieved through high-resolution infrared spectrometer satellite measurements, typically at the absorption bands of 794 cm^{-1} or 1163 cm^{-1} (Gaffney and Marley, 2021). The signature of PAN in the infrared remote sensing spectra in the upper troposphere was first retrieved from the Michelson Interferometer for Passive Atmospheric Sounding (MIPAS)-B2 stratospheric balloon instrument by Remedios et al. (2007). The first global distribution of PAN was then reported by Glatthor (2007) based on the infrared emission spectra between 664-800 cm^{-1} observed with MIPAS-E onboard the ENVIronmental SATellite (ENVISAT) (Fischer et al., 2008) in 150 polar orbits in October to December 2003.
Glatthor (2007) found a strong difference in PAN levels between the northern and southern hemispheres in this year. In the northern hemisphere, high average background levels of low- and mid-tropospheric PAN around 125 ppt at 8 km altitude were present, likely caused by industrial pollution. The highest PAN signal in the northern hemisphere was found above China and the Chinese sea with around 250 ppt. In contrast, in mid- and high latitudes in the southern hemisphere, PAN mixing were substantially lower, ranging between 50-75 ppt, due to less anthropogenic pollution (Glatthor, 2007). The impact of the South American and African biomass burning season was clearly visible in the sub-tropical southern hemisphere by a large biomass burning plume with elevated PAN mixing ratios between 200-700 ppt between 20-40 °S, reaching from Brazil over the Southern Atlantic, Central and South Africa towards Australia at altitudes between 8-16 km. In the tropics, the MIPAS-observations had large data gaps below 8 km altitudes due to cloud contamination. Above 15 km altitude, PAN levels of the northern hemisphere were lower compared to those in the southern hemisphere due to beginning subsidence over the Arctic (Glatthor, 2007).
Further MIPAS-E observations emphasised the high seasonal and spatial variability of PAN. Moore and Remedios (2010) found a strong inter-annual variability of PAN in the upper troposphere and lower stratosphere at high latitudes (up to 400 ppt averaged variability a year) but also in the tropics (150 ppt), which was closely linked to biomass burning regions and growing seasons. The observations in January 2003, which covered the biomass burning season in sub-Saharan Africa, found a layer of PAN mixing ratios higher than 300 ppt at 300 hPa, clearly showing inter-continental transport from Central Africa to the Amazonian region. With the beginning of the growing season on the northern hemisphere in March, PAN mixing ratios over Europe and continental North America drastically increased. The inter-hemispheric difference was most pronounced during August, with maximum PAN above western Siberia.

Further space-borne limb-viewing measurements of PAN other than from MIPAS (Glatthor, 2007; Remedios et al., 2007; Wiegele et al., 2012) have been reported, including those from the Fourier-Transform Interferometer ACE-FTS (Coheur et al., 2007) and the Infrared Atmospheric Sounding Interferometer (IASI) (Coheur et al., 2009). These measurements have addressed the chemical composition of biomass burning plumes. Nadir-viewing satellite observations from MetOp Infrared Atmospheric Sounding Instruments (IASI) and Aura Tropospheric emission spectrometer (TES) (Alvarado et al., 2011; Clarisse et al., 2011; Jiang et al., 2016; Payne et al., 2017; Zhu et al., 2015) have provided higher sensitivity to PAN in the lower troposphere. Payne et al. (2017) compared TES observations of PAN in the tropics in 2005 and 2006 to GEOS-Chem model data, confirming the MIPAS findings of an October maximum, the peak season of biomass burning. However, the strong inter-annual variability observed in northern central Africa in December was not associated with changes in biomass burning, but rather with a combined effect of biogenic emissions and lightning. Combining GEOS-Chem model data, aircraft measurements, and TES satellite observations, the seasonality of PAN was shown to have an important impact on the global tropospheric abundance of ozone (Jiang et al., 2016).

However, satellite data coverage is subject to interferences, particularly with water vapour, which can lead to high uncertainties, especially in the tropics where cloud coverage is frequent.

2.3.2 *Airborne measurements of PAN and PAA in the tropics*

In contrast to satellite observations, which primarily provide columns densities of trace gases, aircraft measurements allow high-resolution vertical sampling between the lower and the upper troposphere. In addition, aircraft observations provide a possibility to target tropical regions where satellite observations are gappy due to the high cloud coverage.

A significant number of aircraft measurement campaigns have targeted the northern hemisphere, with a focus on PAN measurements. For example, the SONEX campaign sampled above the northern Atlantic (Talbot et al., 1999), INTEX-A (Singh et al., 2006), INTEX-B (Singh et al., 2009), and ITCT 2K2 (Roberts et al., 2004) targeted northern America. The TRACE-P campaign (Russo et al., 2003) targeted the western Pacific and Asian continent, while arctic and subarctic regions were sampled during ARCTAS Alvarado et al., 2010; Jacob et al., 2010 and POLARCAT-GRACE (Roiger et al., 2011).

PAN was measured via an electron capture gas chromatograph (GC-ECD) (Singh and Salas, 1983; Singh, Thompson, and Schlager, 1999) aboard the DC-8 aircraft during SONEX, INTEX-A, INTEX-B, TRACE-P, and ARCTAS. The ITCT 2K2 campaign was conducted with the NOAA WP-3D aircraft, where PAN was also measured via GC-ECD (Flocke et al., 2005). During POLARCAT-GRACE, PAN was measured with via a chemical ionisation ion trap mass spectrometer (CI-ITMS) aboard the German Aerospace Center (DLR) research aircraft Falcon. PAA was measured simultaneous to PAN only during the INTEX-A, INTEX-B, and ARCTAS DC-8 aircraft campaigns with a CIMS instrument based on negative ion cluster chemistry of CF_3O^- (Crounse et al., 2006).

In contrast, aircraft observations are sparse in remote, tropical areas, especially in the southern hemisphere.

The first aircraft PAN measurements above the Brazilian Amazon Basin were performed during wet season in April-May 1987 in the framework of the NASA ABLE 2B expedition (Singh et al., 1990) based in Manaus and Belem, Brazil. An electron capture gas chromatographic PAN instrument (Singh and Salas, 1983) was mounted aboard the Lockheed Electra aircraft, which limited measurements to a maximal altitude of about 6 km. In the framework of the NASA Tropospheric Experiments (GTE), a series of aircraft missions with the DC-8 aircraft were performed which included the three cam-

paigns PEM-West A, PEM-Tropics A, and TRACE-A, targeting tropical, remote areas. The campaigns took place in the same time of the year (September-October) within five years (1991, 1992 and 1996) (Singh et al., 2000b). During these campaigns, PAN was measured with a GC-ECD instrument.
A large-scale and multi-seasonal attempt to address the most remote areas of the globe was the ATom experiment, which included four complete nearly pole-to-pole global circuits across the Southern Ocean and the Arctic (Thompson et al., 2022). The first two ATom deployments took place in July-August 2016 (ATom1, south hemispheric winter) and January-February 2017 (ATom2, south hemispheric summer) to evaluate the oxidation capacity over the remote oceans. During the four ATom campaigns, PAN was measured via electron capture gas chromatography (Elkins, Moore, and Kline, 2002; Wofsy, 2011), and PAA with the Caltech CIMS instrument based on negative ion cluster chemistry of CF_3O^-, as described in Crounse et al. (2006).

In Section 5.5.1 and Section 5.5.1, the vertical profiles from HALO aircraft observations during CAFE Brazil and CAFE Pacific, respectively, are compared in detail to those obtained in aircraft campaigns in the free troposphere above the Amazonian rain forest (Singh et al., 1990, 1996a) and Western Pacific (Singh et al., 1996b, 2000b; Travis et al., 2020) from NASA's DC-8 aircraft and remote observations with the Russian Geophysica aircraft (Keim et al., 2008).

2.3.3 *Ground-based measurements of PAN and PAA*

Since the first ground-based measurements of PAN in 1960 in Los Angeles, USA, PAN has been measured at many sites across the globe, reporting daily maximum values up to 70 ppb (Gaffney and Marley, 2021). The reduction of hydrocarbon emissions from vehicles has helped to decrease levels of PAN and its analogs in cities, but still the highest levels of PANs are observed in urban areas, driven by the high abundance of VOC and NO and leading to high photochemical ozone levels (Gaffney and Marley, 2021; Roberts, 2007).

The diurnal cycle of PAN in remote areas is in general characterized by photochemical production, but is also controlled by meteorology. Observations at a highly pristine high-altitude remote site in the southern Tibetan Plateau showed similar diurnal cycles of O_3 and PAN, with a steep morning rise and flat daytime plateau (Xu et al., 2023). Variations in the diurnal cycle were associated with boundary layer development and down-mixing of free-tropospheric air, as well as day-to-day effects like stratospheric O_3 entrainment or transported pollution (Xu et al., 2023).

Simultaneous measurements of PAN and PAA were taken during summertime at the SMEAR II-station in the Finnish boreal forest, within the framework of the HUMPPA-COPEC campaign. Mixing ratios were generally below 1 ppb (except for the sampling of biomass burning affected air masses), reflecting the low abundance of NO_x in the rural area (Crowley et al., 2018). Despite the similar photochemical generation routs, the average diurnal cycle of PAA peaked about 2 hours later than the one of PAN, which was explained by the increasing loss rates of PAN with temperature (Crowley et al.,

2018). PAA formation was favoured over PAN when temperature and photochemical activity were highest.
A good correlation between PAA, ROOH, and H_2O_2 was observed, indicating the important contribution of PAA to total organic peroxides (Crowley et al., 2018; Phillips et al., 2013). Boundary layer measurements of PAA in rural sites in China suggest that PAA was mostly produced in local photochemical production and was increasing with temperature, solar radiation, and ozone, but decreasing with NO_x and humidity (Zhang et al., 2010).

2.3.4 *PAN and PAA in global chemical transport models*

Global chemical transport models have been used to simulate the spatial and temporal distributions of PAN and PAA on Earth. However, the simulation of these species is challenging due to the complexity and uncertainty of NMVOC sources and their corresponding chemistry, as well as the critical impact of vertical transport especially on PAN mixing ratios (Fischer et al., 2014). Uncertainties arise from various factors such as the parametrization of biomass burning emissions, lightning, and convection.

Simulations of PAN with the global 3-D chemical transport model GEOS-Chem have shown that PAN is more sensitivities to NMVOC emissions than NO_x emissions in most regions of the world (Fischer et al., 2014). Observed PAN levels could be reproduced by using updated emission factors of NMVOCs and adapting emissions from open fires and biomass burning (Fischer et al., 2014). However, models still face challenges in resolving the contradiction between measurements of acetaldehyde to simulations and measurements of PAN and NO_x (Millet et al., 2010; Travis et al., 2020). Travis et al. (2024) pointed out the role of higher PANs, which were added to the chemistry to scale the PAN simulations to observations.

GEOS-Chem simulations significantly underestimated both acetaldehyde and PAA compared to aircraft measurements (Travis et al., 2020). The underestimation appeared throughout the year and in both hemispheres. Even the addition of ocean sources of VOCs by 3-9 % could not reconcile the discrepancy between measurements and model, indicating the need for precise emission estimates.

While improvements have been made in the model simulations of PAN (Fischer et al., 2014), the model bias for acetaldehyde and PAA remains a problem (Travis et al., 2020). Having difficulties in correctly representing both PAN and PAA has implications on modeling performance of the oxidative capacity of the atmosphere. In the framework fo this work, the CIMS observations are compared to the global chemical-transport model EMAC.

3

OBJECTIVES AND METHODS OF THIS THESIS

3.1 STRUCTURE OF THE THESIS

This thesis comprises the presentation and analysis of airborne, tropospheric measurements of the two atmospheric trace gases PAN and PAA in remote, tropical regions which were performed with a Chemical Ionisation Mass Spectrometry (CIMS) instrument.

In the first part of the thesis, background information about the principles of tropospheric chemistry were given highlighting the role of PAN and PAA. This chapter points out the objective of this thesis and introduces the analysis tools used for the interpretation of the PAN and PAA measurements.
The instrument details of CIMS are described in Part ii including calibration methods, technical improvements of the instrument, data processing information and an assessment of the measurement uncertainties.
Part iii focuses on the two tropical airborne missions CAFE Brazil and CAFE Pacific presenting the observations of PAN and PAN and investigating the air mass composition with respect to origin, aging and pollution sources.
Lastly, a general picture of PAN and PAA in remote tropical areas is drawn in Part iv by comparison with the previous CAFE Africa campaign.

3.2 AIM OF THE THESIS

This work addresses the investigation of the distribution of the important NO_x-reservoir species PAN and the closely linked organic peroxide PAA in the tropical, remote upper troposphere, where measurement data is rare.

The CAFE aircraft campaigns comprise three measurement between 2018 and 2024 campaigns called CAFE Africa, CAFE Brazil, and CAFE Pacific which aimed to provide a comprehensive understanding of atmospheric chemistry and particle formation processes in the tropical troposphere. The instrumental equipment aboard the research aircraft HALO[6] was identical during all three CAFE campaigns. Measurement data used in the framework of this this provided by other instruments than CIMS aboard HALO are referenced in Section 3.3.

The focus of this work are the CAFE Brazil campaign, based in Manaus, Brazil and the CAFE Pacific campaign based in Cairns, Australia. The first one focused on the air composition above the tropical Amazonian rain forest and took place in December 2022 and January 2023. CAFE Pacific targeted the austral tropical, marine and continental, remote troposphere. A detailed description of the aircraft campaigns and is given in Section 5.2 and Section 6.1, respectively. An overview of the location of the

---

[6] Further information on `https://halo-research.de/`, last access: 07th July 2025.

CAFE campaigns and the measured PAN mixing ratios along the flight tracks is given in Figure 3.2.1. The location of the Hyytiälä forest station (SMEAR II) is also marked in Figure 3.2.1 where I most recently operated CIMS during the ground-based measurement campaign BAIRN-VIP in the boreal forest in Finland. While the CAFE campaigns were dedicated to the tropical, upper troposphere, the BAIRN-VIP campaign focused on the surface layer and its vertical variability. A brief overview of the preliminary PAN data of this campaign is given in Section 9.2.

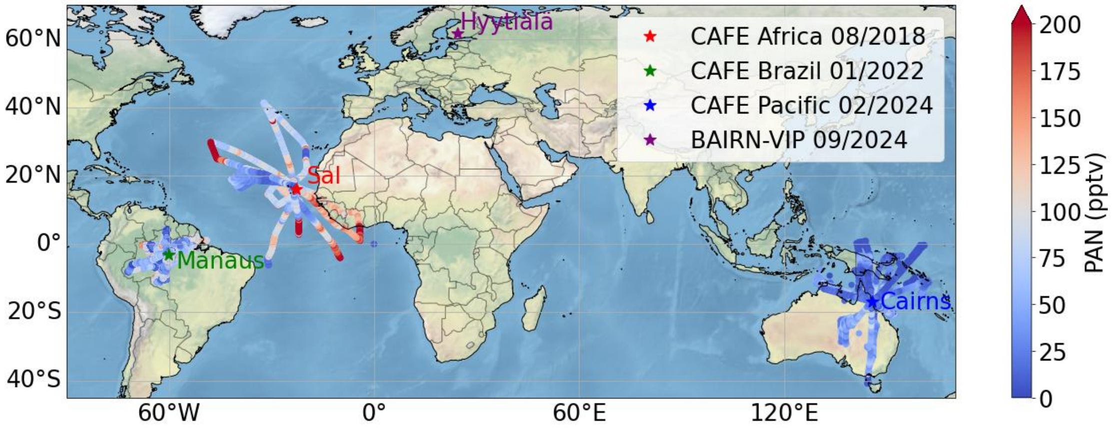

Figure 3.2.1: PAN mixing ratios along the flight tracks of all three CAFE campaigns. The location of our most recent ground-based campaign Biosphere-Atmosphere Interactions and the Reactive Nitrogen Budget: VertIcal Profiles of Key Species (BAIRN-VIP) in Hyytiälä, Finland, is also marked. The PAN data of CAFE Africa was processed and provided by John Crowley.

In this thesis, I present and analyse the measured PAN and PAA data of the CAFE Brazil and CAFE Pacific campaigns with the aim to:

- Provide an observational data basis of vertically resolved PAN and PAA levels in the remote, tropical, upper troposphere for the improvement of global climate models,
- Analyze the origin and transport of PAN and PAA in the sampled air masses above the Amazon rain forest and above Australia and the Western Pacific also in comparison to the measurements above the central Atlantic west of Africa, and
- Quantify the contribution of PAN to the NO_x-budget in the remote, tropical atmosphere in all CAFE measurement campaigns.

3.3 PAYLOAD OF THE HALO AIRCRAFT DURING CAFE CAMPAIGNS

The CIMS instrument was mounted on board of HALO of the DLR as one of 16 meteorological, particle and gas phase instrument from the participating universities and research institutes Goethe University Frankfurt, Max Planck Institute for Chemistry, Mainz (MPIC), Karlsruhe Institute of Technology (KIT), Leibniz Institute for Tropospheric Research (TROPOS) and Forschungszentrum Jülich (FJZ). The HALO aircraft is a modified Gulfstream Aerospace Corporation G550 business jet allowing the flexible installation and operation of scientific instrumentation(Giez et al., 2021). The configuration of the instrumentation aboard HALO was identical for all CAFE campaigns and was described for the BLUESKY/CAFE-EU aircraft campaign above Europe by Voigt et al., 2022. In Table 1, measurement data provided from other instruments than CIMS are listed. They were used in this thesis in order to analyse and interpret the origin of the observed PAN and PAA mixing ratios. The table includes a short overview of the measured species and references to more detailed instrument descriptions.

Instrument	**Used species**	**Data owner/provider**	**Reference**
BAHAMAS	static air temperature, static pressure, longitude, latitude, humidity, altitude[1]	DLR/Andreas Giez	Giez et al., 2022
GC-MS	Acetaldehyde	MPIC/B. Krumm	Bourtsoukidis et al., 2017 Curtius et al., 2024
PTR-MS	Acetone, Acetonitrile	MPIC/N. Tripathi	Tripathi et al., 2025
NOAH	NO	MPIC/C. Nussbaumer[2,3]	Nussbaumer et al., 2021
HYPHOP	H_2O_2, RO_2[4]	MPIC/J. Hamryszczak	Hamryszczak et al., 2023a
TRISTAR/ ATTILA	CO	MPIC/L. Ort	Ort et al., 2024, Röder et al., 2024, Wienhold et al., 1998
FAIRO	O_3	KIT/F. Obersteiner[5]	Zahn et al., 2012
HALO-SR	photolysis rates	FJZ/B. Bohn	Bohn and Lohse, 2017
SP2	black carbon	TROPOS/M. Pöhlker, Y. Yang	Holanda et al., 2020

Table 1: References of used measurement data from other instruments than CIMS aboard HALO during the CAFE campaigns. [1]WGS84 elliptical height. [2]Data for CAFE Brazil available under `https://agupubs.onlinelibrary.wiley.com/doi/full/10.1029/2024JD041168`. [3]Data for CAFE Pacific available under `https://agupubs.onlinelibrary.wiley.com/doi/full/10.1029/2024GL112788`. [4]Data for CAFE Brazil available under `https://zenodo.org/records/10010971`. [5]Data available under `https://zenodo.org/records/15689969`.

The Basic HALO Measurement and Sensor System (BAHAMAS) instrument is a permanent installation in HALO developed by the Data Science Group of the Flight Experiments Facility of DLR. BAHAMAS provides basic meteorological data during all flight experiments from six total air temperature inlets in the aircraft nose section, GPS antennas and an instrumented nose boom (Giez et al., 2021).

The GC-MS instrument is a custom-built fast gas chromatography-mass spectrometry (GC-MS) system with a liquid nitrogen cryogenic system and a commercial quadrupole mass spectrometer measuring 35 VOC species like hydrocarbons, oxygenated VOCs and aromatics from sub-ppt to ppb levels at a time resolution of 3 min (Curtius et al., 2024). For this thesis, the greatest interest was in acetaldehyde measurements of the GC-MS instrument because acetaldehyde is one of the major precursors of PAN and PAA. The GC-MS detects acetaldehyde at $\frac{m}{z} = 29$ and a retention time of 0.42 min. The uncertainty associated with the provided acetaldehyde data varies between 10-20 % between flights depending on the the quality of calibration and background measurements. The LOD was between 30-90 ppt during CAFE Brazil. The status of the acetaldehyde data for CAFE Pacific is still preliminary and has higher uncertainties (personal conversation with Bianca Krumm).

Measurements of acetone, another PAN and PAA precursor, and acetonitrile, a biomass burning tracer, were provided by the PTR-MS which is a proton-transfer-reaction mass spectrometry instrument equipped with a time-of-flight mass spectrometer and had average LODs of 6 ppt and 16 ppt respectively during CAFE Brazil. For CAFE Pacific, only preliminary data is available of these two species. Acetaldehyde was also measured by the proton-transfer reaction mass spectrometry (PTR-MS) but not used because of the still ongoing investigations for interferences with water and ozone in the data. A manuscript about the final PTR-MS data including acetone and acetaldehyde during CAFE Brazil and CAFE Pacific is in preparation (private communication with Nidhi Tripathi)

Nitrogen Oxides Analyzer for HALO (NOAH) measures NO based on chemiluminescence from excited NO_2* from the reaction of NO with O_3 which is added in excessive amounts. In a second channel, NOAH includes a photolytic converter photolysing NO_2 to NO at a wavelength of around 395 nm being able to detect the sum of NO_2 and thermally labile nitrates (Curtius et al., 2024; Nussbaumer et al., 2024).

Due to the interferences of NO_2 reservoir species on the NO_2-channel, no direct measurements of NO_2 are available. However, daytime NO_2 derived from an extended photostationary state (PSS) calculation based on NO, O_3, HO_2 and RO_2 concentrations and NO_2 photolysis frequency for CAFE Brazil by Hartmann (2024) was used. Since measurements of RO_2 and HO_2 measurement data were not available at this point, Hartmann (2024) used simulated data of CH_3O_2 and HO_2 for the calculation of PSS-NO_2. Hence, the measurement based NO_2 data during CAFE Brazil is not independent of model simulations. In comparison to the simple Leighton relationship (Equation 27), which neglects losses of NO with HO_2 and peroxy radicals, the extended PSS equation leads to approx. a factor of two (10-15 ppt) higher results (Hartmann, 2024).

For CAFE Pacific, only the simple Leighton relationship based on the steady-state assumption in Equation 27 was applied to calculate measurement based NO_2 which is valid in the absence of rapid changes in light intensity or reactant concentrations and in polluted areas where the impact of peroxy radicals on NO oxidation is small (Leighton, 2012).

$$[\mathrm{NO_2}]_{\mathrm{PSS}} = \frac{k7[\mathrm{NO_2}][\mathrm{O_3}]}{j\mathrm{NO_2}} \tag{27}$$

where $j\mathrm{NO_2}$ is the photolysis frequency of NO_2 to NO and $O(^3P)$ and k7 is the reaction rate between NO and O_3 forming NO_2 and O_2. As shown by Hartmann (2024) for CAFE Brazil, the impact of peroxy radicals on the photo stationary state concentrations of NO_2 might not be negligible in remote, tropical areas, the uncertainty on the measurement based NO_2 used for the CAFE Pacific analysis has a higher uncertainty possibly also in the range of a factor of 2.

As described in Section 4.4.1, the HYdrogen Peroxide and Higher Organic Peroxides monitor (HYPHOP) monitor was used to calibrate PAA during ground-based experiments because the instruments detects organic peroxides based on dual-enzyme fluorescence spectroscopy (Hamryszczak et al., 2023a). Cross-calibrations with HYPHOP were performed together with Zaneta Hamryszczak, Dirk Dienhart and Antonia Hartmann.

CO was measured with two instruments via infra red absorption spectrometry. One with a tunable diode laser (TRISTAR) and one with a quantum cascade laser (ATTILA) (Ort et al., 2024). The TRISTAR provided 1 s CO data with an flight-dependent total measurement uncertainty between 2.3-9.8 % for CAFE Brazil and between 4.2-7.8 % for CAFE Pacific data.

The Fast accurate airborne ozone instrument (FAIRO) is able to measure ozone (O_3) between an 3-5000 ppb at a frequency of 10 Hz based on a dry chemiluminescence detector calibrated by a dual-beam ultra violet photometer (Zahn et al., 2012).

The charge-coupled device (CCD) array spectroradiometer of FJZ (HALO-SR) derives photolysis frequencies of atmospheric species by measuring actinic flux densities in a spectral range of 280-650 nm (Bohn and Lohse, 2017). For steady-state calculations of PAN, PAA and NO_x I used photolysis frequencies of O_3, HNO_3, HNO_4, CH_3COCH_3, PAN, CH_3CHO, NO_2 and H_2O_2 from the SR instrument at 1 s integration time.

The soot photometer (SP2) instrument is an eight-channel Single particle Soot Photometer with a Nd:YAG Laser at 1064 nm detecting time-dependent scattering and incandescence signals of particles in the size range of 200-400 nm diameter (Holanda et al., 2020). Since the data is not yet calibrated, the raw incandescence signal was used as a qualitative indicator of the presence of refractory black carbon particles.

3.4 CAMS PREDICTIONS FOR FLIGHT PLANNING

For flight-planning during the CAFE campaigns, the PAN forecasts by Copernicus Atmospheric Monitoring Service (CAMS) provided by the European Centre for Medium-Range Weather Forecasts (ECMWF) were used by the mission principle investigators. CAMS provides a global forecast of more than 50 chemical species including PAN in a 0.4 °×0.4 ° resolution for pressure levels between 1-1000 hPa twice a day based on satellite observations merged with an atmospheric computer simulation. The chemical mechanism of the integrated forecast system (IFS) is an extended version of the Carbon Bond 2005[7]. The service package provided by ECMWF extra for the CAFE campaigns in-

---

[7] https://confluence.ecmwf.int/display/CKB/CAMS%3A+Global+atmospheric+composition+forecast+data+documentation, last access: 15th April 2025.

cluded several pressure layers and forecasts for four times a day. CAMS also provides assimilated forecast data with re-processed observations in the EAC4 reanalysis data set with time steps of 3 h (Flemming et al., 2017) which is usually available after several months.

For the post-campaign analysis of CAFE Brazil, I compared measurements to the CAMS reanalysis data EAC4 at five pressure levels (250 hPa, 300 hPa, 600 hPa, 850 hPa, 1000 hPa) and four times per day (0 h, 6 h, 12 h and 18 h coordinated universal time (UTC)). In the case of CAFE Pacific, the reanalysed data was not yet available at the time of the analysis, wherefore I used forecast data for the pressure levels 250 hPa, 300 hPa, 500 hPa, 850 hPa and 1000 hPa at 0 h and 12 h UTC.

3.5 HYSPLIT BACKTRAJETORIES

HYbrid Single-Particle Lagrangian Integrated Trajectory (HYSPLIT)[8] is an atmospheric transport and dispersion model that computes single air parcel trajectories based on the Lagrangian approach provided by National Oceanic and Atmospheric Administration (NOAA) (Stein et al., 2015).The PC-based trajectory model Version 5.2 was used to calculate 10-days backward trajectories along the flight tracks to investigate the origin or sample air masses during CAFE Brazil and CAFE Pacific. One-degree archived meteorological data from the Global Data Assimilation System (GDAS)[9] run by the National Weather Service National Center for Environmental Prediction (NCEP) of NOAA. The HYSPLIT trajectories are a useful tool for a qualitative analysis but are highly dependent on the meteorological conditions and the used vertical transport method which leads to horizontal deviations around 40 % of the traveled distance(Harris, Draxler, and Oltmans, 2005).

3.6 FIRMS SATELLITE OPEN FIRE OBSERVATIONS

A helpful tool, to qualitatively estimate the impact of biomass burning and open fires on the sampled air mass composition are the Fire Information for Resource Management System (FIRMS) satellite observations provided by NASA's Earth Observing System data. The Moderate Resolution Imaging Spectroradiometer (MODIS) instruments globally detect fire events under relatively cloud-free conditions at 1 km-pixel resolution and are mounted aboard the two satellites Aqua and Terra[10].

3.7 EMAC MODEL

In the framework of this work, the observations of PAN and PAA are compared to the general circulation model ECHAM/MESSy Atmospheric Chemistry (EMAC). The EMAC model couples the Modular Earth Submodel System (MESSy2) (Jöckel et al., 2010) to the fifth generation of the General Circulation Model European Centre HAMburg general circulation (ECHAM) model (Jöckel et al., 2006). The horizontal resolution of the

---

[8] `https://www.arl.noaa.gov/hysplit/`, last access: 16th May 2025.

[9] `https://www.ready.noaa.gov/gdas1.php`, last access: 16th May 2025.

[10] `https://modis-fire.umd.edu/af.html`, last access: 29th May 2025.

model is 1.875°× 1.875°and 31 layers up to 10 hPa were used whereof 22 layers are in the troposphere. EMAC includes the Mainz Organic Mechanism (MOM) chemistry scheme (Pozzer et al., 2022; Sander et al., 2019) as well as a lightning parametrization (Grewe et al., 2001; Kurz and Grewe, 2002) and the convection parametrization CONVECT[11]. The model was used to calculate atmospheric species along the flight track every 12 min. Matthias Kohl did the simulation for CAFE Brazil and Anna Martin for CAFE Pacific with the identical model set-up.

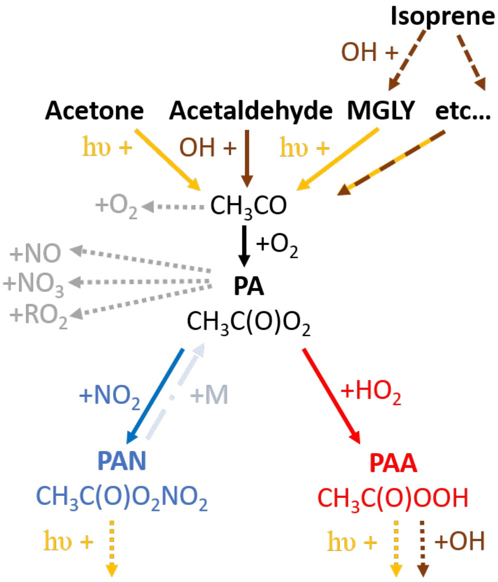

Figure 3.7.1: Schematic of the PAN and PAA chemistry scheme implemented in EMAC. Photolysis are marked with yellow arrows, reactions with OH in brown. Loss reactions of the PA precursor radical and its immediate precursor CH_3CO leading to other products than PAN (blue) or PAA (red) formation are marked with gray arrows.

A schematic of the PAN and PAA-chemistry implemented in MOM is illustrated in Figure 3.7.1. Gas phase reaction rates concerning PAN and PAA formation and loss reactions are take from the latest recommendations from IUPAC[12]. EMAC includes a myriad of organic precursors leading to the formation of the CH_3CO-radical via photolysis (yellow arrows), oxidation with the OH-radical (brown) or by the photo-oxidative degradation of isoprene. The reaction of CH_3CO to $CH_3C(O)O_2$ happens quasi instantaneously and almost completely, only a negligible percentage (3-8 %) follows another reaction pathway with O_2 forming formaldehyde instead of PA. The PA radical is involved in various reactions with organic peroxy radicals (RO_2) as well as NO and NO_3. Both, PAN and PAA are uniquely formed via the PA-radical depending on the abundance of NO_2 and HO_2 relative to the other reactants. The unimolecular decomposition of PAN to PA is highly temperature dependent but can also be induced by photolysis. PAN can also be photolysed to CH_3, NO_3 and CO_2, subsequently forming CH_3CO_2 and being permanently lost. The most relevant tropospheric loss terms of PAA considered

---

[11] https://envmodel.ipa.uni-mainz.de/submodels-convect/, last access: 15th May 2025.

[12] https://iupac.aeris-data.fr/catalogue/#/catalogue/classifications/gap, last access: 15th May 2025.

in the model are photolysis and the reaction with OH. The reaction of PAA with OH (Reaction Equation 42) is in principle also a source of PA but is not depicted as it is very slow with a reaction rate coefficient of $4 \times 10^{-14} \mathrm{cm}^3 \mathrm{molec.}^{-1} \mathrm{s}^{-1}$ (Berasategui et al., 2020) and hence quasi negligible.

3.8 STEADY-STATE CALCULATIONS OF IN-SITU PRODUCED PAN AND PAA

In order to estimate PAN and PAA in-situ production and derive a ***chemical steady-state*** concentration ***based on available measurement data*** for HALO instruments, a simplified chemical scheme compared to EMAC (Figure 3.7.1) is used as shown in Figure 3.8.1. A steady-state condition is reached when the temporal change of a component is zero and hence the sum of all production terms equal the sum of all loss terms. The steady-state concentration of a species ($[\mathrm{species}]_{SS}$) can then be calculated as in Equation 28.

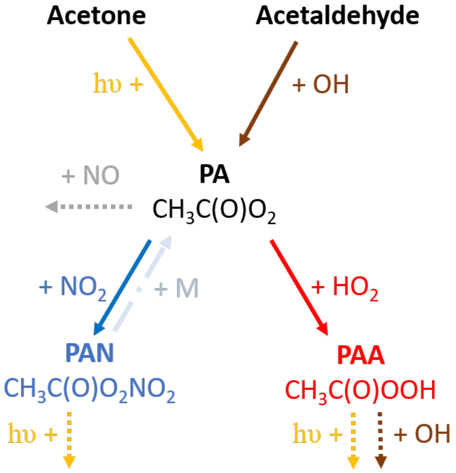

Figure 3.8.1: Schematic of the simplified reaction scheme for PAN and PAA formation and losses used in the steady-state assumption.

$$[\mathrm{species}]_{SS} = \frac{P_{chem} + P_{trans}}{L_{chem} + L_{trans} + L_{depos}} \tag{28}$$

It is worth noting that the simplified steady-state calculation considers only chemical production (P_{chem}) and loss terms (L_{chem}). Specifically, sources (P_{trans}) and losses (L_{trans}) due to vertical and horizontal transport, as well as dry and wet deposition (L_{depos}), are left out. Therefore, the simply chemical steady-state may not be valid under conditions in which other processes than chemical production and loss terms become dominant, e.g. in the case of long-lived species. In addition, the chemical steady-state assumption can also not be applied in phases of twilight, where low photolysis rates are too low to establish a steady state.

In this simplification, which was previously described by Crowley et al. (2025), only the two PA precursors acetone and acetaldehyde (Fischer, Reidmiller, and Jaffe, 2008) which form PA via photolysis (Reaction 29) and oxidation with OH (Reaction 30) respectively are considered. MGLY was not included because none of the instruments aboard HALO measured MGLY.

$$CH_3C(O)CH_3 + h\nu \xrightarrow{2O_2} CH_3C(O)O_2 + CH_3O_2 \tag{29}$$

$$CH_3CHO + OH \xrightarrow{O_2} CH_3C(O)O_2 + H_2O \tag{30}$$

The reaction of PA-radical ($CH_3C(O)O_2$) with NO_2 (Reaction 31) forming PAN competes with the reaction of formation of PA with HO_2 (Reaction 32) and hence the PAA formation (Equation 32a).

$$CH_3C(O)O_2 + NO_2 + M \longrightarrow CH_3C(O)O_2NO_2 + M \tag{31}$$

$$\begin{aligned} CH_3C(O)O_2 + HO_2 &\longrightarrow CH_3C(O)OOH + O_2 && \text{(32a)} \\ &\longrightarrow CH_3C(O)OH + O_3 && \text{(32b)} \\ &\longrightarrow CH_3C(O)O + OH + O_2 && \text{(32c)} \end{aligned}$$

Competing loss reactions with PA other than NO (Reaction 53) are neglected.

$$CH_3C(O)O_2 + NO \longrightarrow CH_3 + CO_2 + NO_2 \tag{53}$$

Daytime mixing ratios of NO_3 are usually very low because of its rapid loss by photolysis (Brown and Stutz, 2012) and are considered not relevant in our simple daytime steady-state assumption. The role of loss reactions of PA with RO_2 is dependent on the availability of organics and will be discussed in the application cases.

3.8.1 *PAN steady-state equations*

From the above equation one can derive the following PAN production rate (P_{PAN}) in $\frac{molec.}{cm^3 \times s}$:

$$P_{PAN} = ([OH][CH_3CHO] \times k30 + [CH_3C(O)CH_3] \times J29) \times f \tag{33}$$

with f being the fraction of the PA-radical leading to PAN formation:

$$f = \frac{k31[NO_2]}{k31[NO_2] + k32[HO_2] + k53[NO]} \tag{34}$$

The considered loss terms of PAN in the simplified reaction scheme are due to thermal decay (Reaction 35) and photolysis (Reaction 36). Losses of PAN towards reaction with OH have been neglected because the reaction rate coefficient of PAN + OH is below $10^{-14} cm^3 molec.^{-1} s^{-1}$ according to IUPAC and is hence not relevant in the UT at typical OH mixing ratios compared the photolysis loss processes.

$$CH_3C(O)O_2NO_2 + M \rightarrow CH_3C(O)O_2 + NO_2 + M \tag{35}$$

$$CH_3C(O)O_2NO_2 + h\nu \rightarrow CH_3C(O)O_2 + NO_2 \tag{36a}$$

$$CH_3C(O)O_2NO_2 + h\nu \rightarrow CH_3CO_2 + NO_3 \tag{36b}$$

Since PAN re-dissociates into the PA-radical (Reaction 35 and Reaction 36a) and leading to reformation of PAN, only the fraction (1-f) is lost via these pathways (Reaction 37). Therefore, the loss rate of PAN (L_{PAN}) can be formulated as given in Reaction 37.

$$L_{PAN} = J36b + (1 - f) \times (J36a + k35) \tag{37}$$

Assuming a steady-state of production and loss terms, where

$$\frac{d[PAN]}{dt} = P_{PAN}(t) - L_{PAN}[PAN](t) = 0$$

the steady-state concentration of PAN (PAN_{SS}) can be calculated as given in Equation 38.

$$PAN_{SS} = \frac{P_{PAN}}{L_{PAN}} \tag{38}$$

3.8.2 *PAA steady-state equations*

Like for PAN, the production rate of PAA consists of a term for acetone photolysis and acetaldehyde oxidation but also includes a term from the PA released due to the thermal dissociation of PAN (Reaction 39).

$$P_{PAA} = ([OH][CH_3CHO] \times k30 + [CH_3C(O)CH_3] \times J29 + [PAN] \times k35) \times g \tag{39}$$

The factor g defines the fraction of PA forming PAA, which corresponds to the factor f in the PAN production (Equation 34).

$$g = \frac{k32[HO_2]}{k31[NO_2] + k32[HO_2] + k53[NO]} \times \alpha \tag{40}$$

The factor g includes the term α which represents the partitioning of the three reaction pathways of PA with HO_2 (Reactions 32a-32c). The fraction α is defined by the ratio of the competing reaction rates(Equation 41) retrieved from IUPAC. Depending on the temperature, in the low and mid-tropospheric region α is usually between 20-40 %.

$$\alpha = \frac{k32a}{k32a + k32b + k32c} \tag{41}$$

Considered losses of PAA in the atmosphere included photolysis (Reaction 43) as well as the reaction with OH (Reaction 42). However, based on the latest research findings, the reaction of PAA + OH Equation 42 takes place very slowly in atmospheric temperatures ($< 4 \times 10^{-14} cm^3 molec.^{-1} s^{-1}$) (Berasategui et al., 2020) and is hence almost negligible compared to the photolysis of PAA.

$$CH_3C(O)OOH + OH \rightarrow CH_3C(O)O_2 + H_2O \tag{42}$$

$$CH_3C(O)OOH + h\nu \rightarrow CH_3O_2 + OH + CO_2 \tag{43}$$

The total loss rate L_{PAA} of PAA can be formulated as in Equation 44.

$$L_{PAA} = J43 + [OH] \times k42 \tag{44}$$

Similar to the steady-state concentration of PAN, the simplified state state concentration of PAA is then given by Equation 45.

$$PAA_{SS} = \frac{P_{PAA}}{L_{PAA}} \tag{45}$$

3.8.3 *Production terms via modelled PA*

For comparison between the EMAC model PAN and PAA mixing ratios and a steady-state calculation, the modelled concentration of the PA-radical ($CH_3C(O)O_2$) can be directly used instead of calculating its production from only acetone and acetaldehyde. The production terms for PAN and PAA are then given by Reaction 46 and Reaction 47 respectively.

$$P_{PANviaPA} = [CH_3C(O)O_2][NO_2] \times k31 \tag{46}$$

$$P_{PAAviaPA} = [CH_3C(O)O_2][HO_2] \times k32a \tag{47}$$

Using the same loss terms for PAN and PAA described in Equation 37 and Equation 44, a steady-state concentration can be derived as described in Equation 48.

$$PAN_{SSviaPA} = \frac{P_{PANviaPA}}{L_{PAN}} \tag{48}$$

$$PAA_{SSviaPA} = \frac{P_{PAAviaPA}}{L_{PAA}} \tag{49}$$

Part II

TECHNICAL BACKGROUND

4

CIMS DATA CALIBRATION

In this chapter, the Chemical Ionisation Mass Spectrometry (CIMS) measurement technique is described in detail. Additionally, the necessary calibrations and correction factors for PAN and PAA data processing of the CIMS instrument are explained. Following a technical description of the instrument, experiments and improvements on the calibration method made in the framework of this thesis are presented. Finally, sources of measurement uncertainties are listed and quantified. The understanding of potential uncertainties related to the CIMS measurements of PAN and PAA is essential for interpreting the results and drawing conclusions from the data collected during the CAFE Brazil and CAFE Pacific campaigns.

4.1 ADVANTAGES OF THE CIMS MEASUREMENT TECHNIQUE

Historically, PAN was first measured during the extensive smog events in Los Angeles in the 1960s by infrared spectroscopy (Stephens, 1969; Stephens, 1987; Tuazon, Winer, and Pitts, 1981). The detection limits of these early measurements were in the range of a few ppb at an almost 1 km long path-length (Tuazon, Winer, and Pitts, 1981). A significant improvement in transportability and sensitivity was achieved with gas chromatography (GC) measurements using an electron capture detector (ECD) (Blanchard et al., 1990; Flocke et al., 2005). These measurements had a LOD of 2 ppt but were limited by slow sampling frequencies of a few minutes (Flocke et al., 2005). In addition, different types of mass-spectrometry methods, such as Negative Ion Chemical Ionization Mass Spectrometry (LOD of approx. 15 ppt at retention times of 2.6 min) (Tanimoto et al., 1999) and PTR-MS (LOD approx. 70 ppt at 15 s integration time) (Hansel and Wisthaler, 2000), were developed to measure different types of PAN-type species. Most recently, the mass spectrometry based on chemical ionisation (CIMS) had been further developed using I^- or SF_6^- as reagent ions and including a thermal dissociation (TD) area, which allows fast measurements of a series of peroxyacyl nitrates and dinitrogen pentoxide by thermally generating acylperoxy radicals (Huey, 2007; Slusher, 2004). The use of these primary ions enables the detection of a broad variety of atmospheric relevant species (Huey, 1995). The major advantage of the CIMS measurement technique is its fast response time of around 1 s at LODs of a few ppt. Additionally the CIMS technique is robust against vibrations, pressure changes, or temperature changes and is transportable, making it suitable for aircraft application in contrast to GC instruments (Roiger et al., 2011; Slusher, 2004).

In the framework of this work, aircraft measurements focusing on the upper troposphere were performed, where PAN levels are expected to be in the range of a few ppt up to a ppb. The CIMS instrument had previously achieved an LOD (2 σ) of 3-4 ppt at an integration time 1 s by using a ^{210}Po ion source (Eger et al., 2019). Details about the current configuration of the instrument and its detection limits are described in this chapter.

4.2 DETECTION OF PAN AND PAA WITH AN I^--CIMS

Mass spectrometry is a widely used tool in atmospheric sciences to separate the components sampled air masses by their mass-to-charge-ration (m/z). The ionisation of the target gas can be achieved by different methods, which vary in the degree of fragmentation. In contrast to hard ionization techniques, such as electron ionisation, chemical ionisation, as used by CIMS, is considered a "soft" technique, resulting in minimal fragmentation of the resulting ions of the target gas. The separation of the resulting ions occurs based on their behaviour in elector-magnetic fields.

4.2.1 *Instrument description*

The configuration of the CIMS instrument, as applied during different aircraft campaigns with the HALO (Gulfstream G550), is depicted in Figure 4.2.1. The CIMS is installed in an aircraft rack with dimensions 65 cm x 55 cm x 140 cm and has a total weight of 135 kg. The measurement principle is based on thermal dissociation of PAN (TD-CIMS) and iodine I^- as reagent ion (Slusher, 2004; Zheng et al., 2011). The instrument details and its ion-source have been described elsewhere (Dörich, 2023; Dörich et al., 2021; Eger et al., 2019; Phillips et al., 2013).

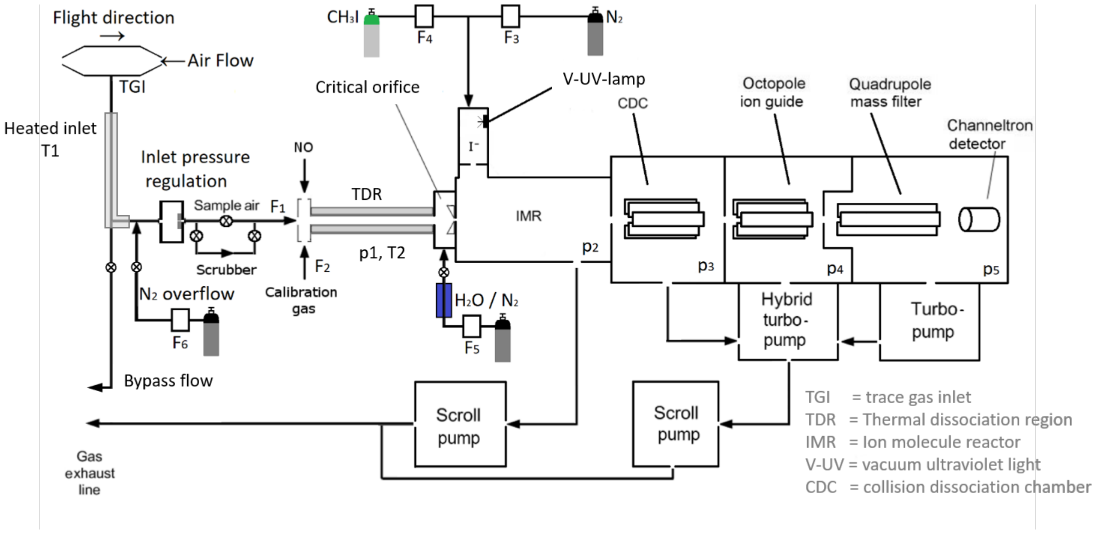

Figure 4.2.1: Scheme of the CIMS instrument designed for aircraft experiments, adapted from Dörich (2023).

A brief description of the measurement principle is given in the following.

Air is sampled via a trace gas inlet (TGI) facing in the direction of flight at the top of the research aircraft at a constant mass flow of 1.4 standard liter per minute (slm) (F1 in Figure 4.2.1) due to a critical orifice with a diameter of 0.8 mm and the inlet pressure regulation which keeps a constant pressure of 100 mbar (p1 in Figure 4.2.1) in front of the Ion molecule reactor (IMR). Due to this set-up, aircraft measurements up to a height of 15 km are possible. The inlet, consisting of 1/4"-perfluoroalkoxyalkane (PFA)-tubing, is heated to 42 °C (T1 in Figure 4.2.1) to reduce the surface-residence time of trace gases. The bypass is connected in such a way that ambient air flows orthogonally to the inlet to reduce the number of large particles entering the instrument. The bypass can be flushed with nitrogen (F6 in Figure 4.2.1) to protect the instrument from extremely polluted air as for example during take-off and landing. For ground applications, the TGI is replaced by a 2 μm pore size teflon membrane filter (Pall).

In order to establish the instrumental background signal, the sampled air is scrubbed by steel wool heated to 140 °C removing acids and nitrates without affecting the mixing ratio of H_2O. Afterwards, the sampled air flows through the thermal dissociation region (TDR), where PAN is converted to $CH_3C(O)O_2$ and NO_2 (Rection 35). The TDR is circa 20 cm long, heated 1/2"-PFA tubing. The optimal temperature of the TDR, where dissociation of PAN is maximal and losses of the PA-radical are minimal, was derived in laboratory experiments as described in Section 4.5.4 and lies between 150-180 °C (T2 in Figure 4.2.1). The IMR is the region where the target gas ionized by the reagent ions I^- and is kept at a constant pressure of 18 Torr (24 mbar, p2 in Figure 4.2.1). The estimated residence time in the IMR is 40 ms (Dörich et al., 2021). The reagent ions are produced by photoionization of methyl iodide (CH_3I) (see Section 4.2.2) wherefore a flow of 5-20 standard cubic centimeter (sccm) (F4 in Figure 4.2.1) is diluted in 750 sccm of dry nitrogend (F3 in Figure 4.2.1).

In the presence of water, I^- forms water clusters ($I^-(H_2O)_n$) which can react at different reaction rates with the target species and form product ions with different numbers of water molecules attached (Jost et al., 2003). Therefore, a careful correction of sensitivity towards humidity must be applied which is discussed in Section 4.5.2. Previous laboratory experiments have shown that in dry air below a relative humidity of 2 % the sensitivity of PAA drops drastically (Phillips et al., 2013) which corresponds to a mixing ration of H_2O of approximately $1e^{16} molec.cm^{-3}$. In the UT at pressures around 240 hPa and -40 °C, typically mixing ratios of water are around 500 ppb which corresponds to $3.9e^{12} molec.cm^{-3}$. To avoid the sensitivity drop in the dry conditions in the UT, the CIMS is equipped with an internal humidifier adding a constant amount of humidity to the IMR. The humidifier consists of a 1/4" PFA tubing filled with distilled water and an inner 1/8" GoreTex tubing flushed with 50 sccm of N_2 (F5 in Figure 4.2.1). It is assumed that the relative humidity inside the inner tubing is about 100 % due to the permeation of water through the inner tubing. The humidified 50 sccm N_2 are diluted in the total flow to the IMR (ca. 2200 sccm) which results in a minimum relative humidity inside the IMR of approximately 2.3 %.

The cluster-ions are de-clustered in the collision dissociation chamber (CDC) region subsequent to the IMR. The CDC region includes an octopole ion guide to accelerate and collimate the ion beam and is kept at a pressure of 0.6 mbar (p3 in Figure 4.2.1). The housing potential ($U_{CDCHouse}$) applied to the CDC is switched between -22.8 V (strong declustering) and -20.5 V (weak declustering) for the detection of the primary ions I^- at $\frac{m}{z} = 127$ and the first water cluster at $\frac{m}{z} = 145$ ($I^-(H_2O)$) respectively. Thus, the number of water molecules inside the IMR can be derived via the ratio between I^- (mass to charge ratio between $\frac{m}{z} = 127$ and $\frac{m}{z} = 145$ as described in Section 4.5.1. Unfortunately, in the CIMS configuration declustering cannot fully be excluded even

the lowest possible declustering potentials and hence the detection of weakly bound adducts is precluded.
After the CDC, another octupole ion guide focuses and guides the negatively charged product ions at a pressure of around $6\text{x}10^{-3}$ mbar (p4 in Figure 4.2.1) and an electric potential of $+20\,V$. The ions are separated by their mass to charge ratio $\left(\frac{m}{z}\right)$ via a quadrupole mass filter at a pressure of approx. $9\text{x}10^{-5}\ mbar$ (p5 in Figure 4.2.1). The direct and alternating voltage at the quadrupole mass filter defining the mass to charge ratio (m/z)-ratio which gets through to the detector is controlled by a radio-frequency generator (Balzer QMH 410-3, 1.44 MHz). During a campaign, 3-10 different m/z-ratios are selected to be monitored. The incoming ions are counted with a channel electron multiplier detector (ITT Ceramx 75550M). Each m/z is resolved into 8 individual channels. The integrated signal in raw counts for at a given m/z are calculated by the sum of these 8 channels.

4.2.2 *Ion chemistry*

Iodide (I^{-}) allows soft ionization with low fragmentation during the ionisation process and is a widely used reagent ion for CIMS instruments (Huey, 2007; Lee et al., 2014; Phillips et al., 2013; Slusher, 2004). I^{-}, which has a large mass-to-charge ratio is ($\frac{m}{z} = 126.905$), is a weak gas-phase base and has a high electro-negativity. Therefore, iodide can be used to detect many ubiquitous atmospheric species via electron transfer or proton abstraction (Huey, 1995; Lee et al., 2014). time-of-flight (ToF) spectrometer coupled CIMS instruments are able to detect a wide range of more polar and acidic VOCs based on I^{-} adduct chemistry in the range of $\frac{m}{z} = 25\text{-}625$ (Lee et al., 2014). High-resolution and lower detections limits are achieved by using the large negative mass defect ($\delta_m = -0.096\,Th$) of iodide as an additional degree of separation of the product ions (Lee et al., 2014) and allowed the detection of adducts with binding enthalpies to iodide higher than about 26 cal/mol (Iyer et al., 2016).

A vacuum ultra violet (V-UV) lamp, as described by Dörich (2023), is used to photo-ionize methyl iodide (CH_3I) at 116.5 nm (photon energy = 19.64 eV) and 123.5 nm (photon energy = 10.03 eV, exceeding the ionization potential of 9.54 eV of CH_3I (Ji et al., 2020)). The photoelectrons attach to CH_3I and form I^{-} which is used to detect both PAN ($CH_3C(O)O_2NO_2$) and PAA ($CH_3C(O)OOH$) as $CH_3C(O)O^{-}$ at $\frac{m}{z} = 59$ via the following reaction scheme:

$$CH_3C(O)O_2NO_2 + M \rightarrow CH_3C(O)O_2 + NO_2 + M \tag{50}$$

$$CH_3C(O)O_2 + I^{-} \rightarrow IO + CH_3C(O)O^{-} \tag{51}$$

$$CH_3C(O)OOH + I^{-} \rightarrow HOI + CH_3C(O)O- \tag{52}$$

PAA is directly ionized by the reaction with I^{-} forming $CH_3C(O)O^{-}$ (Reaction 52). In contrast, PAN is first thermally dissociated in the TDR to form $CH_3C(O)O_2$ (Reaction 50) which is then ionized to $CH_3C(O)O^{-}$ in the IMR (Reaction 51).
To differentiate the signal of PAN and PAA on $\frac{m}{z} = 59$, NO is periodically added in front of the TDR to titrate the contribution of PAN to $\frac{m}{z} = 59$ (Reaction 53).

$$CH_3C(O)O_2 + NO \rightarrow CH_3 + CO_2 + NO_2 \tag{53}$$

Similarly to the PAN-detection method, the CIMS instrument can also detect other PAN-homologues such as PPN ($C_2H_5C(O)O_2NO_2$; $\frac{m}{z} = 73$), MPAN ($\frac{m}{z} = 85$), peroxyisobutyryl nitrate (PiBN) ($\frac{m}{z} = 87$) and trifluoroacetyl nitrate (fPAN) ($\frac{m}{z} = 111$).

4.3 PAN CALIBRATION

The raw CIMS signal is given in ion counts in defined integration time. Assuming that only a few percent of the reagent ions are consumed in the ionisation process and hence their concentration is approximately constant, the concentration of the target gas [P] can be derived from the raw signal of the target gas P^- via the following equation:

$$[P] = \frac{[P^-]}{[R^-] \times S_{eff}} \tag{54}$$

In Equation 54, the raw counts of the target gas [P] ($\frac{m}{z} = 59$) are normalized by the raw signal from the primary ion (R^-, $\frac{m}{z} = 127$) to account for drifts in the primary ion signal for example due to variations in the ion source, ion transmission or detector response. S_{eff} is the effective instrument sensitivity and represents the product of an effective rate constant and an effective reaction time (Huey, 2007). The instruments effective sensitivity can be derived from a calibration standard with a known amount of the analyte. It can be optimized by adjusting flows, electric potentials and resolution (Eger, 2019) but may vary depending on many factors like temperature and humidity. Hence, S_{eff} must be monitored regularly. Therefore, the CIMS contains an internal photochemical source (see Section 4.3.1) producing a PAN calibration standard which is added before the TDR to the IMR (F2 in Figure 4.2.1). The automatized calibration sequence is described in Section 4.3.2.

4.3.1 *Internal photochemical source*

The photochemical source is a quartz glass reactor with a volume of 150 ml in which PAN is formed via the photolysis of acetone at 285 nm and the reaction with NO (Eger et al., 2019; Flocke et al., 2005; Warneck and Zerbach, 1992). A ventilator next to the reactor prevents the reactor from getting too hot. The formation of PAN taking place inside the reactor is described in the following reaction scheme:

$$CH_3C(O)CH_3 + h\nu \xrightarrow{O_2} CH_3C(O)O_2 + CH_3O_2 \tag{29}$$

$$CH_3O_2 + NO \xrightarrow{O_2} HCHO + HO_2 + NO_2 \tag{55}$$

$$CH_3C(O)O_2 + NO \longrightarrow CH_3 + CO_2 + NO_2 \tag{53}$$

$$CH_3C(O)O_2 + NO_2 + M \longrightarrow CH_3C(O)O_2NO_2 + M \tag{31}$$

$$CH_3C(O)O_2 + HO_2 \longrightarrow CH_3C(O)OOH + O_2 \tag{32a}$$

$$\longrightarrow CH_3C(O)OH + O_3 \tag{32b}$$

$$\longrightarrow CH_3O_2 + OH \tag{32c}$$

The CIMS instrument is equipped with gas mixtures (Air Liquide) in bottles of 0.4 - 2 l which are used to run the photochemical source to provide a constant and well-defined amount of PAN for regular calibrations during field experiments. According to the previous reaction scheme, each NO molecule yields to the formation of a NO_2 molecule via Equation 53 or Equation 55 and hence to a PAN molecule. In reality the conversion is slightly less than 100 %. The conversion efficiency of NO to PAN was determined by Eger et al. (2019) to be 0.9 - 0.95 which is in line with reported values in the literature (Pätz et al., 2002; Volz-Thomas, Xueref, and Schmitt, 2002). Based on this assumption, the concentration of PAN produced in the source (c_{PAN}) can be calculated as follows from the concentration of NO (c_{NO}) and the flow rates of NO (F_{NOS}) and acetone (F_{acet}):

$$c_{PAN}(in\ source) = c_{NO}\, x\, \frac{F_{NOS}}{(F_{NOS} + F_{acet})}\, x\, conversion\ efficiency \tag{57}$$

The flow out of the photochemical source is added to the IMR (F2 in Figure 4.2.1) where it is diluted in the total instrument flow ($F_{CIMS} = 1400$ sccm). Hence, the amount of PAN in the IMR is given by Equation 58.

$$c_{PAN}(in\ IMR) = c_{NO} \times \frac{F_{NOS}}{F_{CIMS}} \times conversion\ efficiency \tag{58}$$

The calibration concentration of PAN for the different campaigns is given in Table 2.

	CAFE Brazil	CAFE Pacific	BAIRN-VIP
$CH_3I/N_2(F_{CH_3I})$	200 ppm (5 sccm)	200 ppm (5 sccm)	200 ppm (20 sccm)
Acetone/Synair (F_{acet})	200 ppm (50 sccm)	200 ppm (40 sccm)	10 ppm (37 sccm)
Acetone C-isotope	^{12}C	^{13}C	^{13}C
$NO/N_2(F_{NOS})$	1 ppm (5 sccm)	1 ppm (5 sccm)	0.25 ppm (5 sccm)
$NO/N_2(F_{NOT})$	0.1 % (10 sccm)	0.1 % (5 sccm)	0.1 % (5 sccm)
PAN in source	82 ppb	100 ppb	27 ppb
PAN in IMR	3.214 ppb	3.214 ppb	0.804 ppt

Table 2: PAN calibration concentrations during three measurement campaigns CAFE Brazil, CAFE Pacific and BAIRN-VIP, based on used gas mixtures and flow rates in standard cubic centimeter (sccm).

Based on the calibration concentration, the instruments sensitivity for PAN can be derived in normalized counts per ppt.

4.3.2 *In-flight calibrations*

During field experiments, the CIMS runs in a fully automated cycle, alternating between the following six process states (ProcState) which are controlled by an in-house built controller unit:

1. Ambient: measuring ambient air
2. PanTit: adding NO to ambient air to remove the contribution of PAN type species to the total signal by titration of the $CH_3C(O)O_2$ radical in the inlet
3. Zero: scrubbing ambient air

4. PanCal: adding calibration standard from the internal photochemical source
5. CalTit: adding NO to titrate the contribution of PAN to the total calibration signal
6. Protect: flushing the inlet with N_2 at take-off and landing (triggered by an aircraft speed-limit below 15 m/s)

The duration of Ambient and PanTit ProcStates was set to 2.5 min during CAFE Brazil and BAIRN-VIP and to 2 min during CAFE Pacific. A calibration cycle (Zero + PanCal + CalTit) was performed at least once per hour, usually automatized but could optionally be paused or manually triggered by the in-flight operator in HALO to optimize data coverage. The averaged signal during the PanCal ProctState must be corrected by the subsequent average CalTit signal to obtain the net contribution of PAN from the calibration standard. The result of all in-flight in-situ calibrations for CAFE Brazil (left panel) and CAFE Pacific (right panel) is shown in Figure 4.3.1 with respect to the altitude where the calibration took place. As seen in Figure 4.3.1, the normalised PAN signal per primary ion ($\frac{m}{z} = 127$) is dependent on altitude (and hence humidity) but decreasing almost linearly below an altitude of about 10 km. Since the laboratory experiments described in Section 4.5.2 showed that the instrument sensitivity to PAN is basically independent on humidity, this loss in calibration signal was attributed to matrix effects in wet air masses with by-products of the photochemical source leading to a loss of $CH_3C(O)O^-$ anions in the IMR. As will be discussed in Section 4.5.3, a correction factor of ca. 0.86 was applied to account for these losses of $CH_3C(O)O^-$ anions during calibration and only the high-altitude in-situ calibrations in dry air masses were considered for the in-situ calibration. More specifically, for each flight an average calibration signal from the calibrations above 10 km altitude (gray dashed line in Figure 4.3.1) was used to derive the flight-wise PAN sensitivity.

On average, the normalized PAN signal ($\frac{m/z59}{m/z127}$) from high-altitude in-flight calibrations was 0.15 ± 0.02 during CAFE Brazil and $0.11 \pm 0.0.1$ during CAFE Pacific. Knowing the PAN concentration in the IMR provided by the photochemical source (see Table 2), one can derive the sensitivity in each calibration cycle in the unit of normalized signal per ppt (m59/m127 per ppt) which is $5.6 \pm 0.7 \times 10^{-5}$ and $4.0 \pm 0.4 \times 10^{-5}$ for CAFE Brazil and CAFE Pacific respectively.

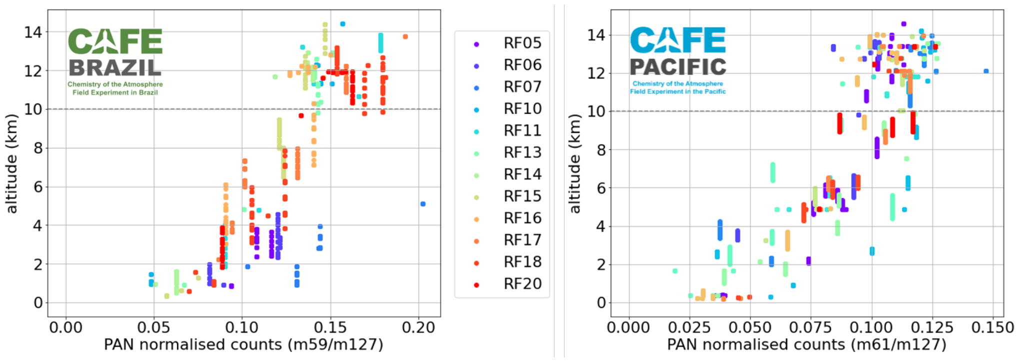

Figure 4.3.1: Normalized PAN signal from calibrations during all PAN measurement flights during CAFE Brazil (left panel) and CAFE Pacific (right panel). The gray dashed line indicates the altitude threshold of 10 km above which data were used for the analysis.

4.3.3 *Isotopic standard*

As shown in Table 2, the PAN concentration used for calibration is approximately 3 ppb, which significantly exceeds the expected PAN levels in remote areas. During CAFE Brazil, a memory effect of the calibration PAN concentration was observed. Specifically, an exponential decrease in ambient PAN was found during the first 30 s after every calibration cycle. To mitigate this issue, the photochemical source was modified to use ^{13}C isotopically labeled acetone instead of the usual ^{12}C in the subsequent measurement campaigns CAFE Pacific and BAIRN-VIP. The ^{13}C-labeld acetone contains two ^{13}C atoms, which allowes the produced PAN (and PAA) in the photochemical source to be detected at $\frac{m}{z} = 61$ instead of $\frac{m}{z} = 59$, thereby differentiating it from ambient PAN. The isotopically labeled ^{13}C-PAN from the calibration standard exhibits the same ion chemical behavior as ^{12}C-PAN (Roiger et al., 2011; Zheng et al., 2011).
A mixture of around 200 ppm isotopically labeled acetone was prepared by mixing a commercial 99 % Acetone-^{13}C (Aldrich) with synthetic air. Furthermore, the mass resolution at small masses was improved to a full width at half maximum of less than 1 amu in order to separate the peak at $\frac{m}{z} = 61$ from neighbouring peaks at $\frac{m}{z} = 59$ and $\frac{m}{z} = 62$, as shown in Figure 4.3.2. The use of isotopically labeled calibration standard eliminates the memory effects of exceeding calibration concentrations on ambient measurement, thereby improving the data quality.

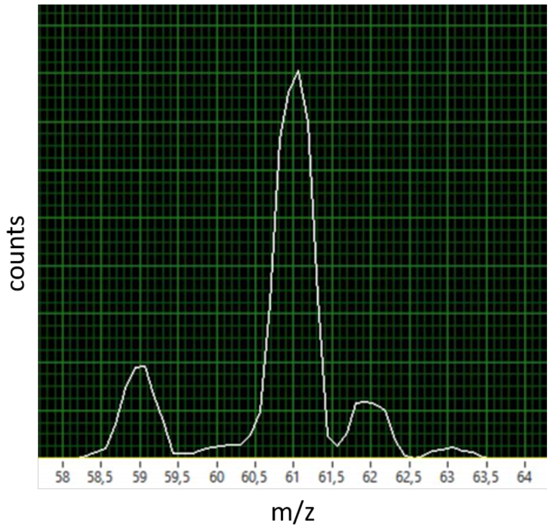

Figure 4.3.2: Spectrum of synthetic air mixed with the CIMS internal photochemical sources run with ^{13}C-acetone, showing that the peak at $\frac{m}{z} = 61$ is clearly separated from the peaks on $\frac{m}{z} = 59$ and $\frac{m}{z} = 62$.

In contrast to periodic calibrations as described in Section 4.3.2, a continuous calibration system can be implemented when using the isotopically labeled standard. The major advantage of a continuously added isotopically labeled standard is a continuous monitoring of the instruments performance and sensitivity in all kinds of air masses. For example, successful airborne CIMS measurements of SO_2 have been performed with a continuously added isotopically labeled calibration standard (Roiger et al., 2011; Thornton et al., 2002; Zheng et al., 2011). A continuous calibration system was tested during CAFE Pacific, but it encountered an interference of the isotopically labeled acetate anion ($CH_3C(O)O^-$, $\frac{m}{z} = 61$) with acetic acid, which is detected as well at $\frac{m}{z} = 59$ via Reaction 59. This process is irrelevant if only ^{12}C-atoms are available, but it leads to a significant overestimation of PAN if acetic acid levels in the atmosphere are high.

$$^{13}CH_3^{13}C(O)O^- + ^{12}CH_3^{12}C(O)OH \rightarrow ^{13}CH_3^{13}C(O)OH + ^{12}CH_3^{12}C(O)O^- \quad (59)$$

4.4 PAA CALIBRATION

In the framework of this thesis, different calibration methods for PAA were tested during and in between the measurement campaigns.

During CAFE Brazil, a PAA diffusion source was used to cross-calibrate against the HYPHOP instrument (see Section 4.4.1). Unfortunately, during CAFE Pacific, the cross-calibrations with HYPHOP did not work due to technical problems with HYPHOP and post-campaign calibrations in the laboratory had to be performed. In the laboratory, a PAA permeation source was analysed using a wet-chemical method involving the oxidation of iodide to triiodide (I_3) and its detection in solution (see Section 4.4.2). This method was also applied during the BAIRN-VIP ground-campaign in Finland.

Figure 4.4.1 shows the resulting relationships between the normalized PAA signal (m59/m127) and the PAA mixing ratio derived with the different methods at the given primary water cluster ratio (m145/m127). The slope of the linear relationship in Figure 4.4.1 gives the calibration factor at the specific m145/m127 ratio during the experiment. The humidity dependency of PAA is discussed in Section 4.5.2.

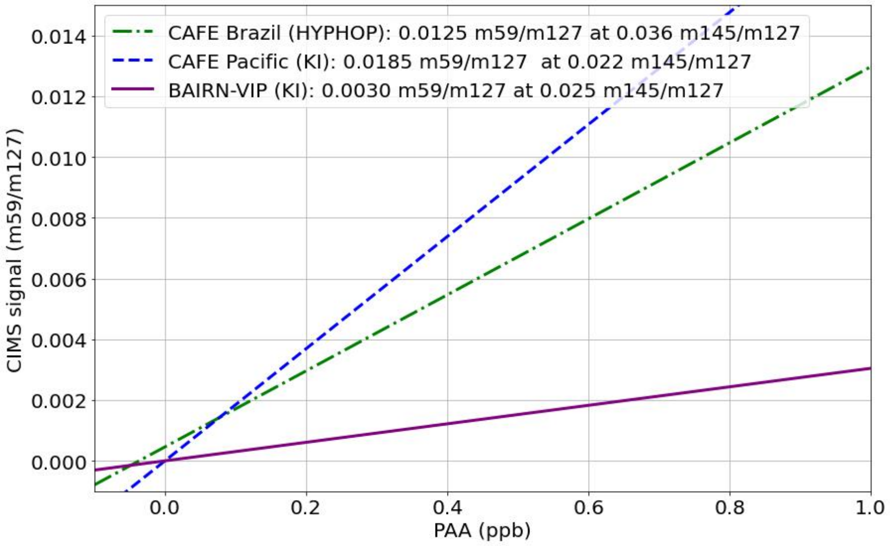

Figure 4.4.1: Calibration factors used for the three measurement campaigns CAFE Brazil, CAFE Pacific, and BAIRN-VIP, based on either a cross-calibration with HYPHOP or the potassium iodide (KI)-method at the ratio m145/m127 at which the experiments were performed.

4.4.1 *PAA cross-calibration with HYPHOP*

The HYPHOP monitor measures hydrogen peroxide (H_2O_2) and organic peroxides (ROOH) by dissolving theses gases into the liquid phase and analysing them based on dual-enzyme fluorescence spectroscopy (Hamryszczak et al., 2023a).

HYPHOP was operated aboard HALO during all CAFE campaigns. In ground experiments during CAFE Brazil, the two instruments CIMS and HYPHOP wer connected in series after a PAA diffusion source diluted in a total flow of synthetic air of 7 l/min at 1.5 bar. The distance between CIMS, mounted in the front of the aircraft, and HYPHOP, mounted in the back, was bridged by a 8 m long 1/4"-PFA tubing. In front of the HYPHOP inlet, a T-piece of PFA was connected serving as overflow. The PAA diffusion source consists of a glass tube filled with a commercial Peracetic acid solution (35 %) in acetic acid (ThermoFisher) and was added to the flow via a bypass in front of both instruments outside of the aircraft. The PAA-diffusion source was closed with a valve which was opened for a few seconds after a stabilisation time of around 1.5 h. The resulting spike in PAA and its exponential decrease is depicted in Figure 4.4.2.

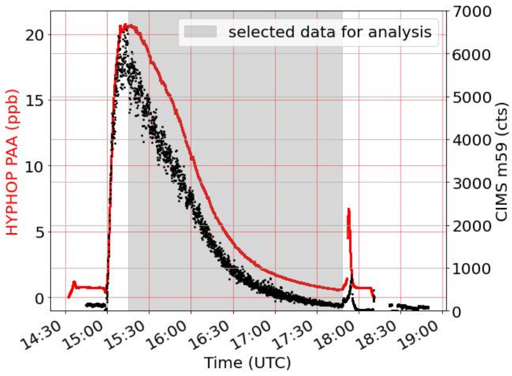

Figure 4.4.2: Measured PAA concentration with HYPHOP (red) and simultaneously measured counts on $\frac{m}{z} = 59$ with CIMS (black) from a PAA diffusion source in a ground experiment on 18th of December 2022 during CAFE Brazil.

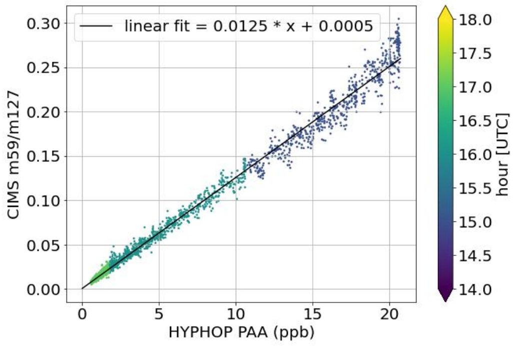

Figure 4.4.3: Linear fit to HYPHOP's PAA measurements versus normalized counts on CIMS, derived from the experiment shown in Figure 4.4.2. The slope gives the CIMS measurement sensitivity for PAA. Data points are colour-coded with the time of the experiment.

Inside HYPHOP, the sampling air first passes through a stripping coil of glass where the peroxides are dissolved in a buffer solution of potassium hydrogen phthalate (KHP) and sodium hydroxide (NaOH) in purified water with a pH of 6. The stripping efficiency of PAA was determined experimentally by Bauer (2012) to 0.89 ± 0.06. Subsequently, the sampling solution is divided into two similar reaction channels, one measuring the total concentration of hydroperoxides and one where catalase is added to destroy H_2O_2 allowing only organic peroxides to survive. The catalase destruction efficiency of H_2O_2 in this channel lies between 0.95 and 0.99, according to Hamryszczak et al. (2023a). Note that in watery solutions, PAA is in equilibrium with H_2O_2:

$$CH_3C(O)OH + H_2O_2 \rightleftharpoons CH_3C(O)OOH + H_2O \tag{60}$$

Hence, inside HYPHOP PAA is partly converted into H_2O_2 while the remaining PAA will be measured as organic peroxide. Assuming that the amount of H_2O_2 in the headspace of the diffusion source is negligible and only PAA diffuses into the sampling air, the H_2O_2 signal given by HYPHOP only results from the reaction of PAA with H_2O (Reaction 60). The total concentration of hydroperoxides provided by HYPHOP divided by the stripping efficiency gives the concentration of PAA during the experiment. Figure 4.4.3 shows the linear correlation between normalized counts on $\frac{m}{z} = 59$ measured with CIMS and the concentration of PAA measured with HYPHOP during the ground experiment performed on 18th of December 2022 during the CAFE Brazil campaign. The slope of the linear fit gives the measurement sensitivity of CIMS on PAA in normalized counts per ppb and is also depicted in Figure 4.4.1 (green dash-dotted line).

4.4.2 *UV/VIS-spectroscopy of PAA in KI-solution*

The method is based on the oxidation of Iodide ions (I^-) by PAA in acidic solution forming triiodide ions (I_3^-) as shown in Reaction 61 (Awad and Ohsaka, 2003) and is from here on referred to as "KI-method". In the KI-method, the mixing ratio of PAA in the outflow of an in-house built permeation source is quantified via optical absorption.

$$CH_3C(O)O_2 + 2I^- + 2H^+ \rightarrow CH_3C(O)OH + I_2 + H_2O \tag{61}$$

$$I_2 + I^- \rightleftharpoons I_3^- \tag{62}$$

The absolute concentration of I_3^- in the solution can be measured via UV/VIS spectroscopy based on Lambert-Beer's law of absorption (Equation 63):

$$A(\lambda) = c \times l \times \epsilon(\lambda) \tag{63}$$

In Equation 63, $A(\lambda)$ is the wavelength dependent absorption, c the concentration of the absorbent in the solution, l the path length, and $\epsilon(\lambda)$ the material specific molar extinction coefficient. The triiodide extinction coefficient $\epsilon(\lambda)$ was determined by Awtrey and Connick (1950) to be 26400 l/mol/cm at 353 nm. The triiodide extinction coefficient spectrum $\epsilon(\lambda)$ measured by John Crowley was used as reference spectrum. The reference spectrum was obtained by adding a known amount of I_2 to a concentrated KI-solution and normalising the absorbance spectrum to the second extinction maximum at 353 nm of the absorbance spectrum by Awtrey and Connick (1950).

The in-house built permeation source consisted of a glass tube where a coiled approx. 1 m long piece of 1/16"- PFA-tubing is immersed in commercial PAA solution (35 % peracetic acid in acetic acid, ThermoFisher). The permeation source was flushed by a constant flow of nitrogen (N_2). To quantify the PAA concentration in the outflow of the permeation source, a solution of 5.2 g KI in highly diluted sulfuric-acid (around $2.5 \text{ x } 10^{-3} H_2SO_4 mol/l$) was prepared. To prevent the iodide from being oxidised by dissolved O_2, the KI-solution was constantly deoxygenated by flowing nitrogen until shortly before using it. After de-oxygenation, a sample volume of 20 ml (V_{sample}) of the KI-solution was taken and filled into a light-protected glass vessel. The sample KI-solution was flushed by the outflow of the permeation source with a flow ($F_{bubbler}$) of 20 sccm for 40-180 min ($t_{bubbling}$). Afterwards, the sample solution was filled in a cuvette of 3 cm length to measure its absorbance in the UV/VIS-spectra of a deuterium

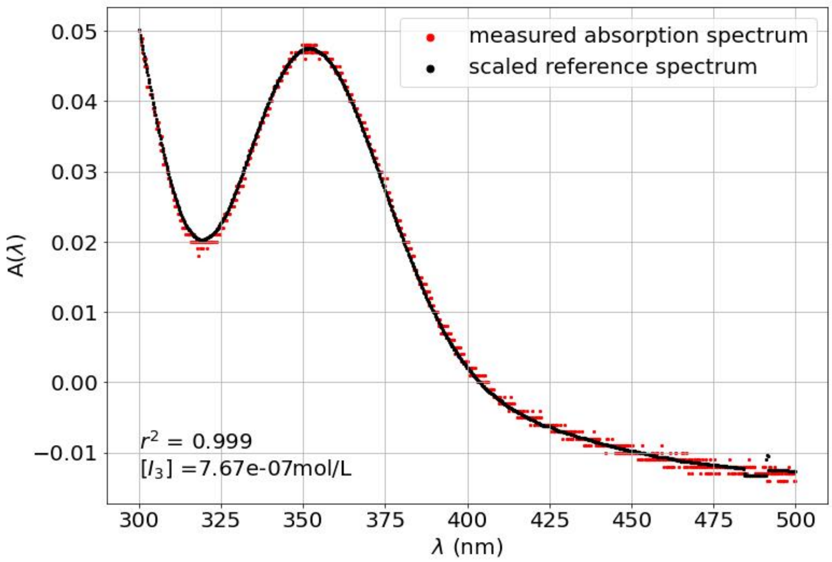

Figure 4.4.4: Absorption spectrum of triiodide measured in the KI-sample solution flowed with PAA from a permeation source for 155 min on 10th September 2024 during the BAIRN-VIP measurement campaign in Finland (red) and fitted triiodide extinction coefficient reference spectrum (black). For further details regarding the reference spectrum, please refer to the accompanying text. The coefficient of determination r^2 and the derived concentration of I_3^- from the experiment is given in the lower left corner.

lamp (Hereus L2D2[13]). The Charge Coupled Device (CDC)-spectrometer (ocean optics USB4000[14]) is responsive to 200-1100 nm. The background subtracted absorbance spectrum of the sample solution was fitted with a ordinary least square method to the reference spectrum of Awtrey and Connick (1950) (Figure 4.4.4). According to Lambert-Beer (Equation 63), the absorption and the extinction are linearly correlated. Hence, dividing the fitting factor by the length of the cuvette gives the concentration of triiodide ions $[I_3^-]$ in the sample solution. Given the sample volume, the bubbling time of KI-solution with PAA, and the bubbling flow, one can calculate the mixing ratio of PAA (MR_{PAA}) from $[I_3^-]$ with the following equation:

$$MR_{PAA} = \frac{[I_3^-] \times V_{sample}}{F_{bubbler} \times t_{bubbling}} \times efficiency_{bubbler} \times frac_{\frac{PAA}{H_2O_2}} \tag{64}$$

Base on experiments by Friedrich (2015) with two bubblers in series which showed quasi no residual PAA uptake in the second sample solution, therefore 100 % uptake of PAA by the KI-solution ($efficiency_{bubbler} = 1$) is assumed. The contribution of H_2O_2 from the permeation source ($frac_{\frac{PAA}{H_2O_2}}$) was set to 0 assuming that H_2O_2 in the liquid phase did not permeate through the tubing of the permation source into the gas flow. Figure 4.4.5 shows that the triiodide ion concentration is indeed linearly correlated to the bubbling time in all experiments ($r = 0.97$) leading to a mixing ratio of PAA (MR_{PAA}) of approx. 120 ppb. Details to all performed KI calibration experiments are

---

[13] https://uvison.com/download/Hamamatsu/L2D2info.pdf, last access: 02.04.2025.

[14] https://spectrecology.com/wp-content/uploads/2020/11/USB4000-Data-Sheet.pdf, last access: 02.04.2025.

given in Figure A.0.4 in the appendix. The permeation rate of the permeation source can be calculated from the derived mixing ration MR_{PAA} and $F_{bubbler}$. Diluting the outflow of the permeation source in a known flow of synthetic air and measuring the PAA signal at CIMS promptly after the determination of the permeation rate, allows to derive the sensitivity of CIMS towards PAA. For the post-campaign calibration of CAFE Pacific PAA data, the average of experiments M21-M26 (see Figure A.0.4) were used to derive the sensitivity of 0.0185 ± 0.0051 m59/m127 per ppt shown in Figure 4.4.1. During the BAIRN-VIP in Finland, the three KI calibration experiments finland-finland3 were performed and led to an average sensitivity of 0.0030 ± 0.025 m59/m127 per ppt.

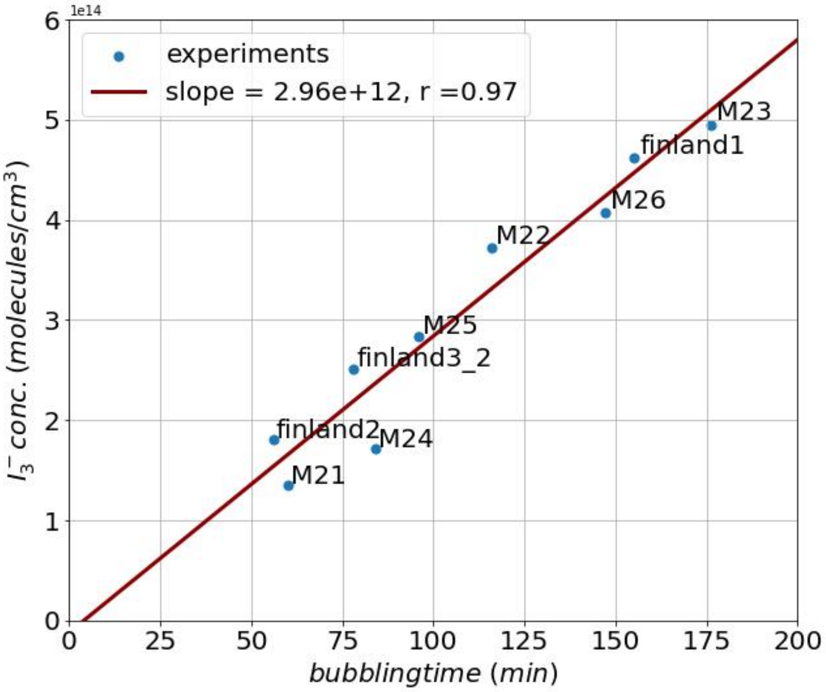

Figure 4.4.5: Linear fit (red line) through the measured triiodide concentration depending on the bubbling time of the KI-solution with PAA. The data is derived from laboratory experiments (M21-M26) and experiments during the field campaign in Finland (finland1-3).

Like PAA, H_2O_2 can produce I_3^- in the same way (Reaction 65) even though the reaction rate is much slower than PAA with I^- (Awad, Oritani, and Ohsaka, 2003; Xiao et al., 2019). Since PAA in water is in an equilibrium with acetic acid and H_2O_2 (Reaction 60), the unknown contribution of H_2O_2 from the permeation source is a source of uncertainty in this method.

$$H_2O_2 + 2I^- + 2H^+ \rightarrow I_2 + 2H_2O \tag{65}$$

4.5 POST-CAMPAIGN LABORATORY STUDIES

The ion chemistry in the IMR of the CIMS is impacted by many factors like absolute humidity, temperature, and impurities in the gas mixtures. To quantify these effects and the accuracy of derived mixing ratios of PAN and PAA, a number of post-campaign experiments were performed in the laboratory and are presented in this section.

4.5.1 *m127/m145 ratio as a measure of humidity*

The primary-ion signal ($\frac{m}{z}=127$) depends on the concentration of CH_3I, the output of the ionization lamp, the ion transmission, and the efficiency of the detector. Changes may be induced each time instrument settings are changed, the instrument is switched on and off or is transported. Even though the effective sensitivity of the instrument (Equation 54) may change, the signal relative to other measured massed should behave similarly. The ratio of $\frac{m}{z}=145$ ($I^-(H_2O)$)) to $\frac{m}{z}=127$ (I^-) was used as a measure of the mixing ratio of H_2O in the IMR to derive the humidity dependency of the measurement sensitivity. As described in Section 4.2.1, the declustering potential applied to $U_{CDCHouse}$ is set to -22.8 V when measuring $\frac{m}{z}=127$ which declusters weakly bound structures like water clusters. Hence, the signal on $\frac{m}{z}=127$ represents the sum of unbound I^- ions and its declustered water clusters $I^-(H_2O)_n$. When measuring $\frac{m}{z}=145$, $U_{CDCHouse}$ is set at -20.5 V and a fraction of approx. 1/6 of $I^-(H_2O)$) survives the CDC region (Dörich et al., 2021).

The relationship between m145/m127 and relative humidity was experimentally derived in ground experiments for each campaign. In the experimental set-up, CIMS sampled an excess of synthetic air with a T-piece in front of the inlet line serving as overflow. To humidify the synthetic air, a bypass through a glass gas wash-bottle containing distilled water was added to the inflow. By partly opening the bypass valves, the amount of humidity can be varied and was measured via a humidity sensor. The maximum reached humidity hereby was around 80 %. All experiments were performed at atmospheric pressure at ambient temperature. Taking into account the pressure reduction until the IMR, one can calculate the number of molecules per cubic centimeter inside the IMR via the saturation water pressure at a given temperature and the ideal gas law.

Figure 4.5.1 shows the m145/m127 ratio plotted against the number of water molecules in the IMR as it was measured during or in the following the different campaigns. The data sets were fitted with a logarithmic function ($f(x) = c \times \ln(a - b \times x)$). I^- and H_2O are in equilibrium in the IMR with the equilibrium constant K_{eq} (Equation 66) which was estimated to be $k_{eq} = 1.16 \times 10^{-15} cm^3 molec.^{-1}$ at 298 K by Dörich et al. (2021). The form of the curve can be explained by the fact that the signal on $\frac{m}{z}=127$ includes not only the equilibrium concentration of I^- but as well the declustered water adduct ($I^-(H_2O)$) which leads to a flattening towards higher humidity.

$$k_{eq} = \frac{[I^-(H_2O)]}{[I^-][H_2O]} \tag{66}$$

The ratio of m145/m127 for the three campaigns followed the same fit function, but resulted in different fit parameters because the relative sensitivities at $\frac{m}{z}=145$ and $\frac{m}{z}=127$ were different. The relationships from Figure 4.5.1 were used to compare the relative sensitivity dependency on humidity for the different campaigns as described in the following Section 4.5.2. The y-axis offset of the curves is caused by the continuous flow of humidified air added inside the CIMS to the IMR as described in Section 4.2.1.

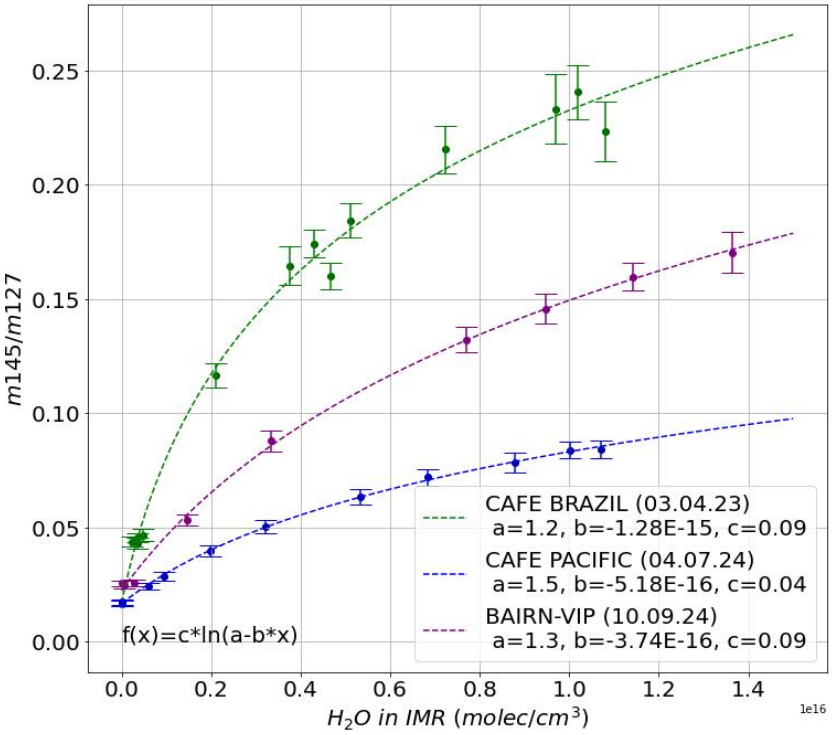

Figure 4.5.1: Relationship between the ratio m145/m127 and water molecules inside the IMR during all measurement campaigns. The error bars indicate the standard deviation for each measurement point. Data points were fitted with the natural logarithmic function, as given in the lower left corner.

During the aircraft campaigns, H_2O mixing ratios were measured aboard HALO with the BAHAMAS instrument. Exemplarily, the correlation between BAHAMAS mixing ratios and CIMS m145/m127 ratio is shown in Figure 4.5.2 which shows a similar logarithmic relationship. It can be concluded that the use of m145/m127 as a measure of H_2O in the IMR was justified.

4.5.2 *Sensitivity dependence on humidity*

The change in sensitivity for PAN and PAA due to humidity was tested in laboratory experiments for the configurations of the CIMS instrument for each measurement campaign. The chemical ionisation measurement technique is sensitive to humidity because the primary ions are able to form water clusters and these cluster may react with different rate coefficients with the trace gas to be detected (Jost et al., 2003; Zheng et al., 2011). Hence, the instrument sensitivity for any particular trace gas may depend on the abundance of H_2O-clusters and the extent of declustering of these weak-bonds (Eger et al., 2019).

It is known that the detection of PAA has a quite complex dependence on humidity (Phillips et al., 2013) while there is no or only little dependency expected for PAN (Eger, 2019; Slusher, 2004).

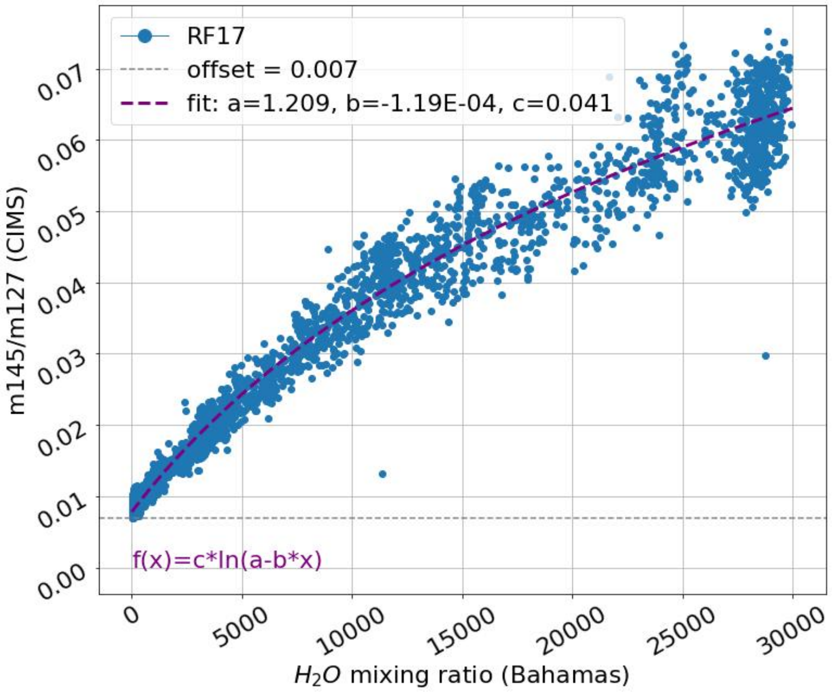

Figure 4.5.2: Relationship between CIMS m145/m127 ratio and measured humidity with the BAHAMAS instrument aboard HALO in research flight (RF)17 on 15th February 2024 during CAFE Pacific. Data was fitted with the logarithmic function given in the lower left corner.

4.5.2.1 *Experimental set-up*

The humidity dependence of CIMS' PAN measurements were quantified for the in-situ calibrations of the internal photo-chemical source as well as for a diffusion source added via a bypass to the flow of synthetic air to the CIMS in ground set-up. The diffusion source is a glass tube closed by valves and filled with PAN sample solution diluted in tridecan (Wüst et al., 2024). To avoid the decay of PAN in the solution, the diffusion source was at 0 °C during the experiments. Relative humidity (RH) was added to the synthetic air flow with a gas washer cylinder of glass as described in Section 4.5.1 and measured with a humidity sensor (Innovative sensor technology[15]) attached to the tubing via a T-piece in approx. 50 cm distance to the gas washer cylinder.

The same set-up applies for the calibration with a PAA diffusion source consisting of a commercial PAA solution (35 % peracetic acid in acetic acid, ThermoFisher). The results of the calibrations subsequent to the respective CAFE campaign are depicted in Figure 4.5.3.

4.5.2.2 *PAA humidity dependency*

As depicted in the right panel of Figure 4.5.3, for PAA, an increase in sensitivity due to humidity was observed in the very low relative humidity region (0-5 %), followed by a drop in sensitivity by a factor of 2.5 at a relative humidity of 60 % compared to

---

[15] https://www.ist-ag.com/en/products/humidity-module-compact-and-pressure-tight-0, last access: 05.05.2025.

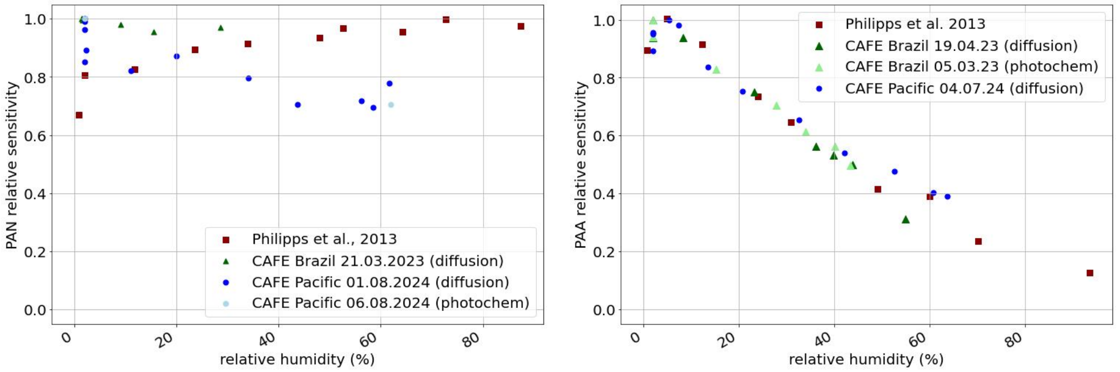

Figure 4.5.3: Changes in the relative measurement sensitivity of PAN (left panel) and PAA (right panel) due to humidity, derived from post-campaign laboratory calibrations with either an internal photo-chemical source (photochem) or an externally added diffusion source (diffusion). For comparison, literature values from Phillips et al. (2013) are added (brown) which were obtained from previous in-house experiments on the CIMS-instrument.

the maximum sensitivity. This non-monotonic humidity dependence is consistent with previous in-house experiments on the CIMS-instrument by Phillips et al. (2013).

The reason for this non-monotonic humidity dependence is not yet clear, but is likely due to different detection mechanisms of PAA. PAA is assumed to be detected via Reaction 52, where I^- ionizes PAA, forming $CH_3C(O)O^-$ ($\frac{m}{z}$ =59). The same reaction could also occur with $I^-(H_2O)$ instead of I^-, at a faster rate, which would explain the increase at very low humidity.

To operate CIMS under dry conditions, such as in the UT, the CIMS instrument contains an internal humidifier that adds a constant relative humidity of approximately 2.3 % to the IMR (see Section 4.2.1). However, the decrease in PAA sensitivity with higher humidity must have a different reason.

Phillips et al. (2013) found that PAA is also detected at $\frac{m}{z}$ =203 and $\frac{m}{z}$ =221 at lower declustering energies and suggested another detection mechanism via Reaction 67 and Reaction 68. If the $CH_3C(O)OOHI^-$ and the $CH_3C(O)OOHI^-(H_2O)$ are not de-clustered in the CDC into $CH_3C(O)O^-$, this would lead to a negative humidity dependence of PAA.

$$I^- + CH_3C(O)OOH \rightarrow CH_3C(O)OOHI^-(m/z = 203) \tag{67}$$

$$I^-(H_2O) + CH_3C(O)OOH \rightarrow CH_3C(O)OOH)I^-(H_2O)(m/z = 203) \tag{68}$$

Based on laboratory experiments, the campaign specific humidity correction factor for PAA with respect to m145/m127 as a measure of humidity (see Section 4.5.1) is given in Figure 4.5.4.

4.5.2.3 *PAN humidity dependency*

The instrument sensitivity on PAN is much more stable towards humidity than for PAA, as depicted in the left panel of Figure 4.5.3. However, a slight loss of sensitivity (factor

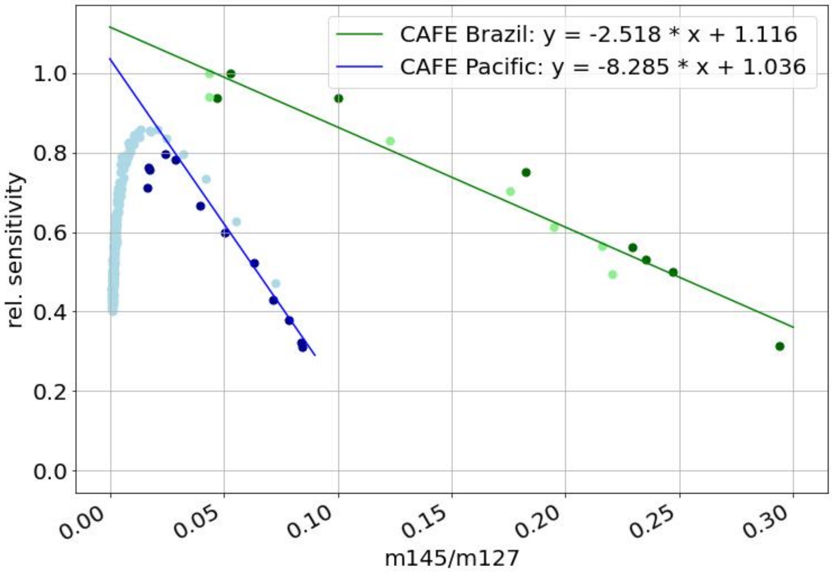

Figure 4.5.4: Linear fits to the relative sensitivity drop in PAA with respect to m145/m127 which are used as humidity correction factor. Bright coloured data points are from experiments with the internal photo-chemical source, dark coloured points from experiments with an external diffusion source.

1.25) at 60 % RH compared to 0 % RH is observed in the laboratory experiments of this work.

The reason for the observed loss in sensitivity could be due to different reaction rates of water-ion-clusters. Slusher (2004) also saw a decrease of approximately 10 % in PAN sensitivity at 80 % relative humidity, which was attributed to the reaction

$$I^-(H_2O)_n + CH_3C(O)O_2 \rightarrow IO + CH_3C(O)O^-(H_2O)_n \tag{69}$$

being much slower $n > 1$ than the reaction of I^- without or with only one water cluster (Reaction 51). As the decreasing trend is observed for both types of PAN sources (diffusion or photochemical) in the experiments, this indicates rather an ion chemistry effect than matrix effect due to co-emitted species by the photo-chemical source.

In contrast to the laboratory experiments with clean synthetic air (20 % O_2 in N_2), matrix effects may play a bigger role during in-flight calibrations. During in-flight calibrations, ambient air is scrubbed by passing through heated steel-wool, which removes acids and thermally unstable trace gases, but does not affect water.

During both CAFE campaigns, a strong negative dependence of PAN's sensitivity with humidity was observed, similar to PAA, during in-flight calibrations, see Figure 4.5.5. This might be due to the high concentration of organic by-products produced in the photo-chemical PAN calibration source which can be react with the acetate anions ($\frac{m}{z}$ = 59). The acetate anions react with organic acids such as formic or propionic acid via proton transfer (Mielke and Osthoff, 2012; Veres et al., 2008) (see Reaction 59) with different dependencies on humidity.

Due to this complexity, only calibrations under dry conditions at high altitudes (>10 km) were used. In the dry air masses the PAN calibration concentrations were reproducible, see Figure 4.3.1.

Since the laboratory experiments showed no or only weak dependence on humidity for PAN, which was in agreement with literature, no humidity correction factor was applied to the PAN field measurements. The variations in PAN calibrations under dry conditions are added to the total measurement uncertainty (see Section 4.7).

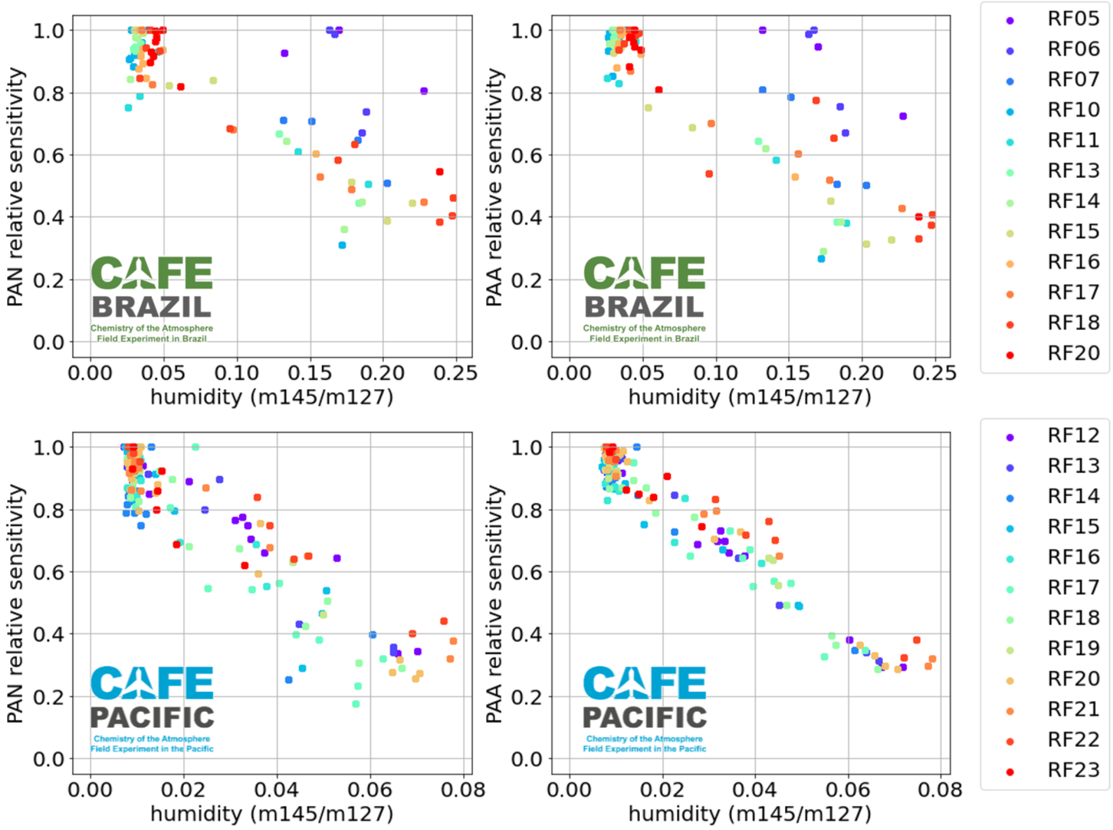

Figure 4.5.5: Humidity sensitivity of in-flight calibrations for PAN (left column) and PAA (right column) during CAFE Brazil (upper row) and CAFE Pacific (bottom row).

4.5.3 *Losses of acetate anion from the internal photo-chemical source*

During CAFE Pacific campaign, the ^{13}C-isotopically labeled PAN source was used. During the flights, a significant increase in signal at $\frac{m}{z}=45$ and $\frac{m}{z}=46$ was observed every time the internal calibration source was added to the flow (increase in $\frac{m}{z}=61$), as shown exemplarily for RF12 data in Figure 4.5.6. The shown detail in Figure 4.5.6 was taken at a constant measurement altitude with little variation in primary ion signal ($\frac{m}{z}=127$) and ambient PAN and PAA signal ($\frac{m}{z}=59$). Therefore, the increase on $\frac{m}{z}=45$ and $\frac{m}{z}=46$ is clearly caused by the addition of the calibration source, what is discussed in this section.

The photochemical source not only produces PAN. but also significant amounts of other trace gases such as acetic acid (AA) ($CH_3C(O)OH$), formic acid (HCOOH), formaldehyde (HCHO), and methyl hydroperoxide (MHP) (CH_3OOH). Previous studies suggested high concentrations of acids and other oxidised organics formed in the photochemical PAN source (Wüst et al., 2024). This was also underscored by simulations

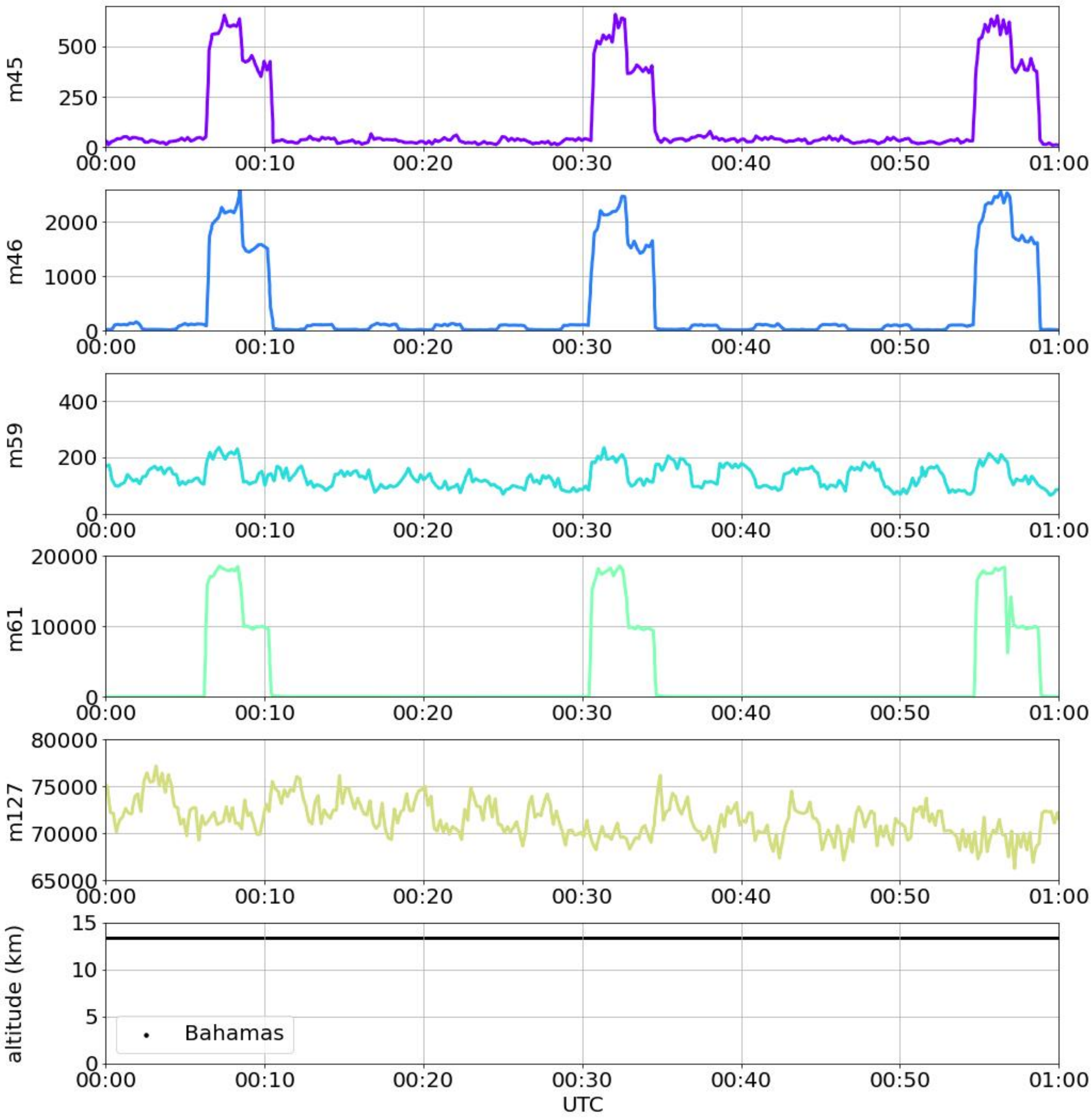

Figure 4.5.6: Raw counts at $\frac{m}{z} = 45$, $\frac{m}{z} = 46$, $\frac{m}{z} = 59$, $\frac{m}{z} = 61$ and $\frac{m}{z} = 127$ from RF12 on 2nd February 2024 during CAFE Pacific, including three in-flight calibrations indicated by the rise of counts on $\frac{m}{z} = 61$ (fourth row). The data was taken at constant flight altitude of around 14 km (last row).

of the chemical processes happening inside the photochemicaly source performed by John Crowley in a Flow and chemistry simulator (FACSIMILE) model (Chance et al., 1977), the results are shown in Figure A.0.5 in the Appendix.

After leaving the photochemical source, the products pass through the TDR region and then reach the IMR within less than 0.2 s via a 1.2 m long 1/8" metal tubing. The thermal dissociation of PAN in the TDR creates acetate anions (CH_3COO^-, $\frac{m}{z} = 59$), which can react with other trace gases from the photochemical source (Veres et al., 2008) leading to a loss of signal on $\frac{m}{z} = 59$.

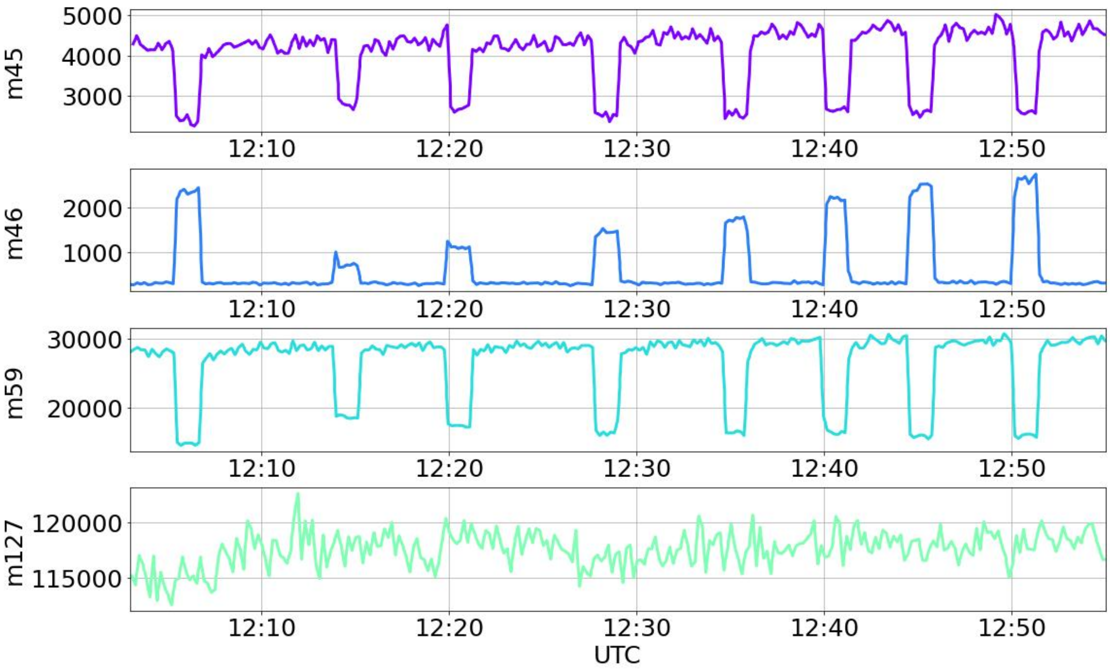

Figure 4.5.7: Raw counts on m/zs during a laboratory experiment performed on 21st September 2023. CIMS was run with synthetic air in calibration mode adding the outflow of the internal photo-chemical source run with non-isotopic acetone (^{12}C). The stepped changes in counts indicate the addition of NO for titration. Different titration flows of NO were set for each titration step, varying between 1-10 sccm.

In Laboratory experiments, CIMS was run with synthetic air and added the internal photochemical calibration source. When adding NO to titrate the PA-radical and measure the background signal at $\frac{m}{z} = 59$, a drop on $\frac{m}{z} = 45$ and an increase on $\frac{m}{z} = 46$ (Figure 4.5.7) was observed. The effect intensified when varying the flow of NO for titration (F_{NOT}) between 1-10 sccm. However, the ratio of $\frac{m}{z} = 59$ over the sum of $\frac{m}{z} = 45$ and $\frac{m}{z} = 59$ stays constant for all flows of F_{NOT} and is the same when titrating or not (Figure 4.5.8). This indicates a constant loss of acetate anions ($\frac{m}{z} = 59$) to $HCOO^-$ ($\frac{m}{z} = 45$) via the detection of formic acid as shown in Reaction 70:

$$CH_3C(O)O^- + HCOOH \rightarrow CH_3C(O)OH + HCOO^- \qquad (70)$$

Equation 70 is possible because of the low gas-phase acidity of the acetate ion and has been reported in literature (Mielke and Osthoff, 2012; Veres et al., 2008). Since $\frac{m}{z} = 45$ and $\frac{m}{z} = 46$ were not measured during CAFE Brazil, a constant correction factor of 0.86 based on these laboratory experiments was used. In the case of CAFE Pacific, where $\frac{m}{z} = 45$ and $\frac{m}{z} = 46$ were measured, a flight-wise correction factor was derived. The measured correction factor for $\frac{m}{z} = 45$ and $\frac{m}{z} = 46$ during CAFE Pacific was in the range of 0.86-0.87, which is in agreement with the post-campaign laboratory derived factor of 0.86 used for the analysis of CAFE Brazil measurements. This agreement supports the assumption that the ^{13}C-Acetone (see Section 4.3.3) used during CAFE Pacific and the non-isotopic acetone used during CAFE Brazil behave chemically similarly. Note that isotopic formic acid is detected on $\frac{m}{z} = 46$ instead of $\frac{m}{z} = 45$ during CAFE Pacific, see Figure 4.5.9 and the correction factor is hence defined as m61/(m45+m46+m61). For

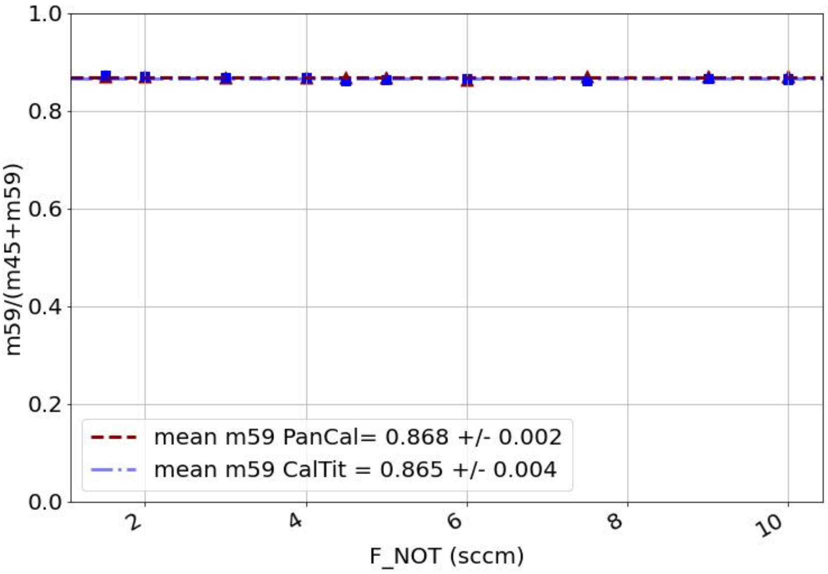

Figure 4.5.8: Ratio of m59/(m45+m59) from the internal photo-chemical source with (blue squares) and without (brown triangles) titration for different titration flows of NO (F_{NOT}). Derived from the laboratory experiments on 21st September 2023, as displayed in Figure 4.5.7.

each flight the average factor of all in-flight calibrations is used.

In the ^{12}C ion-chemistry, the increase of $\frac{m}{z}=46$ during titration seen in Figure 4.5.7 is more difficult to explain. One may expect possible reactions of the acetate anion with NO, NO_2, HNO_3 and HONO, which can lead to the formation of $NO_2{}^-$ ($\frac{m}{z}=46$) (Reactions 71-74).

$$CH_3C(O)O^- + NO_2 \rightarrow CH_3C(O)O + NO_2^- \tag{71}$$
$$CH_3C(O)O^- + NO \rightarrow CH_3CO + NO_2^- \tag{72}$$
$$CH_3C(O)O^- + HNO_3 \rightarrow CH_3C(O)OOH + NO_2^- \tag{73}$$
$$CH_3C(O)O^- + HONO \rightarrow CH_3C(O)OH + NO_2^- \tag{74}$$

However, with respect to electron affinities and enthalpies of formation, only Reaction 74 is possible, as demonstrated in the following:
The electron affinity of the acetyloxyl radical ($CH_3C(O)O$) is 314 kJ/mol or 3.25 eV (Wang, Woo, and Wang, 2006), which is higher than the one of NO_2 (2.27 eV[16]). Hence, the donation of an electron to NO_2 in Reaction 71 will not happen. Looking at the enthalpy of formation at room temperature ($\Delta_f H^\circ$) for $CH_3C(O)O^-$ (-506 kJ/mol)[17], NO (90 kJ/mol)[16], and $NO_2{}^-$ (-192 kJ/mol)[16] shows that Reaction 72 is endothermic and will also not take place. Same applies for Reaction 73 where $\Delta_f H^\circ$ of HNO_3 is -134 kJ/mol[16] and -337 kJ/mol for $CH_3C(O)OOH$ (Tyndall et al., 2001).
In contrast, Reaction 74 is exothermic because $\Delta_f H^\circ$ of HONO and $CH_3C(O)OH$ is -77 kJ/mol[16] and -432 kJ/mol[16], respectively.

---

[16] After NIST Chemistry WebBook recommendation, `https://webbook.nist.gov`, last access: 03.04.2025 .

[17] `https://atct.anl.gov/Thermochemical%20Data/version%201.122e/species/?species_number=365`, last access: 03.04.2025.

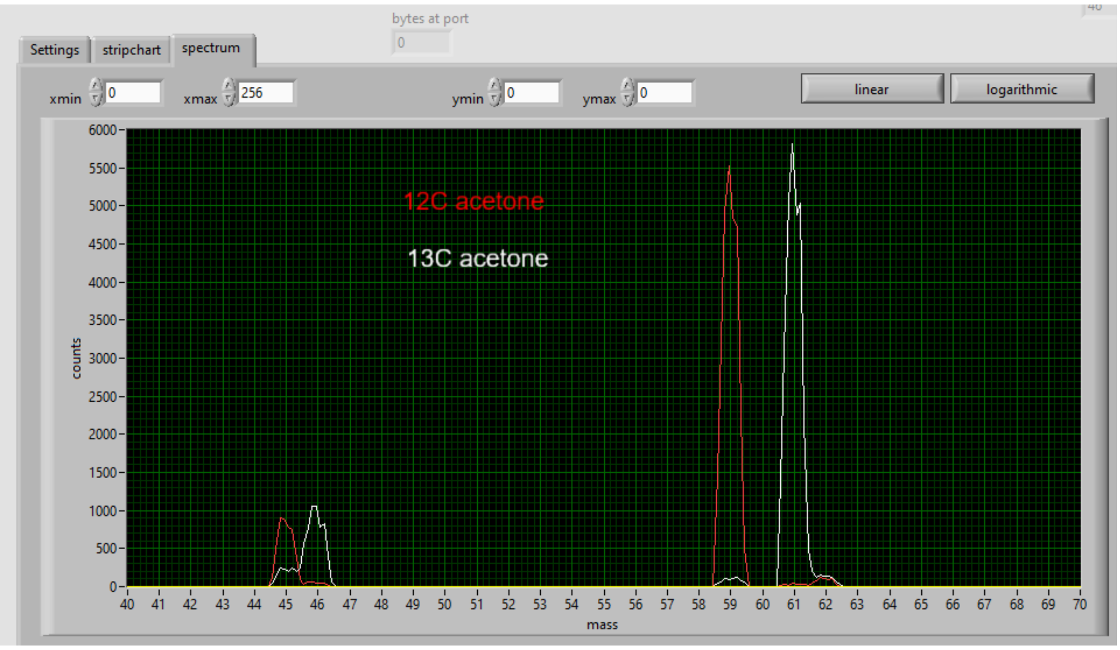
bytes at port 0

xmin 0

xmax 256

ymin 0

ymax 0

Figure 4.5.9: CIMS spectrum of the internal photo-chemical source in synthetic air for m/z between 40 and 70. The internal photo-chemical source was first run with ^{12}C-Acetone (white) and afterwards with ^{13}C-Acetone (red). Taken from laboratory experiments on 20th September 2023.

Hence, HONO remains the most likely candidate for the conversion of $\frac{m}{z} = 59$ to $\frac{m}{z} = 46$ even though the origin of HONO is not entirely clear. A possible source could result from impurities of NO_2 in the NO titration flow which can form HONO in surface reactions with water.

The following measures were applied to reduce the unwanted losses of acetate anion to organic acids like formic acid ($\frac{m}{z} = 45$ resp. $\frac{m}{z} = 46$ with ^{13}C-acetone) and HONO ($\frac{m}{z} = 46$).
First, a 15 cm long 1/2"-PFA tubing filled with a 0.3 nm molecular sieve of metal aluminosilicate (ROTH, Typ 564[18]) was added to the flow of titration NO in front of the IMR in order to remove HONO in the NO titration gas, which can be formed from possible impurities of NO_2. The molecular sieve reduced the signal on $\frac{m}{z} = 46$ by around 40 % (see Figure A.0.1 in the Appendix).
Secondly, a lower flow of NO titration gas (F_{NOT}) was used during CAFE Pacific compared to CAFE Brazil (see Table 2). As seen in Figure 4.5.7, a lower flow of NO titration lowered the absolute signal on $\frac{m}{z} = 46$ during titration but not the organics to PAN ratio (Figure 4.5.8).
To reduce the matrix effects from organic acids co-emitted from the source (Mielke and Osthoff, 2012), a factor 20 lower gas mixture of acetone was used during the BAIRN-VIP campaign (see Table 2). This is an effective measure to simplify the chemistry in the photo-chemical source, since the formation of organic acids is quadratic in radical density and thus ion acetone concentration. To ensure an excess of acetone and stay in the

---

[18] `https://www.carlroth.com/de/de/molekularsiebe/molekularsieb-3-%C3%A5/p/8487.3`, last access: 06.05.2025.

NO limited linear regime of PAN formation, also the concentration of NO inserted in the photo-chemical source (F_{NOS}) had to be lowered by a factor of 4. The PAA to PAN ratio from the internal photo-chemical source was reduced from approximately 50 % during CAFE Brazil and CAFE Pacific to approximately 10 % during BAIRN-VIP.

4.5.4 *TDR temperature*

The fundamental principle of the thermal dissociation (TD)-CIMS relies on the thermal decomposition of PAN, which happens in the TDR region (see Figure 4.2.1). The TDR is an approximately 20 cm long heated 1/2"-PFA tubing. With a total mass flow of 1400 sccm the residence time in the TDR is in the order of 60 ms at 1 Bar. Zheng et al. (2011) found that the instruments sensitivity strongly depends on the structure of the molecule and the dissociation temperature and is hence specific for each PAN-type species.

In the experimental set-up to determine the optimum TDR-temperature, an identically TDR tubing to the one inside the CIMS was built and mounted it outside of the instrument. This ensures that sensitivity changes result purely from TDR temperature changes and are not related to changes in temperature in the IMR. In the experimental set-up, the internal photochemical source was used and CIMS run with synthetic air. For the given PAN levels, the NO titration signal (CalTit) was already subtracted from the total signal on $\frac{m}{z} = 59$ and the PAA is given by the CalTit ProcState.

In the beginning of the experiment, the TDR was switched off at room temperature and then switched on leading to a continuous increase in temperature until T_{TDR} reached 100 °C. From here on, manual steps of 10-20 °C were made to receive a higher resolution in the most sensitive temperature range. Since the temperature sensor is wrapped with glass wool around the heating wire and does not give the temperature directly inside the TDR. Therefore, between the manual set temperature steps 5-7 minutes conditioning time were given to ensure the inside TDR temperature can adapt to the set TDR temperature. The results of the laboratory experiment on 17th April 2023 are shown in Figure 4.5.10. In the case of PAA, the normalized counts during titration stay more or less constant with increasing TDR temperature until 150 °C, before they drop by around 15 % at 180 °C indicating a loss of PAA due to thermal decay.

In the case of PAN, below 75 °C the signal on the normalized counts only a few percent because PAN is not thermally dissociated to PA and hence not detected at $\frac{m}{z} = 59$. The thermal decay of PAN to PAN increases with temperature leading to steep increase of the normalised counts by a factor of 6 from low TDR temperatures compared to the maximum at 150 °C. Above 150 °C, the sensitivity decreases again indicating losses of PA due to thermal decay. The results are in agreement with other TD-CIMS characterizations (Mielke and Osthoff, 2012; Zheng et al., 2011), which also found optimal dissociation temperatures between 160-180 °Cfor PAN. Based on these experiments, T_{TDR} was changed from the previously used 180 °C during CAFE Brazil to 150 °C for CAFE Pacific and BAIRN-VIP to optimize both, the yield of PAN and PAA through the TDR region.

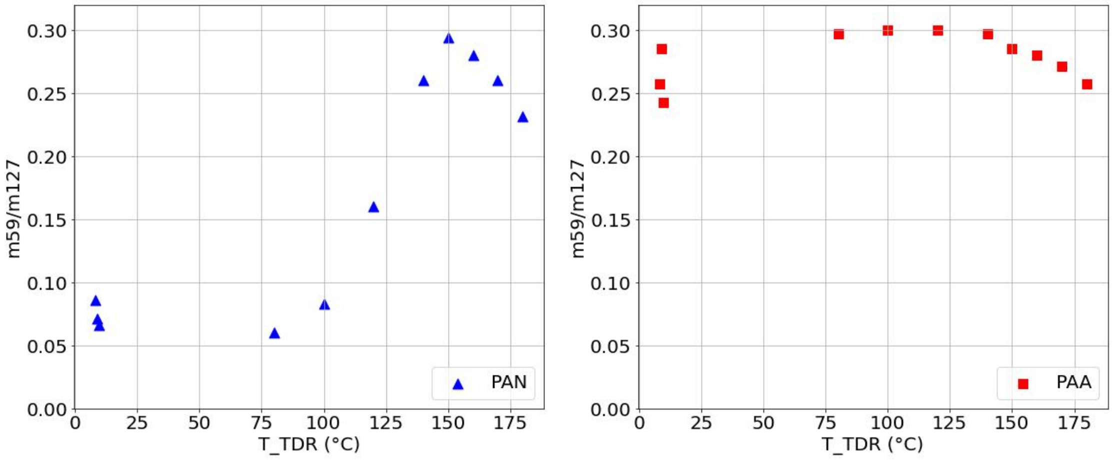

Figure 4.5.10: Laboratory experiment on 17th April 2023: Sensitivity of PAN (left panel) and PAA (right panel) dependent on the temperature of the TDR (T_{TDR}).

4.6 DATA PROCESSING AND UNCERTAINTY ANALYSIS

As described in Section 4.3.2, during measurement campaigns CIMS runs with a programmed data capturing cycle which means it switches automatically between ambient, titration and calibration process states (ProcStates). For the analysis, the raw data was treated in the following steps, which are described in detail in this section:

1. Separating data per ProcState
2. Basic data filtering (Section 4.6.2)
3. Determination of LOD and background subtraction from raw signal (Section 4.6.3)
4. Smoothing of primary ion signal and normalization of signal (Section 4.6.4)

Similar, to the treatment of the in-flight calibrations, the net PAN signal is extracted from the total PAN+PAA ambient signal on $\frac{m}{z} = 59$ by subtracting the average PAA signal on $\frac{m}{z} = 59$ from the subsequent titration step (PanTit). The PAN data was finalized by applying a calibration factor from the high-altitude in-flight calibrations, as discussed in Section 4.3.2, with a correction for $\frac{m}{z} = 59$ loss on $\frac{m}{z} = 45$ and $\frac{m}{z} = 46$ (see Section 4.5.3).

In the case of PAA, the counts measured during the PanTit ProcState were corrected for instrument background (typically around 5 counts) and converted into mixing ratios using the calibration factors given in given in Figure 4.4.1, as discussed in Section 4.4. Additionally, a correction for sensitivity loss due to humidity was applied, according to Section 4.5.2.

4.6.1 *Sampling frequency*

The sampling frequency is dependent on the number of measured m/zs, the averaging time per mass (dwelltime), and the timestep (dwellwait) in between. A dwellwait of typically 30 ms is applied between the scanning of each m/z to ensure that changed

m/z	detected species	dwelltime	dwellwait	$U_{\mathrm{decluster}}$
dummy	10	10 ms	50 ms	-22.8 V
59	PAN, PAA	100 ms	30 ms	-22.8 V
73	PPN	100 ms	30 ms	-22.8 V
85	MPAN	100 ms	30 ms	-22.8 V
87	PiBN	100 ms	30 ms	-22.8 V
111	fPAN	100 ms	30 ms	-22.8 V
127	I^-	10 ms	30 ms	-22.8 V
145	$I^-(H_2O)$	10 ms	150 ms	-20.5 V

Table 3: Initial settings during the CAFE Brazil campaign defining measured mass to charge ratios (m/zs), corresponding timings, and declustering potential $U_{\mathrm{decluster}}$. A measurement frequency of 0.22 Hz is obtained by adding together the integration time per channel of each m/z (dwelltime) and the waiting time in between the different m/z's (dwellwait). For technical reasons, a dummy m/z is added, which also adds up to the total measurement frequency.

voltages by the radio-frequency generator are leveled out. The monitored m/zs and their corresponding timings and voltage settings per channels during the different field campaigns are given in Table 3, Table 4, and Table 5.

The time between two consecutive measurements at $\frac{m}{z} = 59$ is given by the sum of dwellwait times and 8 times the sum of dwelltime times, because each m/z is measured on 8 channels (see Section 4.2.1). The time between two consecutive measurements is about 5 s, 12 s and 9 s for the three different campaigns CAFE Brazil, CAFE Pacific and BAIRN-VIP, which corresponds to the sampling frequencies 0.22 Hz, 0.08 Hz and 0.11 Hz, respectively. For an easier handling of the measurement data, raw data time stamps were resampled to full seconds directly after separating the data per ProcState.

The time between two PAN measurements, which are separated by a PAA measurement (PanTit), depends on the duration of the ambient and the PanTit ProcStates. As mentioned in Section 4.3.2, this duration was 2.5 min during CAFE Brazil and 2 min during CAFE Pacific leading to a measurement frequency of 0.007 Hz and 0.008 Hz respectively.

Calibrations for other PAN-type species mentioned in Table 3, Table 4, and Table 5 have not been performed in the framework of this thesis but the analysis would be similar to the procedure applied to $\frac{m}{z} = 59$.

4.6.2 *Data filtering*

Data, where technical issues appeared, were flagged and excluded from the analysis.

This concerns parts of the first three flights during CAFE Brazil, where the pressure regulation in the IMR failed during altitude changes due to a blockage in the scrubber. Therefore, a filter was applied dropping data when P_{IMR} was outside 18 ± 0.5 Torr. A loose contact in the preamplifier of the detector led to sudden drops in $\frac{m}{z} = 127$, wherefore, a high pass filter was applied to $\frac{m}{z} = 127$. Research flight RF12 in CAFE

m/z	detected species	dwelltime	dwellwait	$U_{decluster}$
dummy	10	10 ms	50 ms	-22.8 V
45	HCOOH	200 ms	30 ms	-22.8 V
46	HONO, $H^{13}COOH$	200 ms	30 ms	-22.8 V
59	PAN, PAA	200 ms	30 ms	-22.8 V
61	^{13}C-PAN, -PAA	200 ms	30 ms	-22.8 V
73	PPN	200 ms	30 ms	-22.8 V
127	I^-	200 ms	30 ms	-22.8 V
145	$I^-(H_2O)$	200 ms	30 ms	-20.5 V

Table 4: Like Table 3, but for initial settings during the CAFE Pacific campaign. The defined number of target mass to charge ratios (m/zs) and timings add up to a measurement frequency of 0.08 Hz.

m/z	detected species	dwelltime	dwellwait	$U_{decluster}$
dummy	10	10 ms	50 ms	-22.8 V
45	HCOOH	100 ms	30 ms	-22.8 V
46	HONO,$H^{13}COOH$	100 ms	30 ms	-22.8 V
59	PAN, PAA	100 ms	30 ms	-22.8 V
61	^{13}C-PAN, -PAA	100 ms	30 ms	-22.8 V
62	$HNO_3{}^a$	100 ms	30 ms	-22.8 V
73	PPN	100 ms	30 ms	-22.8 V
87	PiBN	100 ms	30 ms	-22.8 V
127	I^-	100 ms	30 ms	-22.8 V
145	$I^-(H_2O)$	100 ms	30 ms	-20.5 V
173	$HCOOH^b$	100 ms	30 ms	-22.8 V
190	$HNO_3(H_2O)$ [a]	100 ms	30 ms	-20.5 V

Table 5: Like Table 3, but for initial settings during the BAIRN-VIP campaign. the defined number of target mass to charge ratios (m/zs) and timings add up to a measurement frequency of 0.11 Hz. [a]Dörich et al. (2021), [b]Leather et al. (2012) and Treadaway et al. (2018).

Brazil had to be entirely rejected because of a continuous loss of $\frac{m}{z} = 127$. As mentioned in Section 4.3.3, in CAFE Brazil, the first 30 s of ambient measurements after a calibration where excluded due to memory effects resulting from high concentrations of PAN during calibration.

During CAFE Pacific, in total less than 6 hours of data gaps occurred. During the transfer flight from Cairns back to Germany, the instrument was not working.

Overall, the data coverage in all campaigns was nearly complete except the before mentioned minor technical issues. An overview of flight specific analysis parameters and results is given in Figure A.0.2 and Figure A.0.3 in the appendix.

4.6.3 *Limit of detection*

The limit of detection (LOD) for PAA is determined by background counts in the absence of a source.
Due to the memory effect of the calibration signal, the zero measurements during the flights could not be used.
However, the instrumental background can be derived during Protect mode, when the instrument is flushed with pure nitrogen. This mode is automatically active on ground before take-off and after landing when HALO moves below a speed limit of 15 m/s. Consequently, CIMS is protected from heavily polluted air on the ground.

After switching on, CIMS usually needs at least 15-20 min conditioning time for example to stabilise the ion source, the calibration source and flush out humidity or other contaminates which may have accumulated on ground. Therefore, the background counts before take-off are usually 50 % higher than after landing. As shown exemplarily for RF15 during CAFE Pacific in Figure A.0.6 in the Appendix, typical background counts before takeoff are round 6 counts and 3 counts after landing. NO information of the temporal evolution of the background signal during the flights is available.
To determine the LOD for PAA, the averaged counts during protect mode after landing were used, which are listed in Table 8. Since the difference in background signal before takeoff compared to after takeoff is only a few counts. Given the PAA sensitive of around 1 counts per ppt, the drift in the background signal impacts the final PAA signal only in the order of 3-5 ppt and is hence negligible compared to the uncertainty resulting from the humidity correction and the calibration factor, as will be discussed in Section 4.7.

The LOD for PAN is dependent on the variability of consecutive PAA signals which are interpolated and subtracted from the total signal on $\frac{m}{z} = 59$. To account for variability induced by rapidly changing PAA background signals for example when the aircraft changed the flight altitude, a rolling window method was applied to derive the standard deviation from consecutive PAA measurements. Since one PanTit ProcState takes 2-2.5 min, the chosen interval of 10 min assures that at least two consecutive PanTit periods are included in the rolling standard deviation. The LOD on PAN measurements is given by three times the standard deviation (3σ) from the rolling window method on $\frac{m}{z} = 59$ counts during titration and is typically around 60 counts (approx. 20 ppt) as shown exemplarily for RF15 during CAFE Pacific in Figure 4.6.1.

In Table 6 the range of the derived LODs for flights during CAFE Brazil and CAFE Pacific are given. A detailed overview of the LOD for the single flights are given in Figure A.0.2 and Figure A.0.3 in the Appendix.

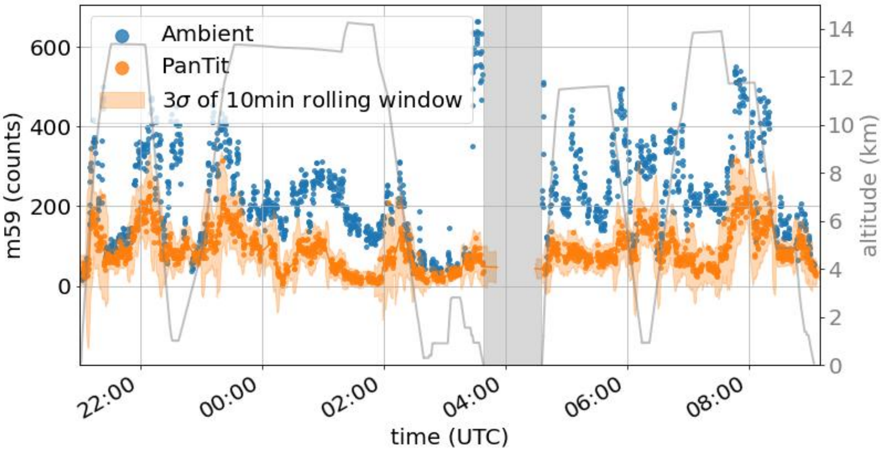

Figure 4.6.1: Counts on $\frac{m}{z}=59$ recorded in research flight RF15 during CAFE Pacific in ambient air (blue) and added titration (orange). The threefold standard deviation of a rolling window with the time interval 10 min on the averaged and interpolated counts in PanTit mode is marked by the shaded area. The gray shaded area marks the time on ground during a refueling stop. The gray line indicates measurement altitude.

	CAFE Brazil	**CAFE Pacific**
PAN LOD	20-60 ppt	10-22 ppt
PAA LOD	5-33 ppt	4-10 ppt

Table 6: Range of the limit of detection (LOD) of CIMS for PAN and PAA, derived for all measurement flights during the two aircraft campaings CAFE Brazil and CAFE Pacific.

4.6.4 *Smoothing of primary ion signal*

Since the raw signal on $\frac{m}{z}=59$ is normalized to the primary ion signal ($\frac{m}{z}=127$ and $\frac{m}{z}=145$), a high noise in the primary ion signals would introduce an artificially high variability on both PAN and PAA measurements. Applying a rolling mean of 25 data points, reduces the original noise of around 6 % in $\frac{m}{z}=127$ by half, as shown in Figure 4.6.2.

For the analysis of CAFE Pacific data, instead of the rolling mean method, the interpolated ProcState average was used to smooth $\frac{m}{z}=127$, because $\frac{m}{z}=127$ was effected by titration. During ambient measurements $\frac{m}{z}=127$ was almost 5 % higher than during titrating (Figure 4.6.3). This decrease during titration is probably due to a chemical matrix effect with the titration NO as discussed in Section 4.5.3.

4.7 DISCUSSION OF MEASUREMENT UNCERTAINTIES

This section aims to assess total measurement uncertainty (TMU) associated with the PAN and PAA measurements during CAFE Brazil and CAFE Pacific. An overview of the quantifiable uncertainties are presented in Table 7 and Table 8 for PAN and PAA, respectively, during both campaigns CAFE Brazil and CAFE Pacific. However, not all uncertainties can be quantified exactly due to the lack of statistics and will add up to

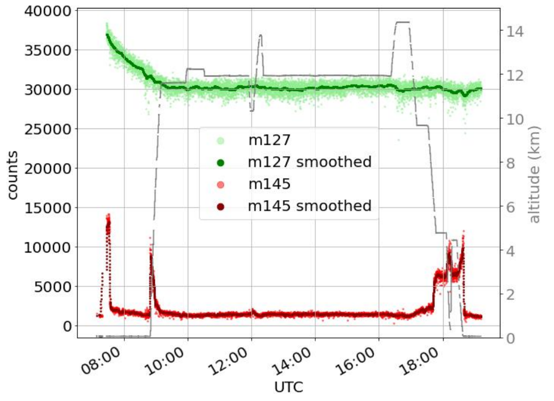

Figure 4.6.2: Raw (light colours) and smoothed (dark colours) primary ion signal at $\frac{m}{z}=127$ (green) and $\frac{m}{z}=145$ (red), shown exemplary for research flight RF20 during CAFE Brazil.

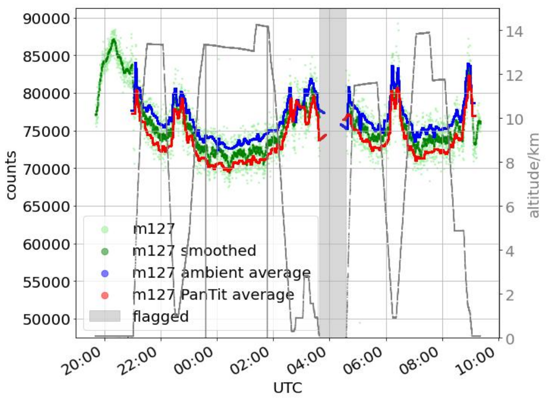

Figure 4.6.3: Raw (lime) and smoothed (darkgreen) primary ion signal $\frac{m}{z}=127$ compared to interpolated averages per ProcState ambient (blue) and PanTit (red), shown exemplary for research flight RF15 during CAFE Pacific.

the TMU. Additionally, flight-wise information is given in Figure A.0.2 and Figure A.0.3 in the Appendix.

4.7.1 *Measurement uncertainty on PAN*

The range of measurement sensitivities for PAN given in Table 9 represents the range of PAN sensitivities derived in the 12 analysed measurement flights during each campaign based on the high-altitude in-flight calibrations in dry air (see Section 4.3.2). The sensitivities were obtained by dividing the average of the dry in-flight calibrations for PAN by the calculated PAN concentration of the internal source (Equation 58). The uncertainty range listed in Table 7 associated to the measurement sensitivity is statistically derived from the standard deviations of the in-situ calibrations during a flight, excluding possible systematic errors.

Additional sources of uncertainties for PAN measurements arise from imprecise gas mixtures for the calibration gas, the NO conversion efficiency, possible impurities in the NO titration gas, and losses of the calibration signal on formic acid ($\frac{m}{z}=45$ or $\frac{m}{z}=46$ with ^{13}C calibration standard).

The uncertainty on the calibration NO standard supplied by the manufacturer is around 5 %. The conversion efficiency of NO to PAN had been determined previously by Eger et al. (2019) with an uncertainty of about 5 %, too.

The loss of the acetate anion in the IMR to formic acid, which is a by-product of the photo-chemical source, was estimated in post-campaign laboratory experiments for CAFE Brazil during which $\frac{m}{z}=45$ was not measured. It was observed that during CAFE Pacific, that the ratio between $\frac{m}{z}=45$ and $\frac{m}{z}=46$ to $\frac{m}{z}=59$ and $\frac{m}{z}=61$ ($^{1}3CH3COO^{-}$) varied between the flights between 6 % (0.85-0.89) between the flights, hence this relative error is assigned on the formic acid correction factor of 0.86 applied to CAFE Brazil PAN data. The uncertainty on the formic acid correction factors measured during CAFE Pacific represent the standard deviation of the during the in-flight calibrations. Hence, the statistical relative errors on the PAN measurements sum up to 10-15 % during CAFE Brazil and 7-13 % during CAFE Pacific.

However, potential systematic errors have to be taken into account.
An unquantified source of uncertainty is the potential loss of the calibration signal due to complex matrix effects with organic acids (Mielke and Osthoff, 2012), which were only quantified for formic acid. As shown in Figure A.0.17 in the Appendix, the ratio between other reactants with $\frac{m}{z} = 59$ formed in the photo-chemical source to formic acid ($\frac{[PAA]+[HONO]+[HNO3]}{[HCOOH]}$) inferred from the FACSIMILE simulation of the photo-chemical source, is close to one. Hence, it can be assumed that potential losses of the acetate anion to other by-products of the photochemical source, notably acids, could be similar in size to that due to formic acid. The correction factor of 0.86 is similar to a loss of 14 % , therefore the potential uncertainty from other acids could be in the range of 14 % but also more.
The formation of HONO, which is most likely responsible for the signal on $\frac{m}{z} = 46$ (NO_2^-) is a potentially significant source of uncertainty. The impact of HONO, which is introduced by impurities of NO_2 in the NO titration flow, could be different every time the NO bottle is replaced. Unfortunately, $\frac{m}{z} = 46$ was not monitored during CAFE Brazil. During CAFE Pacific $\frac{m}{z} = 46$ was monitored but overlapped with the isotopic formic acid signal and hence cannot be quantified separately.
To account for this potential systematic uncertainties, an upper limit TMU for PAN measurements of around 30 % is recommended instead of the lower limit for the statistical error as given in Table 7.

PAN **uncertainty**	**CAFE Brazil**	**rel. err.**	**CAFE Pacific**	**rel. err.**
in-flight cal. signal	0.13-0.20 $\frac{m59}{m127 \times ppt}$	4-12 %	0.09-0.12 $\frac{m/z59}{m/z127}$	2-9 %
cal. correction for loss to formic acid	0.86	ca. 6 %	0.85-0.89	1-2 %
NO concentration gas standard	$< 5\,\%^a$			
NO conversion efficiency	$0.9 \pm 5\,\%^b$			
Total error		**10-15 %***		**7-13 %***

Table 7: Quantified statistic uncertainties and their relative errors for PAN measurements with CIMS during CAFE Brazil and CAFE Pacific. [a]Air Liquide, [b]Eger et al. (2019). *Lower limit of uncertainty. The recommended TMU including possible systematic errors is 30 % (upper limit) for PAN during both campaigns, as discussed in Section 4.7.1.

4.7.2 *Measurement uncertainty on PAA*

The major source of uncertainty for PAA measurements is the instrument's sensitivity to PAA, specifically the applied calibration factors given in Table 9.
Since the CIMS instrument lacks an integrated in-flight PAA calibration system, calibra-

tions were performed in ground-experiments as described in Section 4.4. The derived calibration factors, presented in Figure 4.4.1, were scaled for the humidity e.g. the average $\frac{m}{z} = 145$ to $\frac{m}{z} = 127$ ratio during the calibration.

As evident from Figure 4.4.1, the sensitivity on PAA significantly changed between the campaigns possibly due to transport. The CIMS sensitivity on PAA actually varied by a factor of 1.5 between the two subsequent aircraft campaigns and by a factor of 4 between CAFE Pacific and the subsequent ground campaign BAIRN-VIP.

Hence, using post-campaign calibrations, like in the case for CAFE Pacific, is possibly error prone. Therefor, a factor of 1.5 on the uncertainty of the calibration factor for CAFE Pacific based on inter-campaign variations seems realistic. It is also noteworthy that four attempts were made to derive the PAA sensitivity during CAFE Pacific via the cross-calibration of a permeation source with the HYPHOP instrument. Unfortunately, these measurements had to be rejected due to instrumental problems of HYPHOP leading to unstable signals on organic peroxides and H_2O_2. In post-campaign laboratory experiments, a PAA permeation source was quantified simultaneously via the KI-method and the HYPHOP. The resulting sensitivities of the CIMS instrument for PAA were by a factor of three different. Since the HYPHOP issues had not been resolved until that point, the sensitivity derived from the KI-method was considered more reliable. However, the high discrepancy between the different calibration methods could indicate a potential systematic error and both calibration methods, the KI-method and the cross-calibration wiht HYPHOP, should be further developed.

A similarly high factor of uncertainty could be argued to apply for CAFE Brazil measurements due to the lack of reproducibility of the calibration. In the case of CAFE Brazil, only one successful cross-calibration of a diffusion source sampled simultaneously by CIMS and HYPHOP was performed during the first half of the campaign. A second attempt for a cross-calibration was made in January but had to be rejected due to calibration issues of the HYPHOP instrument caused by intruded water. Yet, the resulting sensitivity of this failed calibration experiment was almost twice than the one derived in December. Since between December and January, there was a break of about 10 days without measurement flights due to Christmas holidays, and potential change in sensitivity cannot be excluded during the time of inactivity in the humid, and warm tropical environment. RF12, which took place directly after the break, had technical issues, indicating that the instrument conditions may have changed. Eight out of the twelve analysed flights during CAFE Brazil took place in January and may therefore have a higher uncertainty on the PAA sensitivity.

In addition, it has been assumed that the sensitivity does not significantly change during a single campaign, which may not be the case. To estimate the potential error of a constant calibration factor for PAA during one campaign, it is assumed that variability of the instrument's PAA sensitivity during the flight is comparable to the variability of the sensitivity for PAN. The PAN calibration varied by maximum 12 % in a flight during CAFE Brazil and 9 % in a flight during CAFE Pacific.

An attempt to quantify a lower limit of the TMU on the PAA measurements based on statistical errors is given in Table 8. The TMU on the HYPHOP measurements during the cross-calibration is taken from Hamryszczak et al. (2023a) and includes the uncertainty on the stripping efficiency as well as systematic errors on titration, mass flow controllers, reading errors, and others.

Since the measurement principle of HYPHOP is based on the detection of H_2O_2, there could be an interfering contribution of H_2O_2 from the head-space of the diffusion source. Berasategui et al. (2020) estimated the contribution of H_2O_2 from the head-space to be about 1 %, which is consistent with the ratio of water vapour pressures between PAA and H_2O_2. This error is negligible compared to the major uncertainty on sensitivity from the lack of reproducible experiments, as discussed above.

The given statistical error of 27 % on the KI-method results from the standard deviation of the six performed calibration experiments. Further uncertainties result from the extinction cross-section off triiodide used as a reference, as discussed by Friedrich (2015). Friedrich (2015) listed literature values of the extinction cross-section which varied by 15 % (Awtrey and Connick, 1950; Bichsel and Von Gunten, 1999; Jung et al., 2014; Palmer, Ramette, and Mesmer, 1984; Troy et al., 1991).

Additional uncertainties may result from systematic experimental errors, the spectrometer resolution (1.5 nm), measurement uncertainties on volume, time, and mass measurements, which are not quantified. The interference with H_2O_2 can also be an issue in the KI-method because the oxidation of iodide to triiodide is not only possible via PAA but also via H_2O_2 (Reaction 65). It is unknown how much of the dissolved H_2O_2 in the PAA solution permeates through the PFA tubing and contributes to the source signal.

Besides the calibration method itself, another significant source of uncertainty on the PAA measurement data is the humidity correction of the sensitivity. The given uncertainty of 5-8 % in Table 8 is the statistical error on the slope of the linear fit derived from laboratory experiments on relative sensitivity loss with respect to the ratio m145/m127. The relative uncertainty for each PAA measurement resulting from the humidity correction ($\mathsf{RE}_{\mathsf{Hum}}$) is calculated by multiplying the error on humidity calibration slope ($\mathsf{RE}_{\mathsf{lin}}$) and by the humidity factor ($\mathsf{fac}_{\mathsf{Hum}}$) depending on the m145/m127 ratio at each measurement point with Equation 75.

$$\mathsf{RE}_{\mathsf{Hum}} = \mathsf{RE}_{\mathsf{lin}} \times \mathsf{calfac} \tag{75}$$

Hence, the relative uncertainty reaches from the humidity correction reaches up to 40 % in for the wettest measurement points during CAFE Brazil and up to 10 % for the wettest measurement points during CAFE Pacific.

Adding the TMU from the respective PAA calibration method, the total statistic error on PAA measurements is between 15-42 % during CAFE Brazil and 45-90 % during CAFE Pacific, as given in Table 8. As discussed previously, the potential uncertainties on the calibration methods are more likely a factor of 2 on the dry PAA data points, exceeding the given statistical TMU of each calibration method by far.

4.8 SUMMARY OF MEASUREMENT SENSITIVITY, TOTAL UNCERTAINTIES AND LIMITS OF DETECTION

The instrument sensitivity on PAN and PAA has been discussed previously in this chapter and is summarized in Table 9 for both campaigns CAFE Brazil and CAFE Pacific.

PAA uncertainty	**CAFE Brazil**	**rel. err.**	**CAFE Pacific**	**rel. err.**
off-line calibration	TMU HYPHOP[a]	13 %	KI stat. error I_3^- extinct. coeff.	27 % 15 %
H_2O_2 contribution	diffusion source	1 %	permeation source	1 %
humidity calibration	-2.5 ± 0.2 $\frac{m145}{m127}$	8 %	-8.3 ± 0.4 $\frac{m145}{m127}$	5 %
humidity corr. factor	1-5		1-2	
Total error		**15-42 %***		**31-62 %***

Table 8: Quantified statistic uncertainties and their relative errors for PAA measurements with CIMS during CAFE Brazil and CAFE Pacific. [a]Hamryszczak et al. (2023a).*Lower limit of uncertainty. The recommended TMU including possible systematic errors is a factor of 2 for PAA measurements during both campaigns, as discussed in Section 4.7.2.

	CAFE Brazil	**CAFE Pacific**
PAN sensitivity	$4.8 - 7.3 \times 10^{-5} \frac{m/z59}{m/z127 \times ppt}$	$3.2 - 4.5 \times 10^{-5} \frac{m/z59}{m/z127 \times ppt}$
PAA sensitivity	$1.21 \times 10^{-5} \frac{m/z59}{m/z127 \times ppt}$	$2.16 \times 10^{-5} \frac{m/z59}{m/z127 \times ppt}$

Table 9: CIMS instrument sensitivities for PAN and PAA derived during CAFE Brazil and CAFE Pacific. The sensitivity range for PAN represents the span of the flight-wise derived calibration factor based on in-flight calibrations. The PAA sensitivity was calculated campaign-wise from ground experiments.

The range of LODs for PAN and PAA reached in the flights during CAFE Brazil and CAFE Pacific have been listed previously in Table 6. In average the LOD of PAN during CAFE Brazil was 29 ppt ± 24 % 13 ppt ± 15 % during CAFE Pacific. In the case of PAA the average LOD during CAFE Brazil was 11 ± 7 ppt and 6 ± 2 ppt during CAFE Pacific, respectively.

The total measurement uncertainty of PAN and PAA has been discussed in Section 4.7.1 and Section 4.7.2 and were estimated to around 30 % for PAN and 100 % for PAA, respectively. In contrast to the PAN measurements, the CIMS sensitivity for PAA decreases with humidity. To account for the uncertainty induced by the humidity correction for PAA data, a humidity dependent uncertainty is added to each PAA measurement point. A maximum uncertainty of 40 % and 10 % was assigned to the wettest PAA measurement points during CAFE Brazil and during CAFE Pacific, respectively.

In summary, the total measurement uncertainty in ppt attributed to PAN and PAA during both campaigns CAFE Brazil and CAFE Pacific is calculated as follows:

$$TUM_{PAN} = LOD + [PAN] \times 0.3 \tag{76}$$

$$TUM_{PAA} = LOD + [PAA] \times RE_{Hum} \times 2 \tag{77}$$

Here, [species] denotes the measured mixing ratios in ppt and $\mathrm{RE}_{\mathrm{Hum}}$ the relative humidity correction error as given in Equation 75.

Part III

RESULTS AND DISCUSSION

5

CAFE BRAZIL

In this chapter, the measurements of PAN and PAA above the Amazonian rainforest during the CAFE Brazil measurement campaign are presented. The derived vertical profiles are compared with reported tropospheric measurements above the rainforest. Trajectories of sampled air masses are shown and the potential transport of biomass burning plumes from Africa is discussed. The PAN and PAA measurements are compared to the EMAC model, with a focus on understanding the observed levels and vertical distributions of these species. Additionally, the EMAC simulation is used to quantify the relative contribution of different precursor species to the in-situ formation of PAN and PAA. Furthermore, the role of PAN as a source and reservoir of NO_x relative to other nitrogen containing (NO_y) species, as well as the role of PAA as a reservoir species of HO_2, is analysed. This analysis aims to provide insights into the complex PAN and PAA chemistry in the remote, tropical troposphere above the Amazonian rainforest and the importance of PA-precursor related chemistry during CAFE Brazil.

5.1 THE ROLE OF THE AMAZONIAN RAINFOREST

The Amazonian rainforest has a profound impact on the regional weather and climate in the tropics, as well as on a global scale, due to its role as the largest global source of VOC (Guenther, 2013). This results in a high abundance of organic precursors to PAN, which in turn affects the production and distribution of PAN and its homologues. However, the impact of specific NMVOC, particularly isoprene, lightning-NO_x and biomass burning on the PAN production and is not yet well quantified (Roberts, 2007). Aircraft measurements of PAN in this region are sparse, with only a few studies available (Singh et al., 1990, 1996a). Furthermore, measurements of PAA are even less common in this region. Yet, these kind of measurements are needed to answer open questions such as the role of PAN as a source of NO_x in remote areas and hence its impact on O_3 chemistry. Moreover, the Amazonian region is particularly sensitive to climate change and threatened by deforestation (Malhi and Phillips, 2005), which further complicates the prediction of future PAN levels and distributions.

5.2 CAFE BRAZIL CAMPAIGN DESCRIPTION

Between 20.11.2022 and 29.01.2023 16 research flights (RF05-RF20) were performed above the Amazonian rainforest as part of the CAFE Brazil aircraft measurement campaign, which was based at Manaus Airport, Brazil (3.03° S, 60.04° W, UTC-4 hours). The instrumental payload used during these flights is described in Section 3.3.

CIMS successfully measured PAN and PAA in 12 RFs with only minor data gaps (see Section 4.6.2). The flight tracks used for further analysis are depicted in Figure 5.2.1

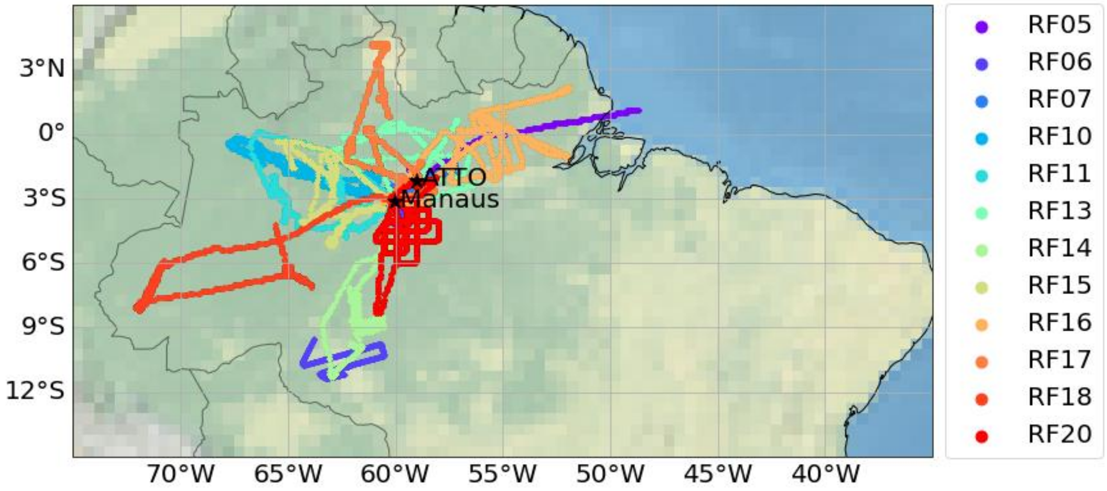

Figure 5.2.1: Flight tracks where CIMS measured PAN and PAA during the CAFE Brazil campaign between December 2022 and January 2023. The campaign base in Manaus is marked as well as the location of the Amazon Tall Tower Observatory (ATTO) research station.

and covered a geographical extent from approximately. 75° W to 47° W and 12° S to 5° N, as well as an altitude range of approximately 300-14000 m, resulting in a total traveled distance of almost 70.000 km.
Note that, flight RF12 was excluded from the analysis due to technical issues. Additionally, during the transfer flights between Germany and Brazil (RF03, RF04, RF21, RF22) as well as during RF08, RF09 and RF19, the CIMS instrument was run with an SF_6^- chemistry scheme to detect SO_2 on a trial basis, and therefore did not measure PAN and PAA.

The primary objective of the CAFE Brazil campaign was to investigate the tropospheric oxidation photochemistry and the mechanisms of new particle formation (NPF) in the anthropogenically almost unperturbed and natural environment of the Amazonian rainforest (Curtius et al., 2024). The city of Manaus, with a population of 2 million inhabitants, is surrounded by 1000-2000 km of pristine rainforest in each direction, allowing for the investigation of unpolluted air masses (Wendisch et al., 2016).
Furthermore, the CAFE Brazil aircraft measurements aimed to bridge the gap between the permanent tower observations at the Amazon Tall Tower Observatory (ATTO) sit, which are limited to 340 m altitude, and satellite observations of the upper troposphere, lower stratosphere (UTLS). Therefore, the ATTO station was overflown in most of the flights.
As depicted in Figure 5.2.1, the research flights targeted almost exclusively continental regions. The research flights RF06 and RF14 towards the far south of Manaus targeted deforested areas, in contrast to the intact rainforest in the surroundings of Manaus. The flight patterns also included late evening and nocturnal flights (RF13, RF16, RF18) and early morning flights (RF15, RF17, RF20) to cover night time chemistry and particle formation after the onset of sunrise.
The highest data capture was in the high altitudes between 9-15 km, since many flights included parts focusing on the sampling of outflow from convective cumulus clouds.

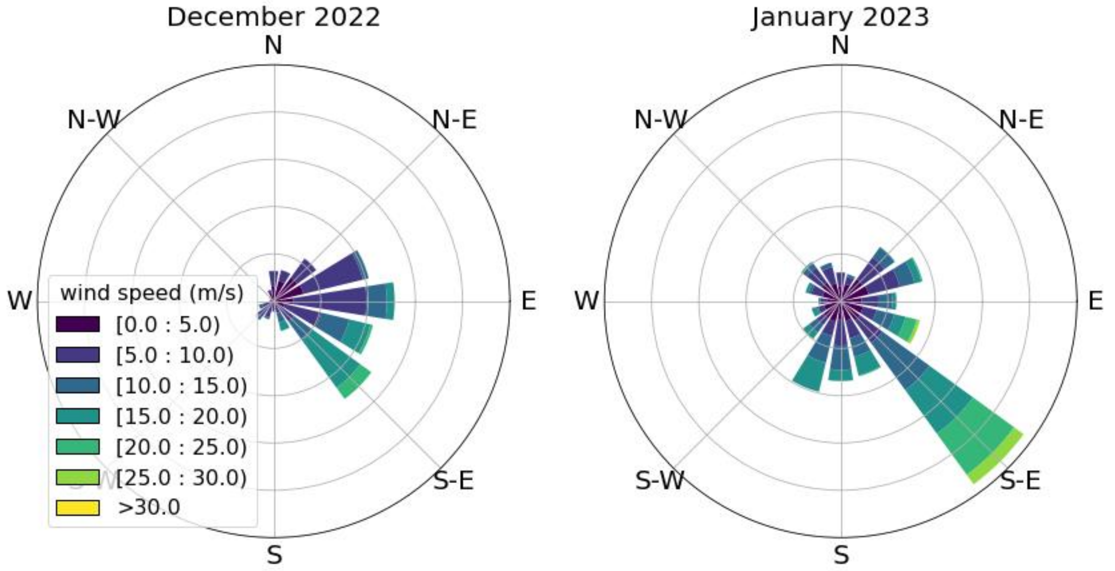

Figure 5.2.2: Frequency of measured wind directions with BAHAMAS aboard HALO in December 2022 (left) and January 2023 during CAFE Brazil. The wind speed is colour-coded.

Some flights were also dedicated to sample the tropical forest boundary layer (RF15) and perform vertical profiling (RF05, RF07, RF18).

5.2.1 *Meteorological conditions and back trajectories*

The CAFE Brazil campaign took place during the transitioning phase of dry to wet season. The campaign was divided into two halves, with the first half in December, when the conditions were still relatively dry and hot. After the Christmas break, the second half of the campaign took place in January, during which time rain events became more frequent.
Basic meteorological parameters including wind speed and direction, cabin and outside temperature, pressure etc. were recorded during the flights by the BAHAMAS instrument onboard the HALO aircraft (Giez et al., 2022).

As depicted in Figure 5.2.2, the predominant wind direction captured during the January flights was clearly from the South East, indicating a continental origin. In December, the wind direction was more equally distributed, ranging from northeast to southeast. In addition, high wind speeds between 25-30 m/s were slightly less frequent during December than during January.

5.3 HYSPLIT TRAJECTORY ANALYSIS

In order to investigate the origin of the sampled air mass, 10-days backward trajectories were calculated for every minute along the flight track using the HYSPLIT model of NOAA in Version 5.2. (see Section 3.5)

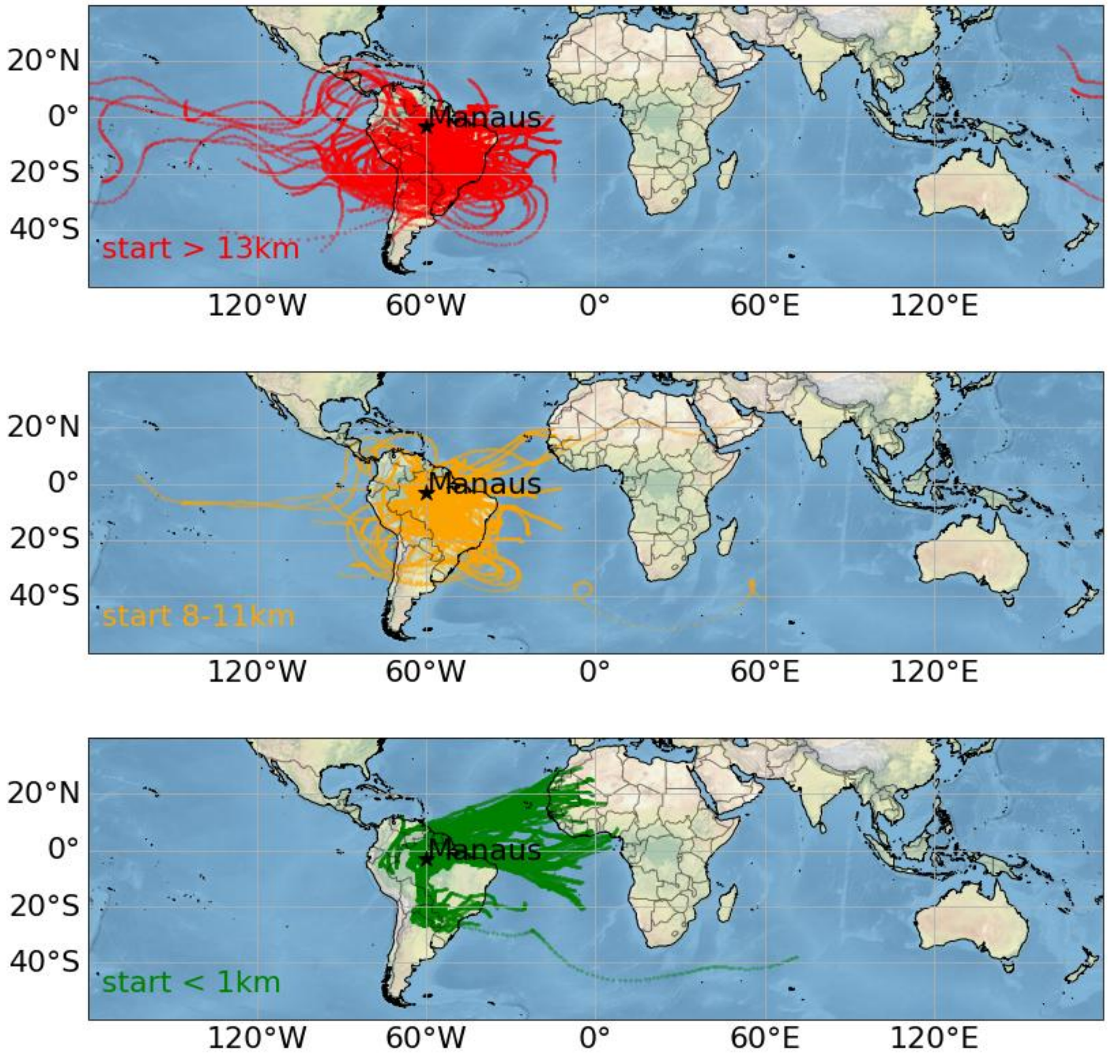

Figure 5.3.1: Backward trajectories calculated with HYSPLIT every ten minutes along the flight tracks of CAFE Brazil. The panels are separated by altitude of the starting point along the flight track: Low altitudes (green, bottom panel), mid-altitudes (orange, middle panel), and high altitudes (red, upper panel). The trajectories go back 10 days in time.

The trajectories of the sampled air masses circulated above the continent, showing no distinction between December and January. As depicted in Figure 5.3.1, the origin of the sampled air masses was largely dependent on the sampling altitude.
Trajectories starting at mid- (8-11 km, yellow) and high altitudes (> 12 km, red) with few exceptions randomly circulate over the continent. This suggests that the impact of long-range transport from other continents on the observed PAN and PAA levels in mid- and upper troposphere was likely low.

In contrast, most of the low altitude trajectories (<3 km, green) originated from the central Atlantic and West Africa, and surpass the north-west coast of Brazil, where satellite observations recorded biomass burning events (see Section 5.3.1). Hence, the low-altitude trajectories could potentially be impacted by urban pollution and/or biomass burning for source regions on the South American continent or West Africa.

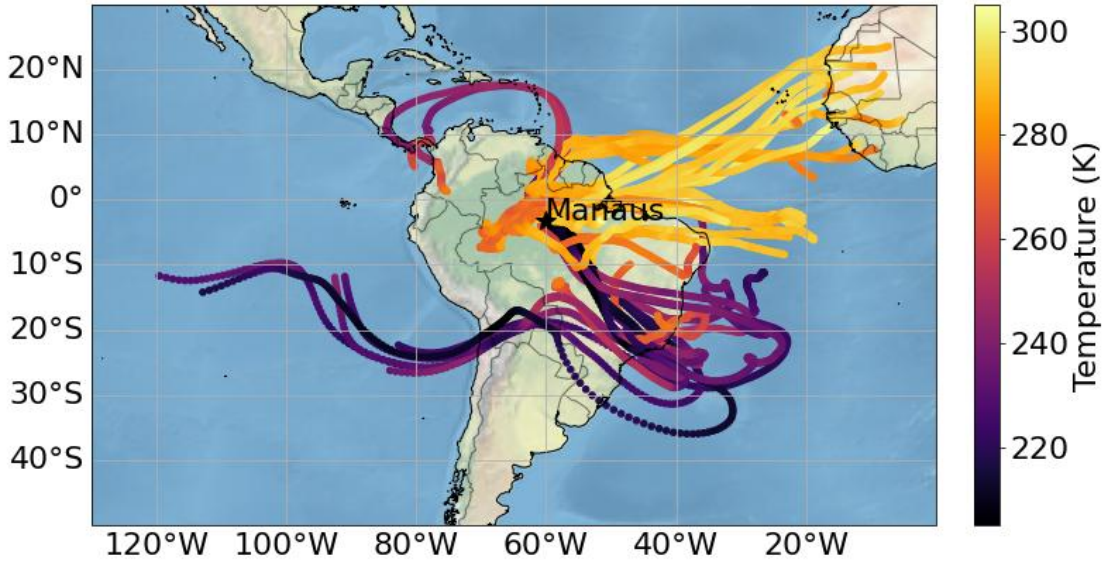

Figure 5.3.2: 10-day back-trajectories calculated with HYSPLIT for every 10 min along the flight track of RF17 on 18th January 2023 during CAFE Brazil, colour-coded by air temperature.

However, with respect to trans-Atlantic transport, it remains unclear whether the conditions during these low-altitudes trajectories were conducive for the long-range transport of PAN and PAA over such a long distance, considering potential photochemical and thermal losses as well as wash-out by precipitation.

To address the question of thermal decay of PAN during the travel from West Africa to Amazonia, the temperatures along the trajectory are depicted in Figure 5.3.2 for the example of RF17. In Figure 5.3.2, it is observed that the air masses which traveled from west Africa stayed at low altitudes, with relatively high temperatures ranging from approximately 280 to 300 K. With respect to the short lifetime of PAN at these temperatures in the order of maximum a few days, it would not be possible to transport PAN from West-Africa to Brazil. However, during transport PAN and PAA are continuously generated in hydrocarbon-rich air masses. The continuous photochemical formation of PAN and PAA in aged biomass burning plumes (5-9 days) has been reported showing an increasing importance of PAA compared to PAN with air mass age (Crowley et al., 2018).

5.3.1 *FIRMS observations of open fires and biomass burning*

Biomass burning is a significant source of air pollution in Brazil, particularly in the Amazon region during the dry season (July-December) (Holanda et al., 2020). The pollution from biomass burning is not only a result of local fires but also of long-range transport from other continents. Previous studies have shown that transatlantic transport of pollution dominates the northern and central Amazonian aerosol population during the early biomass burning season (July to September) (Holanda et al., 2020). However, this transport is less significant in the later biomass burning season (October

- December) (Holanda et al., 2020).
Given that the CAFE Brazil campaign took place at the end of the Amazonian dry season and outside the peak-season of transatlantic transport, low impact of biomass burning on the air mass composition is expected.

In Figure 5.3.3 depicts the open fires detected with confidence higher than 95 % by the MODIS instrument provided by the NASA FIRMS[19] tool during the CAFE Brazil campaign. The total total number of events in the depicted area above central and southern America and tropical Africa during two months of December and January is approximately 16000, with hot spots in northern tropical Africa at around 10 °N and coastal areas in southern America.
Upon comparing to the detected fire events from the previous month, it is evident that fires above Brazil decreased from November to December, whereas fires in northern tropical Africa increased (see Figure A.0.7 in the Appendix).

In Brazil, most of the fire events were observed along the north-east coast. In this region, the vast majority of the fire events took place in the beginning to mid-December 2022, while fire events during January 2023 were few. In contrast, the density of fire events in the sampling area for CAFE Brazil is low during both months.
In summary, the satellite observations indicated that fire activities in Amazonia during CAFE Brazil were generally low, but exhibited a temporal pattern that was consistent with expectations in the region during this time period. Specifically, fire activities were more pronounced at the beginning of the campaign and decreased during the transition from dry to wet season.

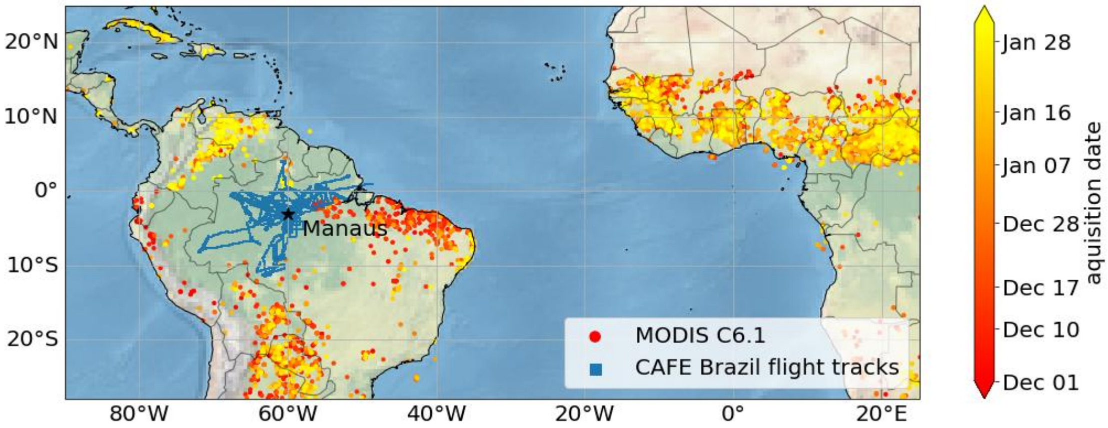

Figure 5.3.3: Detected open fires by MODIS with high confidence (>0.95) above Brazil and tropical Africa between December 2022 and January 2023, colour-coded by date. The flight tracks during CAFE Brazil are marked in blue.

5.4 PAN AND PAA MEASUREMENT RESULTS DURING CAFE BRAZIL

Figure 5.4.1 shows the measured PAN and PAA during the CAFE Brazil campaign with the CIMS instrument along the flight tracks. In general, PAN and PAA levels were ele-

---

[19] `https://firms.modaps.eosdis.nasa.gov/map`, last access: 08.04.2025.

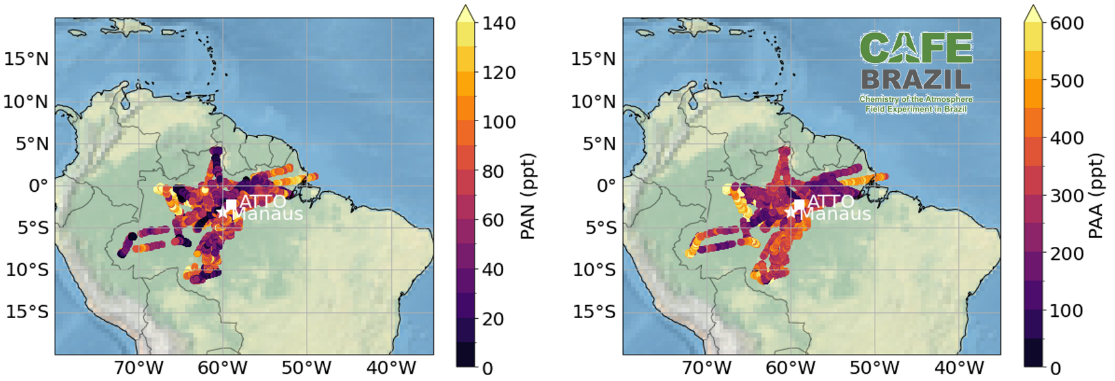

Figure 5.4.1: Measured PAN (left panel) and PAA (right panel) with CIMS along the flight tracks during CAFE Brazil.

vated during December compared to January, reflecting the change of season from dry to wet season. Overall, PAA levels dominated over PAN levels, which is in agreement with the expectation for low-NO_x and high biogenic emissions.

As seen in Figure 5.4.2, the highest PAN values were observed during RF05 on 4th December and RF10 on 16th December 2022, peaking around 320 ppt at around 10 km altitude. RF10 was designed to measure convective outflow and is analyzed in detail in Section 5.4.2.
A sharp single PAN peak occurred around 16:45 UTC in RF14, reaching almost 350 ppt when HALO crossed a local biomass burning plume. Visible biomass burning plumes were also spotted during RF11.

PAA mixing ratios generally varied strongly with altitude Maximum PAA at low altitudes was measured above ATTO in RF07 on 9th December 2023, as shown in detail in Section 5.4.1. Due to the constant high altitude during RF20 on 26th January 2023, PAA and also PAN were varying little during this flight, as shown in detail in Section 5.4.3.

5.4.1 *RF07: Stacked profiles above ATTO*

In order to investigate the vertical distribution of PAN, PAA and related precursors species above the unperturbed Amazonian rainforest, the example of RF07 was chosen, which was designated to vertical profiling. In contrast to most of the other flights during CAFE Brazil, RF07 did not explicitly target convective outflow, and therefore can be considered as a pristine background flight. In addition, the data coverage of this flight was almost complete, since most of instruments were running without any issues. This makes RF07 an ideal candidate for the applications of steady-state calculations, which are useful to understand the production and loss processes of PAN and PAA during CAFE Brazil.

RF07 was conducted on 9th December 2022, starting at 11:00 local time in the morning and lasting until 20:00 local time in the night, hence covering the transition phase to darkness. The target area was the pristine Amazonian rainforest above the ATTO re-

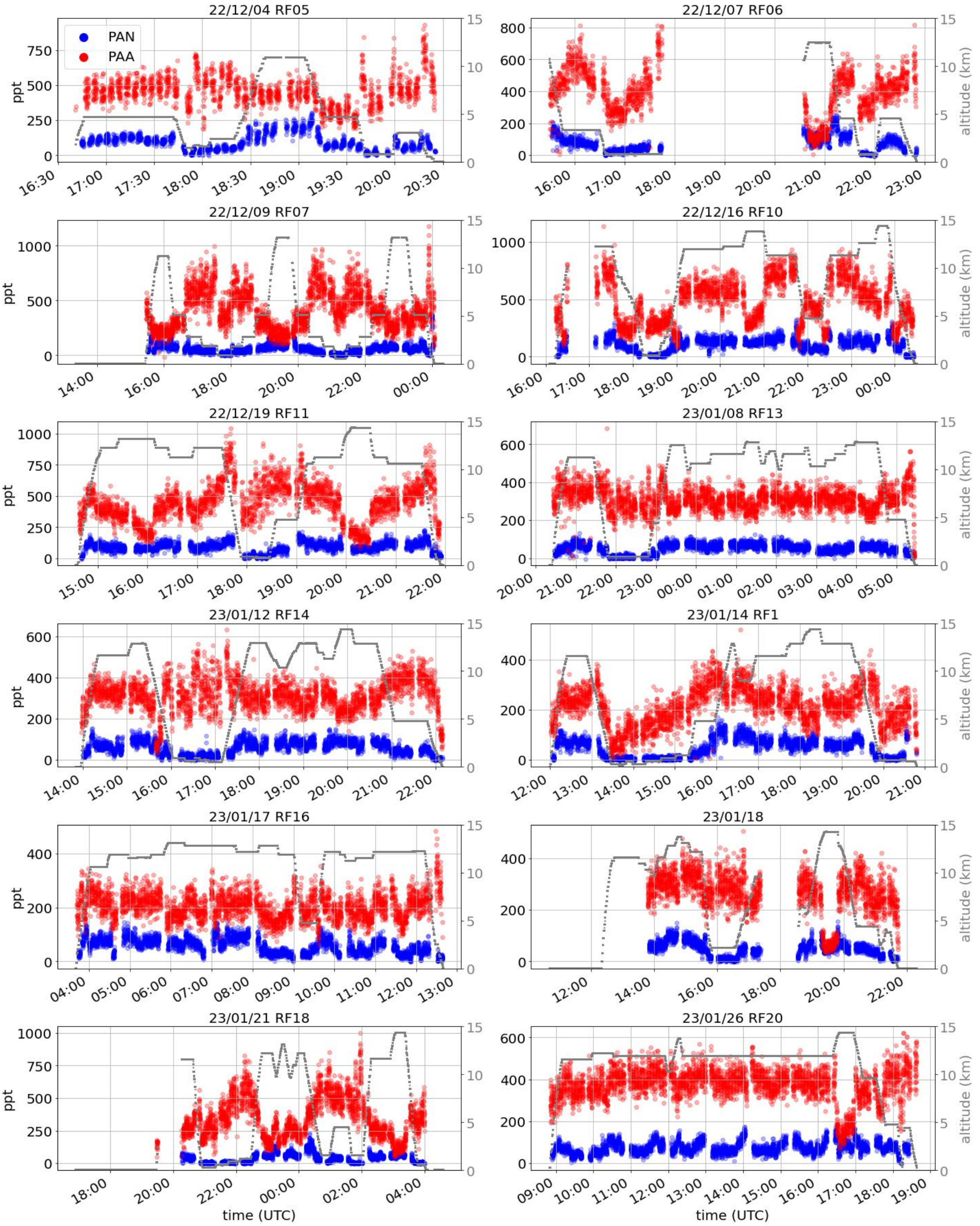

Figure 5.4.2: Time series of PAN (blue) and PAA (red) measured by CIMS aboard HALO for all analysed flights during CAFE Brazil. The flight altitude is depicted in gray.

search tower, where a stacked flight pattern was performed. The flight altitude ranged from less 1 km above the ground to more than 13 km altitude.

5.4.1.1 *PAN and PAA along the flight track of RF07*

A three-dimensional depiction of PAN and PAA measured along the flight pattern of RF07 is shown in Figure 5.4.3. It is apparent that PAA mixing ratios were highest close to the boundary layer and decreased with altitude. In contrast, PAN was elevated in the mid-troposphere and was close to the detection limit at the lowest altitudes due to its rapid thermal decay. Notably, when approaching Manaus, an urban pollution peak in PAN and PAA was captured during the descending phase of the flight.

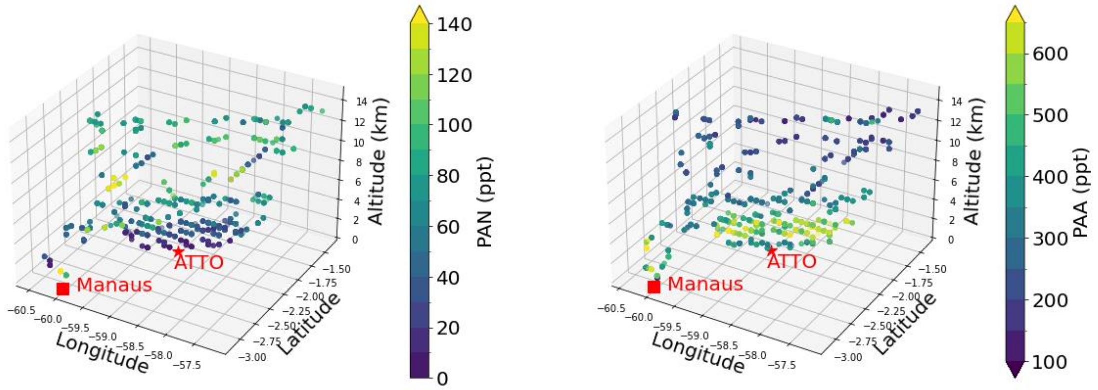

Figure 5.4.3: 3D-representation of measured PAN (left panel) and PAA (right panel) along the flight track of RF07 on 9th December 2022. The location of Manaus and the research station ATTO are marked for orientation.

5.4.1.2 *Vertical profiles of measured species during RF07*

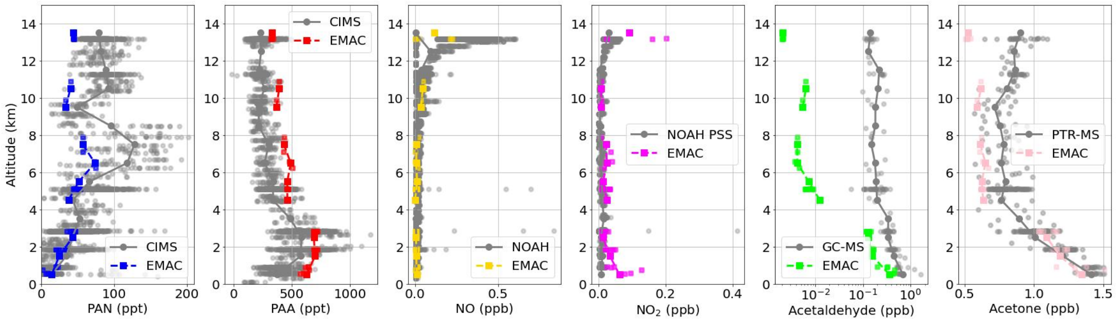

Figure 5.4.4: Vertical profiles of measured (grey round dots) and modelled (coloured squares) species aboard HALO during RF07 on 9th December 2022 during CAFE Brazil.

Figure 5.4.4 presents the vertical profiles of PAN and PAA in RF07, along with the vertical profiles of simultaneously measured precursor species aboard HALO, namely NO, NO_2, acetaldehyde and acetone. Additionally, the vertical profiles of the corresponding model simulations of the EMAC model for each species are also depicted.

The measured median vertical PAN profile exhibits an inverse C-shaped distribution, with a maximum around 8 km, reaching peak values of single measurements up to more than 200 ppt. Towards higher altitudes, median PAN mixing ratios decrease to less than 100 ppt. This mid-tropospheric PAN maximum is much less pronounced in

the modelled data. The EMAC simulations slightly underestimate PAN at most altitudes with the maximum deviation at mid-altitudes around 55 %.
In contrast, the model generally overestimates PAA (20-85 %), with the maximum deviation at mid-altitudes. However, both the modelled and observed PAA mixing ratios follow the same vertical distribution, with an increase from 0 to 2 km altitude and then a continuous decrease towards higher altitudes.
The vertical profiles of the organic species acetaldehyde and acetone also show decreasing mixing ratios with increasing altitude, which is typical for organic species emitted in the boundary layer and being increasingly subject to photolysis and oxidation towards the free troposphere. The EMAC model and the measured acetone mixing ratios are consistent with the observations below 4 km altitude but underestimate the observations between 15 and 42 %. The discrepancy was highest at the highest altitudes.
However, there is a striking discrepancy of more than an order of magnitude between modelled and measured acetaldehyde levels. This discrepancy was also observed in the other flights during the campaign and in the subsequent CAFE Pacific campaign and will be discussed in Section 7.7.
The EMAC model also represents the NO_x levels well, although it tends to over estimate NO_2 in the boundary layer.

5.4.1.3 *Steady-state PAN and PAA calculated for RF07*

In order to investigate the impact of photochemical production of PAN and PAA, the simplified chemistry scheme, as as previously described in Section 3.8, was applied to RF07.

The steady-state concentrations of PAN and PAA were calculated based on the two precursors acetone and acetaldehyde only to compare their relative impact on PAN and PAA formation. Note that the calculation does not include MGLY, which is also a major PA precursor, because no measurements of this species are available.

The same steady-state calculations were made with two data sets, one mainly based on measured data aboard HALO and one based on the same species simulated in EMAC. In both cases, HO_x mixing ratios provided by EMAC were used because measurement data was not available. In addition, measured and modelled data was filtered at PAN photolysis frequencies below $1e^{-7}$ 1/s to assure a photochemical steady-state. Temperature dependent reaction rates based on IUPAC recommendations were implemented. Since the time steps of the EMAC model output is 12 min, all measurement data was resampled to 12 min averages before doing the calculation. The 12-min resampled input data used for the steady-state calculations along the timeseries of RF07 is depicted in Figure A.0.8.

Figure 5.4.5 presents the vertical profiles of calculated PAN (left panel) and PAA (right panel) with the steady-state assumption for RF07 during CAFE Brazil, compared to the CIMS measurements of PAN and PAA of this flight.
While measured PAN at high altitudes above 12 km was around 100 ppt, the steady-state PAN levels based on measured acetaldehyde and acetone exceeded even 1 ppb at these altitudes. This deviation of more than an order of magnitude is primarily due to the ox-

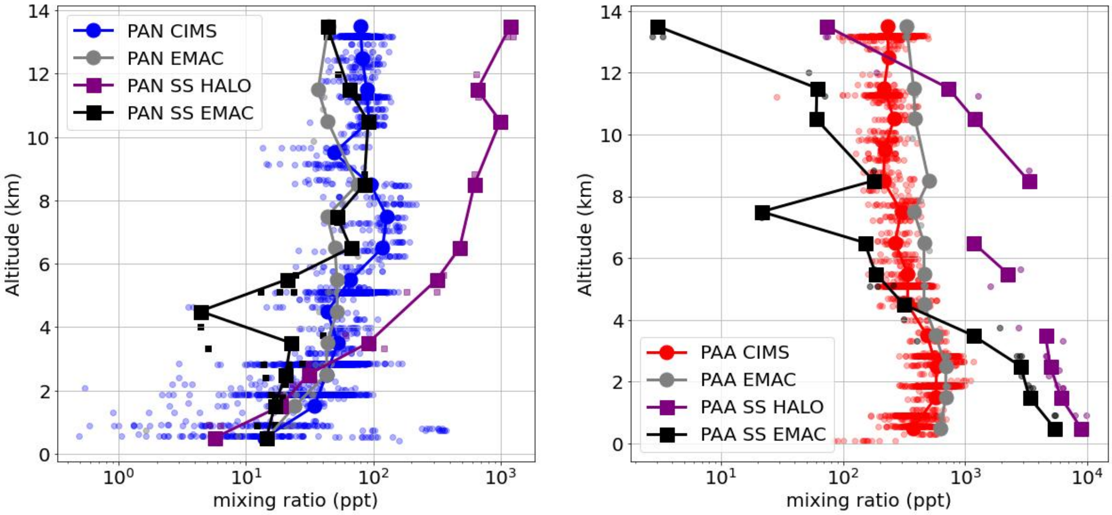

Figure 5.4.5: Vertical profiles of measured (blue dots) and modelled (gray dots) PAN (left panel) and PAA (red and gray dots resp. in the right panel) in RF07 during CAFE Brazil. The profiles are compared to either calculated steady-state concentrations based on measured acetone, acetaldehyde, photolysis frequencies, and NO_x aboard HALO (+HO_x from EMAC) (purple squares) or data of the same species but entirely based on the EMAC model (black squares). The medians are marked by the solid lines.

idation of acetaldehyde, as evident from the production rates depicted in Figure 5.4.6. The high PA-radical production resulting from the high levels of measured acetaldehyde also impacts the steady-state PAA concentration, which overestimated measured PAA levels by more than an order of magnitude, except at the highest altitude bin. Therefore, it becomes clear that the measured acetaldehyde levels are not compatible with measured PAN and PAA levels, unless the used model OH concentrations are wrong by more than a factor of 10.

In contrast, the modelled acetaldehyde, combined with model HO_x, model acetaldehyde, model photolysis frequencies and model NO_x, leads to steady-state PAN-mixing ratios close to the observed ones. If the steady-state assumption was applicable, this would indicate that the only included precursors, acetone and acetaldehyde, were sufficient to explain the observed PAN levels.

However, in the case of PAA, the steady-state assumption based on EMAC model data exceeds the measured and modelled PAA at altitudes below 4 km by an order of magnitude, while it underestimates PAA at higher altitudes by up to two orders of magnitude. This can be explained by vertical transport shifting organics from the lower troposphere to the upper troposphere, which means that steady-state is not applicable.

5.4.1.4 *Production terms of PAN and PAA in RF07*

To compare the relative contribution of the two investigated precursors acetone and acetaldehyde leading to the formation of PAN and PAA in the simple steady-state scheme, the single production terms in Equation 33 and Equation 39, respectively, calculated for RF07 during CAFE Brazil are depicted in Figure 5.4.6. Except for the production term from acetaldehyde, measured (solid lines) and model data (dashed lines) are in good agreement.

Based on model data, the photolysis of acetone (pink) is more important than the oxidation of acetaldehyde by OH (lime) for both PAN and PAA production in altitudes above 4 km. Below 4 km altitude, the reaction of acetaldehyde with OH becomes dominant over acetone photolysis because of the high abundance of acetaldehyde in low altitudes. Due to the enhanced model NO_2 below 2 km compared to the observations, the PAN production term from acetaldehyde even exceeds the one based on measurement data.

The simple steady-state scheme also includes a production term of PAA from the PA-radicals released in the thermal decay of PAN. As seen in the right panel in Figure 5.4.6, the PAA production term from PAN loss (blue) becomes similarly important than production from acetaldehyde at low altitudes, where PAN is thermally not stable but PAA is. Below 4 km altitude, the loss of PAN contributes at a similar rate as the oxidation of acetaldehyde to the formation of PAA based on model data.

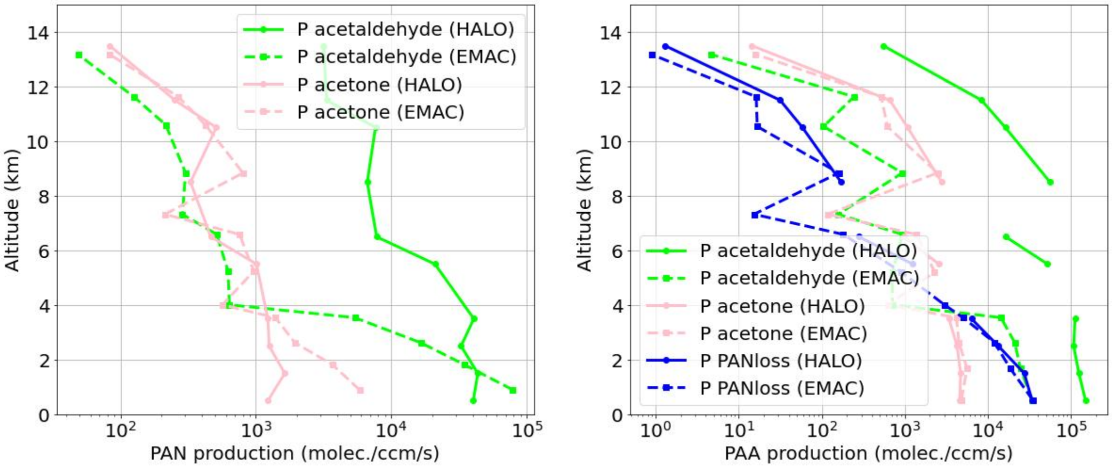

Figure 5.4.6: Contribution of acetaldehyde and acetone to the production of PAN (left panel) and PAA (right panel) from measured (HALO) and modelled (EMAC) data in the steady-state calculation, plotted against altitude, applied to RF07 during CAFE Brazil. The right panel further includes the production of PAA from PA-radicals released by the dissociation of PAN (blue).

5.4.1.5 *Loss terms of PAN and PAA in RF07*

In contrast to the production terms, the loss terms shown in Figure 5.4.7 do not differ significantly between the model (dashed lines) and measurement data sets (solid lines), since they involve less complex chemistry (see Equation 37 for PAN losses and Equation 44 for PAA losses).

As shown in the left panel in Figure 5.4.7, the loss terms of PAN are dominated by photolysis (yellow) in high altitudes. Conversely, the thermal loss of PAN (cyan) dominates below 6 km.

In the case of PAA (right panel), photolysis (yellow) is the primary mechanism for the loss of PAA at all altitudes. The loss rate of PAA via the reaction with OH (cyan) is almost an order of magnitude lower.

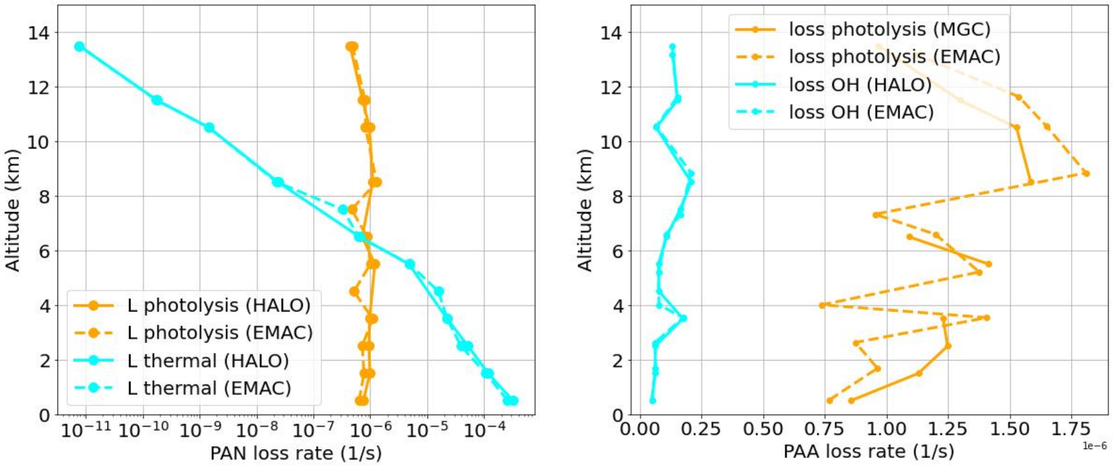

Figure 5.4.7: Vertical profiles of loss terms of PAN (left panel) and PAA (right panel) from measured (HALO) and modelled (EMAC) data in the steady-state calculation, applied to RF07 during CAFE Brazil.

5.4.1.6 *Total atmospheric lifetimes of PAN and PAA during CAFE Brazil*

The sum of the loss terms is the inverse of the total atmospheric lifetime.

Figure 5.4.8 depicts the median total atmospheric lifetimes of PAN (blue) and PAA (red) calculated from all flights during CAFE Brazil via the loss terms in steady-state scheme. As seen in Figure 5.4.8, the lifetime of PAN strongly increases with increasing altitude, from less than an hour in the boundary layer up to 2-3 weeks in the UT. In contrast, the total atmospheric lifetime of PAA decreases with increasing altitude, as photolysis increases. During CAFE Brazil, the total atmospheric lifetime of PAA is more than 10 days in the lower troposphere, while it is only 5-6 days in the UT. Note that deposition of PAA in the boundary layer can play a role, which was not included in this estimate.

This significant difference in atmospheric lifetimes highlights the importance of considering the different thermal stability of these species when interpreting their vertical distributions.

5.4.2 *RF10: Convective outflow*

RF10 was designed to investigate the outflow of convective updraft above the Amazonian rainforest northwest of Manaus, extending even out to deforested areas. Therefore, this flight was chosen as an example to investigate the impact of convection during CAFE Brazil on the vertical profiles of PAN and PAA.

The flight was conducted on 16th December 2022 and lasted for approximately 8 hours.

During the flight, the air masses in the vicinity of several visible convective cloud systems were sampled. The flight pattern included a helix pattern around a convective

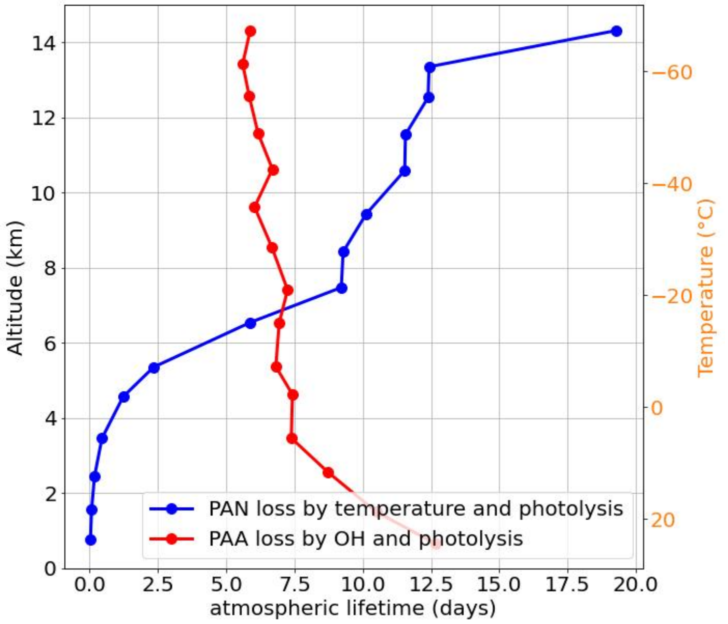

Figure 5.4.8: Calculated median atmospheric lifetimes of PAN and PAA plotted against altitude (left axis) and temperature (right axis) for all flights during CAFE Brazil, based on modelled HO_x, measured temperature, and measured photolysis frequencies.

cell and a zig-zag pattern in the outflow of another convective cell. The first half of the flight covered daylight while the second half occurred in the evening and night.

A time series of measured species during RF10 is depicted in Figure 5.4.9, where some phases of detected convective outflow are marked (green shaded areas) as well as lightning activity (orange shaded area) and the overfly of a deforested area (brown shaded area) based on the flight protocol.

In general, PAN and PAA were highest during RF10 of all flights during CAFE Brazil. During this flight, PAA was notably elevated in high altitudes, reaching up to 1 ppb. Additionally, other organics, such as acetone (magenta), were elevated. Unfortunately, acetaldehyde was not measured during this flight. Frequent spikes in NO (golden) and NO_2 (cyan) where observed, especially in the proximity of convective systems. This suggests, that the observed NO_x during RF10 was strongly influenced by lightning activity, which is the most import source of NO_x in the upper tropical troposphere (Lamarque et al., 1996).

The location of the marked areas along the flight track is depicted in Figure 5.4.10, where PAA mixing ratios along the flight track are colour-coded. Notably, high PAA levels (>750 ppt) were observed at the north-west end of the flight track around 21:00 UTC, when convective outflow was encountered at flight level FL370 (approx. 12 km). Acetone levels were also high during this time,approx. 1.3 ppb, as shown in Figure 5.4.9. Since NO_2 was retrieved with a PSS assumption from the measured NO, O_3, photolysis frequencies of NO_2 and modelled peroxy radicals, observation-based NO_2 is only available during daytime. The EMAC model and observations of NO agree well during both day and night. During night, the modelled NO_2 is strongly elevated. This indi-

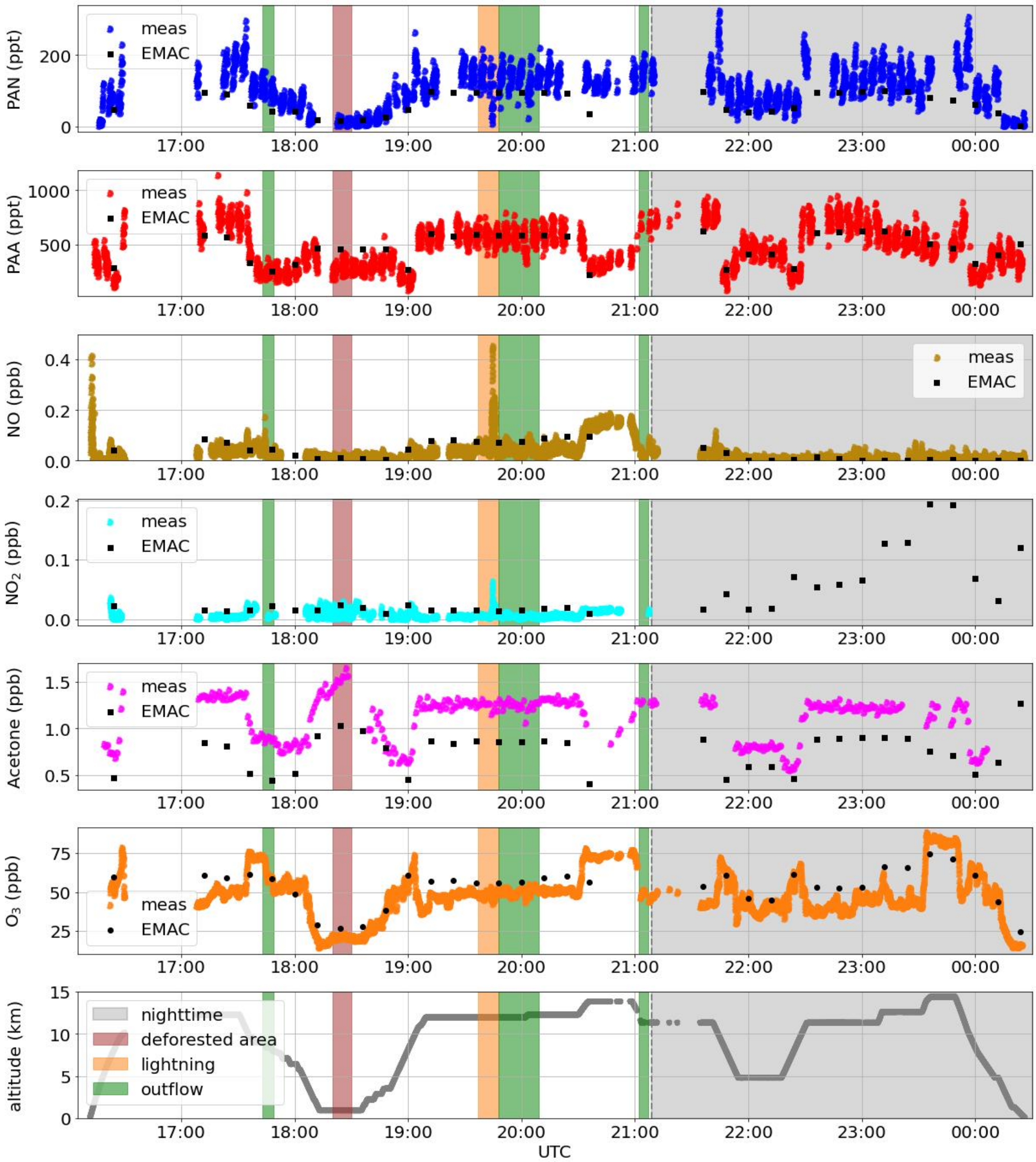

Figure 5.4.9: Time series of measured PAN, PAA, NO, NO_2, acetone, and ozone aboard HALO of RF10 on 16th December 2022 during CAFE Brazil. EMAC 12-min model data for the species are depicted with black squares. The altitude is depicted in gray in the lowest panel. The shaded areas indicate selected times impacted by convection (green), lightning (orange) and above deforested area (brown).

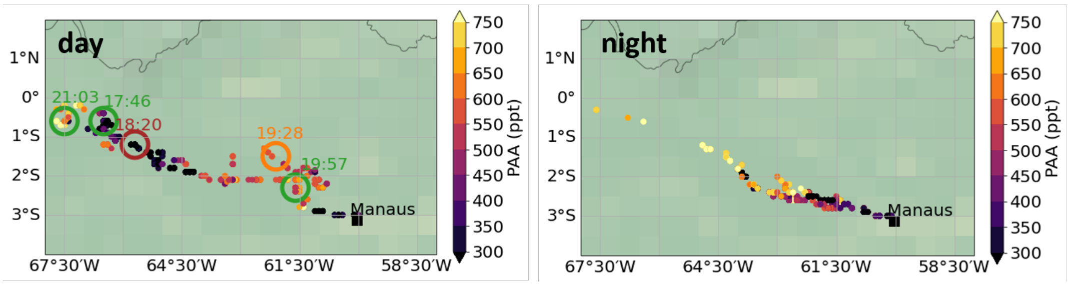

Figure 5.4.10: PAA mixing ratios colour-coded along the flight track of RF10 during day (left panel) and night (right panel). The timings of outflow, lightning, and deforested area are marked as in Figure 5.4.9.

cates the entry of NO_x in the mid- and upper troposphere in the model most likely due to lightning of convection. In addition, ratio between NO_2 and NO increases towards NO_2 due to the absence of photo dissociation.

As a consequence of convection, the profile of PAA depicted in Figure 5.4.11 exhibits a significant maximum between 10-12 km and is similar in shape to that of acetone. In contrast, the vertical profiles of PAA and acetone presented in Figure 5.4.4 derived for RF07, which was not dedicated to convective outflow sampling, does not exhibit such a strong upper tropospheric maximum.

The uplifting of biogenic VOC from the residual layer to the UT up to 12 km altitude above the Amazon by deep tropical convection has been reported for isoprene, isoprene oxidation products and monoterpenes during CAFE Brazil (Tripathi et al., 2025). Tripathi et al. (2025) showed that despite their typical atmospheric lifetimes in the order of minutes to hours, these species could accumulate during night at high altitudes after convective updraft due to the lack of photochemically produced OH radicals, but they rapidly oxidized at daybreak promoting particle formation. In contrast, no significant difference is seen during day and night in the profiles of PAA and acetone, reflecting their longer lifetimes in the order of 5-7 days for PAA and weeks for acetone in the mid- and upper troposphere.

There is also a PAN maximum between 10-12 km, but the low-NO_x conditions clearly favour PAA production over PAN from the uplifted organic precursors.

5.4.3 *RF20: high altitude flight*

RF20 was conducted on 26th January 2023 and was an early morning flight with the objective of tracing the photochemistry-induced temporal evolution of an air mass and particle growth above the cloud deck at sunrise. To achieve this, the aircraft performed a series of eight-shaped patterns, which were shifted downwind of a convective system with time at a constant altitude.

A time series of measured PAN and PAA and relevant precursor species or tracers is depicted in Figure 5.4.12. The onset of photochemistry is indicated by the photolysis frequency of PAN (j(PAN)) provided by the SR instrument.

After 12h21 until 16h30 UTC (8h21-12h30 local time) the aircraft remained at a constant

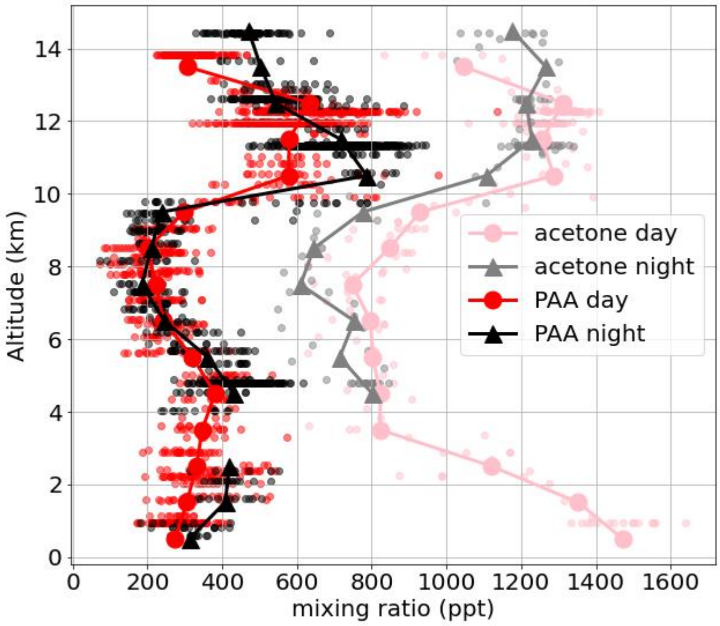

Figure 5.4.11: Vertical profiles of acetone and PAA during day and night in RF10 during CAFE Brazil. The medians are marked by the solid lines.

altitude of around 12 km (FL370), performing eight-shaped patterns. While PAA stayed approximately constant around 400 ppt during this time, PAN was mostly around 50 ppt but showed repeated enhancements up to around 150 ppt. These enhancements are marked in Figure 5.4.12 by the blue shaded areas. NO_x and O_3 were also increased during theses phases while acetaldehyde seemed to be slightly lower. This indicates photochemical production of PAN alongside ozone from organic precursors in the presence of NO_x.
The SP2 instrument measuring BC, a tracer of fresh (< approx. 1 week) biomass burning, registered small peaks of a few counts (<10) during the elevated PAN phases, indicating a possible pollution of open biomass burning or anthropogenic combustion processes. The PAN-to-PAA ratio increased from a background of around 15 % up to 25-32 % during blue shaded phases, reflecting the presence of air masses with a higher content of NO_x favouring PAN production over PAA from the organic precursors like acetaldehyde. As seen in Figure 5.4.12, the EMAC model (squares) does not capture the enhancements of PAN, NO and O_3. The enhancements are probably to small scale to be resolved by the EMAC model. Additionally, the model underestimates the PAA levels in the UT significantly. This could also be a result of the sub-grid parametrization of convection in the model not being able to resolve the traced convective air mass.

Figure 5.4.13 depicts the location of the PAN enhancement phases as circles on the flight track. From this figure, it is observed that the first three PAN elevation phases took place in the north-eastern edges of the flight pattern while the fourth PAN maximum was captured when heading back towards Manaus. Hence, the fourth phase is not part of the eight-pattern and it is unclear if it results from the same air mass or an urban pollution plume.

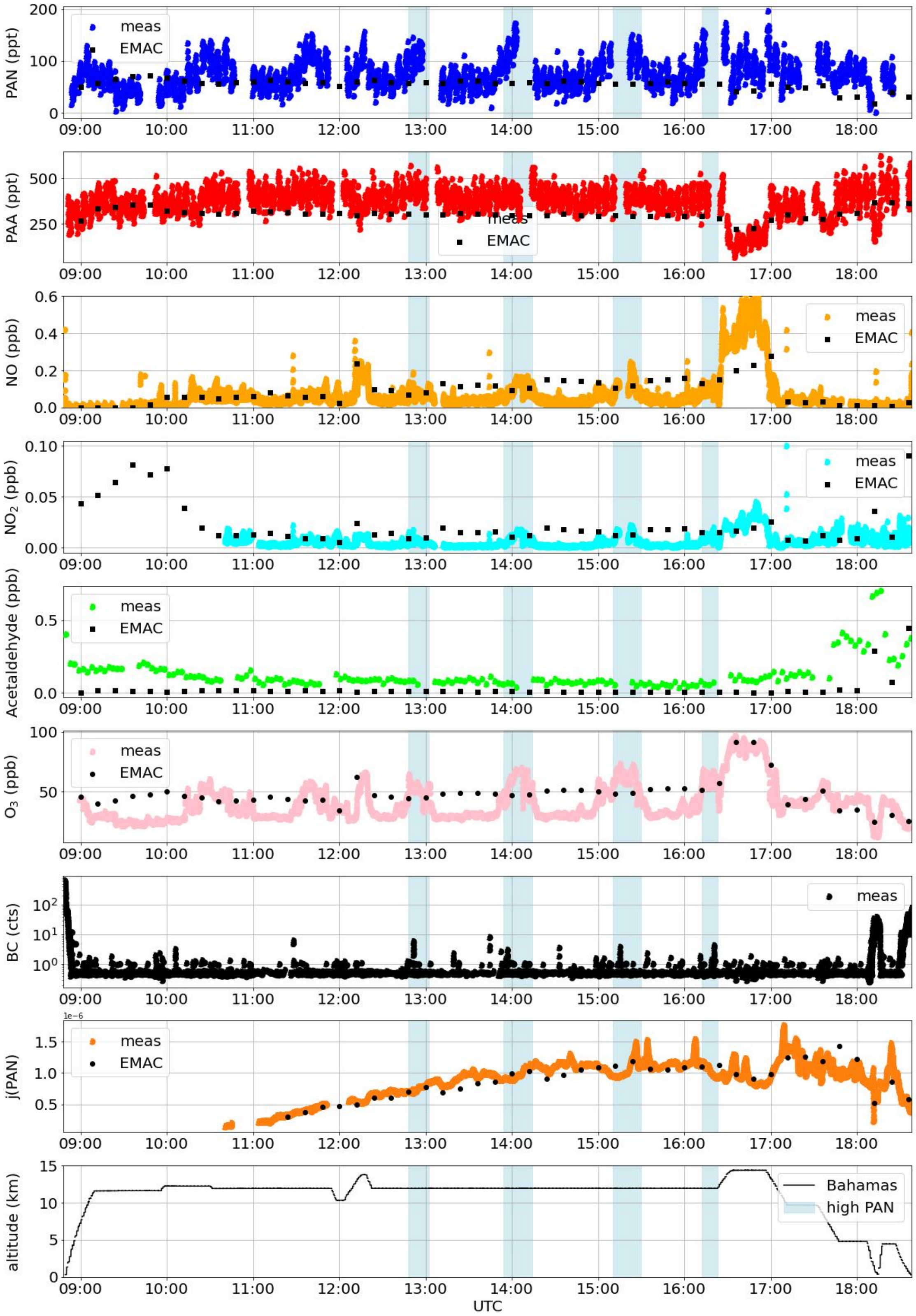

Figure 5.4.12: Time series of measured PAN, PAA and relevant precursor species or tracers (NO, NO_2, acetaldehyde, ozone, black carbon, and photolysis frequency of PAN) aboard HALO in RF20 on 26th January 2023 during CAFE Brazil. The altitude is depicted in the lowest panel. The blue shaded areas mark times of elevated PAN. EMAC 12-min model data for the species is depicted with black squares.

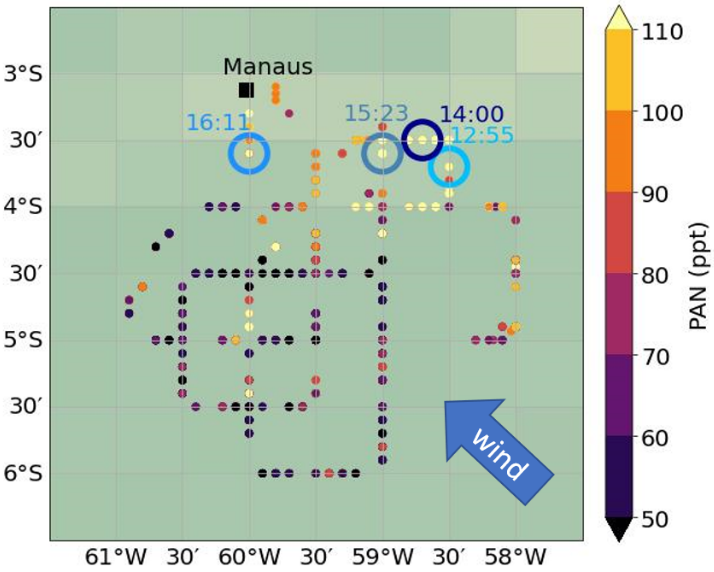

Figure 5.4.13: Measured PAN along the flight track of RF20 during CAFE Brazil. Locations of repeatedly occurring PAN enhancements, as depicted in Figure 5.4.12, are marked. The prevailing wind direction is indicated by the blue arrow.

5.4.3.1 *PAN predictions by the CAMS model during RF20*

The presence of an upper tropospheric PAN plume at this location was also confirmed by the reprocessed Copernicus Atmospheric Monitoring Service (CAMS) model product with EAC4 data, which was analyzed for the pressure levels 1000 hPa, 850 hPa, 600, 300 and 25 hPa.

Figure 5.4.14 depicts the reprocessed CAMS model PAN at 250 hPa at two timings overlapped with the time-wise matched PAN measurements along the flight track at 200 hPa. As seen in Figure 5.4.14, the PAN plume moved between 12h00 UTC and 18 UTC with the direction of the wind from south-east towards Manaus. The flight track probably crossed this plume in its north-eastern extend, as indicated by the elevated PAN measurements at this location.

Away from the PAN plume, the CAMS model estimates generally lower PAN mixing ratios over the pristine rainforest around Manaus in the south-west of Manaus, which is consistent with the CIMS observations. However, CAMS overestimates the absolute level of PAN by around a factor of 25.

5.4.3.2 *Trajectory analysis for RF20*

An examination of the origin of the air mass measured at 11.5-12.5 km altitude during RF20, as depicted in Figure 5.4.15, reveals that approximately half of the 10-days back trajectories calculated wiht HYSPLIT arise from uplift over the South American continent, particularly at the coastal regions and southern Brazil. The other half of the trajectories have traveled at high altitudes from the eastern pacific, descending to 12 km altitude.

The trajectories belonging to the points of elevated PAN are marked in green and originate from southern Brazil/northern Argentina, except for the fourth point, which

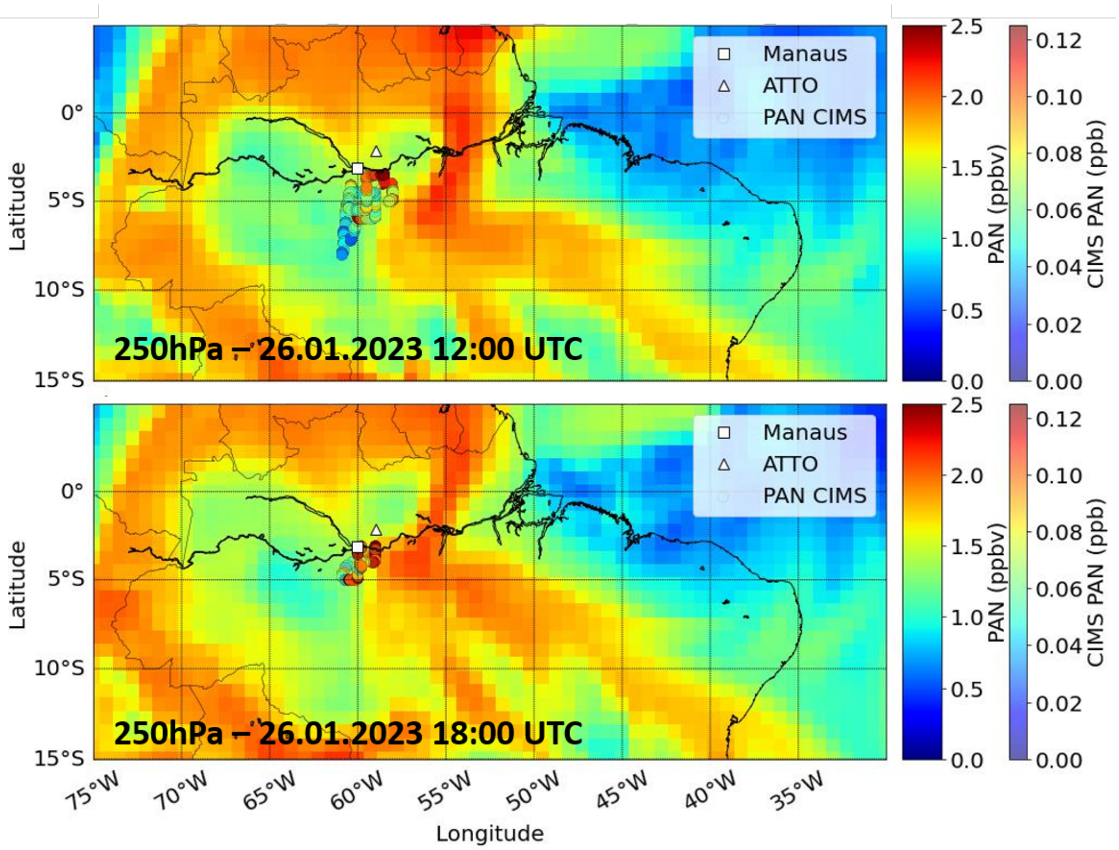

Figure 5.4.14: PAN simulations by CAMS based on EAC4 reanalysis data at 250 hPa altitude for 12h00 UTC (upper panel) and 18h00 UTC (lower panel) with corresponding PAN measurements of CIMS above 200 hPa in a 3h-range around these times. Mixing ratios of PAN are colour-coded with differing scales for CAMS simulations (left colour bar) and CIMS observations (right colour bar) by a factor of 25.

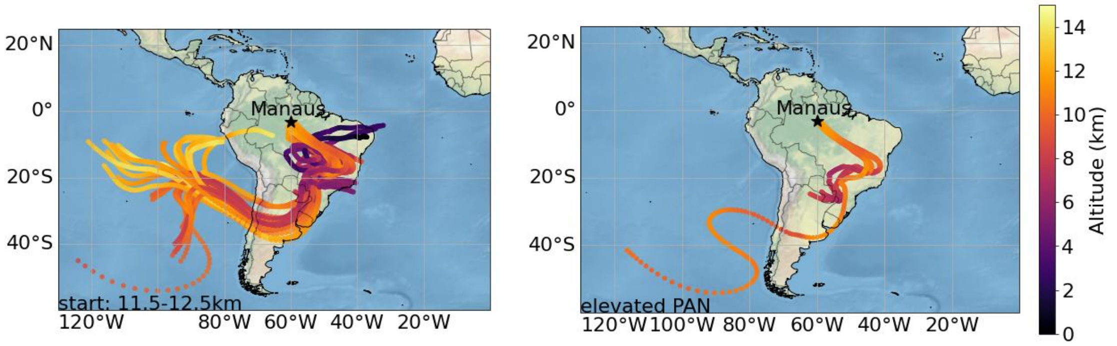

Figure 5.4.15: 10-days back trajectories calculated with HYSPLIT for every 10 min along the flightpath of RF20 during CAFE Brazil, starting at an altitude range between 11.5-12.5 km (left panel). A subset of trajectories belonging to the points of elevated PAN in this altitude range, as marked in Figure 5.4.13, is shown in the right panel. Trajectories are colour-coded with altitude.

originates from the eastern Pacific. It is worth noting that looking at single trajectories has a high degree of uncertainty. However, based on the ensemble of trajectories, it seems likely that the air masses with elevated PAN originate from convective uplift over the Southern American continent potentially containing pollution from open biomass burning or anthropogenic combustion activities possibly mixed with cleaner air masses from the eastern Pacific.

5.5 REGIONAL, VERTICAL AND SEASONAL DISTRIBUTION OF PAN AND PAA

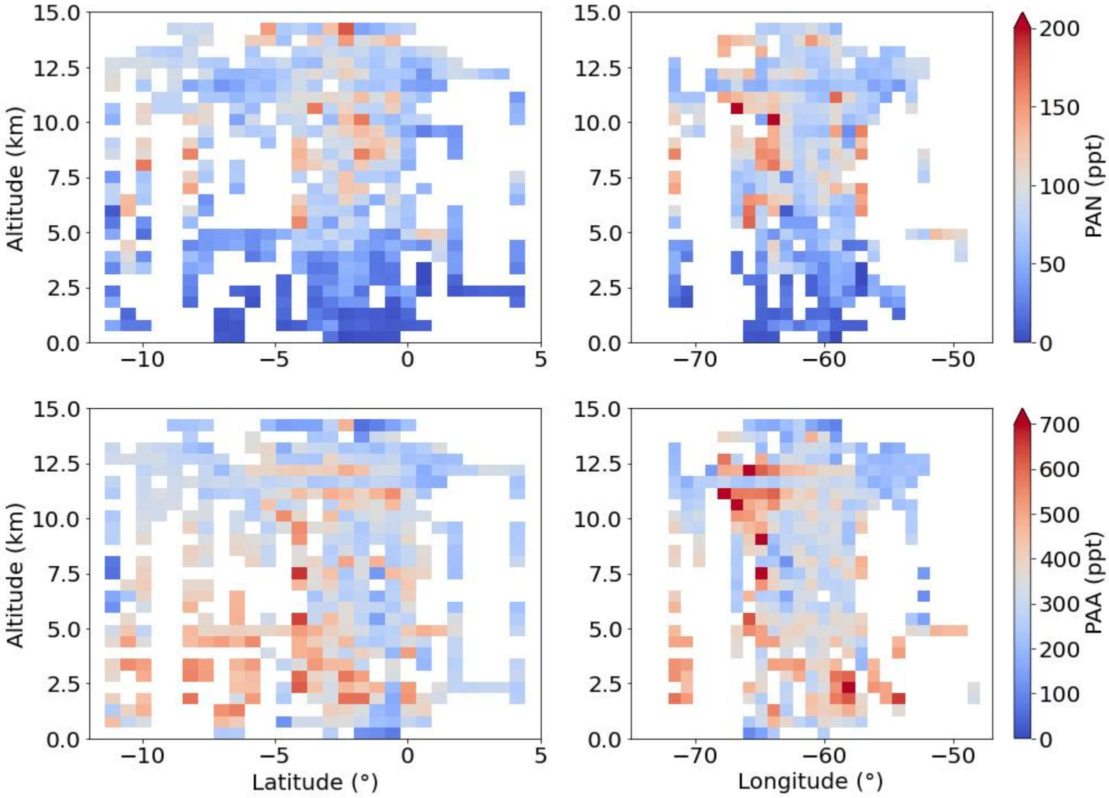

Figure 5.5.1: Binned vertical distribution of PAN (upper panels) and PAA (lower panels) along latitude (left column) and longitude (right column) measured during CAFE Brazil. The colour of the pixels indicate the mean mixing ratio at this location.

Figure 5.5.1 presents the PAN and PAA measurements during the entire CAFE Brazil campaign, plotted against latitude and longitude.

In terms of latitude, the data coverage was highest between 0-5 °S, see left column panels in Figure 5.5.1. Vertical profiles further south, between 5-12 °S, were obtained from the flights RF06, RF14 and RF18. In contrast, very few data points were captured in the northern hemisphere north of 2 °N, which were obtained from RF16 and RF17, only. The limited data coverage north of the equator makes quantitative analysis challenging in this region.

In terms of longitude, most flights sampled east and south-east of Manaus in between 57-67 °W. A significant gradient longitude-wise cannot be observed for either PAN nor for PAA in the right column panels of Figure 5.5.1.

The zonal distribution of PAN derived during CAFE Brazil is consistent with the results from global models, which simulated higher PAN in the tropical southern hemisphere than in the northern tropical hemisphere during the months of December to February. Specifically, no significant difference along the sampled longitude range between 50-70 °W is expected from the models (see Fischer et al., 2014, and references in Section 2.3.4). Hence, the zonal PAN observations are in agreement with simulations from global models in the sampled area and season.

5.5.0.1 *Seasonal changes in PAN and PAA profiles during CAFE Brazil*

As described in Section 5.2.1, during the campaign, the transition between the Amazonian dry and wet season took place. This season change is also observed in PAN and PAA measurements, which were generally higher during December (dry season) compared to January (wet season).

An examination of the vertical profiles in Figure 5.5.2 reveals that the mid-tropospheric maximum PAN is less pronounced in January (approx. 80 ppt) than in December (approx. 120 ppt, but the shape is similar. The mid-tropospheric PAN maximum between 6-11 km is a result of the loss and production terms, as it was shown in Section 5.4.1 for the example of RF07.

The PAA profile differs more significantly between the season and between flights, with a median being almost a factor 2 different, notably at altitudes around 3 km and 11 km. This is connected to the fact, that CAFE Brazil targeted convective updraft in many flights and did not sample background conditions. As it was shown for RF10 in Section 5.4.2, convection contributed to a PAA maximum at high altitude around 12 km. However, the height of convective outflow may be different depending on the convective system and meteorological conditions. For example, in the December plot of PAA (upper right panel in Figure 5.5.2), single measurements of PAA reached up to 1 ppb around 8 km altitude. Theses data points result mainly from RF11, which also targeted convective outflow in a similar region to RF10. During January, the median PAA profile is almost flat with altitude until it decreases above 12 km altitude from around 320 ppt to 140 ppt.

5.5.1 *Comparison to previous field measurements above the Amazon*

Few aircraft measurements of PAN in the mid- and upper troposphere have been reported in literature above the Amazonian rainforest or in the surround regions, to which the CAFE Brazil measurements can be compared, as it was described in Section 2.3.2. PAA was not measured during the campaigns used for comparison, which are described in the following and are shown Figure 5.5.3.

The ABLE 2B expedition above the Brazilian Amazon Basin in April-May 1987 is spatially comparable to the sampling area of CAFE Brazil and was the first time PAN was measured above the Amazonian forest canopy. Singh et al. (1990) found that PAN mixing ratios measured with an electron capture gas chromatographic instrument (Singh and Salas, 1983) increased with height and were 1-5 times higher than NO_x levels (black dash dotted line in Figure 5.5.3). The PAN behaviour was found to be similar to that of ozone and non-methane hydrocarbon-NO_x-precursors, indicating photo-chemical production of PAN (Singh et al., 1990). However, the maximum flight altitude reached during the ABLE 2B campaign was 6 km only.

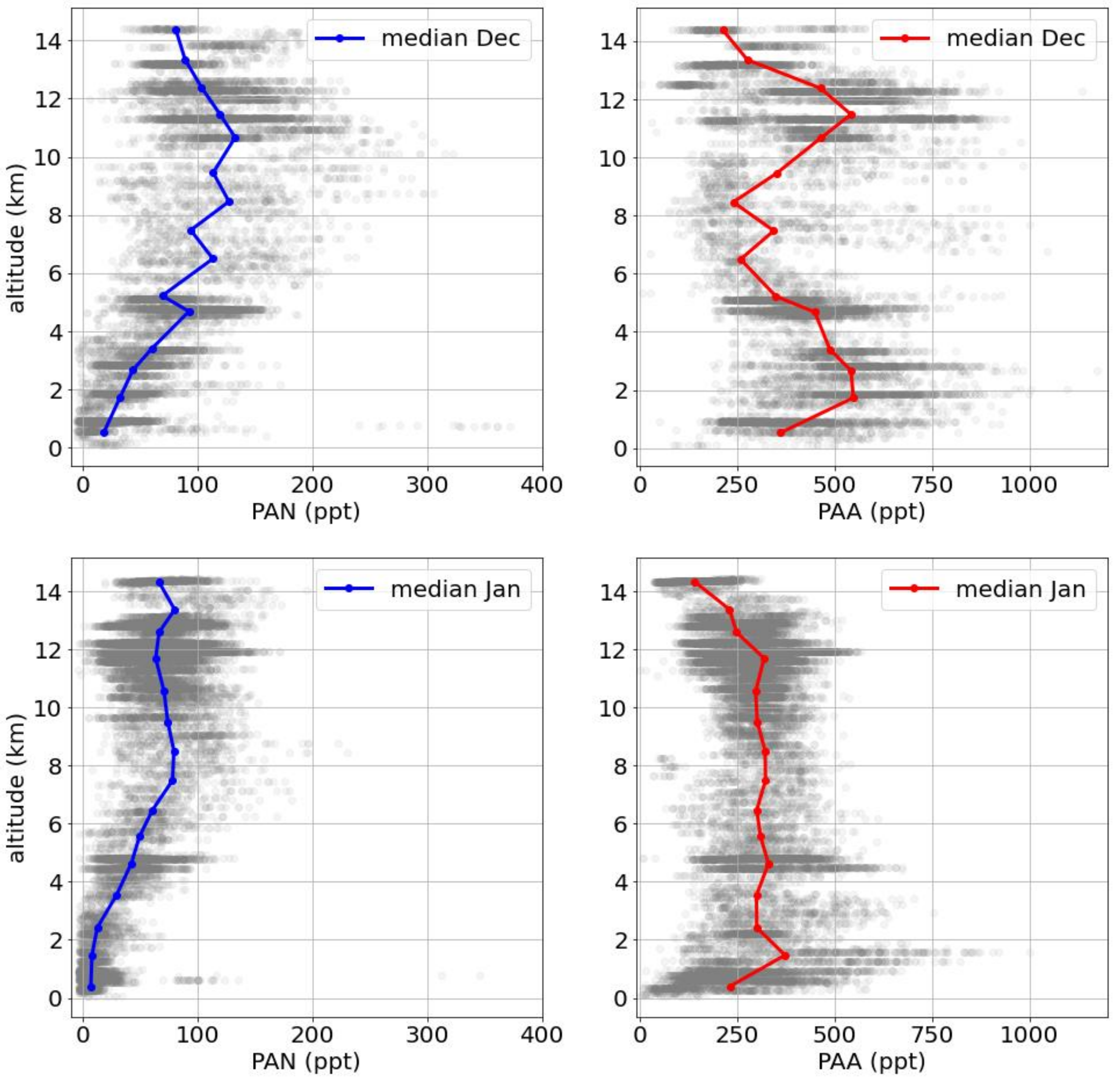

Figure 5.5.2: Measured vertical profiles of PAN (left column) and PAA (right column) during December 2022 (upper row) and January 2023 (bottom row). The medians of the gray data points are marked with solid lines.

Five years later, in September-October 1992, Singh et al. (1996a) measured PAN over the southern tropical Atlantic ocean using another electron capture-gas chromatography instrument (Fishman et al., 1996) during the TRACE-A aircraft campaign. The flight tracks were mainly located above marine regions but also included continental flights above the Amazon rainforest. Air masses were classified by a CO threshold into clean background and biomass burning/anthropogenic pollution influenced (Singh et al., 1996a). The clean background profile (CO < 80 ppb) of the TRACE A campaign is depicted by the dashed black line in Figure 5.5.3.

Keim et al. (2008) retrieved PAN profiles around São Paulo in the UTLS (8-20 km altitude) by aircraft limb measurements in the mid-infrared (775-820 cm^{-1}) with the MIPAS instrument. Although PAN exhibits strong features in thesis spectral range, 10 interfering species had to be considered. The MIPAS-STR instrument was mounted aboard the Russian high-altitude aircraft Geophysica. The part below 15 km of the PAN profile derived from the MIPAS-STR is depicted in Figure 5.5.3 by the dotted lack line.

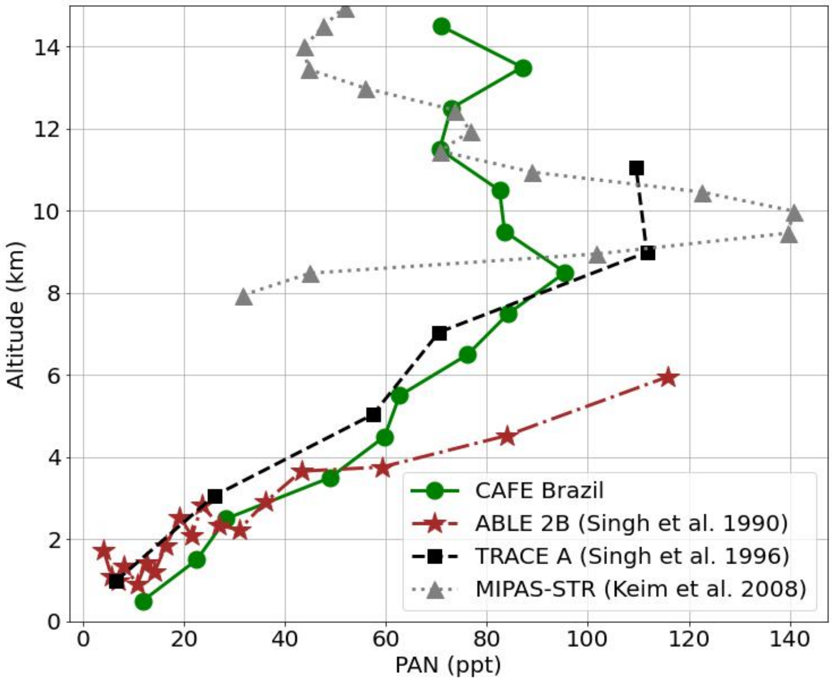

Figure 5.5.3: Comparison of median vertical PAN profiles of CAFE Brazil (green dots, this work) to reported measurements above or close to Brazil from Singh et al. (1990) (brown stars), Singh et al. (1996a) (black squares), and Keim et al. (2008) (gray triangles).

The median PAN profile based on all CIMS measurements during CAFE Brazil (green) is compared to the previously described measurement campaigns in Figure 5.5.3. It is worth noting that during CAFE Brazil, most of the flights had a certain part dedicated to sampling convective outflow. The exceptions were flights RF05-RF07, which all took place in the first half of the campaign. With respect to the seasonal change, it is difficult to separate the influence of convection from this profiles.
However, ABLE 2B took place during the Amazonian wet season, which was characterised by high convective activity, too. Singh et al. (1990) reported high and moderate convective impact for several flights and ABLE 2B might hence be comparable to CAFE Brazil conditions with respect to convective conditions.
The profile from the ABLE 2B is very close to the observe PAN profile of CAFE Brazil below 4 km altitude but increase less steep above 4 km altitude.
The PAN measurements during CAFE Brazil fit well to the non-polluted profile measured during the TRACE-A campaign. Deviations are strongest at low altitudes below 2 km and around the PAN maximum at 10 km. Also Singh et al. (1996a) reported extensive cloudiness and convective activity in the ITCZ region(5-10 °N) impacting the measured air compositions.
MIPAS-STR measurements also found the maximum PAN around 10 km altitude but derived a much more pronounced and narrower maximum.

Overall, the CIMS measurements are consistent with expectations on atmospheric composition based on previous measurements in remote and pristine regions and add an important contribution to the sparse data sets available. In addition, the CIMS measurements provide a unique data set of simultaneous measurements with PAA, which have not been reported for the Amazonian basin until now.

5.6 COMPARISON TO EMAC MODELLED PAN AND PAA DURING CAFE BRAZIL

It was seen in the flight-wise comparison for RF07 in Section 5.4.1, that the EMAC model, in principle, represents the characteristic profiles of PAN and PAA well but tends to underestimate PAN and overestimate PAA. To validate if this holds for the whole CAFE Brazil, in this section, the measured median PAN and PAA of ***all flights*** during the CAFE Brazil campaign are compared to numerical simulations of the EMAC model. Furthermore, the origin of the PA-radical in the model and its partitioning into PAN and PAA are investigated.

5.6.1 *Vertical Profiles of PAN and PAA*

Figure 5.6.1 shows the median profiles of PAN and PAA of all analyzed flights during CAFE Brazil compared to the EMAC simulations, which gives a similar picture as observed in the example of RF07. The order of magnitude and the overall shape of the vertical profiles are quite similar between model and measurements for both PAN and PAA, but the model underestimates PAN on average by a factor of 0.8 and overestimates PAA by a factor of 1.2. The highest deviations between the model and the measurements are in the mid and upper troposphere for PAN and in the mid and lower troposphere for PAA.

As previously discussed for the example of RF07 in Section 5.4.1, these are the altitude regions where the steady-state concentrations of PAN and PAA are expected to be highest. This indicates that the reason of the higher discrepancy between model and measurements in these altitude regions could be related to inaccurate chemical production mechanisms.

5.6.2 *Relation between PAN and PAA*

The PAN-to-PAA ratio is an indicator of the partitioning of the reactions of the PA-radical with NO_2 and HO_2 and the sum of both indicates the availability of the PA-radical. In polluted regions, PAN formation usually dominates PAA formation but in the organic rich, pristine air like during CAFE Brazil, PAA can be dominant, especially when thermal loss rates of PAN become relevant, e.g. in low altitudes or uplifted warm air masses. Accurately capturing the relationship between PAN and PAA correctly is considered as an ultimate test for global chemical models (Crowley et al., 2025).

As seen in the left panel of Figure 5.6.2, the discrepancy in the PAN-to-PAA-ratio between the CIMS measurements and the EMAC model varies from a factor of 1.6 to 2.8 with the largest difference observed in the upper troposphere around 14 km and mid-altitudes around 8 km due to the underestimation of PAN. In the lowermost altitude, the difference reaches even 2.4. However, this must be compared with caution, as at low

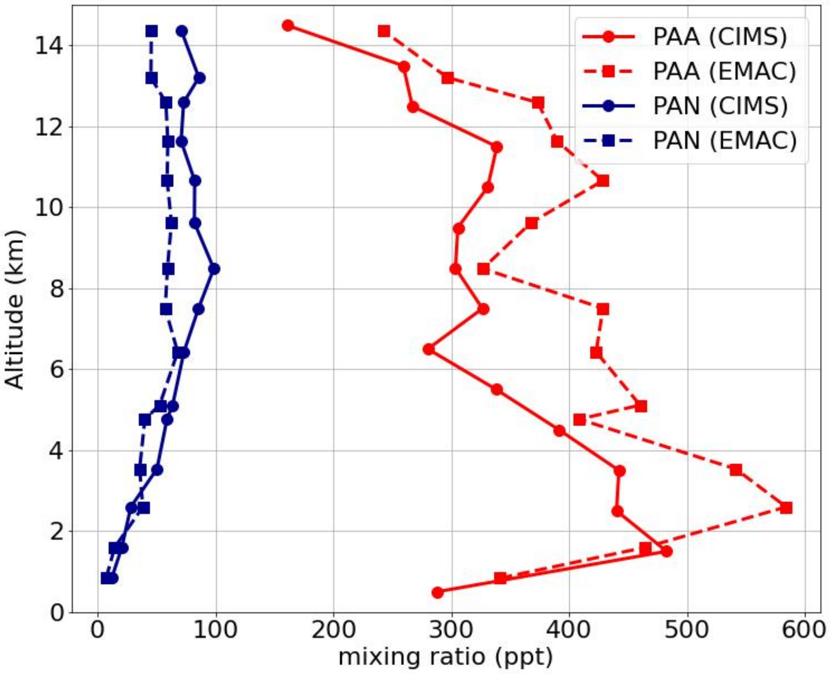

Figure 5.6.1: Vertical median profiles from EMAC model results (dashed lines) compared to CIMS measurements (solid line) of PAN (in blue) and PAA (in red) during CAFE Brazil.

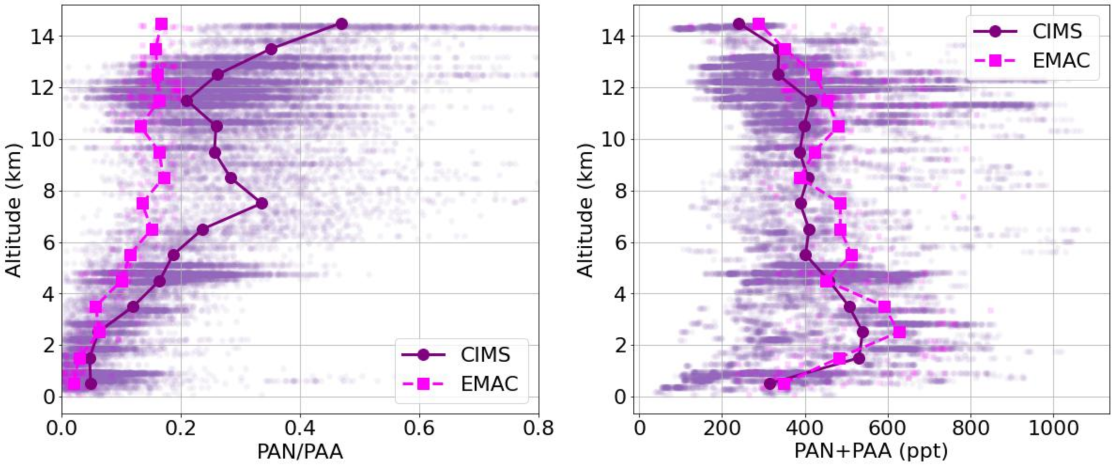

Figure 5.6.2: Vertical profiles of the PAN-to-PAA-ratio (left) and the sum of PAN+PAA (right) for CIMS measurements (purple dots) and EMAC model data (magenta squares) for all analysed flights during CAFE Brazil. The medians are marked by the dashed and solid lines.

altitudes PAN values can be very low and even small differences significantly change the ratio.

As depicted in the right panel in Figure 5.6.2), it is observed that the EMAC model overall represent the sum of PAN and PAA well, taking into account the large measurement uncertainties especially on PAA. The average excess of 13 % of the model compared to the measurements is below possible measurement uncertainties of PAN (ca. 30 %) and PAA (ca. 100 %). The agreement of the sum of PAN and PAA between

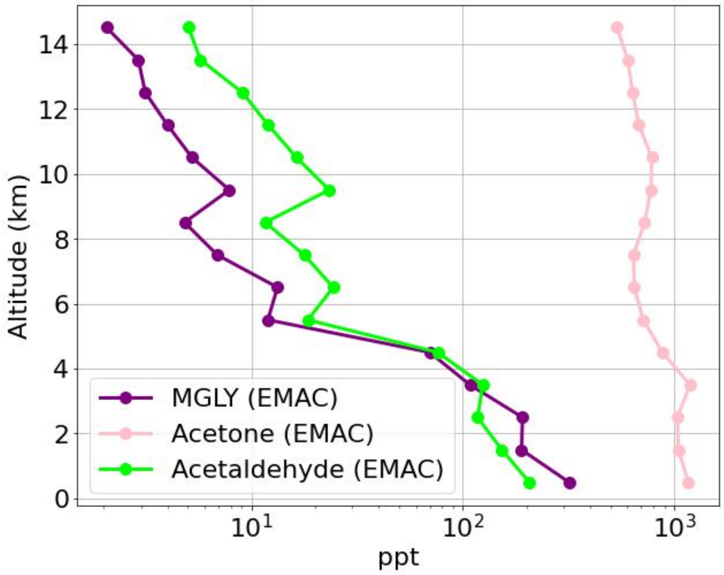

Figure 5.6.3: Median vertical profiles of MGLY (purple), acetone (pink), and acetaldehyde (lime) simulated by EMAC during CAFE Brazil.

model and measurements indicates indicates that the concentration of PA-radicals in the model is well represented but the overprediction of PAA and the underprediction of PAN suggests that there is a model bias towards a high HO_2/NO_2-ratio.

5.6.3 *PA-radical production and loss terms in the model*

As it was explained in Section 3.7 and depicted in Figure 3.7.1, a large number of organic trace gases are implemented in the MOM-Chemistry scheme used in EMAC leading to the formation and losses of the PA-radical. The major direct contributions are expected to come from oxidation of acetaldehyde and the photolysis of MGLY and acetone (Fischer et al., 2014), which will be investigated in this section.

5.6.3.1 *EMAC production terms of PA*

The EMAC model output provides production terms of the PA-radical from single species, which was used to investigate the absolute and relative contribution of the major PA-radical precursors acetone, acetaldehyde and methyl glyoxal (MGLY) to the modelled total PA production.

The median profile of modelled mixing ratios of these three precursors species is depicted in Figure 5.6.3. Generally, the mixing ratios of all three precursors, MGLY, acetone and acetaldehyde decrease with increasing altitude since their major sources are in the boundary layer. Acetone is much more abundant than the other two precursors with mixing ratios reaching up to 1.25 ppb at low altitudes and 600 ppt at high altitudes. At 4 km altitude, mixing ratios of acetaldehyde and MGLY are comparable and both around 150 ppt. Below 4 km altitude, mixing ratios of MGLY are higher than those of acetaldehyde but decrease more strongly with altitude.

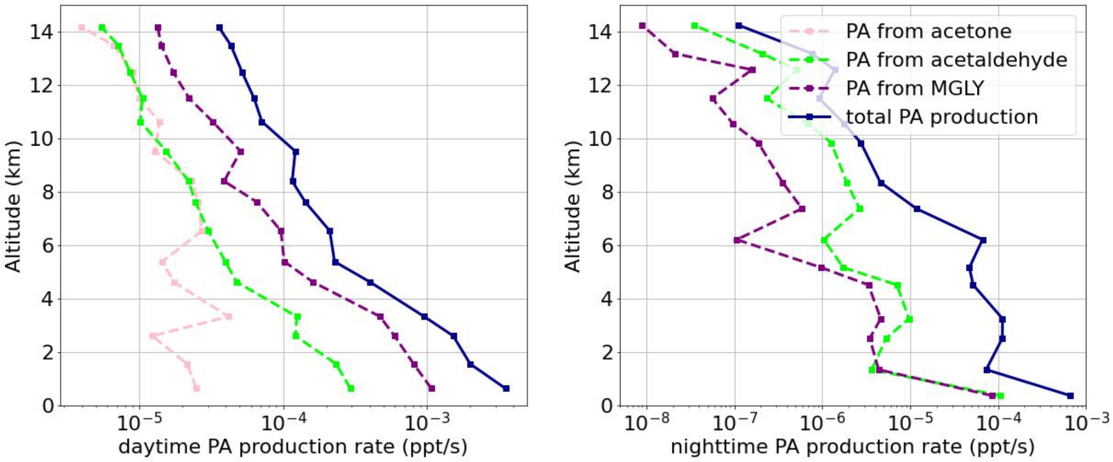

Figure 5.6.4: Median vertical profiles of the absolute contribution of acetone (pink), acetaldehyde (lime), and MGLY (purple) compared to the total modelled PA-radical production (darkblue) during day (left panel) and night (right panel), based on EMAC simulations for the full CAFE Brazil campaign. Note that the scale of the logarithmic x-axes differ by orders of magnitude.

As seen in Figure 5.6.4, despite the lower abundance of MGLY and acetaldehyde, their relative contribution to PA-formation can exceed that of acetone, especially at low altitudes. In Figure 5.6.4, the model data was separated into nighttime and daytime according to the photolysis frequency of PAN ($j(PAN)$). Night was defined where j(PAN) was zero (right panel), and day, when $j(PAN) > 1e^{-7}1/s$, excluding phases of dawn (left panel).
Generally the PA production is highest at low altitudes during both, night and day, due to the availability of organic precursors.

During the day, the production of PA from MGLY (purple) is dominant over acetone (pink) and acetaldehyde (lime) at all altitudes because of the high photolysis frequency of MGLY, which is in the order of 7×10^{-5} at ground level at Manaus according to the Tropospheric Ultraviolet and Visible Radiation Model (TUV) model[20]. This means for the results of the steady-state calculations of PAN and PAA applied previously to RF07, which only included acetone and acetaldehyde, that the expected in-situ production would be significantly higher when including MGLY. The absolute contributions of acetone and acetaldehyde are similar above 6 km altitude, while below this altitude the oxidation of acetaldehyde dominates.

Since the photolysis of acetone and MGLY does not take place during the night, acetaldehyde becomes the most dominant PA-precursor. Note that additional to the photolysis of MGLY, which is the major pathway to form PA from MGLY, the MOM-chemistry scheme also includes oxidation pathways of MGLY with OH and NO_3 forming PA wherefore the production of PA from MGLY is not zero at nighttime.
In general, during the night the total production of PA (darkblue) is between a factor 3 at 6 km up to a factor of 320 at 14 km altitude lower than during the day. Below

---

[20] https://www.acom.ucar.edu/Models/TUV/Interactive_TUV/, last access: 8th July 2025.

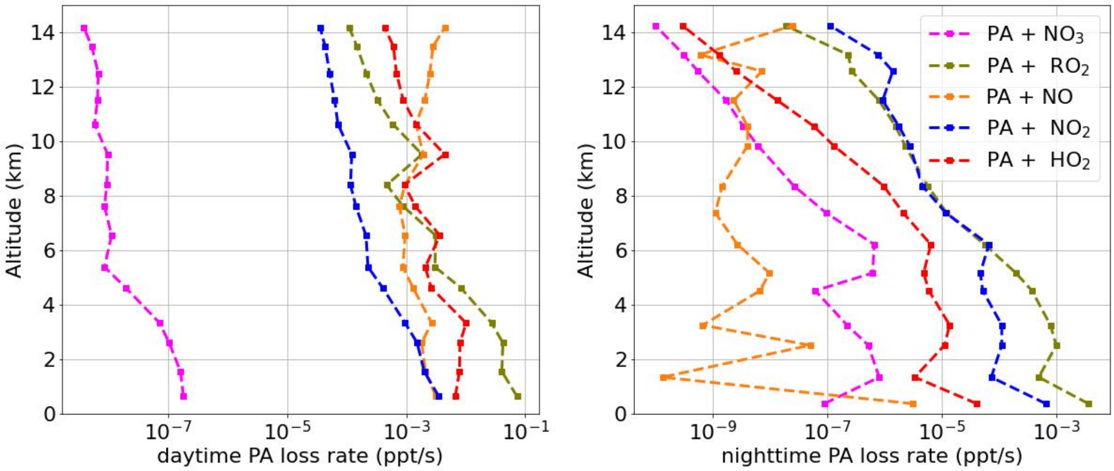

Figure 5.6.5: Median vertical profiles of modeled loss rates of the PA-radical in reactions with NO_3 (pink), RO_2 (green), NO (yellow), NO_2 (blue) and HO_2 (red) during day (left panel) and night (right panel) during the CAFE Brazil campaign. Note that the scale of the logarithmic x-axes differ by orders of magnitude.

8 km altitudes, a significant deviation between total PA production and the sum of PA production from acetaldehyde and MGLY is observed. This indicates that other PA precursor reactions become significant in the model. According to the MOM-chemistry scheme, approximately 15 % of the products of the ozonolysis of isoprene (Reaction 78) lead to the formation of PA. Measured mixing ratios of isoprene at 1 km altitude above the Amazon rainforest during CAFE Brazil were in the order of 1 ppb (Tripathi et al., 2025). With typical ozone mixing ratios of around 20 ppb at this altitude and a reaction rate coefficient of around $1.28 \times 10^{-17} \mathrm{cm}^3 \mathrm{molec.}^{-1} \mathrm{s}^{-1}$ according to IUPAC, production rates of PA from isoprene are in the order of $8.5 \times 10^{-4} \mathrm{ppt/s}$, which may explain the relatively high total PA production in the model during the night at low altitudes. Minor contributions result also from the ozonolysis of isoprene productions products, such as MVK and MACR.

$$C_5H_8 + O_3 \rightarrow \mathrm{products} \tag{78}$$

5.6.3.2 *EMAC loss terms of PA*

Similar to the production terms, also the loss terms of PA are orders of magnitude lower during the night, except for reaction with NO_3, see Figure 5.6.5. As a result, the reaction of PA with NO_3 plays a relatively larger role during the night. However, even during the night, the losses of PA via NO_3 are still a factor of 1000 lower at all altitudes than the dominant loss processes with RO_2.

During both night and day, the losses of PA decrease with altitude, except for the loss due to the reaction of PA with NO, which increases due to increasing NO in the UT. In the UT, NO is the dominant loss of PA during the day, while it is negligible during the night. In the lower troposphere below 6 km altitude, the losses with RO_2 radicals are dominant during both day and night.

The loss of PA with NO_2 is directly linked to the formation of PAN (Reaction 31).

In contrast, only a fraction of the reaction of PA with HO_2 leads to PAA formation

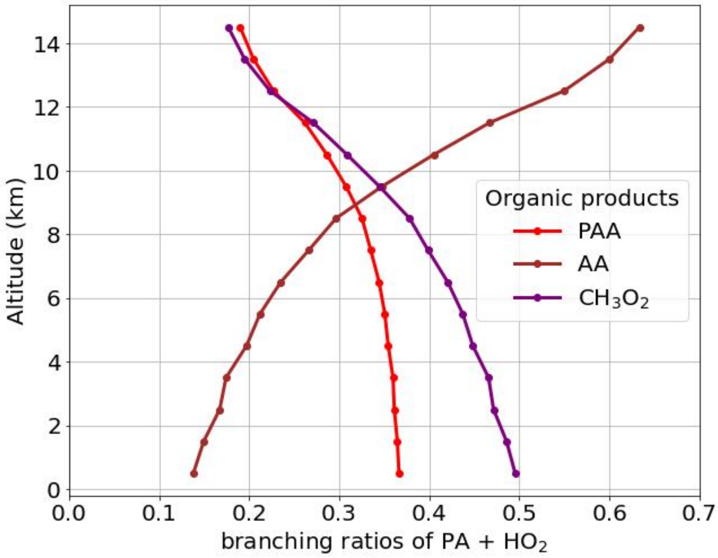

Figure 5.6.6: Vertical profiles of branching ratios of the reaction of PA + HO_2, calculated with reaction rate coefficients recommended by IUPAC and the simulated temperature and pressure profiles during CAFE Brazil.

(Reactions 32a-32c). As seen in Figure 5.6.6, the reaction of PA with HO_2 mainly leads to the formation of acetic acid (AA) in altitudes above 9.5 km and to CH_3O_2 at altitudes below. The branching ratio of the reaction forming PAA (e.g. the fraction α defined in Equation 41) decreases from 37 % at the lowest altitude to 19 % at the highest altitude.

During the day, at all altitudes, the loss with HO_2 significantly exceeds the loss with NO_2, underscoring that in the model the formation of PAA is favoured over the formation of PAN. During the night, the loss reaction of PA with NO_2 leading to PAN formation dominates in the UT but is comparable to the loss via RO_2 in mid-altitudes and less important at lower altitudes than 6 km.

5.6.3.3 *Relative contribution of loss and production terms*

Figure 5.6.7 presents the modelled relative contributions to the PA-radical budget during the entire CAFE Brazil campaign, including phases of dawn.

In the left panel of Figure 5.6.7, it is observed that the three precursor species acetone, acetaldehyde and MGLY contribute together around 50 % to the total PA-production in the model, averaged over all altitudes. The major contribution results from MGLY, with around 27-42 % and a maximum in the lower troposphere. The second biggest contribution results from acetaldehyde (8-18 %), followed by acetone (0.5-12 %), whose contributions both increase with altitude. At altitudes lower than 5 km the photolysis of acetone plays a negligible role. The residual fraction (37-58 %) results mostly from other isoprene photo-oxidation products.

Since acetone and acetaldehyde together only account for a maximum of about 30 % of the PA-radical production in the model, it becomes clear that the steady-state concentrations of PAN calculated for RF07 based on model acetone and acetaldehyde is not sufficient. This is underlined by the fact that PAA steady-state concentrations exhibited

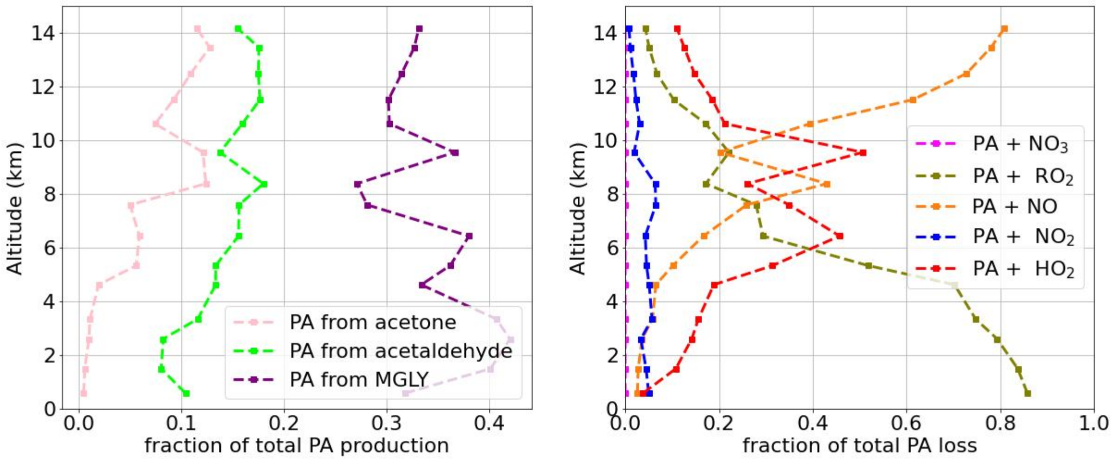

Figure 5.6.7: Relative contribution of the main organic PA-precursors to model PA-production (left panel) and fractional losses of the PA-radical (right panel) in the EMAC model simulations for the full CAFE Brazil campaign, plotted against altitude.

a very different profile than observed PAA, even though the steady-state PAN approximately fitted to the observation.

In contrast to the production terms, the relative significance of the different loss terms of the PA-radical is highly different with altitude, see right panel in Figure 5.6.7. While in the UT above 10 km NO is the major loss process of PA, the reaction with HO_2 peaks in the mid altitude-range and the sum of RO_2-species make up the dominant fraction at altitudes below 6 km. Figure 5.6.7 shows that on average only a few percent (1-7 %, blue line) of the PA-radical actually forms PAN. Over the whole profile, PA + HO_2 exceeds PAN formation up to a factor of 20. Note that the vast majority of flight hours during CAFE Brazil took place during the day, hence the average relative contributions are dominate by the daytime chemistry.

5.6.4 *Role of Isoprene*

The Amazonian rainforest is a huge source of biogenic VOC, with isoprene being the dominant compound emitted from vegetation (Gomes Alves et al., 2023; Guenther, 2013; Wang et al., 2024).
Isoprene (C_5H_8) is an alkene which is emitted by a wide variety of mostly deciduous vegetation as by-product of photosynthesis and/or photo-respiration (Seinfeld and Pandis, 1998). Typical atmospheric concentrations range from 0.2 to 30 ppb (Seinfeld and Pandis, 1998). Due to the combination of high temperatures and high biomass density, isoprene emissions are largest in the tropics (Seinfeld and Pandis, 1998). Isoprene is not only highly reactive towards OH, but also towards ozone and NO_3, which can attack at the double bonds. The atmospheric lifetime is in the order of minutes to hours. The photo-oxidation of isoprene can lead to many products such as PAN-precursors like methacrolein (MACR), methylvinyl ketone (MVK) and in further photo-oxidation steps to acetaldehyde and MGLY (Fischer et al., 2014; Paulson and Seinfeld, 1992). Tropospheric mechanisms suggest that approximately 30 % of isoprene oxidation leads to

MGLY formation (Tyndall et al., 1995).

MGLY is predominantly produced in second- and third-order generation of isoprene oxidation while global primary sources of MGLY such as biomass burning (5 %), biofuel use (3 %) or other anthropogenic emissions (5 %) are minor (Fu et al., 2008).
During the day MGLY ($CH_3C(O)CHO$) has a total atmospheric lifetime around 2 hours, which is mostly due to photolysis. To a smaller extent also OH initiated oxidation, dry and wet deposition and uptake by aerosols and cloud droplets, which lead to SOA formation (Fu et al., 2008), impact the lifetime of MGLY in the atmosphere. The photolysis of MGLY leads to the formation of the PA-radical (Reaction 79).

$$CH_3COCHO + h\nu \xrightarrow{O2} CH_3C(O)O_2 + HCO \tag{79}$$

Similar to isoprene, MGLY can be oxidized by OH and NO_3, which can also lead to PA formation. The reaction of MGLY with OH accounts for 99 % of the gas phase oxidation (Fu et al., 2008). The rate of Reaction 80 is comparable to acetaldehyde reacting with OH at room temperature, but has a distinct negative temperature dependence (Tyndall et al., 1995).

$$CH_3COCHO + OH \rightarrow CH_3C(O)CO + H_2O \tag{80}$$

In Section 5.6.3, it was seen, that the relative contribution of the three major PA-precursors acetone, acetaldehyde and MGLY differs with respect to altitude and time of the day. Averaging the EMAC simulations along the flight track over the full CAFE Brazil campaign, results in the relative contributions depicted in Figure 5.6.8.
Figure 5.6.8 shows that the major contribution to the PA production in EMAC comes from MGLY (purple). This dominant role is readily understood by the high availability of isoprene emissions above the Amazonian rainforest and is in agreement with other global chemical transport model results (Fischer et al., 2014). The global average of PA formation from MGLY estimated by Fischer et al., 2014 was also around 30 %, but the relative contribution varied significantly depending on the altitude, region and season for example being dominant in the tropics above tropical rainforests. The relative contribution of acetaldehyde (lime) and acetone (pink) to PA-production during CAFE Brazil above the Amazon rainforest together account only for about a quarter of the total model PA production.

Figure 5.6.9 depicts selected PA precursor reactions contributing to the residual fraction "others" (red) of 44.1 % in Figure 5.6.8. As seen in Figure 5.6.9, the "other" PA precursors result mainly from isoprene oxidation products, such as diverse MVK (18.7 %, blue) and Hydroxy-Biacetyl (brown).
Almost 10 % of "other" PA precursors is attributed to $CH_3COCH_2O_2$ (orange), which is formed in the reaction of acetone with OH. Relative small contributions to PA formation result from the thermal dissociation of PAN (green) and other PAN-type species (red). Note that during CAFE Brazil, the highest data coverage was at high altitudes, therefore the average over the EMAC simulations along the flight track represents mostly the conditions in the UT, where the thermal decomposition of is PAN very slow. A minor contribution to PA production in the model results from the slow photolysis of PAA. The fraction "unspecified" (pink) includes a number of not further specified reactions as well as reactions which were specified but contributed less then 1% to the total PA

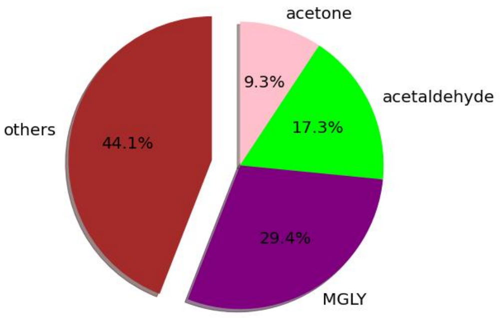

Figure 5.6.8: Mean contributions of the immediate PA-radical precursor species acetone, acetaldehyde, and methyl glyoxal (MGLY) during the CAFE Brazil campaign based on EMAC simulations along the flight track.

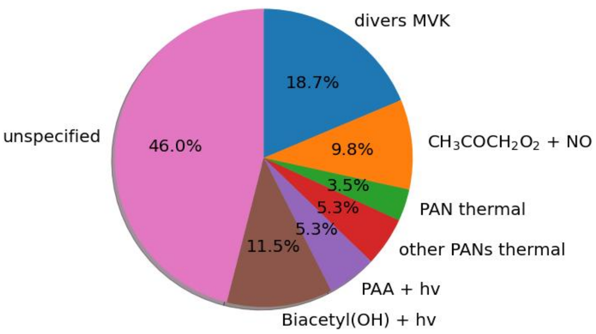

Figure 5.6.9: Relative contributions of selected PA precursors in the EMAC model to the fraction "others" in Figure 5.6.8. The fraction "unspecified" (pink) includes all unspecified reactions and reactions which contribute less than 1% to the total PA production.

production. Most of these reaction also involve isoprene oxidation products.
Hence, this analysis strongly suggests, that the underlying PA formation chemistry above the amazonian rain forest is predominately driven by isoprene and its oxidation products.

5.6.4.1 *Implications for methyl hydroxide production*

The important role of isoprene chemistry during CAFE Brazil raises the question wether non-methane chemistry may be more dominant than methane chemistry with respect to methyl hydroperoxide (MHP) (CH_3OOH) formation in pristine, biogenic hydrocarbon-rich environments like the Amazonian rainforest. It was shown in Section 5.6.3.3, that a large fraction of PA reacts with NO, RO_2 and HO_2 and does not lead to the formation of PAN or PAA. The losses of the PA radical via the reaction with NO, RO_2 and HO_2 lead mainly to the formation of methyl peroxy radicals (CH_3O_2). The methyl peroxy radical forms MHP in the reaction of HO_2 (Reaction 81).

$$CH_3O_2 + HO_2 \rightarrow CH_3OOH + O_2 \tag{81}$$

MHP is one of the most abundant hydroperoxides in the atmosphere reaching maximum mixing ratios between 4.3-8.6 ppb at low altitudes in the remote atmosphere (Allen et al., 2022). The methyl peroxy radical is primarily formed during the oxidation of methane (CH_4) with OH (Reaction 82).

$$CH_4 + OH \xrightarrow{O_2} CH_3O_2 + H_2O \tag{82}$$

The current global average levels of methane are 1934 ppb[21]. Reaction rate coefficients for Reaction 82 are between $6 \times 10^{-15} cm^3 molec.^{-1} s^{-1}$ at low altitudes and $4.5 \times 10^{-15} cm^3 molec.^{-1} s^{-1}$ at about 14 km altitude according to IUPAC. Modelled median OH concentrations during CAFE Brazil increase from $1 \times 10^6 molec.cm^{-3}$ at low

---

[21] https://gml.noaa.gov/ccgg/trends_ch4/, last access: 9th July 2025.

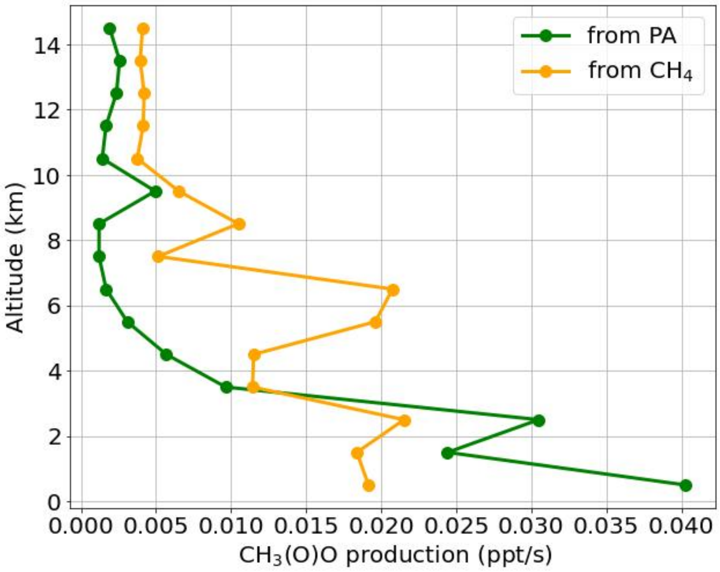

Figure 5.6.10: Median vertical profile of methyl peroxy radical production rates via the loss reactions of PA with NO, RO_2 and HO_2 (green) derived from the EMAC model for CAFE Brazil simulations compared to the production via the oxidation of methane (yellow) assuming a constant CH_4 mixing ratio of 1934 ppb.

altitudes to $4.7 \times 10^6 \mathrm{molec.cm}^{-3}$ at high altitudes, which leads to the altitude dependent production of CH_3O_2 depicted in yellow in Figure 5.6.10.
This production rate is compared to the production form the modelled PA reactions with NO, RO_2 and HO_2 (green in Figure 5.6.10). It can be seen that, in terms of CH_3O_2 production, PA chemistry dominates over methane chemistry at altitudes below 4 km up to a factor of 2 but decrease strongly with increasing altitude. At 14 km altitude CH_3O_2 and hence MHP formation is factor two lower via PA than via methane. This suggests that above the amazonian rainforest, PA chemistry significantly contributes to MHP formation and can even exceed the production from methane. It is worth noting that there is a high uncertainty on the branching ratios[22] of the reaction PA + HO_2 for the low temperatures in the UT. Hence, the formation of CH_3O_2 from the reaction of PA + HO_2 could be even larger if the reduction in branching ratio to this channel with increasing altitude (purple line in Figure 5.6.6) is less strong than IUPAC suggests.

5.7 ROLE OF PAA AS HOX RESERVOIR

It was seen that mixing ratios of PAA exceeded the ones of PAN significantly in the sampled air masses during the CAFE Brazil campaign due to the dominance of HO_2 over NO_2. As mentioned in Section 2.2, PAA is considered as a reservoir of HO_x. To investigate its relative importance of PAA as HO_x reservoir species in comparison to total organic peroxides, the CIMS measurements of PAA are compared with HYPHOP measurements of H_2O_2 and ROOH (Hamryszczak et al., 2023a).

As seen in Figure 5.7.1, the vertical profiles of H_2O_2 and organic peroxides are very similar in shape and magnitude. Both exhibit a maximum between 1-2 km altitude

---

[22] `https://iupac-aeris.ipsl.fr/datasheets/pdf/HOx_VOC54.pdf`, last access: 8th July 2025.

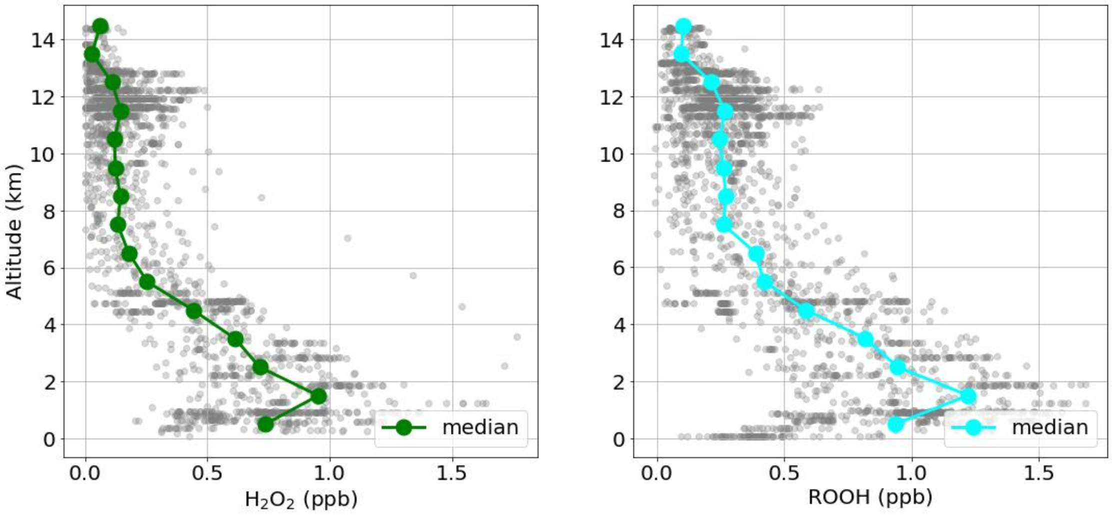

Figure 5.7.1: Vertical profiles of measured H_2O_2 (left panel), and ROOH (right panel) during CAFE Brazil. The medians are marked by the solid lines.

between 1-1.2 ppb and decrease towards higher altitudes to 60 and 100 ppt, respectively.

The ratio of PAA/(PAA + H_2O_2 + ROOH) is depicted in Figure 5.7.2, indicating that the relative importance of PAA increases strongly with altitude. While the median ratio is around 17 % at the lowest altitude, it reaches up to 100 % at high altitudes. Keep in mind the high measurement uncertainties on PAA and total organic peroxides and statistical effects of different sampling frequencies of the two instruments, which can lead to ratios above 1. This indicates that in the UT, PAA is the dominant organic peroxide above the Amazonian rainforest highlighting its importance as HO_x reservoir species.

5.8 ROLE OF PAN AS A NOX RESERVOIR

The partitioning between NO_x and PAN can be used to estimate the conversion of initially abundant NO_x to PAN in chemical aged air masses (Crowley et al., 2025).
The PAN-to-PAN+NO_x ratio is plotted in Figure 5.8.1, where data with NO_x below the detection limit of 8 ppt was excluded. Measurement data was resampled to 2-min frequency, and model data only includes flights during CAFE Brazil when PAN was measured. The median PAN/(PAN+NO_x) ratio has an almost symmetric inverse C-shape with its maximum in the mid-troposphere around 8 km, where also maximum PAN values were observed. Single measurements of the PAN-to-PAN+NO_x ratio reached up to 95 % and the median at 8 km lies around 80 %.
Due to the thermal instability of PAN, the ratio decrease below 8 km with lower altitudes. At higher altitude, the ratio decrease with altitude because of increasing (lightning) NO_x and slightly decreasing PAN. The shape of the profile is similar for both the model and the measurement data, but the model data underestimates the observations in average by a factor of about 0.8 which is consistent to the factor of PAN underestimation by the model.

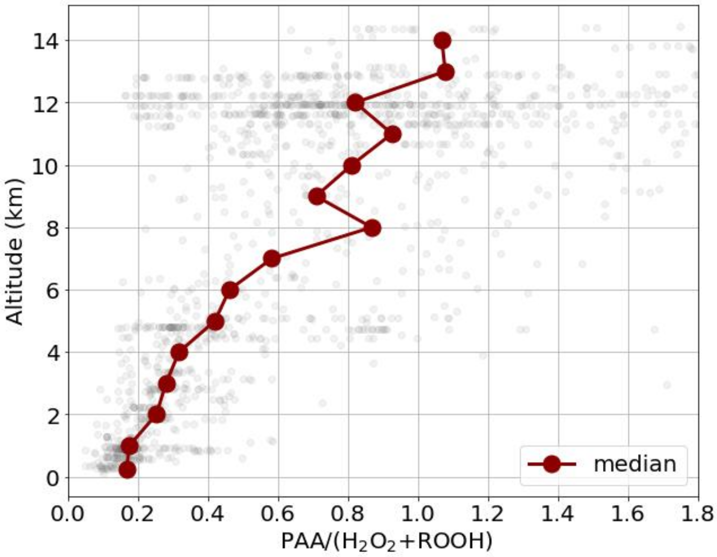

Figure 5.7.2: Vertical profile of the ratio PAA/(PAA + H_2O_2 + ROOH) based on CIMS and HYPHOP measurements during CAFE Brazil. The median ratio is marked by the solid line.

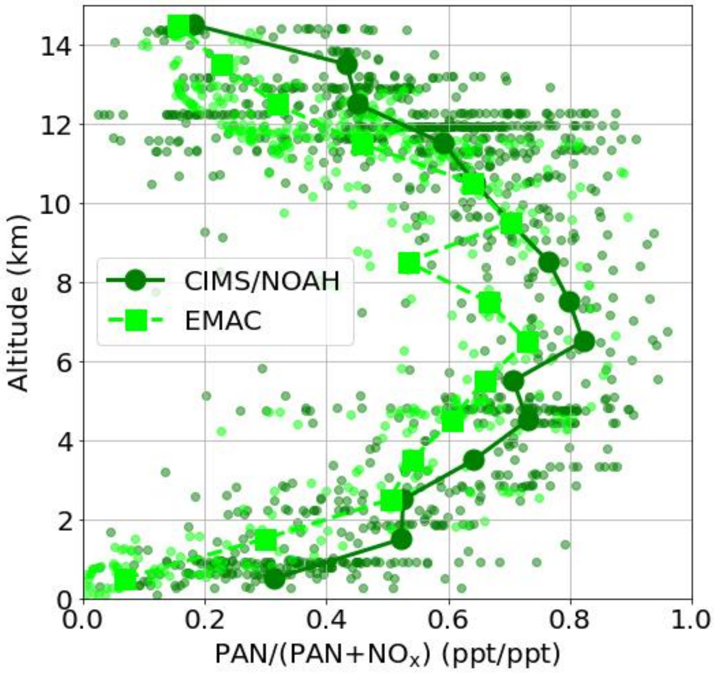

Figure 5.8.1: Fraction of PAN in PAN+NO_x during CAFE Brazil based on measurements (circles) and EMAC model data (squares). The median profiles are indicated by the dashed and solid lines.

5.8.1 *PAN as source of NOx*

It was seen in Figure 5.8.1 that depending on the altitude, a significant fraction of reactive nitrogen can be stored in form of PAN. As a reservoir species, PAN can also release the stored NO_x by photolysis and thermal decay serving as a source of NO_x.
In order to estimate the contribution of PAN to the NO_x budget in comparison to other NO_y-species, a steady-state calculation scheme was applied assuming that the only sources of NO_x in the atmosphere result from a loss of reactive nitrogen. Hence, fresh contributions, like for example from lightning, aircraft exhaust, stratospheric downwelling or convective uplift of pollution, are not included. Therefore, the difference between the steady-state concentration of NO_x to the measured NO_x will give an indication of the role of fresh NO_x sources - most importantly lightning - compared to sources from reservoir species.

The steady-state calculation focuses on the major NO_x-reservoir species in the UTC PAN, NO_3, HNO_4 and methyl peroxy nitrate (MPN) (Wei et al., 2024). The production of NO_x from PAN is calculated from thermal decay and photolysis with correction for reformation of PAN from the PA-radical as given in Equation 37, which was also used for the steady-state calculation of PAN described in Section 3.8. NO_3, HNO_4 and MPN can lead to the production of NO_x in the atmosphere by Reactions 83-88.

$$HNO_3 + OH \rightarrow H_2O + NO_3 \tag{83}$$

$$HNO_3 + h\nu \rightarrow OH + NO_2 \tag{84}$$

$$CH_3O_2NO_2 + M \rightarrow CH_3O_2 + NO_2 + M \tag{85}$$

$$HNO_4 + M \rightarrow HO_2 + NO_2 + M \tag{86}$$

$$HNO_4 + OH \rightarrow H_2O + O_2 + NO_2 \tag{87a}$$

$$\rightarrow H_2O_2 + NO_3 \tag{87b}$$

$$\rightarrow HO_2 + HNO_3 \tag{87c}$$

$$HNO_4 + h\nu \rightarrow OH + NO_3 \tag{88a}$$

$$\rightarrow HO_2 + NO_2 \tag{88b}$$

M denotes a collision partner. Reaction coefficients were taken from latest IUPAC recommendations. Reaction 87b and 87c were neglected as these pathways represent less than 5 % and 1 % respectively [23].
During daytime, NO_3 is rapidly photolysed and leads quasi instantaneously to NO_x-formation via Reaction 89 and 90 and is hence counted as NO_x in the steady-state calculation.

$$NO_3 + h\nu \rightarrow NO + O_2 \tag{89}$$

$$\rightarrow NO_2 + O(^3P) \tag{90}$$

---

[23] `https://iupac-aeris.ipsl.fr/datasheets/pdf/NOx11.pdf`, last access: 6th June 2025.

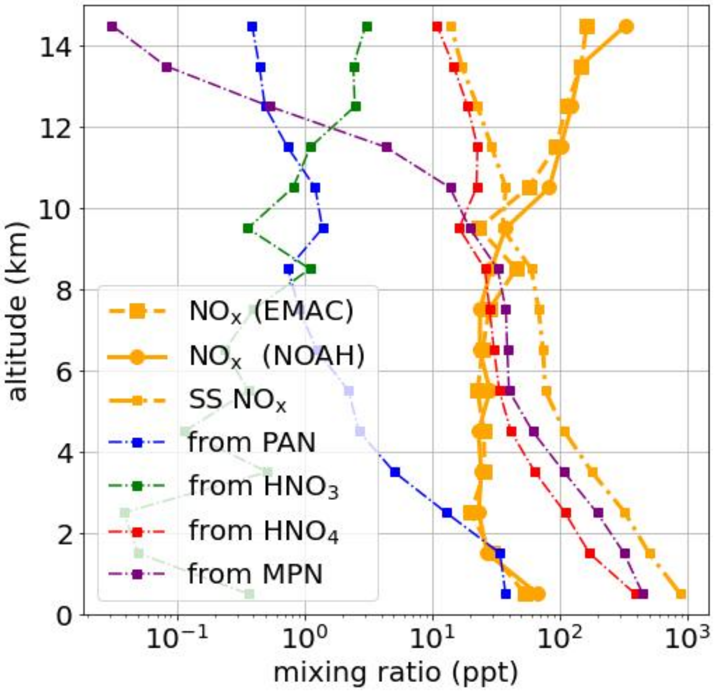

Figure 5.8.2: Vertical median profiles of measured (yellow solid line with dots) and EMAC model NO_x (yellow dashed line with squares). The dash-dotted yellow line indicates the steady-state concentration of NO_x based on contributions of the four NO_y species PAN (blue), HNO_3 (green), HNO_4 (red) and MPN (purple).

The only loss processes of NO_x considered in the steady-state calculation, are the gas-phase reactions of NO_x during day-time (Reaction 91-92). Since photolysis of NO_2 leads to the recycling of NO_x ("Chapman-cycle), it is not a sink.

$$NO2 + OH + M \rightarrow HONO2 + M \tag{91}$$

$$NO + OH + M \rightarrow HONO + M \tag{92}$$

NO_x in the form of HNO_3 is easily removed from the atmosphere by dry and wet deposition and is hence considered as a sink of atmospheric NO_x. Equal to Equation 38 used for the steady-state PAN calculation, the steady-state concentration of NO_x is derived by the ratio between the total production terms and the total loss terms.

Since HNO_3, HNO_4 and MPN were not measured aboard HALO during CAFE Brazil, EMAC simulations of these species were used. The steady-state calculation was applied including daytime EMAC model data defined by a photolysis frequency of PAN greater than $1e^{-7}1/s$.

It is observed in Figure 5.8.2 that in the UT above 10 km altitude, there is an increasing discrepancy with altitude between steady-state NO_x and model output NO_x. In the highest altitude range around 14 km, contributions from the four considered NO_y-species only cover less than 10 % of modelled and measured NO_x during CAFE Brazil. Therefore, the major source of NO_x in the UT results from fresh entries most likely lightning, which is considered to be the most significant source of NO_x in the tropical troposphere (Lamarque et al., 1996). Since during CAFE Brazil targeted outflow areas of convective

updraft during many flights, convection of pollution from the boundary layer may also play a role in explaining the discrepancy.
Among the four species, the oxidation and photolysis of HNO_4 is the dominant source of NO_x from reservoir species followed by HNO_3 and PAN while the thermal decay of MPN is negligible. The fraction of PAN contributing to the NO_x budget in the UT is around 3-4 % decreasing with altitude. Due to the high thermal stability of PAN in the UT, the release of NO_x is slow making PAN only a minor source of NO_x in mid- and high altitudes even though a high fraction of NO_x is stored there in the form of PAN.
Below approx. 8 km altitude, calculated steady-state concentrations exceed measured NO_x which is probably mostly due to the fact that scavenging and dry deposition of HNO_3 and HNO_4 were not included.

5.9 SUMMARY OF THE CAFE BRAZIL ANALYSIS

In this chapter, the unique data set of PAN and PAA measurements above the Amazonian rainforest during the CAFE Brazil campaign was presented and compared to model predictions and previous measurements. Three research flights were analysed in detail with respect to the impact of in-situ production, convection and horizontal transport of PAN and PAA.

Steady-state concentrations of PAN and PAA in RF07

Steady-state concentrations for PAN and PAA from acetone and acetaldehyde precursors were applied to the flight RF07, which sampled staked profiles above the Amazonian rainforest above the ATTO tower. The results showed that the measured high acetaldehyde concentrations in the free troposphere are incompatible with the observations of PAN and PAA.
The discrepancy between measured acetaldehyde, using the GC-MS instrument, and modelled values, using the EMAC model, was around a factor of 25 , indicating that the acetaldehyde measurements are challenging our present understanding of its sources and lifetime in the atmosphere (Millet et al., 2010). The steady-state concentration of PAN derived from EMAC model data fitted well to the observations, showing that acetone and acetaldehyde contribute almost equally to PA formation during RF07 at altitudes above 4 km, while at lower altitudes the oxidation of acetaldehyde becomes more important.
The total atmospheric lifetime of PAN and PAA in the UT was estimated to be 2-3 weeks and 5-6 days respectively.

Convective outflow in RF10

RF10 was investigated as an example of convective outflow measurements. The vertical profile of PAA showed an extraordinary maximum around 12 km altitude during this flight, which was also observed in other VOC profiles, such as acetone. These observations underscore the role of tropical, vertical transport of trace gases from the boundary layer on the air mass composition in the UT.

Horizontal transport in RF20

The chemical aging of an air mass was investigated in a quasi-Lagrangian experiment during the high-altitude flight RF20 in which a PAN-layer around 12 km altitude was observed and was repeatedly probed.
The location of the PAN-layer was compared to the CAMS model used for flight planning. The horizontal extension of the plume in the model fitted to the observations, but was a factor of 25 higher than the measurements.
HYSPLIT backward trajectories were calculated to analyse the origin of the sampled air mass, showing a mixture of updraft from the South American continent and transported maritime air from above the western Pacific.

Regional and seasonal distribution of PAN and PAA during CAFE Brazil

The campaign took place at the onset of rain season. The occurrence of biomass burning events was generally low and decreased from December to January, as indicated by FIRMS satellite observations of open fires. However, according to backward trajectory analysis, a significant fraction of the sampled air masses during CAFE Brazil had traveled at low altitudes above the north-west coast of Brazil, a region with higher densities of fire events, suggesting a potential impact of biomass burning emissions on the sampled PAN and PAA mixing ratios. A slight seasonal distinction in PAN and PAA vertical profiles was observed, with higher mixing ratios during December compared to January, reflecting the transition from dry to wet season.
The regional distribution of PAN was qualitatively in agreement with global chemical-transport models.

Vertical profiles of PAN and PAA compared to previous measurements

Compared to the limited number of reported vertical PAN measurements in the mid- and upper troposphere above the Amazonian rainforest, the vertical PAN profile derived during the CAFE Brazil campaign agreed in shape and magnitude with previous measurements.
The large range of altitudes from a few hundred meters above the ground to almost 15 km altitude probed during CAFE Brazil provides a previously unavailable dataset of simultaneous PAN and PAA measurements above the Amazonian rainforest. This dataset offers a unique opportunity to investigate the vertical distribution and chemistry of these species in the pristine, tropical troposphere above the Amazonian rainforest.

Comparison to the EMAC model

The PAN to PAA relationship was compared between CIMS measurements and the EMAC model, which underestimated PAN observations on average by a factor of 0.8 and overestimated PAA observations by a factor of 1.2. This may indicate that, while the modelled total production and loss rates of the PA radical are reasonable, the partitioning between NO_2 and HO_2, which defines the PAN-to-PAA ratio, is biased towards HO_2
The analysis of the PA-radical production in the EMAC model showed that MGLY was overall the dominant single PA-precursor during CAFE Brazil, followed by acetaldehyde and acetone. During the night, production rates were significantly lower and pathways such as the ozonolysis of isoprene can become relatively more important.
The large residual fraction of PA production in the model, which did not result from the three major precursor acetone, acetaldehyde and MGLY, was dominated by isoprene oxidation products. This highlighted the dominance of biogenic VOCs, notably isoprene, on PA formation above the Amazonian rainforest.
The rate of MHP formation from PA radical reactions was compared to the one from methane oxidation, showing that at low altitudes the production of MHP by non-methane chemistry can be up to a factor of 2 stronger than from methane.

Importance of PAN and PAA as reservoir species of NOx and HOx

The ratio of PAA/(H_2O_2+ROOH) was investigated to evaluate the relative contribution of PAA to the total of organic peroxides. The ratio strongly increased with altitude and reached around 100 % in high altitudes, highlighting the importance of PAA as a HO_x reservoir species.
The role of PAN as NO_x reservoir species was discussed. The median PAN-to-PAN+NO_x ratio reached up to 80 % in the mid-altitudes demonstrating the significance of PAN as a NO_x reservoir. The NO_x-steady-state calculation based on EMAC NO_y species demonstrated that only a minor fraction (3-4 %) of PAN is expected to contribute as a source of NO_x in the UT, where HNO_4 is a more important reservoir species. Measured and modelled NO_x agreed well on average over the whole campaign. The discrepancy between steady-state NO_x from reservoir species and measured and modelled NO_x shows that lightning generated NO_x is rapidly transformed into reservoir species that do not re-release NO_x on short time scales. This will happen following (long-range) transport and e.g. subsidence allowing PAN to thermally dissociate to release NO_x.

6

CAFE PACIFIC

This chapter presents the CIMS measurements of PAN and PAA during the CAFE Pacific aircraft campaign. After an overview of the general findings, three research flights are analysed in detail. Based on these example flights, the role of horizontal and vertical transport, biomass burning and in-situ production is discussed. Lastly, the observations are compared to the global chemical transport model EMAC.

6.1 CAFE PACIFIC CAMPAIGN DESCRIPTION

The CAFE Pacific campaign took place during the Australian monsoon in January and February 2024 and included 18 research flights (RFs) plus 6 transfer flights. The research aircraft High Altitude and Long Range Research aircraft (HALO) had the same instrumental payload as in the other Chemistry of the Atmosphere Field Experiments (CAFE) campaigns (Voigt et al., 2022). The campaign was based at the Airport of Cairns (16.88 °S, 145.75 °E) on the north-east coast of Australia. During RF06-RF11, the CIMS was run with a continuous calibration flow of isotopic ^{13}C-PAN on a trial basis which turned out to suffer from significant impact of acetic acid as described in Section 4.3.3. Therefore, these flights were excluded from further analysis. In all other research flights, a half-hourly calibration cycle was applied using isotopically labeled PAN similar to the cycle during CAFE Brazil. The flight tracks of all included flights in the continued analysis are depicted in Figure 6.1.1. The local time in Cairns is ten hours before UTC.

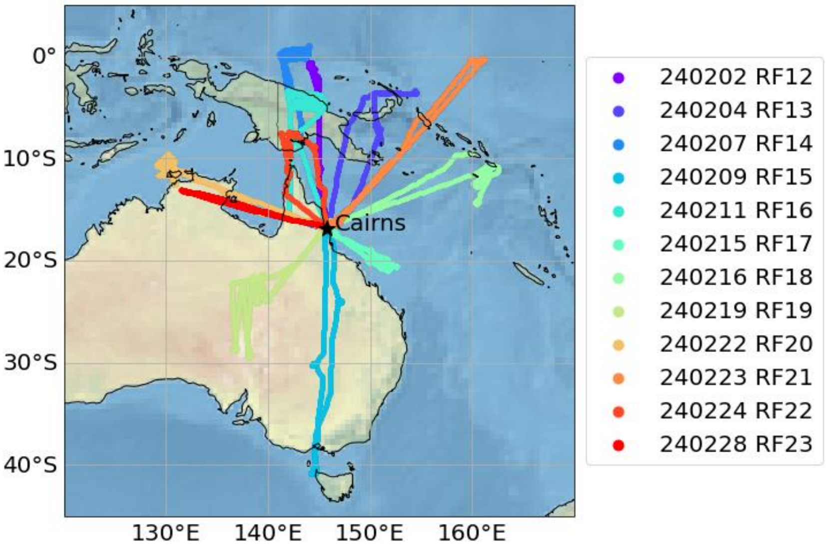

Figure 6.1.1: All flight tracks during CAFE Pacific where PAN and PAA was successfully measured by CIMS.

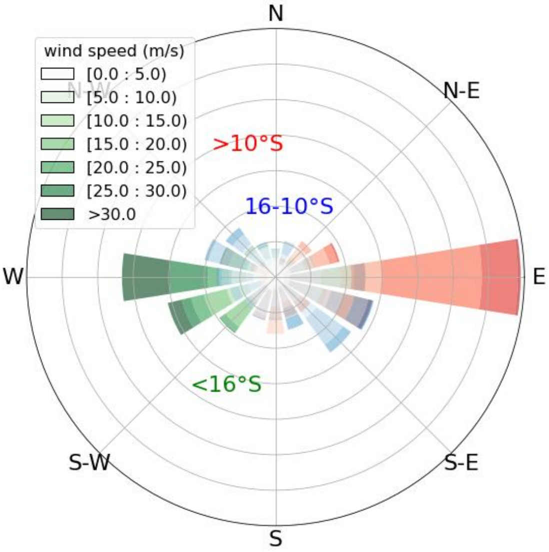

Figure 6.1.2: Occurrence of wind directions during CAFE Pacific, as measured by the BAHAMAS instrument aboard HALO. Colours were assigned according to the sampling location, with red indicating air masses sampled north of 10 °S, blue between 10-16 °S and green south of 16 °S The colour gradation indicates the wind speed, as defined in the legend.

The main aim of the campaign was to investigate pristine, marine tropospheric chemistry including photo-oxidation chemistry, radical cycling and new particle formation. Research flights were performed in a region between 130-165 °E and -45-0 °S.
A special target region was the Indo-Pacific Warm Pool (IPWP) where sea surface temperatures are generally warmer than 28 °C throughout the year and major convective updraft takes place bringing a lot of latent heat into the upper troposphere with global impact (De Deckker, 2016). The warm pool region is also characterized by low ozone concentrations due to the high mixing ratios of water and actinic flux leading to fast losses of O_3 and the formation of OH (Rex et al., 2014). The prevailing El Niño conditions of the Southern Oscillation in the year 2024 shifted the location of the IPWP further north-east towards the central Pacific. Despite the longer distance from Cairns, three specially designed research flights were able to investigate this region. RF21 is described in detail in Section 6.4.
In addition, specific flight routes were dedicated to different focus areas targeting for example: emissions from coastal mangroves, phytoplankton activity above coral reefs, differences between continental-marine air and tropospheric-stratospheric air. To reach these goals, the flight-time had to be extended from the usual 8 h to 10 h in some cases, which required a stop-over for refueling. This concerns RF10 and RF18 targeting the warm pool region, and RF15 which was a north-south transect through the whole Australian continent until Tasmania, where stratospheric intrusions were reached. RF15 is described in detail in Section 6.3.

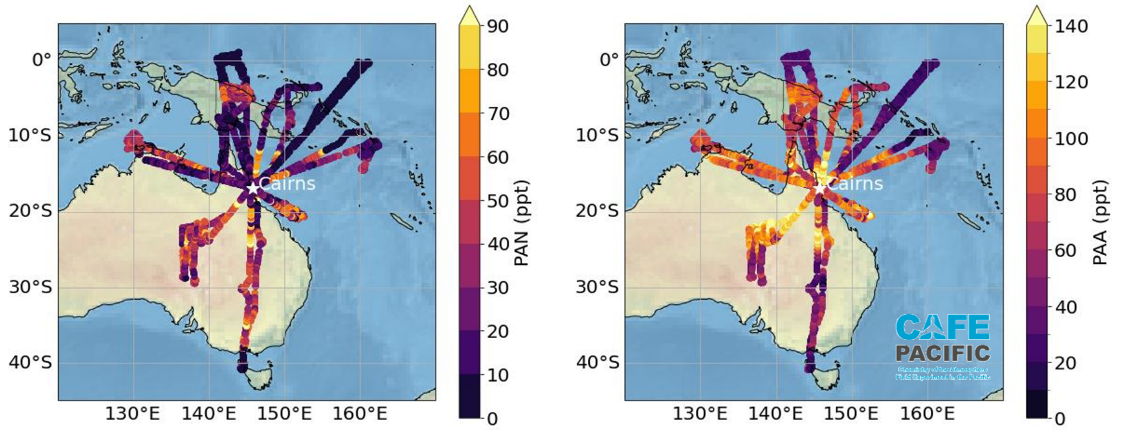

Figure 6.1.3: Measured PAN (left panel) and PAA (right panel) with CIMS along flight tracks, averaged for 2 min during CAFE Pacific.

6.1.1 *Meteorological conditions*

Due to the large sampling area and altitude range, the sampled air masses have very different wind directions and hence origins, see Figure 6.1.2. In measurement flights south of Cairns (<16°S, green), the prevailing wind direction is from the west with frequent high wind speeds above 30 m/s indicating the influence of the southern jet stream. Around Cairns (16-10 °S, blue), wind directions were almost equally distributed. Towards the equator (> 10 °S, red), most sampled air masses came from the Pacific in the east. With respect to altitude, the wind direction of sample air masses above 12 km is clearly dominated by east-winds while mid- and low altitudes wind-directions are more equally distributed with a second slightly favoured direction from north-west (not shown).

6.1.2 *Overview PAN and PAA measurements*

The measured PAN and PAA along the flight track are more heterogeneously distributed than during CAFE Brazil due to the large sampling area and the differences in air mass origins. As seen in Figure 6.1.3, PAN mixing ratios were generally low, ranging from below the LOD to a maximum of 100 ppt in 2 min averages. The lowest values were reached above the Indo-Pacific Ocean north-west of Cairns while enhancements of PAN were seen around Cairns and continental areas. An overview of PAN and PAA measurement during all flights in CAFE Pacific is given in Figure 6.1.4 illustrating the highly different flight designs and measured mixing ratios.

Besides probably urban pollution plumes from Cairns captured at altitudes below 2 km, maximum PAN is found at an altitude of 8-10 km with single values reaching above 100 ppt, see left panel in Figure 6.1.5. Median PAN in the mid-altitude maximum is around 50 ppt.

As seen by the different scaling of the x-axis in Figure 6.1.5, PAA levels generally exceed PAN levels reaching peak values up to 300 ppt. Minimum PAA levels were observed in the lowest and highest altitude bins close or below the detection limit. In the

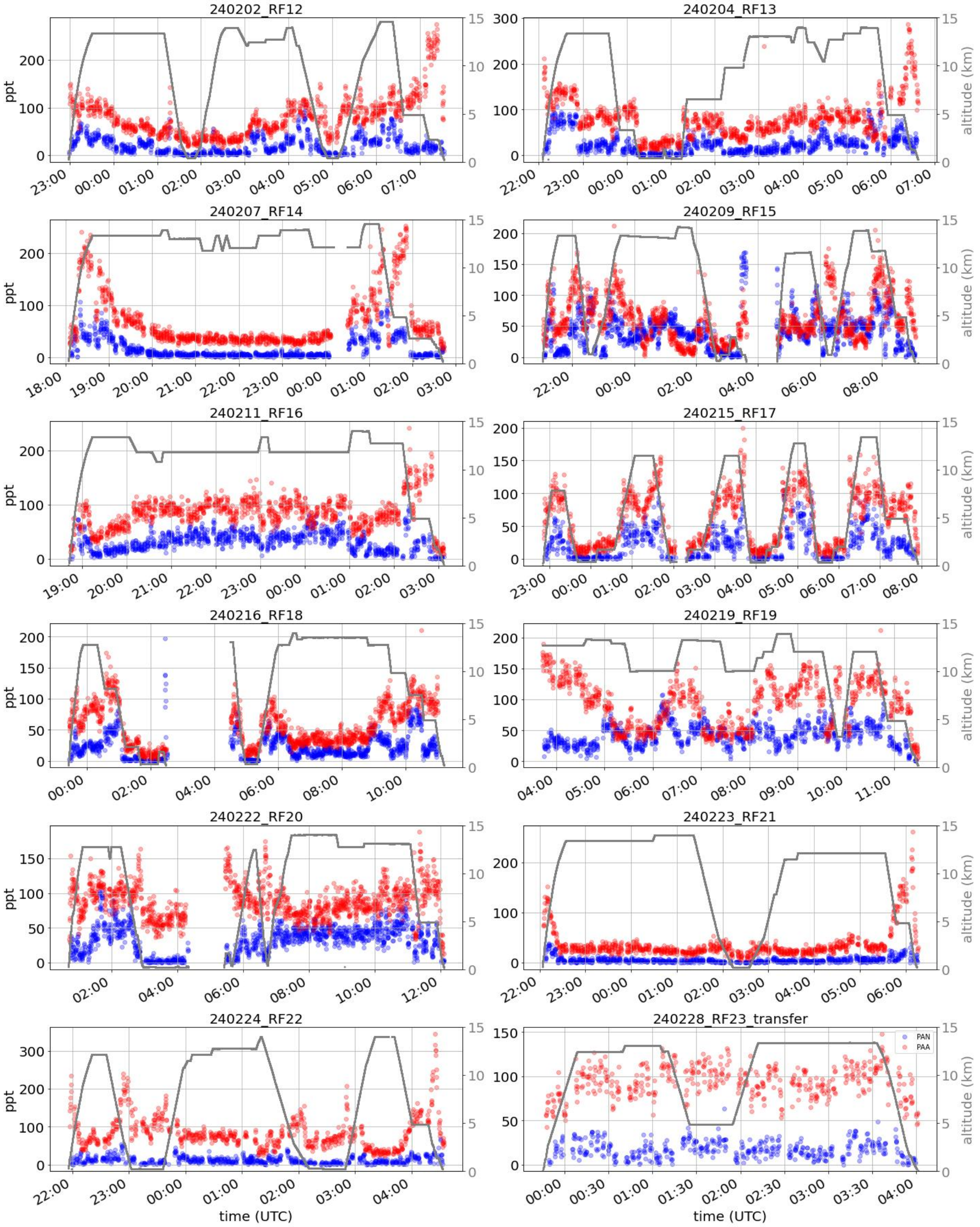

Figure 6.1.4: Time series of measured PAN (blue) and PAA (red) with CIMS aboard HALO of all analysed measurement flights during CAFE Pacific. The flight altitude is marked in gray.

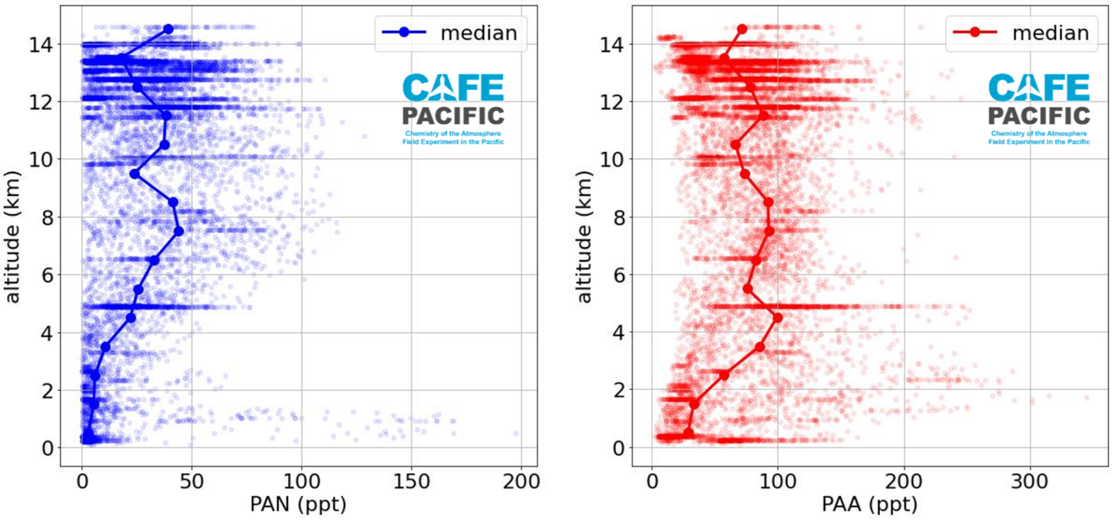

Figure 6.1.5: Median profiles of PAN (left panel) and PAA (right panel) during CAFE Pacific.

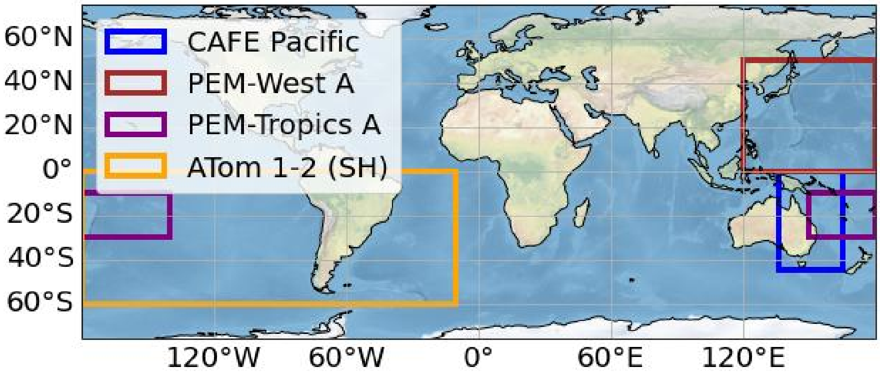

Figure 6.2.1: Sampling areas of the CAFE Pacific campaign (blue) and the compared aircraft campaigns. Note that only the data in the southern hemisphere (SH) of the ATom campaigns within the orange rectangle was included in the comparison.

mid-troposphere between 4-10 km altitude, minimum PAA levels were around 20 ppt, see right panel in Figure 6.1.5.

6.2 VERTICAL PROFILES OF PAN AND PAA ABOVE THE SOUTHERN PACIFIC

Simultaneous aircraft measurements of PAN and PAA above the tropical western pacific and especially the southern hemisphere are rare, as mentioned in Section 2.3.2. In this section, the CAFE Pacific measurements are compared to four aircraft campaigns which were considered to be the most comparable ones in terms of regional and seasonal comparability. However, the sampling area of the compared campaigns do not or only partially overlap with the one investigated by CAFE Pacific, as depicted in Figure 6.2.1. The area studied during the CAFE Pacific campaign is a unique feature of the campaign compared to previous aircraft measurement.

Previous aircraft campaigns in the Southern Pacific

The PEM-West A aircraft campaign of the Global Tropospheric Experiment (GTE) series sampled above the western pacific (0-50 °N and 120-180 °E) during September-October 1991 to study the budget and chemistry of reactive nitrogen at minimum outflow from the Asian continent (Hoell et al., 1996). Since PEM-West A sampled exclusively in the northern hemisphere, the comparison is only conditionally meaningful. Singh et al. (1996b) derived an average tropical/equatorial (15 °N) PAN profile of GC-ECD measurements on board of DC-8 aircraft during PEM-West A for clean background conditions (gray triangles in Figure 6.2.2).
The southern/central Pacific region (10-30 °S) was targeted five years later again in September/October by the PEM-Tropics A mission to show the presence of distinct pollution plumes in the middle-tropical troposphere (Singh et al., 2000a). The sampled air during PEM-Tropics A was characterised by low C_2H_2/CO ratios indicating the aging of fresh pollution plumes from biomass burning regions in South Africa and South America during the long-range transport towards South Pacific (Singh et al., 2000a). Singh et al. (2000a) derived the vertical profile of PAN measured above tropical ocean areas during PEM-Tropics A which is marked in Figure 6.2.2 (gray dash-dotted line with star markers).
The flight tracks of the two campaigns ATom1 and ATom2, were nearly identical sampling above the Atlantic and the Pacific between approximately 60 °N and 60 °S but covered different seasons. The gray dashed line with squared markers in Figure 6.2.2 shows the median PAN profile during the southern hemispheric winter and the dotted line with circle markers the median of southern hemispheric winter. The profile includes only data captured on the southern hemisphere and excludes land crossings episodes (Travis et al., 2020).

Comparison of PAN profiles

As seen in Figure 6.2.2, the median PAN profile during CAFE Pacific (blue) is comparable in shape and magnitude to the profiles derived during the missions ATom1-2 (orange).

The profile of PEM-West A (brown) is slightly lower than the one of CAFE Pacific, which is probably due to the fact that PEM-West A sampled in the northern hemisphere. However, the profile of PEM-West A is still within in the same magnitude than CAFE Pacific.

In contrast, the profile of PEM-Tropics A (purple) exceeds the profile of CAFE Pacific almost up to a factor of 2. This is probably caused by the frequently sampled biomass burning plumes during PEM-Tropics A campaign leading to an enhancement of mid- and upper tropospheric PAN (Singh et al., 2000a). As will be discussed later, biomass burning activity was rather low during CAFE Pacific.

All median profiles are characterised by a continuous increase between boundary layer and mid-troposphere. Median PAN levels in the boundary layer are quasi zero during all campaigns, due to the thermal instability of PAN. In the mid-troposphere around 8 km altitude, PAN levels are approximately between 20-60 ppt in all campaigns.

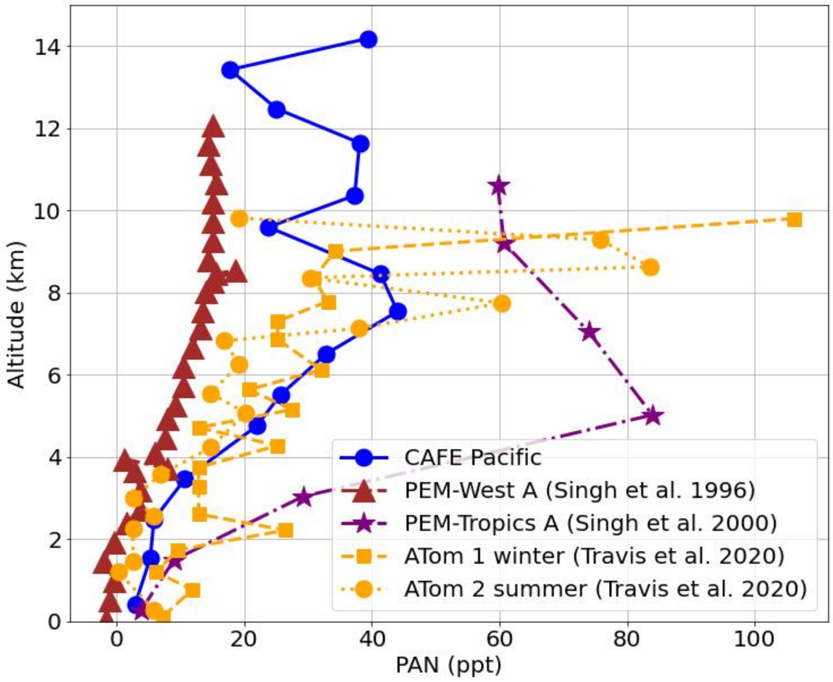

Figure 6.2.2: Comparison of median vertical PAN profiles during CAFE Pacific (blue points, this work) to reported measurements above the western- and southern Pacific by Singh et al. (1996b) (brown triangles), Singh et al. (2000a) (purple stars), and Travis et al. (2020) (orange squares and circles). Further descriptions of the campaigns are given in the text.

While the maximal sampling altitude was limited to 10 km during ATom and 12 km during PEM-West A and PEM-Tropics A, the CAFE Pacific measurements provide a unique data set up to an altitude of more than 14 km. The median PAN levels during CAFE pacific do not significantly decrease between 8 km altitude and 14 km, which could be a result of mixing and transport and will be discussed later.

Comparison of PAA profiles

PAA was only measured during the ATom campaigns with a Caltech negative-ion cluster CIMS instrument (Crounse et al., 2006).

As depicted in Figure 6.2.3, the CIMS measurements of PAA (red) are in a comparable range to the ATom data (orange) reported in Travis et al. (2020) considering the high uncertainty (approx. 30-100 %) on the absolute values of the CIMS PAA data (see Table 8).

However, the shapes of the vertical profiles differ significantly. While the median vertical PAA profiles derived from the first two ATom campaigns have a C-shape with a maximum above 100 ppt at low altitudes and also at 10 km, the median vertical PAA profile from CAFE Pacific is almost constant around 80 ppt above 4 km altitude, as it was also observed for PAN.

The difference is most substantial at the low altitudes, where PAA measured during ATom reaches 120-140 ppt while the median of the PAA measurements during CAFE Pa-

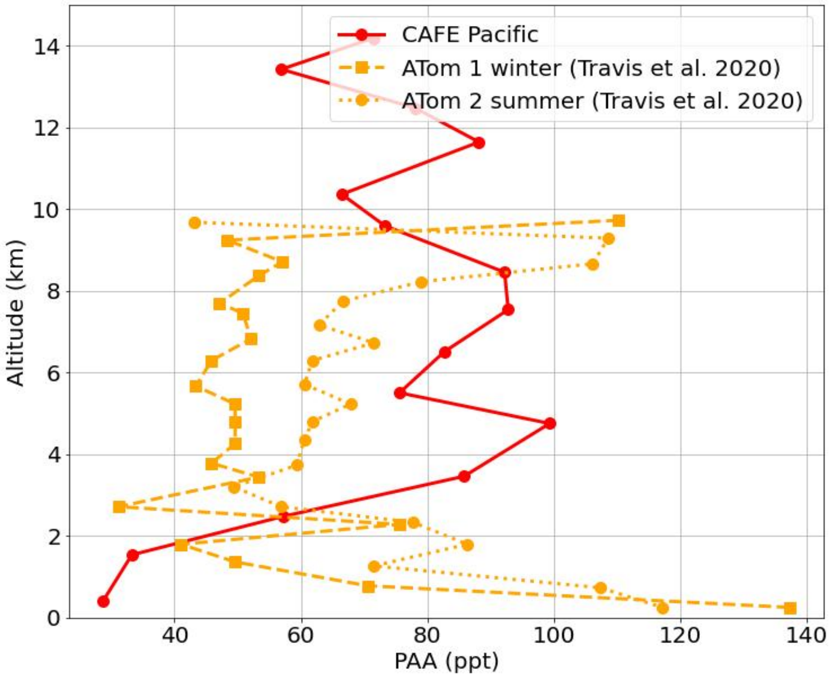

Figure 6.2.3: Comparison of median vertical PAA profiles from CAFE Pacific (red, this work) to reported measurements above the Southern Pacific during ATom1 (orange dashed line with square markers) and ATom2 (orange dotted line with circle markers) (Travis et al., 2020).

cific decreased to close to detection limit.

During CAFE Pacific, PAA data below 2 km altitude was a mixture from samples above the ocean and land masses. PAA above the Australian continent and along coast lines was clearly enhanced compared to above the ocean (see Figure A.0.9 in the Appendix). Note that in the ATom PAA profile, data from land-crossings was excluded, wherefore PAA below 2 km altitude was dominated by maritime boundary layer measurements.

A possible explanation for the substantial difference in shape between the observed vertical profile of PAA during CAFE Pacific and ATom, could be the result of convection and entrainment during CAFE Pacific. If PAA rich air from the boundary layer was shifted to the mid-troposphere by convective updraft leading to an inversely shaped profile to the one of ATom, where deep convection uplifting PAA may have been less frequent.

This hypothesis is supported by the EMAC model results for CAFE Pacific, which also predicted lower PAA in the lower troposphere than in the upper troposphere, which will be discussed later.

6.3 RF15: A NORTH-SOUTH TRANSECT FLIGHT

The highest levels of PAN were detected in research flight RF15 which took place on 9th - 10th February 2024 with respect to UTC time. RF15 was specially designed to reach as far south as possible to probe stratospheric air masses. During the 12 h long flight track, continental air masses were sampled by crossing over the Australian continent in

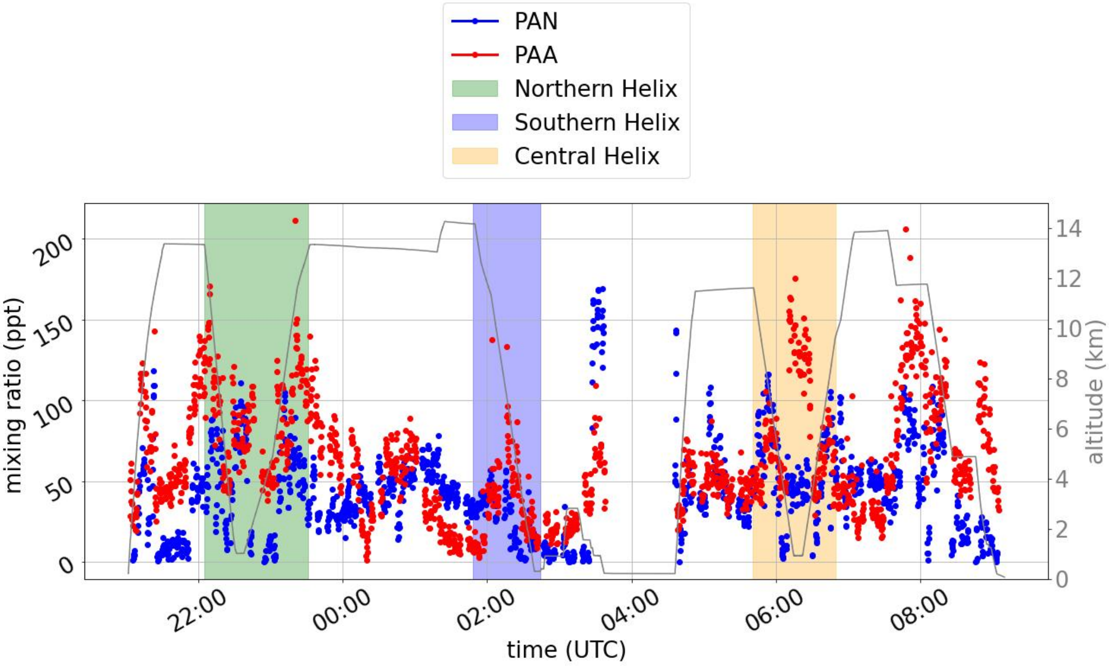

Figure 6.3.1: Time series of PAN and PAA measurements in RF15 on 9th - 10th February 2024 during CAFE Pacific. The timings of helix patterns are marked by the coloured shaded areas.

a north to south transect approximately along 145°E longitude. Between Cairns in the north end of the flight track and Cape Grim on Tasmania in the south, three vertical profile measurements were performed by spiraling up and down between 1-14 km altitude in a helix pattern. A refueling stop was made close to Melbourne (144.5°E, 38.0°S) between 3:38 and 4:35 UTC on 10th February. By reaching a southern latitude of more than 40°S, it was possible to intercept air masses with stratospheric influence.

The three profiling helix patterns were performed between 22:05-23:32 UTC on 9th February (northern helix, 146.8°E, 23.9°S), 1:48 - 2:44 UTC on 10th February (southern helix, 144.4°E, 40.4°S) and 5:41-6:50 UTC (central helix, 144.7°E, 30.4°S) as marked in Figure 6.3.1. The time between the three helices was approximately 4 hours with the first helix (in the north) at 9:00 local time and the third one (central) shortly before sunset around 17:00 local time.

6.3.1 *PAN and PAA vertical profiles during RF15*

The location of the vertical helices is marked on the flight track in the right panel of Figure 6.3.2 and the corresponding measured vertical PAN profiles during the helices are shown in the left panel in Figure 6.3.2 for PAN. The same plot is shown for PAA in Figure 6.3.3 respectively.

The vertical profiles of median PAN mixing ratios showed the typical maximum (40-90 ppt) around 8 km altitude during the two continental (green and brown) helices. The maximum PAN during the southern helix (blues) was located slightly higher around

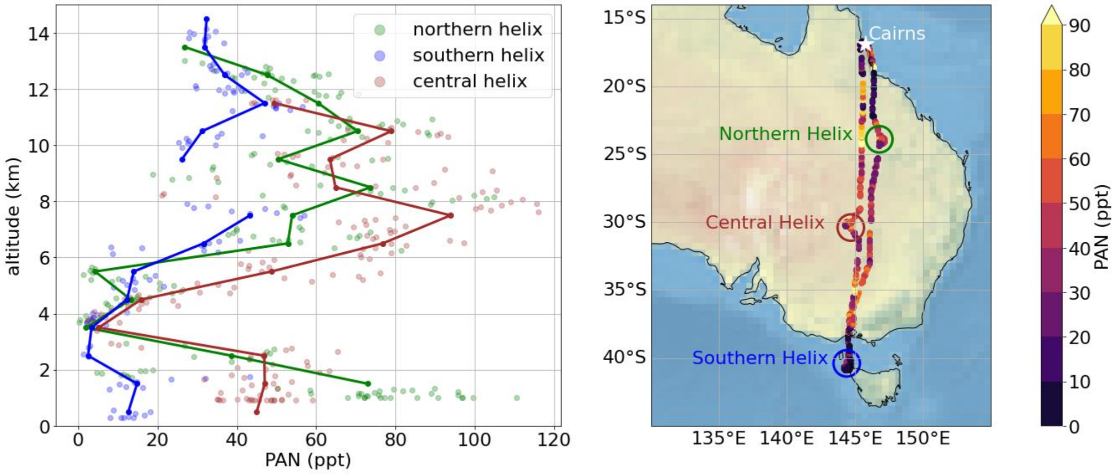

Figure 6.3.2: PAN along the flight track (right panel) and vertical profiles (left panel) corresponding to the encircled positions of up- and downward spirals (helix), measured during RF15 on 9-10th February 2024 during CAFE Pacific. Note that due to geographical overlaps, only the last data points during the helices are visible.

11,km with median mixing ratios around 50 ppt. In general, observed PAN levels during the southern helix were lowest compared to the two other helix. The difference between PAN levels measured during the southern helix and the two other helix patterns is most pronounced at low altitudes. Specifically, median PAN levels were factor 3-5 higher during the central and northern helix compared to the southern helix.

The southern helix was performed above the ocean in the absence of strong anthropogenic sources and captured very low PAN values close to detection limit. In contrast, the two other helix patterns were performed above the continent, where enhanced PAN were observed at low altitudes. Since temperatures at 1 km were around 20°C, the lifetime of PAN was in the order of 1-2 h according to current IUPAC recommendation for the thermal decay coefficient of PAN[24]. This suggests that the observed PAN at low altitudes must have been produced from sources on the Australian continent rather than being transported from distant source regions. Since most of inland Australia is neither inhabited nor industrialised, sources of NO_x and organic precursors of PAN may result from vegetation fires.

In contrast to PAN, PAA is thermally stable in the warm boundary layer and its lifetime is determined by photolysis (Berasategui et al. (2020, and references in Section 2.2.2)). The vertical profiles show, that the mixing ratios PAA in the low altitudes vary strongly depending on wether it was sampled above maritime or continental regions. The three profiles reach similar mixing ratios in the mid troposphere around 4-9 km altitude but differ significantly by their shape.

In the central helix, PAA was highest (up to 150 ppt) below 2 km altitude above the continent decreasing with altitude.

During the southern, maritime helix, only a few ppt were measured in the low altitude probably due to the absence of source. PAA mixing ratios increased with altitude up to around 8 km, where also PAN was maximal, but the decrease again towards higher altitudes.

---

[24] https://iupac-aeris.ipsl.fr/datasheets/pdf/ROO_15.pdf, last access: 10th June 2025.

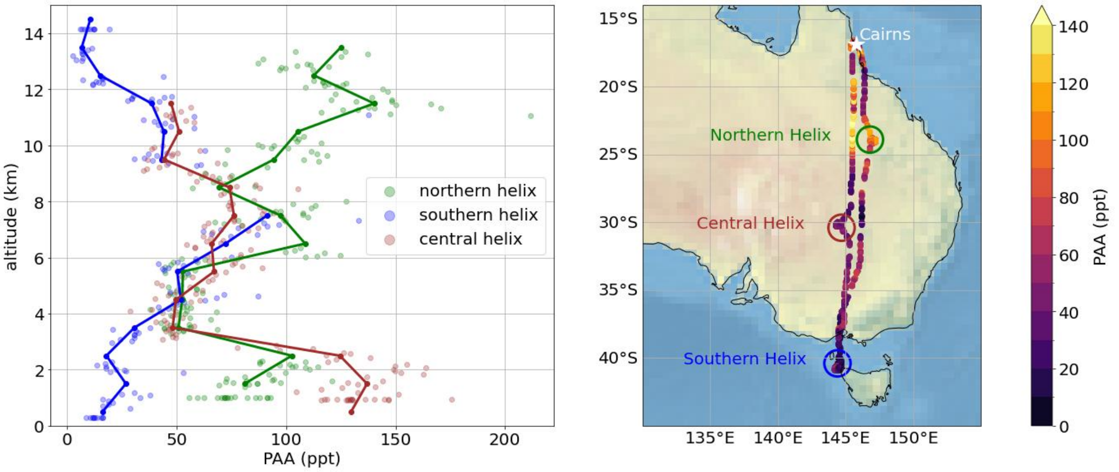

Figure 6.3.3: PAA along the flight track (right panel) and vertical profiles (left panel) corresponding to the encircled positions of up- and downward spirals (helix), measured during RF15 on 9-10th February 2024 during CAFE Pacific. Note that due to geographical overlaps, only the last data points during the helices are visible.

In the case of the northern, continental helix, PAA was almost continuously increasing with altitude. At low altitudes, a median of around 80 ppt was reached while in the upper troposphere around 11 km, a median of about 150 ppt was observed. This high concentration in high altitudes could be a result of in-situ formation of PAA in the boundary layer in the morning which was uplifted in the upper troposphere by convective updraft.
The three very different local PAA profiles underline the high spatial and temporal variability of PAA.

6.3.2 *PAN correlation to other tracers in the northern Helix in RF15*

To gain insights about the potential sources of PAN measured during the helices, the correlations to other measured trace gases was investigated. In Figure 6.3.4, PAN measurements during the first, northern helix pattern are plotted against ozone, carbon monoxide, acetonitrile and acetone.

Figure 6.3.4 shows that the composition of air masses sampled in the northern helix, differ significantly by altitude and can be roughly distinguished into three regimes: low (<4 km), mid (4-7 km) and high altitude (>7 km) air masses. These three regimes are most clearly seen in the correlation of PAN to measured ozone and also to some extent in the plot against CO and acetonitrile. The different regimes indicate the complex mixture of the sampled air masses being a result of different sources.

As outlined in Section 1.4, ozone production depends on similar precursors as PAN (NO_x and VOC). Hence, the linear correlation between ozone and PAN in mid- and high altitude air masses above 7 km underlines the presence of in-situ production contributing to the observed PAN levels.

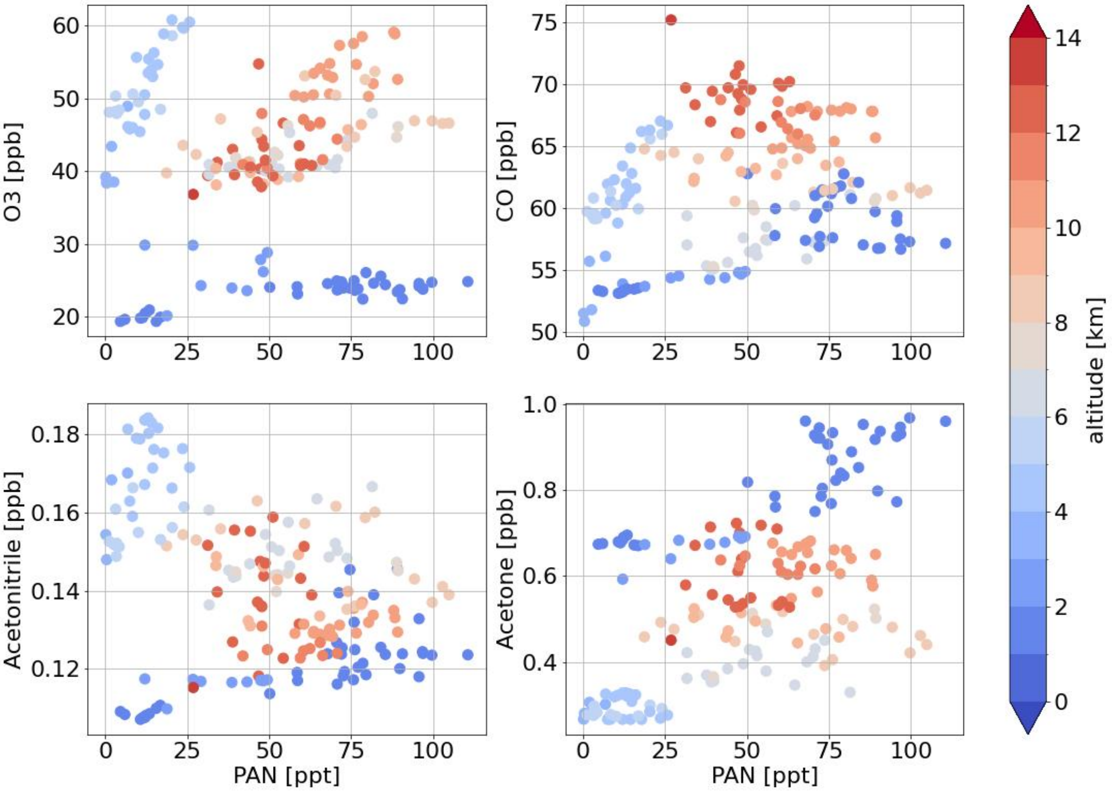

Figure 6.3.4: Correlation of PAN to Ozone (top left panel), CO (top right panel), acetonitrile (bottom left panel) and acetone (bottom right panel) measured aboard HALO during the northern helix of RF15 during CAFE Pacific.

The origin of CO in the troposphere can be biogenic as well as anthropogenic and can hence indicate different types of sources. The major source of CO in the troposphere is oxidation of methane by OH, followed by biomass burning. Since CO is also emitted by combustion and industrial process, CO can be used as a tracer of anthropogenic activity. However, background levels are relatively high because of its long atmospheric lifetime of about 1 month in the tropics and 4 month in mid-latitudes (Seinfeld and Pandis, 1998). In low altitude air masses, PAN and CO showed two distinct linear correlations, one for air masses below 4 km (dark blue) and one for air masses between 4-6 km (light blue).

During RF15, only a few counts on black carbon have been detected by the SP2 instrument indicating no significant impact by fresh biomass burning (Figure A.0.13 in the Appendix). However, a linear correlation between PAN and acetonitrile can be observed in low altitudes (<4 km) as it was seen also for CO. Acetonitrile is a more long lived biomass burning tracer. Hence, the correlation between PAN and CO and acetonitrile indicates a possible impact of aged biomass burning on the air mass composition.

Next to acetaldehyde and MGLY, acetone is an ubiquitous oxygenated species in the atmosphere and one of the most important precursors of PAN (Fischer et al., 2014). Acetone is directly emitted from anthropogenic and biogenic sources as well as biomass burning and is also produced in the atmosphere by VOC oxidation (Fischer et al., 2012). No clear linear correlation between acetone and PAN for all altitudes is seen.

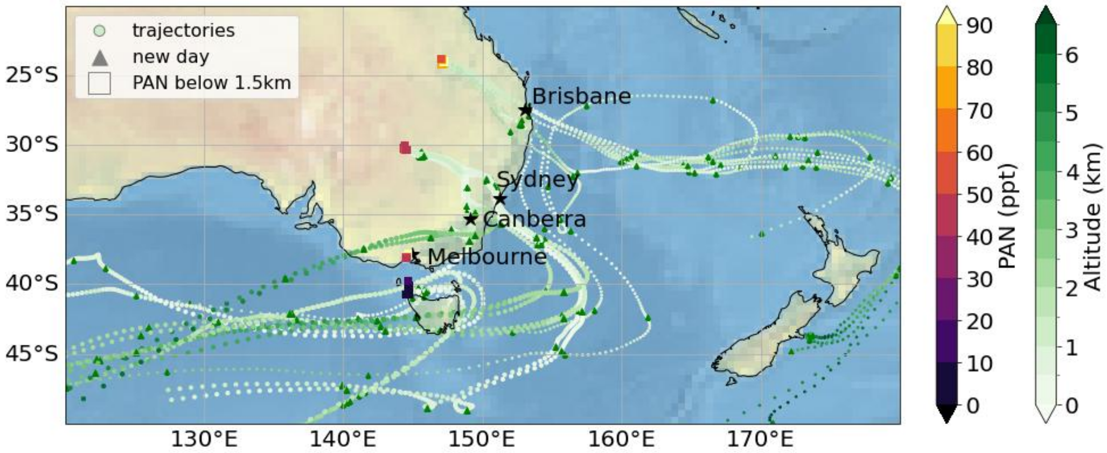

Figure 6.3.5: Calculated 10 day-backward trajectories with HYSPLIT for PAN measurements below 1.5 km altitude during the vertical profiling helices. The trajectories are colour-coded with altitude and PAN mixing ratios are given at the trajectories' starting points.

6.3.3 *Back-trajectory analysis RF15*

To investigate the origin of the air masses measured during the vertical profiling, 10 days-backward trajectories were calculated with HYSPLIT[25] for every minute along the flight track similar as described in Section 3.5 and also applied for the analysis for CAFE Brazil in Section 5.3. Note that trajectory calculations have to be used with caution because they are highly dependent on the starting location, the meteorological input data and the used vertical transport method, which causes the major uncertainty (Harris, Draxler, and Oltmans, 2005).

Figure 6.3.5 shows that the trajectories from air masses sampled below 1.5 km during the central and northern helix have passed in low altitudes above big coastal cities like Brisbane, Sydney and Canberra within the last 1-2 days. Above the cities, air masses would have been loaded with urban pollution allowing PAN to form from NO_x and organic precursors explaining the correlation between CO and PAN depicted in Figure 6.3.4. The trajectories corresponding to the low altitudes during the southern helix, which took place above the ocean close to Tasmania, do not pass over obvious anthropogenic source regions in the previous 1-3 days which fits to the low measured PAN levels.

As shown in Figure 6.3.6, a part of the trajectories of air masses sampled at high altitudes (>10.5 km) during the central and the southern helix traveled in the subtropical jet. This opens the possibility of long range transport of PAN resulting from biomass burning or anthropogenic pollution from southern Africa.

The trajectories which pass above southern Africa traveled there at altitudes above 8 km, so deep convection would be required to mix anthropogenic pollution from the boundary layer to this altitudes. Biomass burning plumes could be effective in bringing up NO_x and organic PAN and PAA precursors. According to NASA's Earth Observing

---

[25] https://www.ready.noaa.gov/HYSPLIT.php, last access: 10th June 2025.

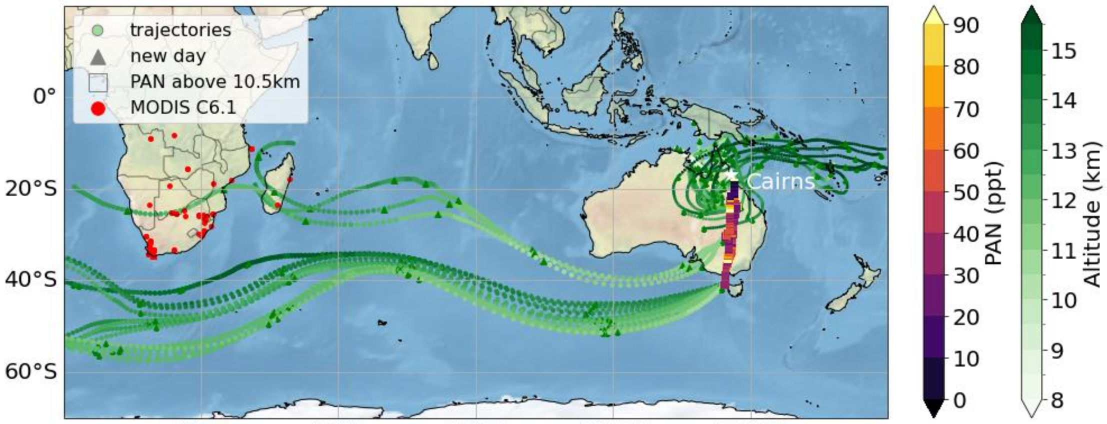

Figure 6.3.6: Calculated 10 day-backward trajectories with HYSPLIT for PAN measurements above 10.5 km altitude during the vertical profiling helices. Trajectories are colour-coded by altitude and PAN mixing ratios are given at the trajectories' starting points. FIRMS Fire events above southern Africa detected with a confidence of 100 % by satellite data from AQUA and TERRA with the MODIS instruments between 1.1.-9.2.2024 are marked in red.

System Data FIRMS from the MODIS instrument on the satellites TERRA and AQUA[26], biomass burning activity in southern Africa was low during January until 9th February 2024 (269 detected events with confidence of 100 %), see red dots in Figure 6.3.6. Therefore, it seems unlikely that long range transport of biomass burning or anthropogenic pollution plays a major role for the measured PAN at high altitudes during RF15 in CAFE Pacific. In addition, in biomass-burning plumes the absolute mixing ratios of PAN and PAA as well as their ratio depend on multiple factors like for example the type and phase of biomass burning, the rate of initial vertical transport, meteorological conditions etc.

The temporal evolution of the air composition in potential biomass burning plumes is highly complex and the ratio between PAN and PAA is quite variable (Crowley et al., 2025), which makes it difficult to draw conclusions on the PAN and PAA ratio in an air mass after 10 days of transport. In the case of the northern helix, all trajectories indicate origins from the east over the ocean, where no strong sources are expected. However, both, PAN and PAA levels, were elevated at 10-12 km so the origin of the PA-radical remains unclear.

6.3.4 *CAMS forecasts of PAN for RF15 during CAFE Pacific*

As explained in Section 3.4, a forecast product of Copernicus Atmospheric Monitoring Service (CAMS) simulating the distribution of several trace gases was used during the campaign for flight planning.

In Figure 6.3.7, the CIMS measurements of PAN are compared with the forecast data set of CAMS[27] in low (1000 hPa, left panel) and high (250 hPa, right panel) altitudes

---

[26] `https://firms.modaps.eosdis.nasa.gov/map/`, downloaded on 16th May 2025.

[27] `https://ads.atmosphere.copernicus.eu/datasets/cams-global-atmospheric-composition-forecasts?tab=download`, downloaded on 18th December 2024.

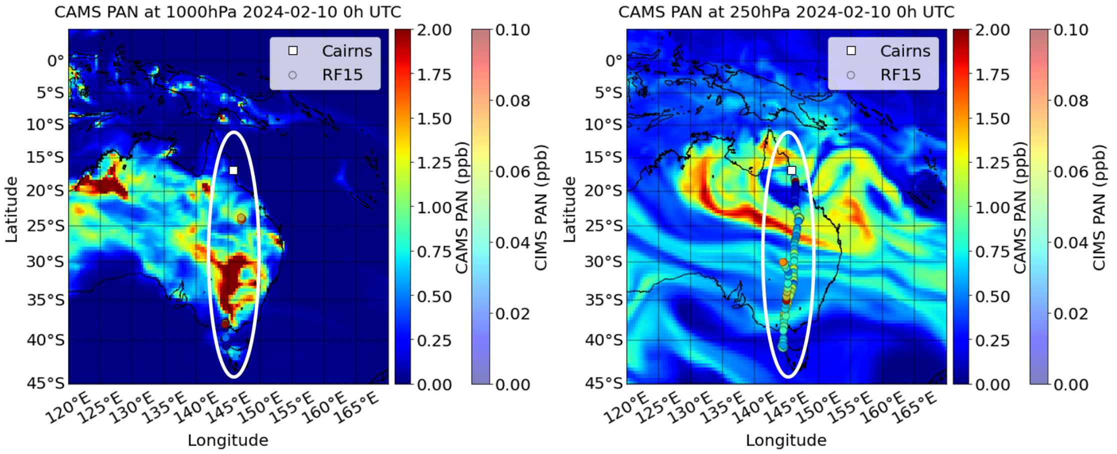

Figure 6.3.7: Global forecast of PAN by CAMS for RF15 during CAFE Pacific colour-coded by mixing ratio. The white ellipses mark the area of the flight track. Measured PAN is plotted for the corresponding pressure levels 1000 hPa (left panel) and 250 hPa (right panel) for 6 hours around midnight (UTC) and is marked as colour-coded dots according to mixing ratio. Note that the scale of the colour-codes differs by a factor of 20 for CAMS and CIMS levels. Generated using Copernicus Atmosphere Monitoring Service information (2024).

around midnight (UTC). Note that the color-code sacles are different by a factor of 20 for CAMS and CIMS PAN data.

Near the ground at 1000 hPa, CAMS predicted elevated PAN levels above 2 ppb above the south-western Australian continent, where CIMS also measured higher PAN levels but only up to around 100 ppt. Also the horizontal location of the predicated PAN layer at 250 hPa by CAMS fits surprisingly well to the hot-spots of the measured PAN, even for the filaments of the plume. However, also here the CAMS PAN levels are a factor 20 higher than the observed ones by CIMS.

The same general observation yields also for the analysis of other measurement flights during CAFE Pacific (see Figure A.0.14 in the Appendix). It seems that the CAMS forecast product is able to predict approximately the horizontal extend of PAN plumes, but the model has crucial deviations (more than factor twenty) in magnitude of predicted absolute mixing ratios. In addition, the predicted altitude of the PAN layer is highly uncertain compared to observations which was seen as well when comparing CAMS reanalysis data to CAFE Africa (not shown) and CAFE Brazil PAN measurements (Figure 5.4.14).

Hence, with respect to flight planning, CAMS is considered as a useful tool to approximately locate the horizontal extent of PAN plumes. However, the CAMS predictions must be regarded with caution considering the essential overestimation in absolute levels of PAN and the uncertainty in the vertical location.

6.4 RF21: WARM POOL FLIGHT

The lowest PAN levels were measured during RF21 which targeted the Indo-Pacific Warm Pool region. The 9 h long flight took place on 23th-24th February 2024 going

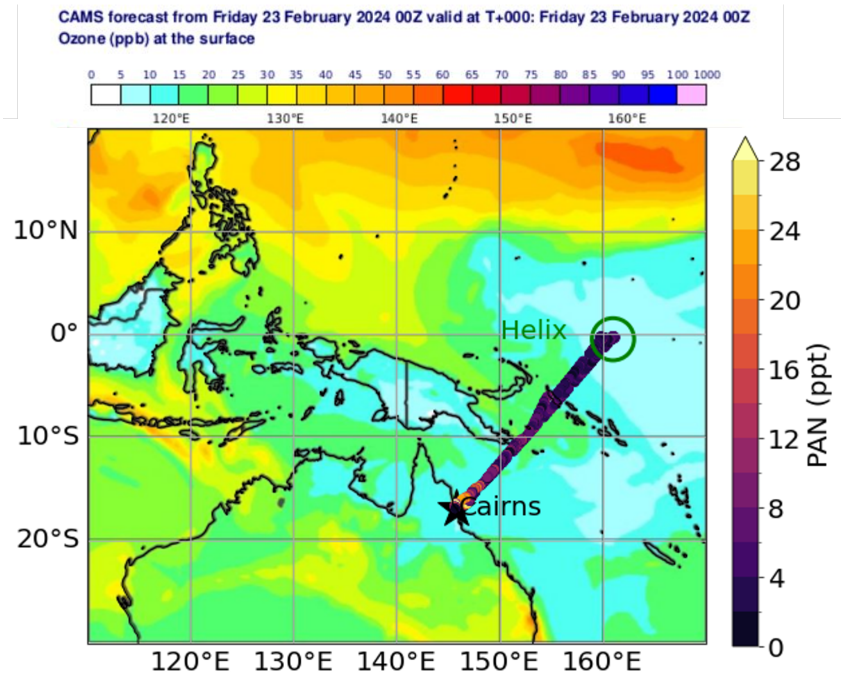

Figure 6.4.1: PAN measurements colour-coded along the flight track of RF21 during CAFE Pacific. The location where a vertical profiling helix pattern was performed is marked by the green circle. The background picture of predicted surface ozone around 0:00 UTC was generated using Copernicus Atmosphere Monitoring Service information (2024).

straight towards the north-east from Cairns until the edge of the warm pool where a helix pattern for vertical profiling was performed (1 °N, 158 °E) between 1:22 and 3:38 UTC, see Figure 6.4.1. The location of the warm pool was estimated with the help of the surface ozone forecast from CAMS[28].

As predicted by the CAMS forecast, ozone levels were low above the Indo-Pacific region, going down to around 10 ppb, see green points in Figure 6.4.2. The low ozone values are a result of HO_x reactions with O_3 and the low NO levels (Nussbaumer et al., 2025). If there is little NO, this will not lead to NO_2 and thus photochemical formation of ozone is stopped. Nussbaumer et al. (2025) explained the lack of lightning induced NO_x in the UT above the warm pool by non-electrified convection.

Apart from take-off and landing, PAN was constantly close to or below the detection limit counting less than 5 ppt in the lowest level above the warm pool (blue dots in Figure 6.4.2). These observations suggests that PAN does not play a major role as reservoir and source of NO_x above the Indo-Pacific warm pool.

Also PAA mixing ratios (red dots in Figure 6.4.2) were the lowest observed during the campaign varying between 10 ppt at low altitudes above the warm pool and around 30 ppt at high altitudes. This is readily understood by the absence of terrestrial VOC sources. At the end of the flight during the calibration leg at an altitude of around 5 km PAA increased up to 250 ppt when approaching the coast together with Ozone and a

---

[28] https://ads.atmosphere.copernicus.eu/datasets/cams-global-atmospheric-composition-forecasts?tab=overview, downloaded on 22nd February 2024 from the service package especially designed for CAFE Pacific and only active during the campaign.

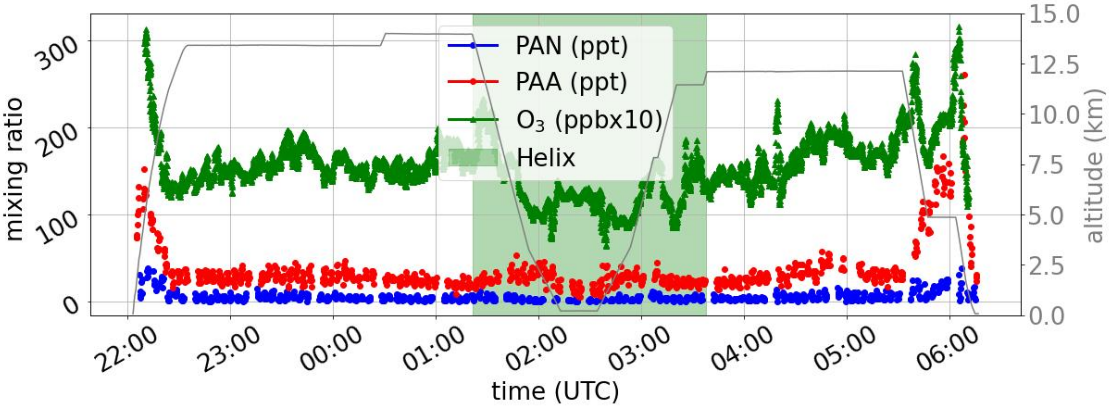

Figure 6.4.2: Time series of PAN (blue) and PAA (red) measurements from RF21 during CAFE Pacific. Ozone data (green) from the FAIRO instrument is given in ppb and scaled by a factor of 10 for better visibility. The time span when a vertical profiling helix pattern in the warm pool region was performed is shaded in green.

slight increase in PAN. This could be an indication for photo-chemical production from organic precursors in warm air with high organic content.

6.4.1 *Maritime versus continental flights*

In total, three flights were dedicated to investigate the IPWP region north-east of Australia (RF13, RF18, RF21). Conversely, two flights were directed south-west of cairns sampling above the Australian continent (RF15 and RF19).

To investigate the characteristics of the maritime flights in contrast to the continental flights, Figure 6.4.3 shows the flight tracks and the mean vertical PAN profile for the continental (brown) and maritime (orange) flights. Both profiles show a maximum around 8 km altitude but in general slightly higher PAN levels were detected during the continental flights. The two PAN profiles differ greatest at altitudes below 3 km PAN, where mean PAN mixing ratios were larger above the continent. At the lowest altitude, the mean of continental flights reached around 50 ppt while above the ocean PAN was close to the limit of detection. The PAN peaks at the lowest level during the continental flights indicate the presence of local pollution plumes and in-situ PAN production. Note that RF18 included a refueling stop on the Solomon islands. When approaching the islands, a peak of PAN up to 200 ppt next to a visible biomass burning plume was measured, which was excluded from the median of the maritime flights (orange line).

Figure 6.4.4 shows the 10-days-backward trajectories investigating the origin of the sampled air masses below 4 km. The trajectories of both groups, maritime and continental flights, traveled most of the time above the ocean. In the case of the Warm Pool flights, most trajectories originated from the Southern Pacific. The trajectories from the continental flights mostly originated from the Southern Ocean but also partly surpassed the continent at low altitudes where air masses could possibly be impacted by pollution or biogenic emissions explaining the enhanced PAN in the profile at low altitudes. Due to the long lifetime of PAN in the mid- and upper troposphere and the manifold of sources, the differentiation between "maritime" and "continental" flights at

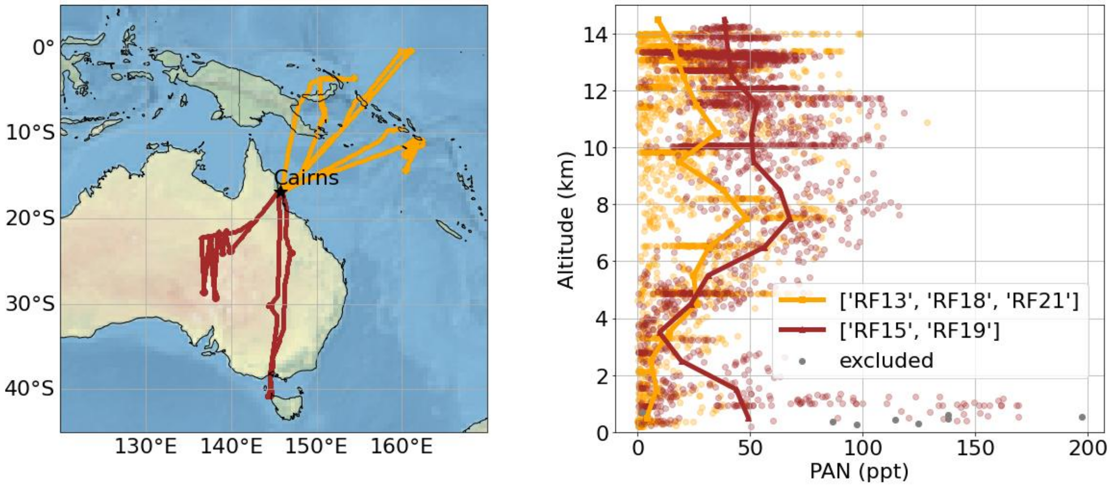

Figure 6.4.3: Flight tracks of selected "continental" (brown) and "maritime" (orange) flights during CAFE Pacific (left panel) and corresponding mean PAN profiles of the grouped flights (right panel). Gray coloured points result from a biomass burning peak in RF18 and were excluded from the mean calculation of maritime flights.

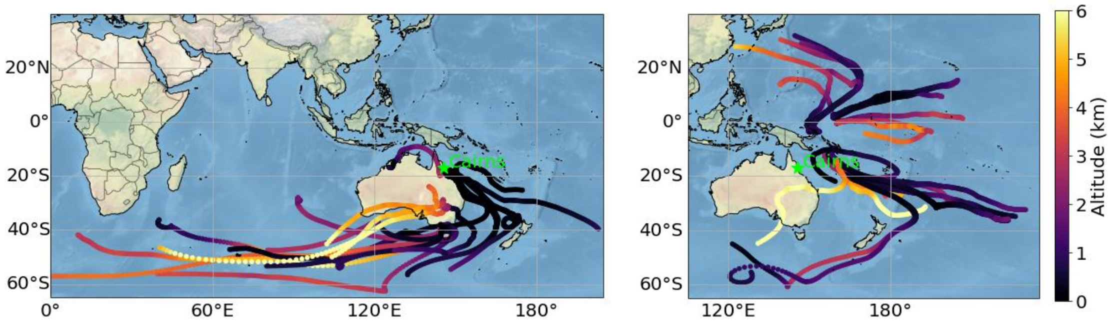

Figure 6.4.4: Calculated 10-days back trajectories with HYSPLIT for every 10 min along the flight tracks. Data only includes trajectories starting below 4 km altitude for continental flights RF15 and RF19 (left panel) and maritime flights RF13, RF18, and RF21 (right panel).

these altitudes is not reasonable. This is underlined by the little difference between the two profiles at mid- and high altitudes.

6.5 RF17: IMPACT OF IN-SITU PRODUCTION

To better understand the role of in-situ production of PAN and PAA during CAFE Pacific from the two measured PA precursor species acetone and acetaldehyde onboard HALO, the simplified reaction steady-state scheme explained in Section 3.8.1 is applied to the CAFE Pacific data set of RF17.

Flight RF17 was chosen because it has a complete data coverage for almost all instruments aboard HALO. In addition, RF17 has a high vertical data coverage in an altitude range between 400 m above sea level and almost 14 km altitude.

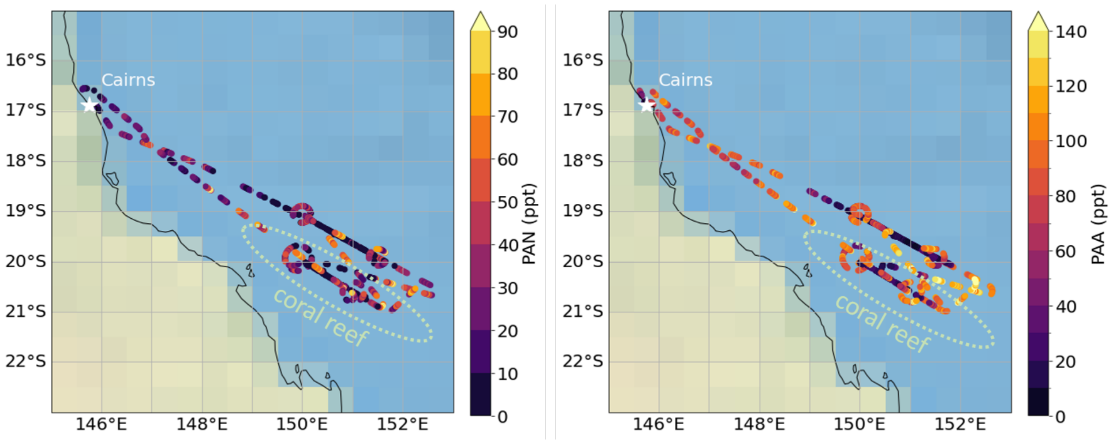

Figure 6.5.1: Measured PAN (left panel) and PAA (right panel) by CIMS along the flight track of RF17 on 14th February 2024 during CAFE Pacific. The approximate location of the targeted coral reef area is encircled (green dotted).

6.5.1 *RF17 flight description*

RF17 took place from midday local time (UTC + 10 h) until the late evening on the 14th of February 2024 and targeted the coral reef area south east of Cairns. The flight pattern depicted in Figure 6.5.1 was 9 h long and included two parallel walls of stacked altitudes, one directly above the coral reef area and the other one above the open ocean, as well as the four vertical helix climbs. PAN measurements reached values up to 100 ppt and PAA up to 200 ppt. No distinction was observed between reef and non-reef areas with regard to the PAN and PAA measurements.

6.5.2 *Input data sets for the steady-state calculation of RF17*

The steady-state calculation was run with two different data sets, a measurement based (HALO) and a model based (EMAC) data set. The species and meteorological parameters long the time series of RF17 for both data sets are depicted a in Figure A.0.10 in the Appendix.

The measurement data in the first data set results from instruments onboard HALO as referenced in Table 1. NO_2 data was derived from ozone, NO and actinic flux data via the simple photo stationary state assumption (Equation 27) which does not include peroxy radicals. Since the concentration of NO is critical for the calculation of the PSS as well as for the steady-state calculation of PAN, a value of 1 ppt was assigned to data reported to be below the detection limit of NO. The median of NO measurements is in agreement with EMAC model simulations of NO, which were only a few ppt low altitudes, as shown in the left panel in Figure 6.5.3. In the original data set, NO data below the detection limit was assigned 5 ppt $(1\,\sigma)$ which would already lead to a significant amount of NO_2 and hence PAN at low altitudes above the sea where no NO source except the rare shipping traffic is expected. Further, for the calculation of the PSS, twilight phases were excluded by filtering data by photolysis frequencies of NO_2 ($j(NO_2)$)

below 0.0045 1/s which represents approx. 20 % of the maximum $j(NO_2)$ reached. Since the data set from the spectroradiometer (SR) aboard HALO does not provide directly the photolysis frequency of PAA, a scaled photolysis rate of H_2O_2 for the HALO data set was used. The fixed scaling factor of about 10 % was derived from the ratio of $j(PAA)$ to $j(H_2O_2)$ simulated by a TUV model provided by the Atmospheric chemistry observations and Modeling Lab[29]for 15th February of 2024 at Cairns (16 °S, 146 °E) and 8 km altitude. This approximation is valid because the absorption cross section of H_2O_2 and PAA in the actinic spectrum behaves similar due to the OOH-group but differs in magnitude[30].

Measurement data of HOx was not available wherefore OH and HO_2 were taken from EMAC simulations along the flight track. All measurement data was resampled to time steps of 12 min to fit with the EMAC data set.

The second data set for the steady-state calculation consists purely out of modelled data by EMAC including PAN, PAA, precursor species, photolysis frequencies and meteorological parameters. The EMAC model configuration was the same as used for the analysis of CAFE Brazil data presented in Section 5.6.

6.5.3 *Modelled and measured photolysis frequencies for RF17*

In both data sets, photolysis frequencies for PAN, Acetone and PAA were filtered by a lower limit of $j(PAN) > 1e^{-7}$, which would otherwise falsely induce extremely high steady-state concentrations when the loss rates become very low.

The median vertical profile of the filtered j-values from the SR instrument and EMAC simulations are shown in Figure 6.5.2. Model and measurements are in good agreement except in high altitudes between 8-12 km for the photolysis rate of PAA where EMAC overestimates j(PAA) by around 50 %. This can be explained by thin cirrus cloud layers above the aircraft reducing the actinic flux, which were observed during the flight but are not resolved in the EMAC model. However, j(PAA) does not affect the steady-state for PAN as it only enhances the loss rate of PAA at these altitudes impacting the steady-state concentration of PAA. The reaction rates for all reactions in the simple steady-state scheme are based on the latest IUPAC recommendations[31] for the HALO measurement data set as well as for the EMAC model data set. Generally, the photolysis frequencies, temperature and pressure data are well represented by the EMAC model.

6.5.4 *Vertical profiles of modelled and measured precursor species in RF17*

Since in both data sets HO_x data is taken from the model, the HALO and the EMAC data set differ in principle only by in NO_x, acetone and acetaldehyde. Figure 6.5.3 shows the vertical median profiles of theses species for measurement data from NOAH, GC-MS and PTR-MS compared to model data from EMAC. The EMAC simulation fits well to the

---

[29] https://www.acom.ucar.edu/Models/TUV/Interactive_TUV/, last access: 1st May 2025.

[30] https://uv-vis-spectral-atlas-mainz.org/uvvis_data/cross_sections_plots/Organics%20(acids)/CH3C(O)OOH_lin.jpg, last access: 12th May 2025.

[31] https://iupac.aeris-data.fr/catalogue/#/catalogue/classifications/gap, last access: 14th May 2025.

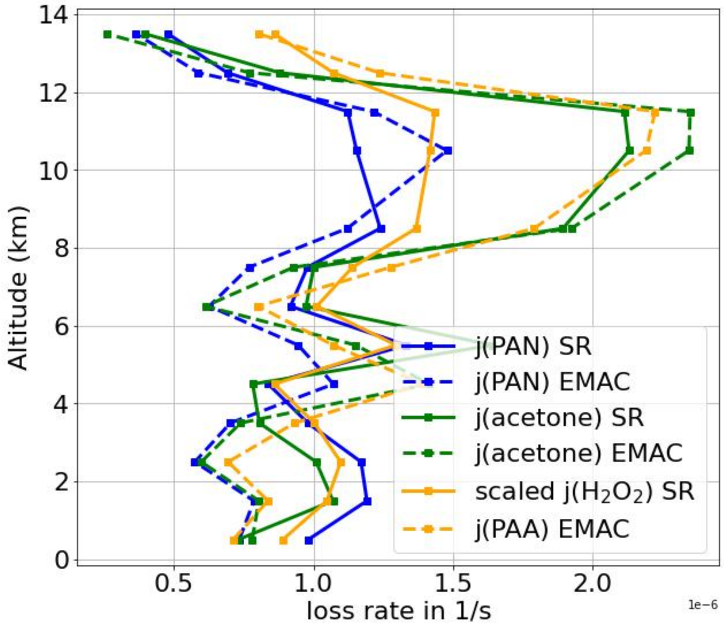

Figure 6.5.2: Median vertical profiles of filtered photolysis frequencies for the data set based on measurements (SR) and model data (EMAC) used for the steady-state calculation for RF17 during CAFE Pacific.

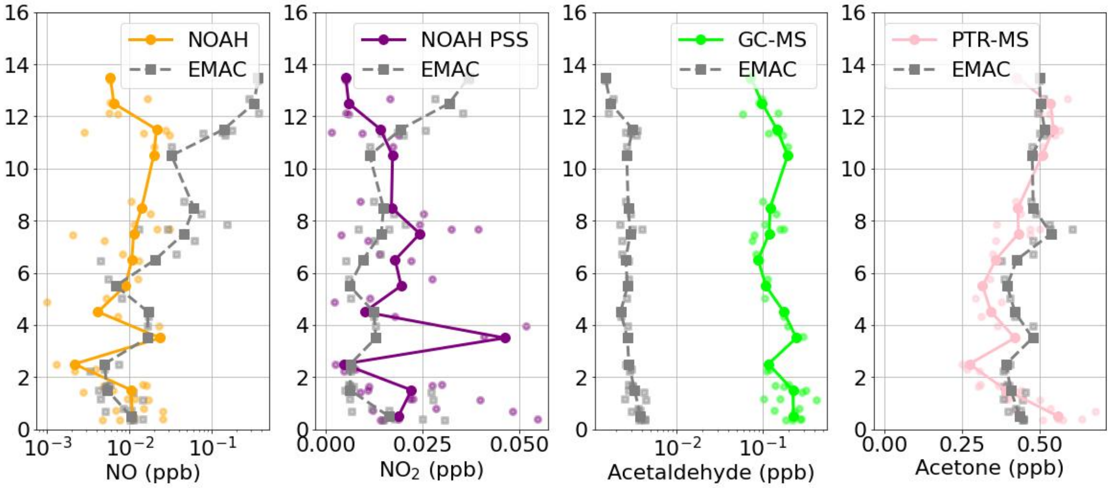

Figure 6.5.3: Vertical profiles of PAN and PAA precursor species of 12-min resampled measurement data (coloured dots) and modelled EMAC data (gray squares) for RF17 during CAFE Pacific. The lines represent the medians.

almost flat profile of acetone around 500 ppt measured by the PTR-MS instrument. In contrast, acetaldehyde simulations are two orders of magnitude (approx. factor 50) lower than measurements from the GC-MS instrument. The EMAC acetaldehyde is highest at 4 km altitude around 40 ppt and decreases with increasing altitude to less than 20 ppt. The medians of measured acetaldehyde varies from around 230 ppt at low altitudes to 70 ppt at high altitudes. Given the LOD of the GC-MS between 30-90 ppt, the instrument would not be able to resolve the low acetaldehyde data simulated with EMAC. Looking at the NO_x profiles, EMAC fits well to the NO observations below 8 km, where basically

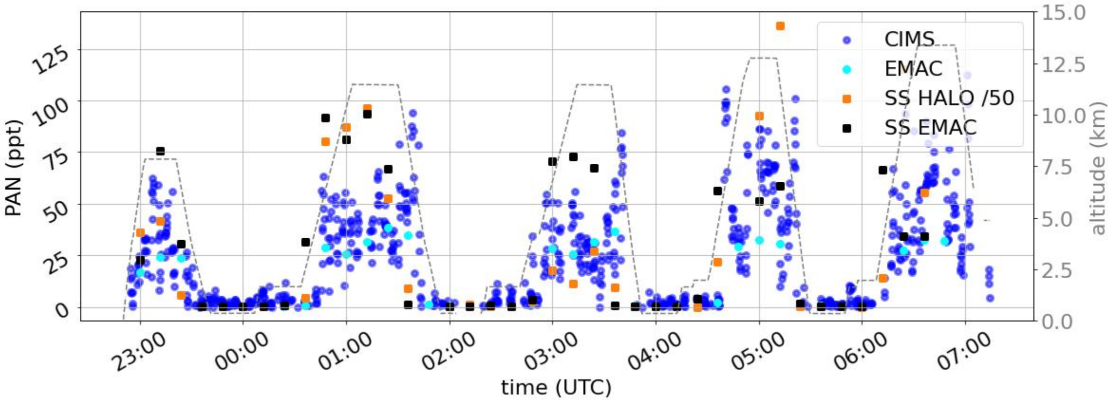

Figure 6.5.4: Measured PAN (blue dots) and simulated PAN by EMAC (cyan dots) along the flight track of RF17 on 14th February 2024 during CAFE Pacific. Squares indicate calculated steady-state concentrations for PAN based on measurement data aboard HALO (orange) and EMAC data (black). Note that the data from HALO instruments is divided by a factor of 50 to fit the scale.

no NO is present. Above 8 km altitude, EMAC substantially overestimates NO by a factor of 4 at 8 km altituden up to a factor of about 60 at 14 km altitude. Consequently, EMAC also overestimates NO_2 above 11 km altitude. The strong enhancement of NO_2 PSS between 3-4 km altitude is not seen in the EMAC data and may be a result of a sampled local pollution plumes.

6.5.5 *Steady-state PAN along the flight track of RF17*

As seen in Figure 6.5.4, on 14th of February during RF17, measured PAN levels were between 0 and approximately 100 ppt. At the low flight legs above the ocean below 1 km altitude, PAN signals were below the detection limit of the CIMS, indicating the absence of PAN, which is expected due to its short thermal lifetime in the boundary layer. Maximum PAN appears around 8 km altitude. In general, the EMAC model (cyan dots) agrees well with the measured PAN (blue dots in Figure 6.5.4). Since the model has time steps of 12 min, shorter features of PAN enhancements cannot be represented by the model. However, the model results fit to the lower limit of PAN enhancements.

In Figure 6.5.4, the steady-state concentration from the HALO data set is divided by a factor of 50 (orange squares) to be comparable to the PAN measurements (blue points) and the results of the steady-state calculation based on the EMAC data set (black squares). The factor 50 represents approximately the difference in acetaldehyde data between EMAC and GC-MS measurements.

It is observed that the steady-state results of the HALO data set qualitatively follows the PAN measurements even though it is quantitatively off by more then the factor 50. This substantial difference is not understandable with the current knowledge of photochemical production of PAN from acetaldehyde. That means that the acetaldehyde measurements from the GC-MS and the PAN measurements from CIMS are not compatible which is discussed in detail in Section 7.7.

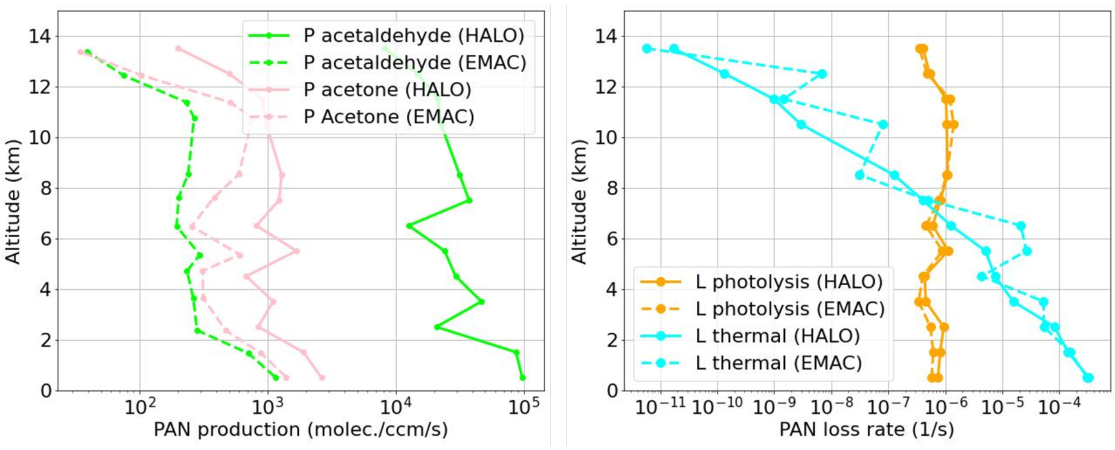

Figure 6.5.5: Vertical profiles of production terms (left panel) and loss terms (right panel) of PAN, calculated with the simplified chemical reaction scheme for steady-state calculations for RF17 during CAFE Pacific, based on measurement data from instruments aboard HALO (solid lines) and model simulations by EMAC (dashed lines).

The steady-state concentration of PAN calculated based on EMAC data is much closer to the PAN measurements, but it still overestimates the measured PAN levels at altitudes higher than 5 km. This means the expectations from in-situ production of PAN via acetone and acetaldehyde are higher than the observation indicating non-steady-state conditions.

This is also underlined by the fact that the steady-state results based on EMAC data of just the two precursors acetone and acetaldehyde exceeds the EMAC PAN simulation also by more than factor of 3 at mid and high altitudes. This suggests that the steady-state assumption might not applicable to long-lived trace such as PAN in the mid- and upper troposphere, which are subject to both vertical and horizontal transport.

6.5.6 *Production and loss terms of PAN in RF17*

The contributions of the different two production terms (left panel) and loss terms (right panel) of PAN included in the steady-state scheme are depicted in Figure 6.5.5.

The production terms depicted in Figure 6.5.5 result from the photolysis of acetone (pink) and the oxidation of acetaldehyde (lime) based on measured (solid lines) and modelled (dashed lines) data. Note that the model includes a number of other sources of PA-radical precursors such has MGLY or other isoprene oxidation products which are not considered in this steady-state analysis.

The relative contribution of acetone and acetaldehyde to PAN production is quite different between the HALO and the EMAC data set: Due to the high levels of acetaldehyde provided by the GC-MS instrument, the production terms for the HALO data set are entirely dominated by acetaldehyde. In contrast, the production derived from the EMAC data set is slightly dominated by acetone at all altitudes (pink dashed line) compared to acetaldehyde oxidation (lime dashed line).

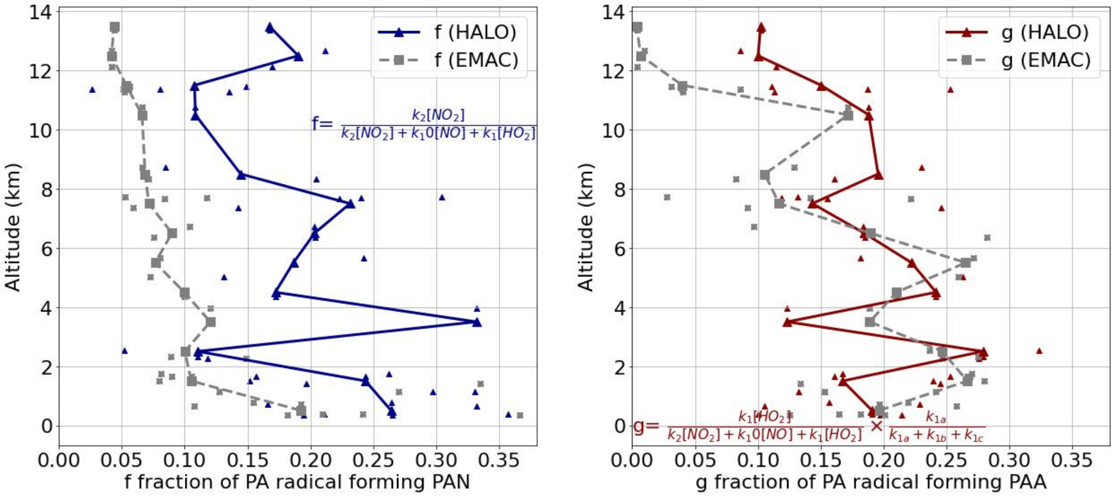

Figure 6.5.6: Median vertical profiles of the fraction f (left) and g (right) of the PA radical forming PAN (blue) or PAA (red), respectively, calculated based on measurement data (solid lines) and model EMAC data (gray dashed lines) in RF17 during CAFE Pacific.

The difference in the loss terms between both data sets is much less significant and is comparable for the photolysis loss as well as for the thermal loss. The less smooth shape of EMAC thermal loss is an effect of the 12 min coarse data.

As seen in the right panel in Figure 6.5.5, the loss of PAN is dominated by thermal decomposition until an altitude of approximately 7 km. At this altitude, both loss terms, photolysis and thermal decomposition, are around $1e^{-6}1/s$ leading to a total atmospheric lifetime of PAN around 6 days. At low altitudes, PAN rapidly decomposes thermally. At high altitudes, the atmospheric lifetime is determined by the photolysis rate and is around 1-2 month at 14 km altitude.

6.5.7 *Fractions of PAN and PAA formation from the PA-radical in RF17*

The formation of PAN and PAA exclusively happens via the reaction of the PA-radical ($CH_3C(O)O_2$) with either NO_2 or HO_2 (Atkinson et al., 2006). The fraction of PA forming PAN or PAA crucially depends on the availability of NO_2 and HO_2 and their ratio to the major competing loss reaction with NO (see Section 3.8). In the simple reaction scheme used for the steady-state calculations, this fraction is denoted as f (Equation 34) for PAN and g (Equation 40) for PAA.

The median vertical profile of f and g is shown in Figure 6.5.6 including the definition of f (Equation 34) and g (Equation 40) in the respective panels. The fractions f and g were calculated using either EMAC data for NO, NO_2 and HO_2 or a mixture of measurement data (labeled HALO) for NO and NO_2 and EMAC simulation of HO_2 as the HALO-HO_2 data are not yet available.

The fraction f of PA forming PAN during RF17 generally decreases with altitude except for the enhancement around 4 km in the HALO measurement data set caused by the peak in NO_2 (left panel in Figure 6.5.6). At low altitudes, as much as 20 % (25 %) of PA is converted into PAN for the EMAC (HALO) data set because of the availability of NO_2.

However, at these altitudes PAN is thermally not stable and the high f fraction will not lead to an increase in PAN concentration. At around 14 km altitude, where PAN is much more long-lived, less than 5 % of the PA leads to PAN formation according to the EMAC data set. In contrast, f is still around 5-20 % when calculating with measurement based NO_x because of lower NO concentrations favouring PAN production over losses of the PA radical to NO. When using measurement data from HALO instruments, the derived median fraction f is between 1.5-4.5 times higher than the f from EMAC data. The fraction f not only affects the production rate of PAN but it also impacts the loss terms, which are modified by (1-f) (see Equation 37) to account for the reformation of PAN from the PA-radical. Since f becomes smaller at high altitudes, the term 1-f gets closer to 1 which means recombination of PAN is less important there compared to low altitudes.

As seen in the right panel of Figure 6.5.6, the fraction g of PA forming PAA is in the range of 5-25 % but decreases less steeply with altitude. The deviation between the measurement and model data set are negligible below 8 km altitude. At high altitudes, g is close to 0 according to the EMAC data set, while with the low measured NO g is still around 10 %.

The low fractions of both, f an g, in the UT show that most of the PA-radical neither forms PAN nor PAA. The major loss of the PA-radical in the UT is most likely NO, which forms CH_3 rapidly oxidising to CH_3O_2. Reactions with RO_2 may also play a role and also the the competing reactions with HO_2 forming $CH_3C(O)OH$ (Reaction 32b) and CH_3O_2 (Reaction 32c). The fraction α, which represents the fraction of the reaction of PA with HO_2 forming PAA, decreases from 38 to 24 % from the low to the high altitudes. Hence, the majority of the PA reactions lead to the formation of methylperoxy radicals and acetic acid.

The ratio between f and g - which is the same as $NO_2/HO_2 \times \alpha$ - is depicted in Figure 6.5.7 for the example flight RF17 for measured (HALO) and modelled (EMAC) data. When relying on measured NO_x data, the ratio f/g varies around 1 and is in average 1.2 indicating a slight preference for PAN. In contrast, the f/g fraction from purely EMAC data has a clear preference for PAA below 11 km altitude with a ratio of around 0.5. In the highest altitude, EMAC data leads to a value of 12 for f/g due to the high modelled NO_2 and low modelled HO_2 in theses altitudes. The differences in f and g between measurements and model result from differences in NO_x because in both data sets HO_x data from EMAC was used. As shown in Figure 6.5.3, EMAC simulations underestimated NO_2 and overestimated NO compared to measurements resulting in lower f and g. The analysis of f and g showed how critical the relation between HO_x and NO_x data are for the formation of PAN and PAA and highlights the importance of an accurate model representation of NO. The lightning parametrization in the model is a probable cause for the overestimation of NO in the UT is discussed in Section 6.7.

6.5.8 *Steady-state calculation of PAN and PAA via the modelled PA-radical for RF17*

Since EMAC also provides model concentrations of the PA-radical, the production rate of PAN can be calculated directly via PA and its reaction with NO_2 instead of its pre-

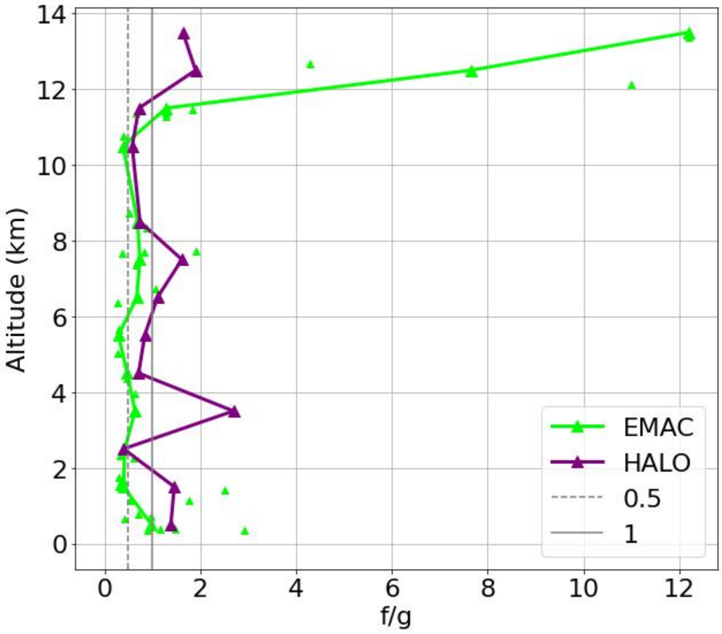

Figure 6.5.7: Ratio between f/g factors in RF17 during CAFE Pacific defining the ratio between PAN and PAA production based on measurement data (purple) and EMAC model data (lime).

cursors acetone and acetaldehyde as described in Section 3.8.3. The calculation directly via the PA-radical can be used as a test of consistency for the model. The production terms of PAN and PAA are simply calculated based on the concentration of PA and NO_2 and HO_2, respectively, and the corresponding reaction coefficient (Equation 46 and Equation 47). For the calculation, the same loss terms as in the steady-state calculation via acetone and acetaldehyde are used because they are only depending on photolysis frequencies and thermal decay.

The resulting vertical profile of steady-state PAN calculated via the model PA concentration is depicted in the left panel in Figure 6.5.8 (gray squares). The calculation via PA exceeds measured PAN (blue points in left panel) and modelled PAN by EMAC (light blue points) by approximately a factor of 3-5 in mid and high altitudes. This discrepancy demonstrates that a simple chemical steady-state assumption is not sufficient to explain the vertical distribution of PAN, because it neglects vertical and horizontal mixing as well as the complex organic chemistry associated with the PA radical. Theses processes are included in global-chemical transport models like EMAC, which provide a more accurate representation of the PAN profile.

6.5.9 *Role of RO2 in as a loss of PA-radical in RF17*

The equation for the factor f (Equation 34) neglects the fact that the PA radical may also react with other peroxy radicals (RO_2) apart from HO_2. RO_2 are formed from OH initiated oxidation of VOCs and play an important role for the oxidation processes in the atmosphere (Atkinson and Arey, 2003).

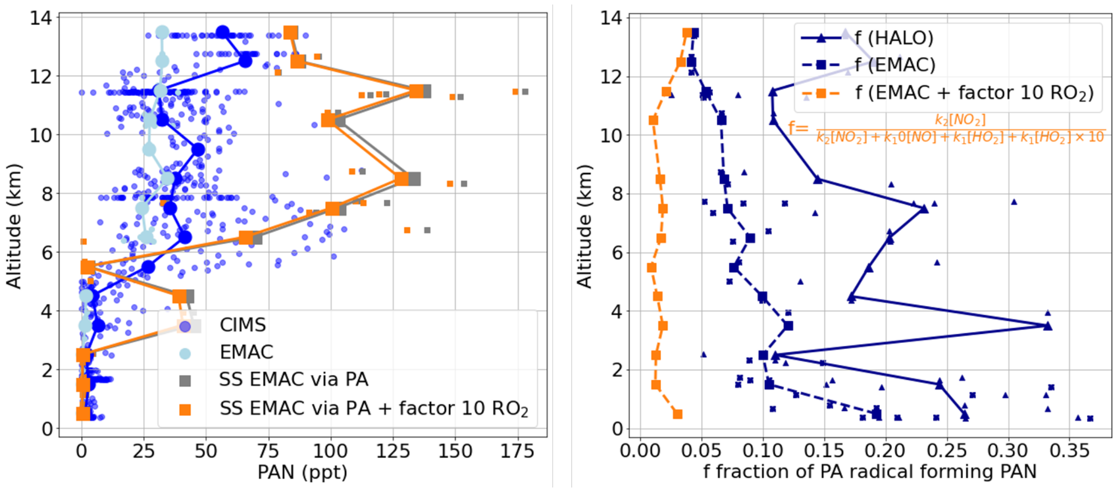

Figure 6.5.8: Left panel: Median vertical profile of PAN calculated in steady-state directly via the concentration of the PA-radical given by EMAC (gray squares) with a f-factor neglecting RO_2 (dark blue dashed line in the right panel) compared to measured PAN by CIMS (blue dots) during RF17 in CAFE Pacific. The orange line represents the result of the calculation via PA radical with a modified f-factor including an additional term for losses of PA by reactions with RO_2 shown in the right panel (orange dashed line).

Since EMAC includes a multitude of RO_2 reactions with PA at corresponding reaction rates, the extraction of the sum of RO_2 and an average reaction rate is not simple. To estimate the possible impact of the neglected RO_2 reactions in the example of RF17, another term in the denominator of f is added which is proportional to the reaction with HO_2:

$$f = \frac{k31[NO_2]}{k31[NO_2] + k32[HO_2] + k53[NO] + k32[HO_2] \times factor_{RO_2}} \tag{93}$$

The orange curve in the left panel in Figure 6.5.8 shows the resulting steady-state PAN profile assuming a factor ten higher PA loss with RO_2 than with HO_2. This increased PA loss does only change the resulting steady-state concentration of PAN by a few percent, because f is already very small in the upper and lower troposphere. The right panel in Figure 6.5.8 shows that f in the model is around 7 %, at 8 km (blue dashed line). The additional RO_2-losses decreased f to around 1 % at this altitude (orange dashed line). The factor f is only included in the loss terms in the calculation directly via the PA-radical, which becomes then close to 1 and is hence negligible. Therefore, even an infinitely high RO_2 contribution can not explain the factor 3-5 difference to the model PAN of EMAC. Hence, the major difference must result from vertical transport and also horizontal transport of air masses with different chemical histories at different altitudes.

6.6 ROLE OF CONVECTION DURING CAFE PACIFIC

Convective vertical mixing is a key process in understanding and modeling the distribution of atmospheric species due to transport of precursors, energy and moisture changing the chemical reactivity and sink processes. Specifically in the tropics, convection plays a significant role in transporting substantial amounts of VOC between the boundary layer, middle and upper troposphere (Bardakov et al., 2022). Lelieveld and Crutzen (1994) estimated that convective updrafts in thunderstorms impact the O_3 lifetime significantly and lead to a net 20 % reduction in total tropospheric ozone. For shorter lived compounds, this difference may even reach up to 100 % (Tost et al., 2010). Without convection at clear sky conditions, vertical transport from surface to the top of the troposphere takes weeks in contrast to hours due to convective transport in form of cumulus clouds (Ouwersloot et al., 2015).

However, accurately representing this process in global models remains a challenge. Convective clouds are too small scale to be resolved in models and need to be parameterised, which is associated with high uncertainty (Arakawa, 2004; Tost et al., 2010). In the global chemical-transport EMAC model, convection is parameterized with CONVECT[32] by sub-grid processes in grid boxes of approximately 200 km × 200 km.

Since the mass exchange rate due to convection is difficult to extract from the model, the average vertical updraft speed per grid-cell derived from the EMAC output is used to roughly estimate the strength of convection compared to calculated in-situ production rates and losses.

For example, a single convective system may have dimensions such as 20 km × 20 km, which is a factor 100 smaller than a grid-cell in EMAC. Hence, the local velocity could be a factor 100 higher than the average updraft velocity of a grid cell. As seen in Figure A.0.19 in the Appendix, the maximum deep convective updraft velocity during January 2023 reached in both grid cells, above ATTO and above Cairns, was approximately 0.3 m/s at 6 km altitude. This suggests that a single convection cell may have speeds around 30 m/s, allowing an air parcel to rise to 6 km altitude within around 3-4 min (Personal communication with Matthias Kohl).

In contrast, the time it takes to establish a steady-state can be approximated by the loss rate constant and the first order production rate). In the case of PAN, this duration is estimated via Equation 94 for altitudes where thermal decay dominates the dominant loss of PAN.

$$t_{SS} \approx \frac{1}{k50 + k31[NO_2]} \tag{94}$$

Typical reaction coefficients, retrieved from the steady-state calculation for RF17 during CAFE Pacific, at 6 km altitudes are around $1.0 \times 10^{-11} \mathrm{cm}^3 \mathrm{molec.}^{-1} \mathrm{s}^{-1}$ for k31 and $1.5 \times 10^{-6} 1/\mathrm{s}$ for k50. With typical NO_2 concentrations of around $2.3 \times 10^{8} \mathrm{molec.cm}^{-3}$ at this altitude, this results in an approximate time to establish a steady state of about 7 min.

Hence, vertical mixing due to convection can be much faster than in-situ production in mid-tropospheric altitudes during CAFE Pacific.

Convection processes are suggested to significantly contribute to the flattening of the PAN and PAA vertical profiles compared to the expected shape from a steady-state calculations via the modelled PA- radical during CAFE Pacific.

---

[32] https://envmodel.ipa.uni-mainz.de/submodels-convect/, last access: 14th May 2025.

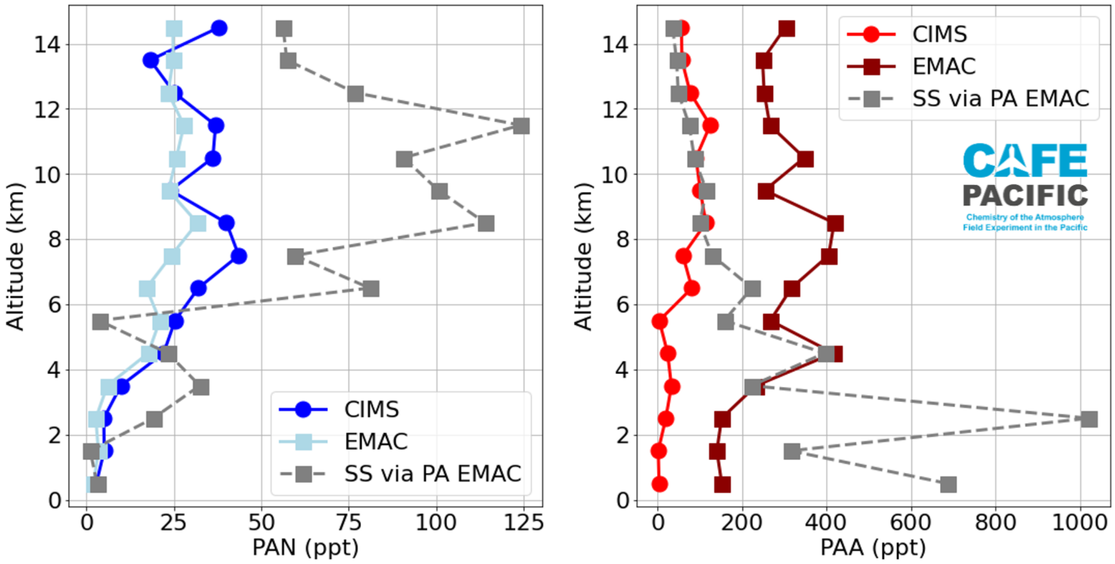

Figure 6.6.1: Vertical median profiles of calculated steady-state (SS) mixing ratios of PAN (left panel) and PAA (right panel) via EMAC PA (gray dashed lines) for all flights during CAFE Pacific, compared to the observations by CIMS (solid lines with circles) and modelled results from EMAC (solid lines with squares).

It was seen in the example of RF17 (left panel in Figure 6.5.8), that the calculated steady-state concentration of PAN via PA PAN (gray) has a pronounced maximum between 8-12 km altitude, while the measured and modelled profile is rather flat in this altitude range, only slightly increasing towards higher altitudes.

The same observation is made, when applying the steady-state calculations to the EMAC data set including all flights during CAFE Pacific, as depicted in Figure 6.6.1.

Modelled median PAN (light blue) of all flight of CAFE Pacific is more than a factor 3 lower than calculated steady-state PAN via PA (gray dashed line in the left panel of Figure 6.6.1) in the mid- and upper altitude range.

In the case of PAN, vertical updraft from the boundary layer would lead to a dilution of PAN levels in the mid- and upper troposphere. This is because almost no PAN is present below 2 km altitude due to the short thermal lifetime of PAN in the tropical boundary layer of less than 1h (see Figure 6.6.2). Since the mixing of PAN-free air from the boundary layer with PAN-richer air in the mid- and upper tropospheric is faster than it takes to establish the steady-state between in-situ production via the organic precursors and the photolysis dominated loss rates, dilution of PAN mixing ratio at these altitudes is expected.

On the other hand, steady-state calculation of PAA via model PA (dashed gray line in the right panel of Figure 6.6.1) leads to comparable PAA levels to observed median PAA (red) in the upper troposphere, but exceeds the observation by more than a factor 200 in low altitudes <3 km. While the profile of the steady-state PAA steeply decreases with altitude, the median measured and modelled PAA profile increase with altitude until 4 km and is rather flat above.

In contrast, the lifetime of PAA in the boundary layer due to photolysis is almost two weeks (see Figure 6.6.2). Therefore, the vertical transport of PAA-rich air in the boundary would lead to an increase of PAA levels in mid- and upper troposphere.

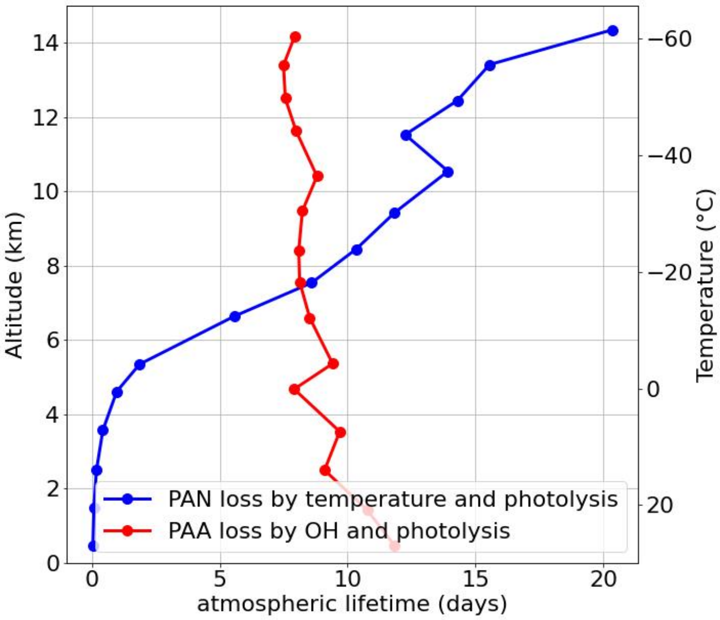

Figure 6.6.2: Vertical profiles of median lifetimes of PAN and PAA during CAFE Pacific, calculated from the loss rates in the steady-state scheme based on measurement data.

Since the shape of EMAC modelled PAN and PAA is in good agreement to the observations, it is suggested that the vertical profiles of PAN and PAA during CAFE Pacific are controlled by vertical mixing rather than chemistry in the UT but also by altitude dependent chemistry in the source regions and along back-trajectories.

A similar plot to Figure 6.6.1 for all flights during CAFE Brazil is depicted in Figure A.0.16 in the Appendix showing that the same discrepancy between model PAN and PAA and corresponding steady-state calculations via model PA is also prevalent for the EMAC simulations above the Amazon rainforest. Since production and loss rates for PAN and PAA were in similar orders of magnitude during CAFE Brazil than those of CAFE Pacific, this indicates, that convection plays also a significant role on the vertical distribution of sampled PAN and PAA during CAFE Brazil and a chemical steady-state assumption for PAN and PAA may not be applicable.

6.7 ROLE OF LIGHTNING NOX DURING CAFE PACIFIC

NO_x from lightning is one of the largest natural global atmospheric sources as the high temperatures in lightning strikes can break the triple bond of unreactive nitrogen (N_2) and produces NO in the atmosphere together with molecular oxygen (Galloway et al., 2004).

NO quickly reacts with O_3 in the atmosphere and forms NO_2 leading to a steady-state when photolysis frequencies of NO_2 are high. In the tropics, where most lightning occurs, lightning is clearly the dominant source of NO_x in the upper troposphere compared to aircraft emissions, stratospheric intrusions or convective uplift from the boundary layer (Lamarque et al., 1996), but still its quantification is highly uncertain. Estimates for produced NO molecules per flash vary between 2-40 $\times 10^{35}$ (Schumann and Huntrieser, 2007). Beirle, Huntrieser, and Wagner (2010) derived NO_2 column densities from satellite observations above active thunderstorms based on the analysis of 1800 flash events per hour which were below expected literature NO_2 column densities by more than one order of magnitude.

The precise representation of lightning in deep convective transport in models and its influence on the air composition in the tropical UT is a subject of scientific research (Barret et al., 2010).

The lightning parametrization used in the EMAC model is based on Grewe et al. (2001) and Kurz and Grewe (2002). Tost, Jöckel, and Lelieveld (2007) evaluated the EMAC model towards lightning observation and NO_x production comparing the two different parametrisation schemes based on Grewe et al. (2001) and Price and Rind (1992) and found a wide range of spatial and temporal variability in both cases. Even though satellite observations of flashes were very accurate, the NO production per flash is not a constant but among other dependent on flash strength, extension, flash type and branching (Tost, Jöckel, and Lelieveld, 2007).

The comparison of modelled NO by EMAC to measured NO using the NOAH instrument during CAFE Africa showed in general a good agreement, with median $NO_{EMAC}/NO_{NOAH} = 0.97$, but had substantial deviations in single flights above 10 km altitude due to inaccurate representation of lightning NO (Tadic et al., 2021). The importance of lightning NO during CAFE Africa and CAFE Brazil was also highlighted by Nussbaumer et al. (2024), who compared the measured NO with modelled NO from EMAC with and without lightning emissions. The location of flight tracks during CAFE Africa coincided with the location of the ITCZ and hence maximum deep convection and lightning activity leading to 40 % of the data points being impacted by lightning (Nussbaumer et al., 2024).

During CAFE Brazil flight tracks were a little further away from the ITCZ but still leading to 20 % of measurements being impacted by lightning (Nussbaumer et al., 2024).

During CAFE Pacific, lightning NO was only found in Northern Australia while in all other target regions lightning was absent (Nussbaumer et al., 2025).

Comparing the vertical median profiles of modelled NO from EMAC and measured NO from the NOAH instrument for all flights in February 2024 during CAFE Pacific, shows that the model overestimates NO substantially in mid and upper troposphere (left panel in Figure 6.7.1). Generally, measured NO was low during CAFE Pacific and measurements were often below the 1 σ detection limit of NOAH of approx. 5 ppt. Data points below the LOD were originally assigned 5 ppt (1 σ) as an upper limit. However, 5 ppt would lead to a significant amount of NO_2 which was derived via the PSS calculation from NO, Ozone and $j(NO_2)$. Therefore, the value for data below the LOD was reduced to 1 ppt for a more realistic calculation of NO_2. As seen in the right panel in Figure 6.7.1, the NO_2 vertical median profiles of EMAC and the PSS NO_2 based on measurement data with reduced values below the detection limit agree well except at the highest altitude above 14 km. Below 14 km the profiles are almost constant between 9-14 ppt for EMAC and 2-17 ppt for measurement based NO_2. At low altitudes below

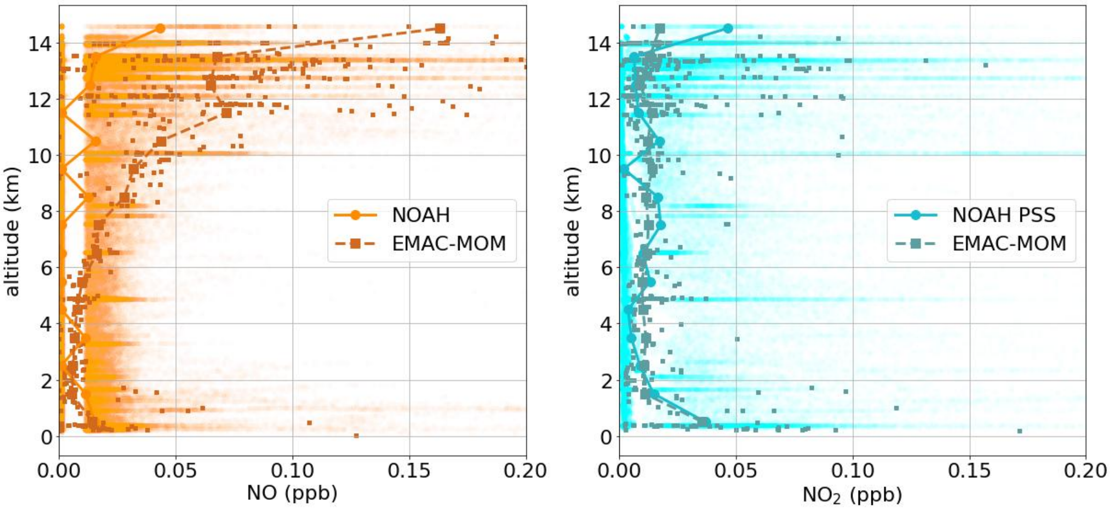

Figure 6.7.1: Vertical profiles of NO (left panel) and NO_2 (right panel) of measurement data (medians as solid lines) and EMAC simulations (medians as dashed lines) for all flights in February during CAFE Pacific. Measured NO below the detection limit of the NOAH instrument of approx. 5 ppt (1σ) was set to 1 ppt to not induce false signals on NO_2 which was derived with a photostationary state (PSS) assumption.

2 km median NO_2 of 35 ppt is reached in both data sets.

The discrepancy between measured and modelled NO seen in Figure 6.7.1 during CAFE Pacific, was already addressed by Nussbaumer et al. (2025), who found that the EMAC model was able to represent NO from lightning above the continent, but substantially overestimated maritime lightning NO especially in the Warm Pool region. The non-electrified deep convection taking place in the Warm Pool region leading to low NO and hence low ozone in the UT was not represented in EMAC (Nussbaumer et al., 2025). Nussbaumer et al. (2025) estimated the model overestimation of OH resulting from the overestimation of NO in the remote regions by a factor of 3-4, which is also crucial for the formation of PAN and its precursors.

In the case of RF17, the model overestimation of NO was shown in Figure 6.5.3 and can also be explained by the difficulties of modeling lightning NO. Calculated back-trajectories with HYSPLIT for RF17 showed that the air masses measured at high and mid altitudes traveled above the Northern Australia (see Figure A.0.12 in the Appendix) where high lightning activity took place Nussbaumer et al. (2025).

With respect to the model discrepancies to NO, it is surprising that EMAC simulations of PAN are fitting so well to measured PAN and also the results of the steady-state PAN with EMAC based precursor data in the showcase RF17. To investigate the sensitivity of the steady-state PAN to NO_x, the model NO_x in the steady-state calculation was replaced by measured NO_x.

Figure 6.7.2 shows the resulting steady-state concentration of model data with measured NO_x (olive) compared to steady-state purely based on model data (black). Measured (blue) and modelled PAN (light blue) are also depicted as reference. Replacing

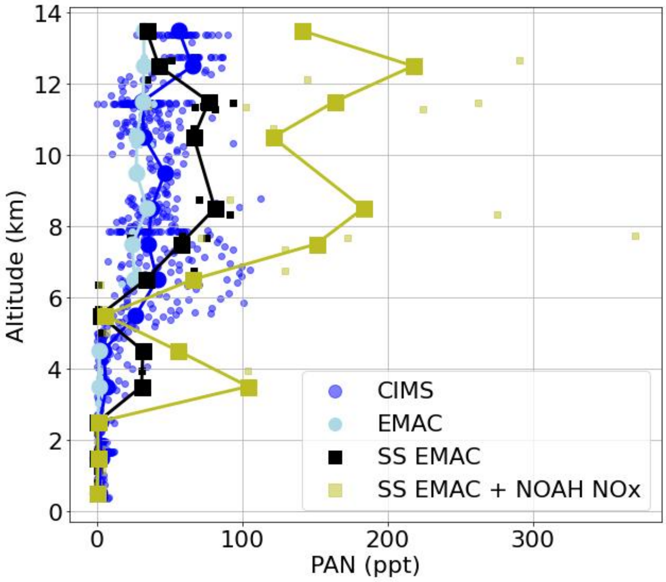

Figure 6.7.2: Vertical profiles resulting from steady-state (SS) calculations for PAN during RF17 when using data from the EMAC model (black) compared to measured (blue) and modelled PAN (lightblue). The olive coloured profile was calculated by replacing the modelled NO_x by measured NO from the NOAH instrument and the derived NO_2 from the PSS with ozone.

the modelled NO_x from EMAC in our steady-state calculation by NO_x based on measurement data, leads to about a factor 2 higher PAN levels in mid- and higher altitudes than with model NO_x because of the slower losses of the PA-radical to NO even though less NO_2 is available.

Despite the high uncertainty involved on the "measured" NO_2, which was derived from the Leighton ratio without considering peroxy radical reactions with NO, these calculations illustrate the high sensitivity of PAN levels to NO_x levels. Given the discrepancy of model NO to measured NO in the mid- and upper troposphere, it is possible that EMAC predicts PAN values right for erroneous reason.

6.8 COMPARISON OF PAN-TO-PAA RATIO TO THE EMAC MODEL

As already mentioned in Section 5.6.2, the relationship between PAN and PAA indicates whether a PA-radical forms a PAN or PAA molecule. The PAN-to-PAA ratio can be used to evaluate the consistency of global chemical models, as it is in principle predicated on the ratio between NO_2 and HO_2.

Figure 6.8.1 shows the ratio between modelled and measured PAN (blue) and PAA (red) in the median vertical profile. The ratio of PAN is slightly below 1 below 9 km altitude and almost 1 above 9 km altitude. Hence, the EMAC simulation only slightly underestimates the measured PAN, which was also seen in the example of RF17.
In contrast, PAA is overestimated by the model by a median factor of 3-4.5 at mid altitudes and up to a factor 6 at low and high altitudes.

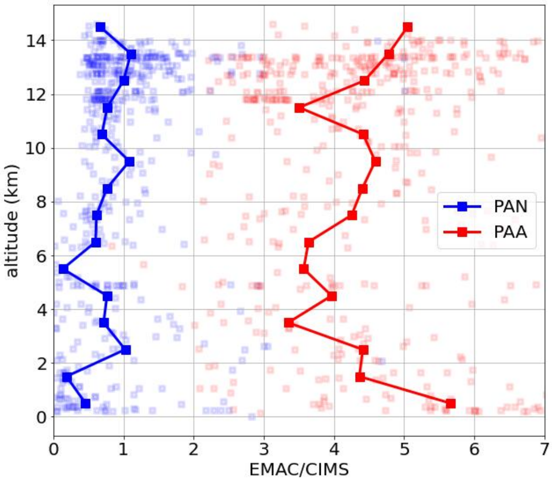

Figure 6.8.1: Vertical median profiles of the ratio between EMAC modelled and CIMS measured PAN (blue) and PAA (red) for all analysed flights during CAFE Pacific.

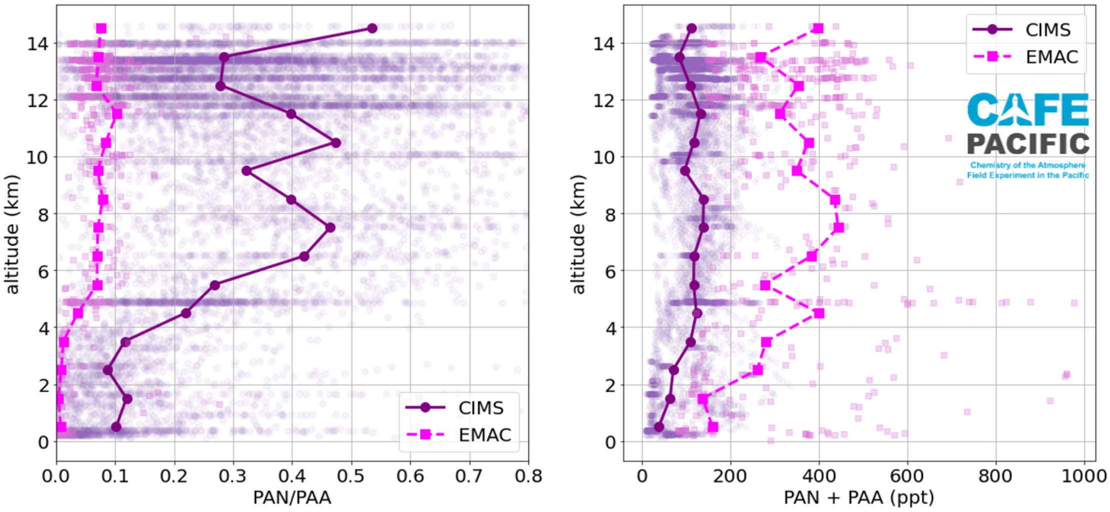

Figure 6.8.2: PAN-to-PAA ratio (left panel) and sum of PAN and PAA (right panel) for measured data by CIMS (purple circles) and modelled data by EMAC (magenta squares). The lines represent the medians.

Figure 6.8.2 compares the ratio (left panel) and the sum (right panel) between measured and model PAN and PAA for all analysed flights during CAFE Pacific.
The left panel in Figure 6.8.2 shows the resulting PAN-to-PAA ratio from Figure 6.8.1. As a result of the strong overestimation of PAA in the model, the PAN-PAA-ratio of the model (purple) is around a factor of 5-6 lower at mid- and high altitudes compared to the observed PAN-to-PAA ratio (magenta).
As can be seen in the right panel in Figure 6.8.2, the sum of PAN and PAN is a factor of 2-4 higher in the model compared to the observations.

This indicates, that EMAC's substantial overestimation of PAA is not only attributable to a wrong partitioning between PAN and PAA based on a wrong ratio between NO_2 to HO_2, but also to the total amount of the available PA-radicals i.e. most likely due to an overestimation of PA production.
The ratio between f and g as a measure of the partitioning between PAN and PAA formation was discussed in the example of RF17 (Section 6.5.7) and showed that, based on model data, PAA formation dominates PAN formation by roughly a factor 2 almost up to 11 km altitude. In addition, convective updraft of warm, PAN-free but VOC- and PAA-rich air from the boundary layer to the mid- and high altitudes would shift the PAN-to-PAA even further in favour of PAA.

This discrepancy between model and measured PAN and PAA ratio is not only an issue in EMAC but was also observed in other global chemical transport models. Travis et al. (2020) simulated the ATom observations above the remote southern Pacific with the GEOS-Chem global chemical transport model and reported substantial differences in PAA model predictions even though the results for PAN were comparable. In contrast to EMAC, GEOS-Chem slightly overestimated PAN and largely underestimated PAA underlining the difficulty in modeling the partitioning between PAN and PAA.

6.9 SUMMARY OF THE CAFE PACIFIC ANALYSIS

In this chapter, the CIMS measurements of PAN and PAN above the Australian continent and the remote southern tropical Pacific during the CAFE Pacific campaign in January and February 2023 were presented and were shown to be a valuable contribution to the sparse available observational data in the mid- and upper-troposphere in this region, expanding the altitude range of observations up to 14 km. The research flights RF15, RF21 and RF17 were analysed in detail in order to evaluate the role of vertical and horizontal transport, biomass burning and in-situ production of PAN and PAA.

Vertical profiles of PAN and PAA during CAFE Pacific

To summarise the observations made during the CAFE Pacific campaign in January and February 2023, it was noted that the sampled air masses above western Australia and the southern pacific ocean were dominated by PAA compared to PAN by more than a factor of 2. PAN mixing ratios were generally low with a median maximum around 50 ppt between 8-10km altitude. The median profile of PAA median was rather flat around 100 ppt but decreased below 4 km.

The median vertical profiles for PAN and PAA during CAFE Pacific were in agreement with reported measurements in literature except for the decrease of PAA in the low altitudes.

Air mass composition in the north-south transect flight RF15

The vertical distribution of PAN and PAA was analysed for the continental flight RF15 which included three vertical helix patterns. The correlation with other trace gases showed that the composition of the sampled air masses was distinct for different altitude. It was suggested that the measured PAN during RF15 resulted from a mixture of sources on the Australian continent whereas biomass burning seemed to play a minor role compared to in-situ production from biogenic and anthropogenic pollution based on the tracer-tracer correlation.

The role of long-range transport of polluted air from southern Africa via the subtropical jet for air masses sampled south of 30 °S was investigated with the help of HYSPLIT trajectories and NASA's FIRMS fire observations which proposed that transported PAN and PAA resulting from biomass burning in Africa was rather unlikely.

The CAMS forecast used for flight planning was compared to observations of PAN. The CAMS model predictions fitted well with respect to horizontal location of PAN layers but overestimated the magnitude of PAN levels by more than a factor 20.

Sampling the Indo-pacific Warm Pool in RF21

The analysis of RF21 showed the absence of PAN above the Indo-Pacific warm Pool wherefore PAN is probably not a significant source of NO_x in this region. Low PAN and PAA mixing ratios where also observed during the two other maritime flights heading towards the north-east of Cairns (RF13 and RF18). The PAN profile of the three maritime flights was compared to the continental flights RF15 and RF19. PAN was only slightly high in mid- and upper tropospheric altitudes during continental flights compared to the maritime flights but below 4 km altitude PAN was enhanced by about 50 ppt above the continent.

Steady-state calculations for RF17

The role of in-situ production PAN and PAA was investigated in the example of flight RF17 with the help of of steady-state calculations based on measurement data and EMAC model data. These calculations assume acetaldehyde and acetone to be the only precursors of PAN. The results for RF17 pointed out, that measurements of PAN and acetaldehyde were not compatible with respect to expected PAN production from acetaldehyde. The large discrepancy between measured and modelled acetaldehyde around a factor of 50 leads to a similarly large discrepancy in the steady-state calculation of PAN between modelled and measured data sets.

The PAN steady-state concentration derived from model overestimated the observations by a factor of two. The sensitivity of the steady-state PAN to NO_x was demonstrated, thereby showing that overestimation of model NO in the high altitudes led to lower PAN formation at these altitudes.

The production of PA-radical in the steady-state calculation with model data was dominated by acetone compared to acetaldehyde. The difference to steady-state calculation directly via the model PA showed that acetone and acetaldehyde together account for only half of the PA-production in the model.

The steady-state PAN based on the direct calculation from model PA concentrations was a factor of 4 higher than observations. The discrepancy was discussed with respect to the role of RO_2 and convection. The neglect of loss reactions of the PA-radical with RO_2 in the simple steady-state scheme could only account for a difference of maximally around 10 % due to the low fraction of PA forming PAN or PAA. It was hypothesised that vertical transport in the form of convection would be dominant over in-situ production, and that this would consequently define the PAN profile during CAFE Pacific.

Comparison to the EMAC model

The comparison of PAN and PAA measured by CIMS to simulations of the global 3D-model EMAC for all flights during CAFE Pacific showed generally good agreement to the PAN observations but overestimated PAA mixing ratios by a factor 4-6. The major differences between model and measurements in the PAN-to-PAA ratio highlights the complexity and challenges in modeling tropospheric chemistry in state-of-the art global models like the EMAC model. In view of the considerable uncertainty surrounding atmospheric acetaldehyde levels and the model discrepancy for the significant reactive precursor NO, it is conceivable that the good model-measurement agreement for PAN may result from a fortunate cancelling of systematic biases.

7

INTER-COMPARISON BETWEEN THE CAFE AIRCRAFT CAMPAIGNS

In this chapter, the two previously presented campaigns CAFE Brazil and CAFE Pacific are compared with each other and with the CAFE Africa campaign, which was the first of the three tropical CAFE aircraft campaigns. Together, these three campaigns provide an comprehensive measurement basis in the tropical, remote areas, see Figure 3.2.1.

This comparison aims to highlight the differences and similarities between the three CAFE campaigns and the characteristics of the sample air masses. The three CAFE campaigns are compared with respect to their vertical profiles of PAN and PAA, the PAN-to-PAA ratio, as well as the significance of PAN as a NO_x reservoir species. The role of fresh biomass burning during the three campaigns is discussed with respect to black carbon measurements, and example flights are shown for each of the three campaigns.

Based on EMAC simulations, the contributions of biogenic PA-radical precursors are compared between CAFE Brazil and CAFE Pacific and set in relation to simulated global averages. In addition, the correlation of PAN with peroxy propionyl nitrate (PPN) is compared between CAFE Brazil and CAFE Pacific to investigate the impact of anthropogenic emissions on the sampled air masses during the campaigns.

7.1 CAFE AFRICA CAMPAIGN DESCRIPTION

The CAFE Africa aircraft campaign was conducted in August and September 2018 above the Atlantic west of the African coast, utilizing the HALO research aircraft with the same instrumental pay load as during CAFE Brazil and CAFE Pacific. A total of 12 scientific measurement flights (FL04-FL15) were performed from Sal, Cape Verde (16.75°N, 22.95°W), excluding test flights and transfer flights. The location of the campaign provided an opportunity to investigate the impact of the ITCZ on the tropospheric physical and chemical processes in this region (Tadic et al., 2021). CIMS was operated by Philip Eger and Raphael Dörich and PAN and PAA data was analyzed by John Crowley. PAN and PAA measurements along the flight tracks are depicted in Figure 7.1.1 where the flights which Crowley et al. (2025) identified as biomass burning impacted are labeled with flight number.

The corresponding vertical profiles of PAN and PAA during CAFE Africa are depicted in Figure 7.1.2.

7.2 VERTICAL PROFILES OF PAN AND PAA DURING ALL CAFE CAMPAIGNS

The median vertical profiles of measured PAN and PAA mixing ratios for all three airborne CAFE campaigns are depicted in Figure 7.2.1.

The observed PAN mixing ratios were highest during CAFE Africa, followed by CAFE Brazil and then CAFE Pacific. Notably, during CAFE Africa, individual PAN data points

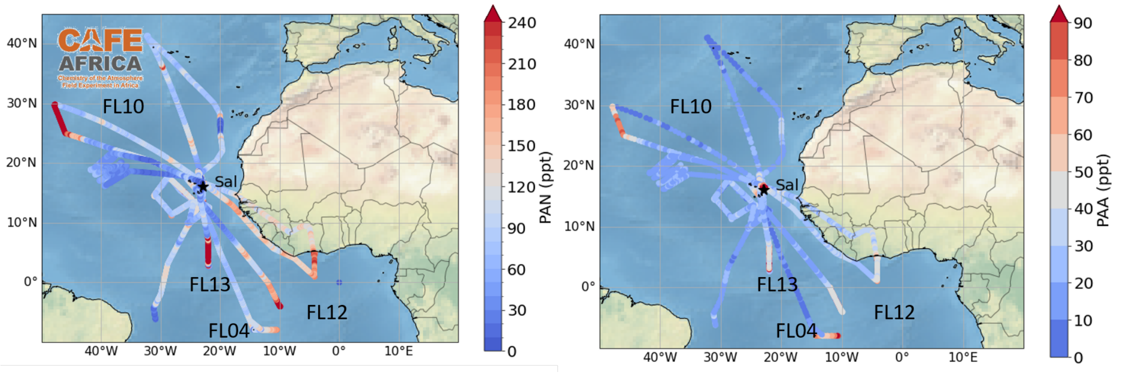

Figure 7.1.1: Measured PAN (left) and PAA (right) mixing ratios along the flight track during the CAFE Africa campaign in August-September 2018 based on Sal, Cape Verde. Data provided by John Crowley. The measurement flights which were clearly affected by biomass burning, according to Crowley et al. (2025), are marked with their flight numbers.

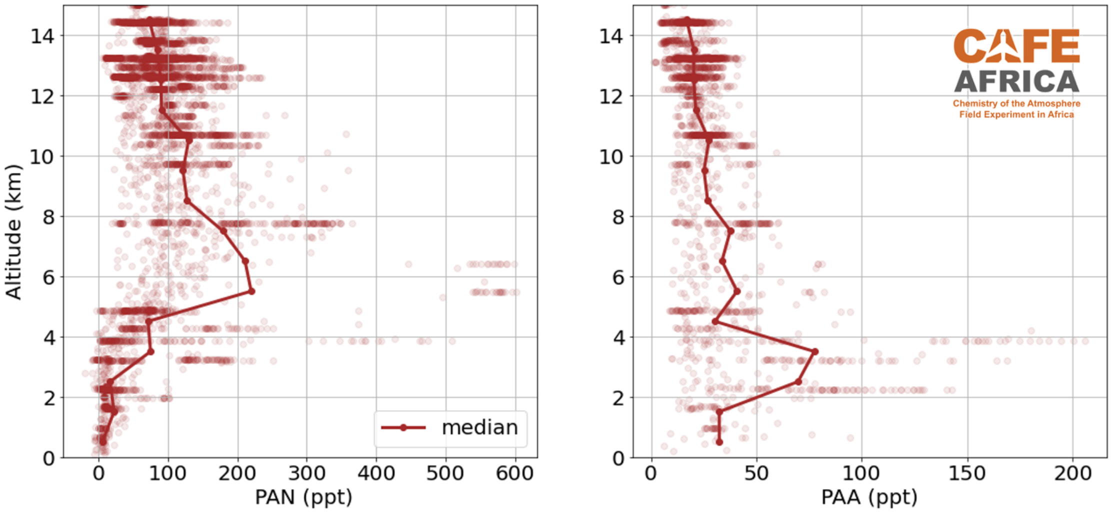

Figure 7.1.2: Measured vertical profiles of PAN (left) and PAA (right) during CAFE Africa. The solid lines denote the medians, points represent individual data points.

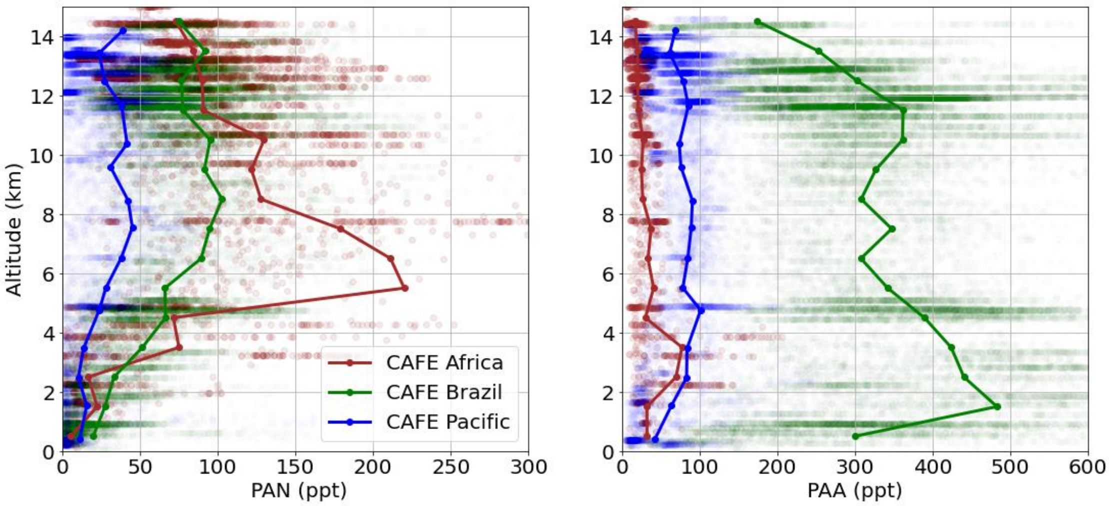

Figure 7.2.1: Measured PAN (left panel) and PAA (right panel) profiles for the three CAFE campaigns CAFE Africa (brown), CAFE Brazil (green), and CAFE Pacific (blue). The solid lines indicate the medians, dots represent individual data points.

reached a maximum of approximately 600 ppt in the mid-troposphere around 6 km. These points were significantly influenced by biomass burning, as previously reported by Crowley et al. (2025), and contributed to the pronounced mid-tropospheric maximum of PAN with a median above 200 ppt.

This mid-tropospheric PAN enhancement is also seen during CAFE Brazil, albeit at approximately two times lower levels. Furthermore, PAN mixing ratios remained elevated until the maximal flight altitude of approximately 14.5 km, which was attributed to in-situ PAN formation from uplifted VOCs and lightning-generated NO_x, as discussed in Chapter 5.

In contrast, air masses sampled during CAFE Pacific were generally much less polluted by PAN compared to the other two CAFE campaigns. Peak PAN values were detected at low altitudes (<2 km) and reached only up to 150 ppt, indicating the presence of local pollution plumes. The vertical profile of CAFE Pacific exhibited a similar shape to that of CAFE Brazil (i.e. low PAN below 8 km altitude, almost constant above) but mixing ratios approximately two times lower.

Generally, the median vertical distribution of observed PAA during the three CAFE campaigns exhibits a relatively flat or slightly decreasing trend with increasing altitude, but the magnitude of the median PAA differs at certain altitudes by more than a factor 5 between the campaigns.

As previously discussed, the major sink of PAA is photolysis, which increases with altitude (see Figure 5.4.7). Consequently, a decreasing trend of PAA with increasing altitude is anticipated. Convection was explicitly targeted during CAFE Brazil and CAFE Pacific, which may contribute to the less steeply decreasing vertical profile as a result of vertical updraft (see Section 6.6).

During CAFE Africa, PAA mixing ratios were generally very low (< 100 ppt) with a clear decreasing trend with altitude. The high PAA mixing ratios observed at 2-4 km

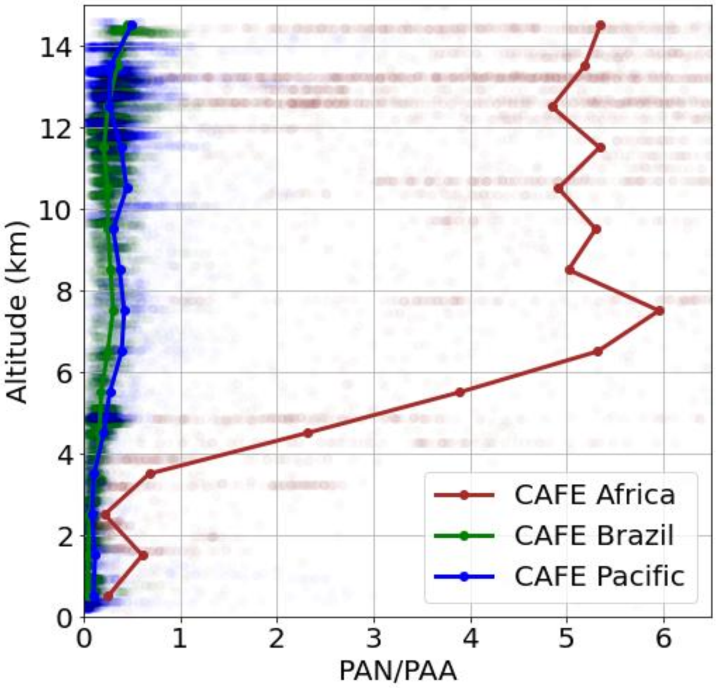

Figure 7.3.1: Measured vertical profiles of PAN/PAA-ratio during all three CAFE campaigns. The solid lines indicate the medians, dots represent individual data points.

altitude may be attributed to the transport of organic-rich air from the continental boundary layer, potentially via biomass burning plumes.
In contrast, the highest levels of PAA were observed during CAFE Brazil, with a median maximum of around 500 ppt at low altitudes above the boundary layer and individual data points exceeding mixing rations above 1 ppb.
PAA during CAFE Pacific was relatively evenly distributed above 4 km altitude, indicating the role of vertical mixing. However, below 4 km altitude, PAA was highly variable in median decreasing towards the ground.

7.3 PAN-TO-PAA RATIO DURING ALL CAFE CAMPAIGNS

As discussed in Section 5.6.2 and in Section 6.8, the partitioning between PAN and PAA gives an indication about the availability of NO_2 and HO_2 since both PAN and PAA are competitively formed via the PA radical depending on the availability of NO_2 and HO_2 respectively. The median vertical profile of PAN-to-PAA ratios for all three CAFE campaigns is depicted in Figure 7.3.1.

During CAFE Africa (brown), PAN dominated over PAA up to a median factor of 6, indicating a significantly higher abundance of NO_x relative to HO_2 as a result of the high impact of biomass burning on the sampled air masses. Crowley et al. (2025) demonstrated that the PAN-to-PAA ratio in biomass-burning plumes changes due to cooling, dilution and chemically aging etc., and is quite variable. At high altitudes, individual data points resulted in PAN-to-PAA ratios even higher than 40 due to the low PAA values, which result from the flights Fl04, Fl10, Fl12 and Fl13 marked in

Figure 7.1.1 during which plumes with highly elevated PAN and BC were observed. Removing these flights from the data set does not significantly change the median PAN-to-PAA ratio (see Figure A.0.18). This indicates that the sampled air was generally mixed with a high load of biomass burning products, as the campaign took place in the middle of the African biomass burning seasons (see Section 7.5.1).

In contrast, during the CAFE Brazil and CAFE Pacific campaigns, PAA was more abundant than PAN. The median PAN-to-PAA ratio was always below one, highlighting the role of biogenic organics driven chemistry in pristine, low-NO_x regions.
VOC induced HO_x-chemistry was found to be especially important during CAFE Brazil, which is expected since tropical forests, notably the Amazonian rainforest, are known to be a significant source of biogenic VOCs (Guenther, 2013). During CAFE Brazil, the PAN-to-PAA ratio was lowest among the three campaigns. The median ratio was close to zero at the lowest altitudes. The mid-tropospheric PAN maximums led to a slight maximum (approximately 0.3) of the PAN-to-PAA ratio between 6-8 km altitude. In high altitudes, the ratio increased again up to almost 0.5 above 14 km.

During CAFE Pacific, the median PAN-to-PAA ratio was similar to that during CAFE Brazil, but with a slightly more pronounced maximum between 6-8 km altitude, with a ratio of approximately 0.4. In addition, variations of the PAN-to-PAA-ratio were significantly higher during CAFE Pacific than during CAFE Brazil, notably in the highest and lowest altitude range, where peak ratios up to 12 were reached. The high variability of the PAN-to-PAA-ratio during CAFE Pacific reflects the diverse mixture of PAN sources during CAFE Pacific.

The comparison of the PAN-to-PAA ratio between the three campaigns revealed significant differences in air mass composition in the probed regions and seasons which was most drastically seen in the differences of PAA levels. Presumably HO_2 from the oxidation of organics dominated over NO_x during CAFE Brazil and CAFE Pacific in comparison to CAFE Africa, where, biomass burning PAN dominated over PAA.

7.4 PAN-TO-NOX RATIO DURING ALL CAFE CAMPAIGNS

The PAN/(PAN+NO_x)-ratio during the three CAFE campaigns was used to investigate the significance of PAN as a reservoir species of NO_x in the tropical troposphere. Figure 7.4.1 depicts the measured median vertical profile of the PAN/(PAN+NO_x)-ratio derived from the three campaigns, including only data measurement data above the instruments LODs for each species. The underlying profiles of NO and NO_2 from the NOAH instrument are depicted in Figure A.0.15 in the Appendix.

As depicted in Figure 7.4.1, the median profiles of the PAN/(PAN+NO_x)-ratio exhibited a maximum at mid-altitudes and decreasing trends towards low and high altitudes across the three campaigns, even though the trends are much more pronounced during CAFE Africa (brown) and CAFE Brazil (green) than during CAFE Pacific (blue).

The decreasing trend of the ratio towards low altitudes can be attributed to the thermal decomposition of PAN to NO_x, resulting in a lower partitioning of PAN in the PAN+NO_x mixture.

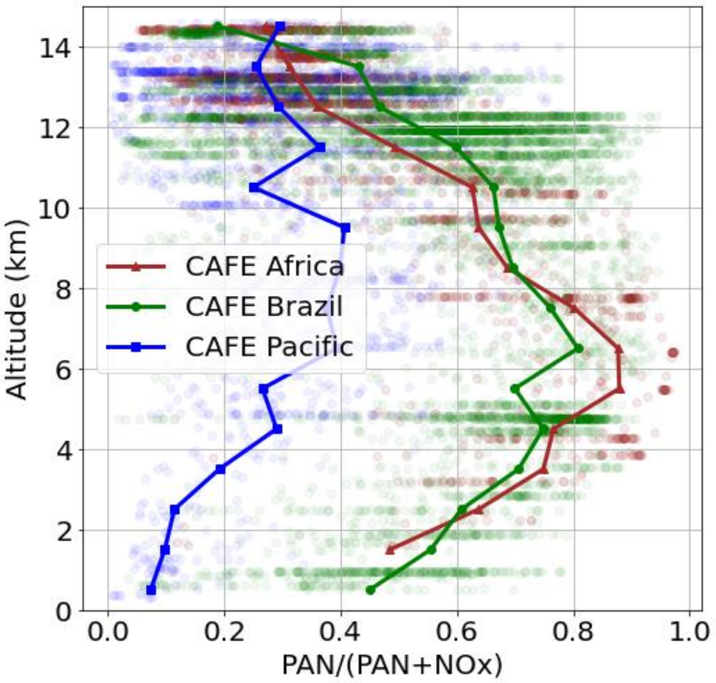

Figure 7.4.1: Vertical profiles of the PAN/(PAN+NO_x) during all three CAFE campaigns. Data below the LODs were excluded. The solid lines indicate the medians, dots represent individual data points.

Conversely, the decrease towards high altitudes, reaching a ratio of approximately 0.3, is not only an effect of the slightly decreasing PAN with altitude (see Figure 7.2.1) but primarily due to an increase in NO_x, especially during CAFE Africa and CAFE Brazil (see Figure A.0.15 in the Appendix). High NO in the UT results most likely from fresh NO_x from lightning, as previously discussed in Section 6.7.

Since lightning NO_x was rarely observed during CAFE Pacific (Nussbaumer et al., 2025), this could explain the less steep decrease of the PAN/(PAN+NO_x)-ratio in the high altitudes during CAFE Pacific compared to the other two CAFE campaigns.

However, the magnitude of the ratio during the CAFE Pacific campaign differs substantially to CAFE African and CAFE Brazil, being roughly a factor of 2 lower at the mid-tropospheric maximum.

During CAFE Africa, the mid-tropospheric maximum in the PAN/(PAN+NO_x)-ratio between 5-8 km was the most pronounced one, with a median ratio around 0.8-0.9. The strong impact of biomass burning during the campaign lead to ratios near 1 in individual air masses due to the chemical conversion of NO_x into PAN in biomass-burning plumes (Crowley et al., 2025). The inverse-C-shape of the profile resembles the shape of the vertical PAN profile (see Figure 7.2.1).

Similarly to CAFE Africa, an inverse-C-shaped profile of the PAN/(PAN+NO_x)-ratio was observed during CAFE Brazil even though the impact of biomass burning was much less significant during CAFE Brazil. The mid-tropospheric maximum during CAFE Brazil is slightly lower than during CAFE Africa with a ratio between 0.7-0.8. (Crowley et al., 2025) proposed that PAN formation during CAFE Africa was NO_x limited, rather than VOC limited. Based on the almost similarly high PAN/(PAN+NO_x), this hypothesis seems to also apply to CAFE Brazil where air masses were even richer in organics than during CAFE Africa yet the PAN levels were lower.

The lowest ratio of PAN/(PAN+NO_x) was observed during CAFE Pacific. Note that data below the detection limit was removed as PAN and NO observations were frequently close or below the detection limit during CAFE Pacific.
The maximum median ratio reached during CAFE Pacific was around 0.4, which reflects the low observed PAN levels and suggests that the formation of PAN might be VOC limited or that there is a greater entry from fresh NO_x in relative terms. However, there is a higher uncertainty during CAFE Pacific on the NO_2 levels which were derived from the Leighton-ratio (Equation 27) without the consideration of peroxy radical reactions which were included for the NO_2 calculation in CAFE Brazil (Hartmann, 2024).
In contrast to CAFE Africa and CAFE Brazil, where a strong decrease of PAN/(PAN+NO_x) in high altitudes was observed, the profile of CAFE Pacific decreased only slightly from 0.4 to 0.3 above 8 km altitude. The flatter profile in high altitude was a result of the flat PAN and NO profiles (see Figure A.0.15) at these altitudes. The low observed NO in the UT was attributed to non-electrified convection (Nussbaumer et al., 2025).

The amount of NO_x stored in PAN has its maximum at mid-tropospheric altitudes around 6-10 km varying between 40-90% across the three tropical aircraft campaigns. The measurements showed that PAN is a significant reservoir of NO_x during all CAFE campaigns, yet the PAN/(PAN+NO_x) ratio was significantly lower during CAFE Pacific than during CAFE Africa and CAFE Brazil.

7.5 THE ROLE OF BIOMASS BURNING DURING ALL CAFE CAMPAIGNS

Biomass burning (BB) plays a crucial role in shaping the composition of the Earth's atmosphere and is considered one of the largest sources of trace gases and aerosols globally (Andreae, 2019; Andreae and Merlet, 2001). Open vegetation fires not only release greenhouse gases such as CO_2 or CH_4, but also of VOCs and NO_x(Andreae, 2019), which are precursors to PAN and PAA.
Aircraft and satellite observations have confirmed the photochemical formation of PAN in biomass burning plumes (Clarisse et al., 2011; Coheur et al., 2007; Holzinger et al., 2005). In boreal BB plumes, it has been found that approximately 40 % of initial NO_x is converted into PAN within the first few hours after emission (Alvarado et al., 2010). Pyroconvective updraft of BB emissions are considered the primary source of PAN in the UTLS, which is supported by the clear correlation between the seasonality of PAN enhancements to fire activity observed globally by satellite measurements (Moore and Remedios, 2010; Tereszchuk et al., 2013). Due to its high instability towards temperature, the formation and transport of PAN in aged biomass burning smoke plumes are complex and dependent on various factors, including the height of injection, the composition of vegetation etc. (Crowley et al., 2025).
The detection of PAA in biomass burning plumes has also been reported in literature recently (Wang et al., 2016; Wolfe et al., 2021).

To investigate the impact of BB, the correlation of PAN and PAA with typical biomass burning tracers such as CO, ozone, acetone, acetonitrile (CH_3CN) and black carbon (BC) can be analyzed. This approach was employed in Section 6.3.2 for a section of flight

RF15 during CAFE Pacific. These species are co-emitted in plumes and were measured onboard of HALO during the campaigns.

The tracer-tracer correlations can provide valuable insights into the type and age of biomass burning emissions.

For example, CO is relatively long-lived (approximately 58 days) in the atmosphere with respect to OH-oxidation (Crowley et al., 2025) and is ubiquitous in the troposphere due to a variety of primary and secondary sources such as the oxidation of methane and non-methane hydrocarbons, industrial combustion processes and biomass-burning (Andreae, 2019; Seinfeld and Pandis, 1998). Hence, CO is a general marker for burning activities and organic oxidation processes. CO is also involved in tropospheric ozone production (Fishman and Crutzen, 1978).

Acetonitrile has been shown to be a useful indicator of biomass burning which is assumed to be its predominant source in the atmosphere (De Gouw et al., 2003). However, the lifetime of CH_3CN in the UT with respect to OH can be in the order of years which leads to high background levels making it difficult to identify aged biomass-burning plumes (Crowley et al., 2025).

In contrast, BC has very low background levels and has an atmospheric lifetime of several days making it an ideal tracer of fresh BB. Holanda et al., 2020 demonstrated this by calculating backward trajectories for the air masses sampled during the ACRIDICON-CHUVA campaign in September 2014, which showed that the detected black-carbon rich layer at 3.5 km resulted from biomass burning smoked transported from west Africa over the South Atlantic to the Amazon basin (Holanda et al., 2020).

Ozone is produced from the same precursors as PAN (see Section 2.1.1) and hence is also a by-product of biomass burning.

Beside anthropogenic and biogenic sources, acetone was found to be directly emitted by biomass burning but also secondarily formed within the plume (Holzinger et al., 2005). The global annual mean lifetime of acetone is around 2 weeks (Fischer et al., 2014).

7.5.1 *Biomass burning during CAFE Africa*

The African biomass burning season occurs during November-March in the northern hemisphere and between May-October in the southern hemisphere (Ichoku, 2020). Satellite observations have shown a peak in transatlantic transport of pollution layers in August/September (Holanda et al., 2020). Consequently, the CAFE Africa campaign took place during the expected maximum of the Southern Hemispheric African biomass burning season.

Crowley et al. (2025) analysed the CAFE Africa CIMS measurements and identified significant impact of biomass burning, particularly during the four flights FL04, FL10, FL12 and FL13 (see Figure 7.1.1). These flights were characterized by clearly enhanced levels of BC, CO and CH_3CN. FL04, FL12 and FL13 sampled biomass burning from the African continent, while biomass burning during FL10 was traced back to Canada and north-west America (Crowley et al., 2025). FL10 probed north of the ITCZ, which was located around 10°N during CAFE Africa measurements (Crowley et al., 2025).

The air masses impacted by biomass burning contributed to the pronounced PAN maximum at mid-tropospheric altitudes (Crowley et al., 2025).

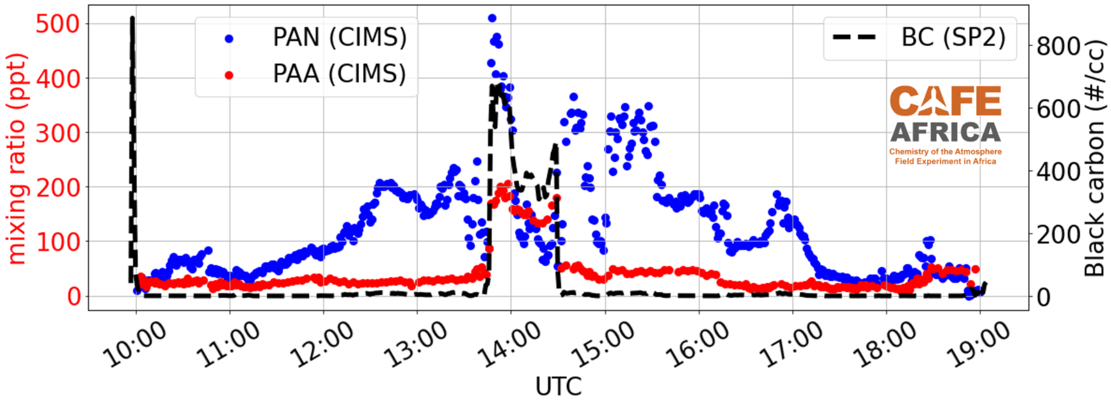

Figure 7.5.1: Time series of PAN (blue), PAA (red), and black carbon (BC) (black) measurements at FL12 during CAFE Africa. BC is given in raw counts per cubic centimeter (#/cc).

Exemplary, the time series of PAN, PAA and black carbon (BC) measurements during FL12 are shown in Figure 7.5.1. The signal from BC was very clear, with counts reaching up to approximately 700. The coincidence of PAN, PAA and BC peaks demonstrates the impact of fresh (within approx. a week) biomass burning on PAN and PAA observations.

7.5.2 *Biomass burning during CAFE Brazil*

The CAFE Brazil campaign took place at the end of dry season/beginning of wet season and hence outside the major biomass burning season in Amazonia.
In Figure 5.3.3 in Section 5.3.1, it was shown that FIRMS satellites observations of fire events were low above the Amazonian rainforest during CAFE Brazil and decrease towards the second half of the campaign when the rain-season started.
Based on the back-trajectory analysis for CAFE Brazil described in Section 5.3, it seemed unlikely that PAN formed in BB plumes from the west coast of Africa was transported to the Amazonian basin at high altitudes.

In contrast to CAFE Africa, the signal of the SP2 instrument from BC was mostly only a few counts during the CAFE Brazil campaign. The BC signal was strongest during RF07, reaching up to 50 counts per cubic centimeter, as depicted in Figure 7.5.2. Peaks in BC above 400 counts were observed twice, once during RF11 and once during RF14, when HALO passed through visible biomass burning plumes below 1 km altitude. These peaks were accompanied by a spike in NO (> 500 ppt). However, the time inside the plume was so short that CIMS captured only one data point for PAN and none for PAA.

RF07 targeted the pristine Amazonian rainforest above ATTO and was analyzed in detail in Section 5.4.1.
Note that the shown SP2 data in Figure 7.5.2 represents the uncalibrated incandescence signal of refractory BC, which is linearly proportional to the mass of rBC in the particle (Holanda et al., 2020; Laborde et al., 2013).
Like PAA, BC was enhanced in the boundary layer during RF07 on 9.12.2022, see Fig-

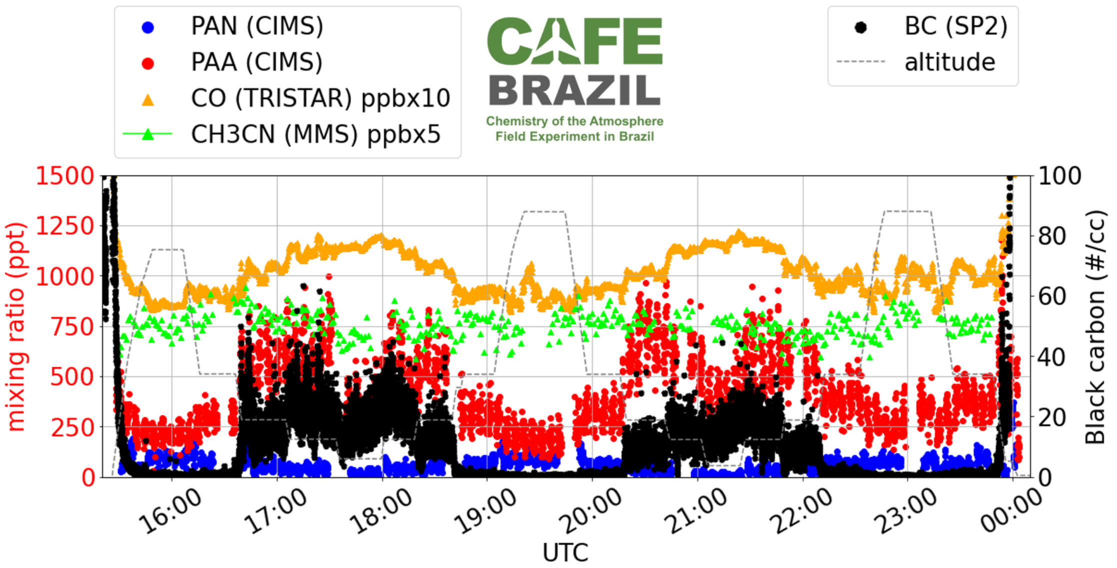

Figure 7.5.2: Time series of PAN (blue), PAA (red), CO (orange), and acetonitrile (lime) mixing ratios as well as counts per cubic centimeter of the SP2 BC (black) in RF07 during CAFE Brazil. The flight altitude is marked in gray in the background. Note that CO and acetonitrile mixing ratios are given in ppb and have been multiplied with a factor of 10 and 5, respectively, for better visibility in the plot.

ure 7.5.2. The increased PAA in the boundary layer could result from biogenic hydrocarbon chemistry but the coincidence of peaks with BC indicates aged biomass burning. Also CO (orange) is enhanced in the boundary layer, which suggest burning emissions. The enhancements of BC in the low altitudes were not correlated with PAN, which aligns with the hypothesis of aged biomass burning plumes in the low altitudes, where PAN has thermally dissociated and PAA is formed in the organic rich air masses. Acetonitrile measurements showed no enhancements during the whole flight (lime), so the biomass burning effect is probably weak.

Hence, the effect of biomass burning on the probed air masses during CAFE Brazil is much less obvious than during CAFE Africa. With respect to BC measurements, fresh BB probably plays only a minor role on the PAN and PAA mixing ratios during CAFE Brazil. The impact of aged biomass burning plumes, where the PAN-to-PAA ratio shifted towards PAA, could be possible.

7.5.3 *Biomass burning during CAFE Pacific*

During CAFE Pacific, the uncalibrated signal from BC in the SP2 signal was generally below 20 counts and hence even less than during CAFE Brazil. It is worth noting that the SP2 instrument had technical problems especially in high altitudes during several flights during CAFE Pacific. However, the contribution of fresh biomass burning during CAFE Pacific seemed to be generally low when the instrument was working with the exception of a few distinct biomass burning plumes plumes.
The maximum of registered counts on BC occurred during RF18, when the aircraft

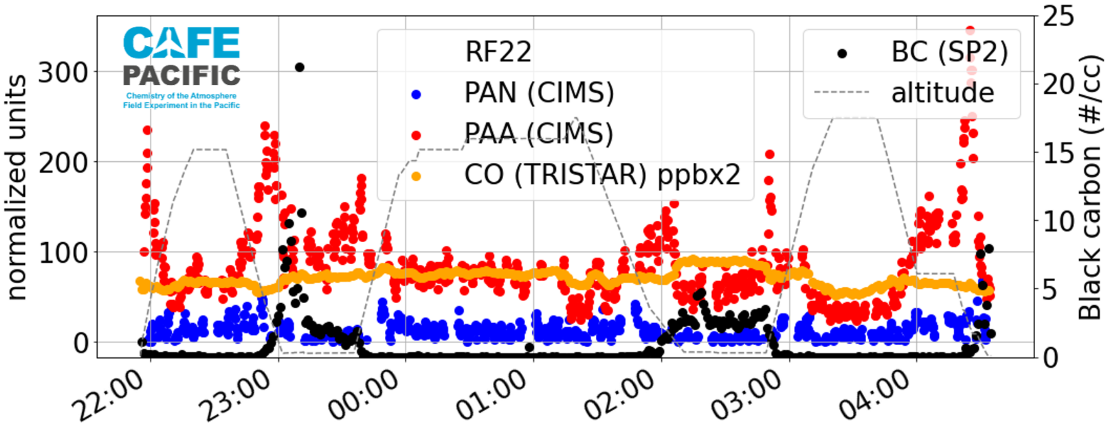

Figure 7.5.3: Time series of PAN (blue), PAA (red), and CO (orange) mixing ratios as well as counts per cubic centimeter of the SP2 BC (black) in RF22 during CAFE Pacific. The flight altitude is marked in gray in the background. Note that CO mixing ratios are given in ppb and have been scaled by a factor of 2 for better visibility.

passed close to a visible biomass burning plume just before landing in Honiara on the Solomon islands, with a BC peak up to 600 counts.

As an example of the general low BC levels, the time series of PAN, PAA and BC measured in RF22 during CAFE Pacific is shown in Figure 7.5.3. During RF22, the SP2 instrument was running throughout the whole flight. The flight headed north of Cairns, sampling at low altitudes above the mangrove coast regions, and reached until Papua New Guinea. The maximum BC (above 20 counts) was reached in the boundary layer, but the peaks where not correlated with neither PAN nor PAA. CO is slightly enhanced in the low altitudes, especially between 2:00-3:00 UTC, but is generally much lower compared to the example flight RF07 considered for CAFE Brazil in Section 7.5.2. Also acetontirile was constantly low during RF22 (not depicted), indicating no significant sources of biomass burning.

7.6 ROLE OF BIOGENIC EMISSIONS DURING CAFE BRAZIL AND CAFE PACIFIC

In Section 5.6.4, the role of biogenic emissions and notably isoprene was discussed during CAFE Brazil by analysing the modelled contributions to the PA-radical concentration.

Figure 7.6.1 compares the relative contributions of the immediate PA-radical precursors acetone, acetaldehyde and MGLY in the EMAC simulations of CAFE Brazil (left panel) to the simulations of CAFE Pacific (right panel). The fraction "others" includes essentially isoprene photo-oxidation products other than MGLY.

In Section 5.6.3, it was found that methyl glyoxal (MGLY) plays a dominant role in producing of the PA-radical in the EMAC simulations for CAFE Brazil as a result of high isoprene emissions. The sum of MGLY and other isoprene oxidation products were responsible for almost three quarters of the total modelled PA-production (left panel in Figure 7.6.1) highlighting the importance of isoprene emissions from the Amazonian rainforest and their subsequent photo-oxidation on the formation of PAN and PAA.

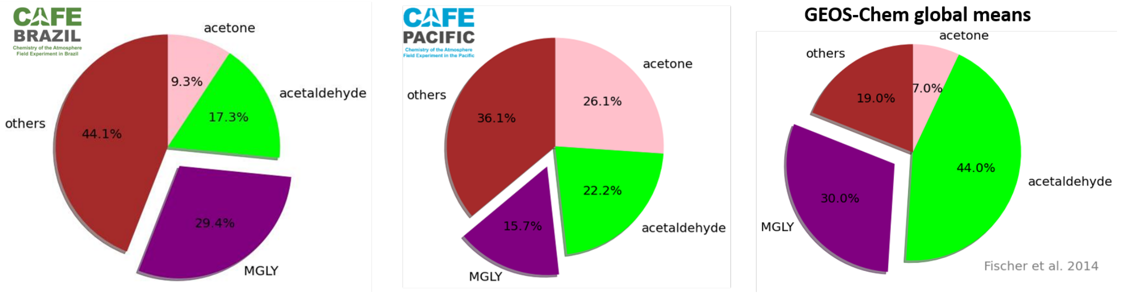

Figure 7.6.1: Relative contribution of different PA-radical precursor species to total PA-production in the EMAC model for CAFE Brazil (left pie) and CAFE Pacific (middle pie). The right pie represents global means of immediate PA-precursors derived with the global GEOS-Chem model based on Fischer et al. (2014).

According to the EMAC simulations, the relative contribution of MGLY during CAFE Pacific is around 16 %, which is almost half of the contribution during CAFE Brazil. Acetone was found to be the major PA-precursor during CAFE Pacific (approx. 26 %), closely followed by acetaldehyde (approx. 22 %). Hence, acetone and acetaldehyde together made up almost half of the total PA-production, indicating a higher relative contribution of non-biogenic emissions resulting probably from a mixture of industrial and (anthropogenic) biomass burning processes.

The right pie-plot in Figure 7.6.1 shows that in the EMAC model results for CAFE Brazil and CAFE Pacific the contribution of acetaldehyde as immediate PA-precursor was less than half compared to the global mean derived with the GEOS-Chem model by Fischer et al. (2014). In contrast, the fraction of "others" was notably higher during EMAC simulations than the global mean of GEOS-Chem. While the contribution of acetone to PA-formation during CAFE Brazil was comparable to the global mean, the fraction simulated for CAFE Pacific exceeded the global mean by more than a factor 3. Since the EMAC simulations for acetone agreed well during both campaigns, CAFE Brazil and CAFE Pacific, the different relative importance of acetone highlights the regional differences between Amazonia and southern Pacific and its impact on PAN and PAA formation.

Overall, the discussed deviations from the global average area are in agreement with the regional and seasonal differences stated by GEOS-Chem for the sampled tropical regions.

7.7 DISCREPANCY BETWEEN MEASURED AND MODEL ACETALDEHYDE

According to global simulations, acetaldehyde (CH_3CHO) is a major precursor of PAN accounting for around 44 % of global PA production (Fischer et al., 2014).

Acetaldehyde is ubiquitous in the atmosphere and has direct as well as indirect sources. Photo-oxidation of VOCs like alkanes, alkenes and ethanol is the largest source of acetaldehyde in the atmosphere (Atkinson et al., 2006). Global 3-D simulations using the GOES-Chem model estimated net ocean emission to be the second largest global source of acetaldehyde followed by terrestrial sources from decaying plants, biomass burning, and anthropogenic emissions (Millet et al., 2010).

The major sink of acetaldehyde is the reaction with OH leading to atmospheric life-

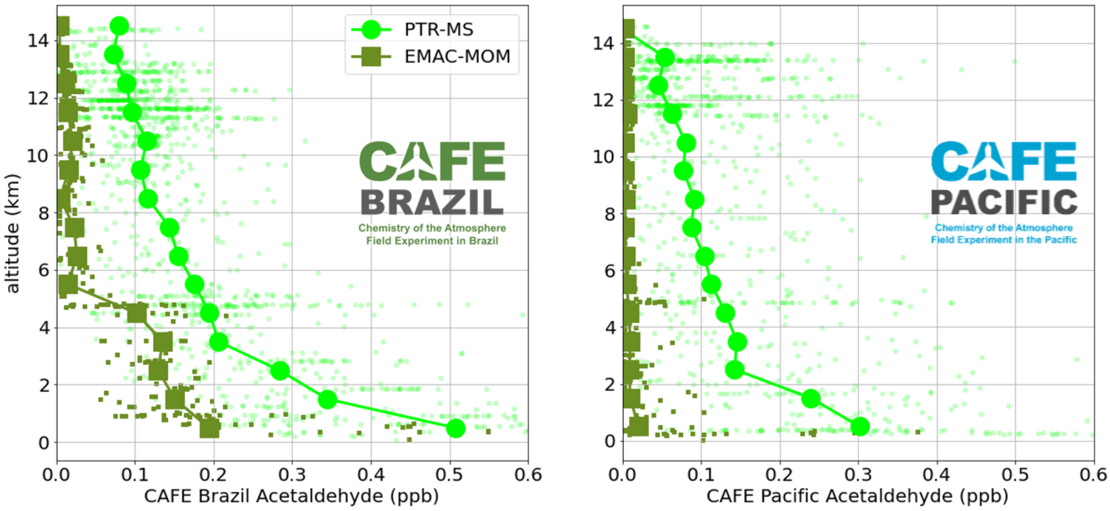

Figure 7.7.1: Vertical profiles of measured (lime dots) and modelled (olive squares) acetaldehyde for all analysed flights during CAFE Brazil (left panel) and CAFE Pacific (right panel). Solid lines represent medians.

times in the order of a day (Atkinson et al., 2006). The concentration of acetaldehyde decreases with increasing altitude as its major sources are at ground level and the lifetime is short enough to prevent mixing to high altitudes. Generally, over the ocean lower acetaldehyde concentrations and weaker vertical gradients are observed (Millet et al., 2010).
While simulated and measured acetaldehyde mixing ratios in the continental boundary layer generally agree well, aircraft measurements using PTR-MS or GC-MS instruments reported high acetaldehyde levels in the free troposphere, which are not represented by models and disagree with measured and modelled PAN-to-NO_x ratios (Millet et al., 2010). The discrepancy between acetaldehyde measurements and models has led to a debate about a potential missing global source of oxygenated VOC and is a long-standing problem (Singh et al., 2001, 2004; Travis et al., 2020; Wang et al., 2019).

The comparison of modelled and measured vertical profiles of species involved in PAN and PAA formation in the example of RF17 during CAFE Pacific, showed that EMAC predicted lower concentrations of acetaldehyde by more than one order of magnitude, while acetone was well represented, see Figure 6.5.3 in Section 6.5.5. The observation that EMAC represents well the vertical profile of measured acetone while the difference to measured acetaldehyde is very large holds not only for RF17 during CAFE Pacific but also in general for all flights during both campaigns CAFE Brazil and CAFE Pacific.

Figure 7.7.1 shows the median vertical profiles of measured (lime) and modelled (olive) acetaldehyde for all analysed flights during CAFE Pacific and CAFE Pacific.
In the case of CAFE Brazil (left panel), GC-MS measurements of acetaldehyde excess EMAC acetaldehyde mixing rations by a factor between 2-25, with a tendency to increase with altitude.
Similarly, in the case of CAFE Pacific (right panel), measured acetaldehyde exceeds the model by a factor of 14-28. For example, at the lowest altitudes the GC-MS instrument recorded a median acetaldehyde of around 300 ppt while EMAC simulations resulted

in around 20 ppt. While EMAC acetaldehyde in the upper troposphere has decreased to a few ppt only, measured acetaldehyde is still around 50 ppt. Note that, acetaldehyde data for CAFE Pacific is still in a preliminary status and may vary in a finalized version by 30-50 % (personal conversation with Bianca Krumm).

It is known that measurements of acetaldehyde with mass spectrometry suffers from background problems (Apel et al., 2008; Northway et al., 2004) which is critical especially in pristine regions like those sampled during CAFE Pacific. Northway et al. (2004) suspected the formation of acetaldehyde from ozonolysis of unsaturated organic compounds on Teflon tubing leading to a falsely enhanced signal on acetaldehyde. Artificial signal enhancement in the presence of high ozone (>150 ppb) in dry air was also found in acetaldehyde measurements of the GC-MS instrument mounted aboard (Ernle, Ringsdorf, and Williams, 2022). An ozone scrubber was added at the inlet of the HALO-GC-MS to minimize this effect. However, before the sampled air reaches the scrubber, it passes through a 2 m long heated Teflon tubing between the trace gas inlet (TGI) of the HALO aircraft and the instrument. Therefore, the possibility of an artificial acetaldehyde background can not be completely ruled out.

In summary, it is questionable if the high acetaldehyde levels in the southern tropics provided by the GC-MS aboard HALO are reliable as the acetaldehyde measurements stand in stark contrast to modelled acetaldehyde from EMAC and is beyond the range of possible measurement uncertainties assigned to acetaldehyde. In addition, it was shown in Section 6.5.6 that the production rates of the PA-radical derived from the measured acetaldehyde in a steady-state assumption would lead to PAN levels around a factor 50 higher than observed PAN. Hence, the GC-MS measurements are in contradiction to the CIMS measurements of PAN.

7.8 PPN AS A TRACER OF ANTHROPOGENIC POLLUTION DURING CAFE BRAZIL AND CAFE PACIFIC

Peroxy propionyl nitrate (PPN) ($C_2H_5C(O)O_2NO_2$) is a PAN-type species almost exclusively formed via propanal (Roberts et al., 2001), resulting from anthropogenic hydrocarbon sources (Roberts, 2007). Therefore, PPN can be used as a marker for anthropogenic-driven atmospheric chemistry (Hansel and Wisthaler, 2000; LaFranchi et al., 2009). The lifetime of PPN is approximately 30 % lower than that of PAN (LaFranchi et al., 2009). While the thermal decomposition of PPN is about 15 % slower than PAN, the photolysis of PPN is approximately double as fast as that of PAN (Roberts, 2007).

The ratio of PPN/PAN gives an indication of the contribution of urban/anthropogenic pollution. The PPN-to-PAN ratio has been frequently observed in field studies, suggesting that anthropogenic hydrocarbon sources lead to ratios in the range of 12-20 % (Roberts, 2007). Theses ratios can be lowered by the presence of biogenic driven hydrocarbon chemistry favouring the production of PAN over PPN production (Roberts, 2007). For example during the INTEX-B aircraft campaign, which focused on tracing long-rang transport of Asian pollution, a strong correlation of PPN with PAN was found (r_2=0.96) with an average PPN-to-PAN ratio of approximately 6.5 %(Wolfe et al., 2007).

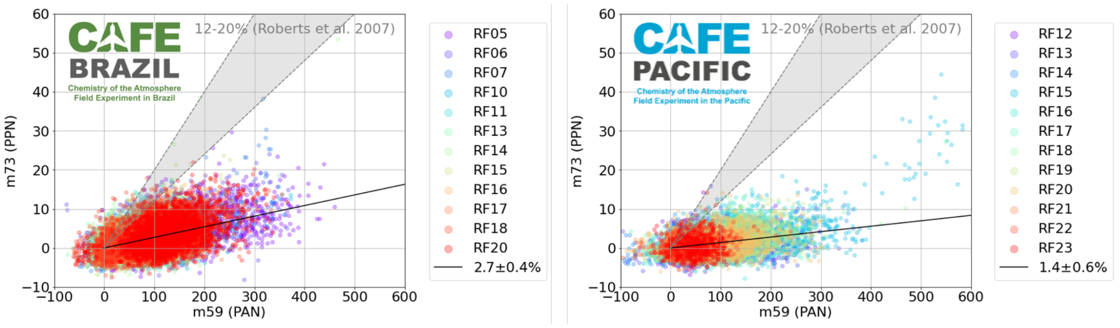

Figure 7.8.1: Raw counts from PPN ($\frac{m}{z}=73$) versus raw counts from PAN ($\frac{m}{z}=59$) for all flights during CAFE Brazil (left panel) and CAFE Pacific (right panel). The gray shaded area marks the range of typical PPN-to-PAN ratios reported by Roberts (2007). The black line indicates the mean slope of the measurements and its standard deviation.

The CIMS detects PPN on $\frac{m}{z}=73$ (Flocke and Weinheimer, 2003; Wolfe et al., 2007, 2009). Previous studies showed, the CIMS sensitivity towards PAN and PPN is almost similar (Dörich, 2023; Roiger et al., 2011; Slusher, 2004). Hence, the ratio of the titration-subtracted counts between $\frac{m}{z}=73$ and $\frac{m}{z}=59$ approximately represents the PPN-to-PAN ratio. Note that the PPN measurements were not calibrated and it is assumed that the relative sensitivity to PAN does not change.

Figure 7.8.1 shows the measured PPN-to-PAN ratios during all analysed flights of the two campaigns CAFE Brazil (left) and CAFE Pacific (right) compared to the typical ratios reported by Roberts (2007).

As seen in the left panel in Figure 7.8.1, during CAFE Brazil, the PPN-to-PAN ratio was very similar during all flights with an average of of 2.7±0.4 % (black line) and hence significantly lower than the reference values of 12-20 % in anthropogenic influenced areas. In general, raw counts on PPN were few during CAFE Brazil, ranging between 0 and 40 counts, which indicates low contribution of anthropogenic hydro carbon chemistry. In addition, PPN and PAN were not very well correlated during CAFE Brazil, with r-values between 0.27 and 0.55.

During CAFE Pacific, the slopes of PPN plotted against PAN varied between 1-3 % and were in average almost half as steep (1.4±0.6 %, black line) as during CAFE Brazil. The higher relative standard deviation of about 45 % during CAFE Pacific indicates the higher variability between flights and the presence of distinct anthropogenic pollution plumes. In most of the flights during CAFE Pacific, no clear correlation between PPN and PAN was observed (r-values below 0.5), except during the continental flight RF15 (r = 0.63). In this flight counts on PPN reached above 40 in a single plume when approaching the city Melbourne for a refueling stop (see detailed analysis of RF15 inSection 6.3).

Overall, based on the small signal on $\frac{m}{z}=73$ and the low PPN-to-PAN ratios of maximum 3 %, the total anthropogenic influence in the remote areas sampled during both campaigns, CAFE Brazil and CAFE Pacific, is rather low compared to biogenic chemistry.

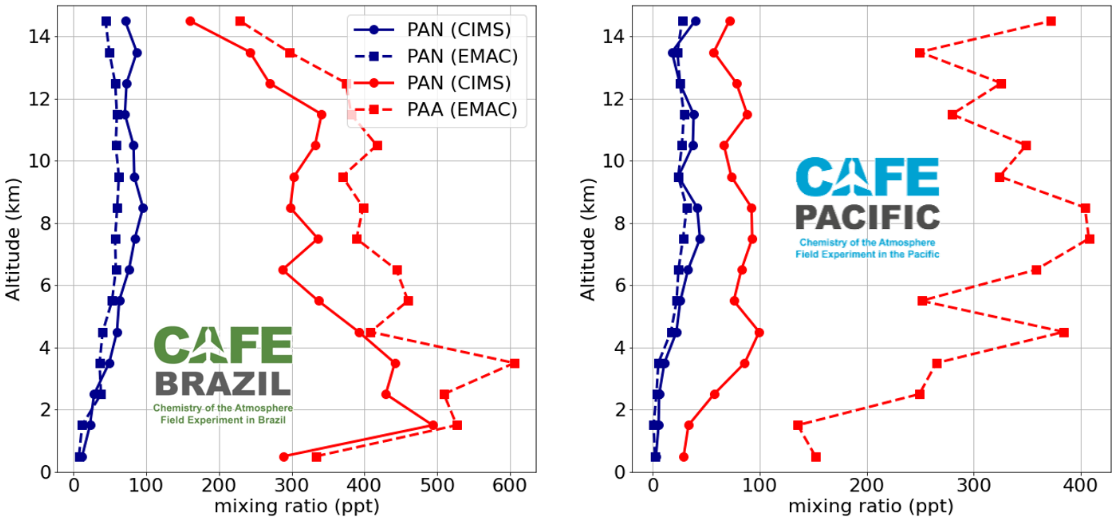

Figure 7.9.1: Comparison between measured (solid lines) and EMAC model (dashed lines) median vertical profiles of PAN (blue) and PAA (red) during CAFE Brazil (left panel) and CAFE Pacific (right panel).

7.9 PAN AND PAA PROFILES IN CAFE BRAZIL AND CAFE PACIFIC COMPARED TO THE EMAC MODEL

The vertical profiles of PAN and PAA have been compared between the observations and the EMAC model results for CAFE Brazil and CAFE Pacific in Figure 5.6.1 and Figure 6.8.2. To highlight the differences between the performance of the EMAC model for both campaigns, Figure 7.9.1 compares PAN (blue) and PAA (red) median vertical profiles of simulations and measurements of both campaigns.

In both campaigns, the EMAC simulations underestimated PAN only slightly, but overestimated PAA much more significantly.
The underestimation of PAN during CAFE Brazil was generally low (between 20-50 %) with a maximum at mid-tropospheric altitudes around 8 km. This also holds for the EMAC comparison with the CAFE Pacific PAN observations, where at some altitudes the EMAC model even closer to the observations with deviations of only a few percent.

In contrast, the overestimation of model PAA becomes much more drastic during CAFE Pacific. While the difference to the observations during CAFE Brazil was between 12-70 %, during CAFE Pacific model PAA exceeded the observations by 300-500 % increasingly with altitude. Even though the uncertainty on the PAA calibration might be as high as a factor of 2, this discrepancy is beyond possible measurement uncertainties. As previously discussed, the production of PAN and PAA in the atmosphere is closely linked to each other.
Hence, the deviations between modelled and observed PAN-to-PAA ratios indicate that the chemical model Mainz Organic Mechanism (MOM) used in EMAC needs to improve on NO_x and HO_x predictions and their relative abundance to get both species PAN and PAA right.
As previously discussed in Section 6.5.8, the correct representation of all of the many

reactions contributing to the production and the loss of the PA-radical in the model is essential.
In addition, a for the strong deviation of modelled PAA could be related to underestimated losses by wet deposition, such as rainout in clouds, which is implemented in the model based on the Henry's solubility of a substances (Discussions during the CAFE data meeting on 23_{rd} June 2025).
It has been reported for CAFE Africa, that the EMAC model tends to overestimate H_2O_2 particularly at high altitudes in the southern hemisphere (Hamryszczak et al., 2023b), which was attributed to an underestimation of cloud scavenging. Since H_2O_2 is a reservoir species of HO_x, it is closely linked to PAA. Hence, a possible underestimation of cloud scavenging could also lead to an overestimation of PAA especially under tropical, cloudy conditions. A detailed look into solubility thresholds for cloud scavenging within the EMAC-MOM model could be subject of further investigation in order to improve the model's performance in predicting PAA concentrations.

Part IV

CONCLUSION

8

SUMMARY

Within the scope of this work, the performance and data calibration system for the CIMS instrument were thoroughly described. Additionally, the measurement results obtained from its deployment in the aircraft campaigns CAFE Brazil and CAFE Pacific were presented. The key findings of this research are summarized in this chapter.

8.1 SUMMARY ON CIMS CHARACTERISTICS AND DATA CALIBRATION

In Section 4.1, the CIMS measurement technique was described and the instrument set-up during campaigns and in laboratory experiments was explained in detail. The overall performance of the CIMS instrument during CAFE Brazil and CAFE Pacific was excellent, with only a few hours of data loss observed throughout the duration of the experiments.

Limit of detection

The limit of detection (LOD) for PAN was derived from the variability of consecutive PAA measurements and varied between flights between 20-60 ppt during CAFE Brazil and between 10-22 ppt during CAFE Pacific.
The instruments LOD on PAA was based on the background counts when flushing with pure nitrogen directly after the flight and was between 5-33 ppt for flights during CAFE Brazil and 4-10 ppt for flights during CAFE Pacific.

Instrument sensitivity on PAN

The flight-wise derived instruments sensitivity for PAN during CAFE Brazil and CAFE Pacific in count on $\frac{m}{z} = 59$ per primary ion signal ($\frac{m}{z} = 127$) and per ppt ranged between $4.8 - 7.3 \times 10^{-5}$ and $3.2 - 4.5 \times 10^{-5}$, respectively.
The PAN calibration-factors resulted from the average of in-situ calibrations above 10 km per flight to avoid matrix effects of by-products of the photochemical-calibration source in humid air masses on the detecting acetate anion ($CH_3C(O)O^-$). As a reason for the losses of the acetate anion, the detection of formic acid and HONO via $CH_3C(O)O^-$ ($\frac{m}{z} = 59$) in the IMR was suggested. A correction factor of about 0.86 was applied to account for these losses of the acetate anion leading to signals on $\frac{m}{z} = 45$ and $\frac{m}{z} = 46$.
In contrast to the in-flight calibrations with the internal photochemical source, this matrix effect with humidity was not observed in the post-campaign laboratory studies, which showed no or only a weak humidity dependency on the instruments sensitivity on PAN. This was in agreement with reported experiments in literature and justified the neglect of a humidity effect on the PAN sensitivity.

Instrument sensitivity on PAA

The instruments sensitivity on PAA was derived via two different ground calibration methods. For CAFE Brazil a cross calibration between CIMS and the HYPHOP instrument of a PAA diffusion source was used. This resulted in a sensitivity of 1.2×10^{-5} normalised counts on $\frac{m}{z} = 59$ per ppt, which is about a factor 4-6 lower than for PAN.
For CAFE Pacific (and also during the subsequent BAIRN-VIP campaign), PAA was calibration via the absorption of triiodide formed by the reaction of PAA in a potassium-iodide solution ("KI-method"). The derived calibration factor for PAA during CAFE Pacific was 2.16×10^{-5}, which is a factor 1.8 higher than during CAFE Brazil. This big difference between the PAA calibration between the campaigns underlines the instruments variability with transport and the need of regular calibration during campaigns to quantify potential sensitivity changes between flights.
In addition, the PAA data was corrected for sensitivity losses due to humidity with a factor -2.5 mz145/mz127 for CAFE Brazil and -8.3 mz145/mz127 for CAFE Pacific. The relative loss of the instruments sensitive on PAA measurements with respect to relative humidity was shown due be consistent between the campaigns and experiments reported in literature leading to a loss in signal of about 60-70 % at 60 % relative humidity.

Total measurement uncertainties

The total measurement uncertainty (TMU) of CIMS for PAN including potential systematic errors was estimated to be up to 30 %, but at least 10-15 % for CAFE Brazil and 7-13 % for CAFE Pacific based on statistic errors, which could be quantified. The quantifiable statistic error for PAA was 15-42 % for CAFE Brazil and around 45 % for CAFE Pacific depending on the humidity. However, it was highlighted the uncertainty on PAA calibration factor for dry measurements could be up to a factor 2 including potential systematic uncertainties and due to the lack of reproducible calibration experiments.

Isotopic calibration standard and technical improvements

Between the two aircraft campaigns the instruments sensitivity on $\frac{m}{z} = 61$ was improved to use ^{13}C-isotopically labeled PAN as calibration standard. The ^{13}C-isotopically labeled PAN-standard was successfully applied to the CIMS instrument for the first time during CAFE Pacific. In addition, the temperature of the TDR was reduced from 180 °Cto 150 °Coptimizing the yield of PAN and PAA through the TDR region.

8.2 FIELD MEASUREMENT RESULTS

In this work, airborne field measurements of PAN and PAA in two tropical regions, the Amazonian rain forest and the Southern Pacific/north-east Australia have been analysed and compared with each other and to the previous CAFE Africa campaign above the tropical Atlantic west of Africa. The analysis of CAFE Brazil and CAFE Pacific, which took place approximately 1 year after each other, comprised 12 measurements flights each.

The CAFE Brazil and CAFE Pacific results provide a valuable contribution to the sparse in-situ data basis in tropical remote troposphere.

CAFE Brazil

A detailed summary for the CAFE Brazil campaign analysis was given in Section 5.9). In brief, the observations PAN and PAA during CAFE Brazil showed that PAA exceeded PAN mixing ratios by up to a factor of 5 in the mid-troposphere underlining the dominance of HO_2 over NO_2 chemistry due to the high biogenic emissions and low NO_x conditions.

The meteorological conditions (winds from south east, transition from dry- to wet season, few open fire events in the sampling area) indicated that the role of biomass burning was rather low in the beginning of the CAFE Brazil campaign and decreased further towards the end of the campaign.

As a general trend, mixing ratios of PAN and PAA were higher in the first month of the campaign, than in the second month, reflection the change of season.

The analysis with HYSPLIT trajectory analysis indicated that air masses originated or had circulated above the South American continent within 10 days before. Only few trajectories traced back to east Africa where biomass burning took place.

CAFE Pacific

CAFE Pacific covered a large sampling area (130-160 °E, 0-40 °S) and was characterised by generally low PAN (median <50 ppt) and low PAA (median <100 ppt) levels. Especially low values with mixing ratios close or below the detection limit were observed above in the Indo-Pacific warm pool area.

The tracer-tracer correlations of PAN to CO, Ozone, acetone and acetonitrile during an example flight above the continent showed that air masses results from mixture of anthropogenic and biogenic precursors. HYSPLIT trajectories to sampling areas as far south as 40 ° were shown to have traveled with the subtropical jet stream. However, a significant contribution of long-range transported PAN and PAA from pollution in southern Africa was not observed. A more detailed summary for the CAFE Pacific campaign is given in Section 6.9).

Impact of Biomass burning compared to CAFE Africa

BC observations were used as a tracer of fresh biomass burning and exemplarily compared during all three CAFE campaigns. The strong BC signature and correlation to PAN observed during CAFE Africa, was not applicable during CAFE Brazil and CAFE Pacific where only few and relatively low peaks in BC were observed. In addition, few open fire events were detected by FIRMS satellite observations, which indicated low impact of fresh biomass burning pollution during both, CAFE Brazil and CAFE Pacific.

Acetaldehyde discrepancy

Calculated PA formation from measured precursors revealed that observations of acetaldehyde are in contradiction to observed PAN and PAA levels. In addition, measurements of acetaldehyde exceeded model simulations of EMAC in both campaigns, CAFE Brazil and CAFE Pacific, by more than an order of magnitude. Considering known artifacts of the GC-MS measurement technique and the fact, it was suggested that measured acetaldehyde mixing ratios most likely have a large positive bias.

EMAC comparison

The comparison of CIMS measurements during CAFE Brazil to the EMAC simulations showed overall a good agreement for both PAN and PAA, with a tendency of the model to underestimate PAN (in average factor 0.8) and overestimate PAA (in average factor 1.2). While EMAC simulations were very close to the PAN observations during CAFE Pacific, the model overestimated PAA even more drastically (in average factor 4.5) indicating a large positive model bias towards HO_2.
While NO observations and model predictions fitted well during CAFE Brazil, the model overestimated NO substantially in the UT during CAFE Pacific. With respect to the high sensitivity of the PAN-to-PAA ratio on the NO_2-to-HO_2 ratio, the good model-measurement agreement in terms of PAN may reflect a fortuitous cancelling of system biases in the model.

Steady-state from model PA

The calculated levels of PAN and PAA from the steady-state calculations based on model PA-radical showed that the model PA concentrations would lead to a multiple times higher PAN levels than observed in the mid- and upper troposphere during both campaigns, CAFE Brazil and CAFE Pacific. Besides horizontal transport processes, convection was proposed to explain the discrepancy between steady-state and model as mixing times were estimated to be faster than the time a chemical steady-state for PAN needs to be established. The neglect of losses of the PA-radical to RO_2 in the steady-state assumption was found to only be able to account around 7 % in the upper troposphere during CAFE Pacific but could explain the factor 3-5 discrepancy.

PA-radical precursors

The analysis of contribution the three PA-radical precursors acetone, acetaldehyde and methyl glyoxal (MGLY) in the EMAC simulation showed, that MGLY was the dominant single PA precursor above the Amazonian rain forest (approx 30 %). In general, isoprene oxidation products, including MGLY, made up almost three quarter of the total model PA production, which highlighted the importance of biogenic emissions, notably isoprene, during CAFE Brazil. It was pointed out that the non-methane driven chemistry may exceed the impact of methane oxidation with respect to MHP formation at low altitudes, indicating the significance of PA-precursor related chemistry during the CAFE Brazil campaign.

In contrast, isoprene oxidation products including MGLY only represented half of the model PA concentrations during CAFE Pacific. During CAFE Pacific, acetone contributed the most to total model PA production (approx. 26 %), closely followed by acetaldehyde (approx. 22 %). This indicated both, biogenic as well as anthropogenic sources of PA-precursors.

9

OUTLOOK

9.1 CIMS AIRCRAFT MEASUREMENTS

PAA calibration

To reduce potential uncertainty of PAA sensitivity and to quantify possibly sensitivity variation during a campaign, in future campaigns more frequent calibrations should be done. Mor laboratory tests would be required,especially in inter-comparison with instruments such as HYPHOP.

Measurements of Acetaldehyde

The steady-state calculations showed that the GC-MS acetaldehyde measurements are in contradiction to the CIMS measurements. Therefore, the GC-MS acetaldehyde measurements need to be evaluated with respect to possible interferences from formation of acetaldehyde, for example in surface reactions with ozone at the PFA tubing inside the instrument. Alternatively, new methods (e.g. mass spectrometry with new ionisation schemes) and new sampling strategies need to be developed.

Model investigations

The results demonstrated the importance of simultaneous and precise measurements of PAN and PAA and its precursors species in order to validate and improve the models simulations especially in remote areas.
In addition, an evaluation of the convective mass-transport in the EMAC model could be helpful to quantify its relative importance compared to in-situ formation of PAN and PAA from the PA-radical. Further, the cloud scavenging of organic peroxides, notably PAA, should be checked in the MOM-chemistry scheme used in EMAC to improve the model predictions on PAA.

9.2 BAIRN-VIP: GROUND-BASED MEASUREMENTS IN FINLAND

I prepared and operated the CIMS instrument during the BAIRN-VIP campaign. As the finalization of the data is still in progress, preliminary findings are presented in this section to provide an outlook on possible research questions.

BAIRN-VIP campaign description

The Biosphere-Atmosphere Interactions and the Reactive Nitrogen Budget: VertIcal Profiles of Key Species (BAIRN-VIP) ground campaign was conducted in the boreal forest around Hyytiälä, Finland, from 27th August to 28th September 2024. The CIMS was installed in a measurement container alongside a suite of instruments measuring NO_x, NO_y, ozone, NO_3-reactivity, PANs and alkyl nitrates (ANs) at the foot of the 35 m high walk-up tower of the SMEARII forest station[33] at 61,8 °N, 24.3 °E surrounded by Scots pine stand.
As a follow-up campaign of the previous Influence of Biosphere-Atmosphere Interactions on the Reactive Nitrogen budget (IBAIRN) campaign in 2016, BAIRN-VIP focuses on the vertical gradients of reactive nitrogen species during both, day and nighttime, with the aim of understanding NO_3, OH and O_3 initiated biogenic VOC oxidation within and above the canopy. In contrast to IBAIRN, where CIMS was stationed at a fixed location at 6 m altitude on the tower within the canopy (Eger et al., 2020), an automated vertically moving inlet system was implemented to sample a step-wise altitude profile between 1-28 m altitude within approximately half an hour.

CIMS performance

The CIMS instrument was operated continuously throughout the entire campaign, utilizing the gas mixtures listed in Table 2 and the target mass-to-charge ratios specified in Table 5. The resolution on $\frac{m}{z} = 61$ had been improved since the isotopic ^{13}C-PAN calibration standard was applied.
In total, ambient measurements of PAN and PAA were only interrupted for less than 27 h during the one month of measurements, primarily due to the regular replacement of the particle filters in the vertical inlet and for the purpose of experiments with CIMS. The ground-based experiments included recording of mass spectra, humidity sensitivity studies, variations of NO flow studies and PAA calibration with the KI-method. Specifically, three KI-calibrations of PAA were performed on 10th September 2025, and were found to align with previous laboratory results, as it was shown in Figure 4.4.5.

Preliminary data treatment

The PAN signal was derived by subtracting the interpolated titration signal, similar to the procedure applied during the aircraft campaigns. However, this procedure might not be applicable in phases when the vertical inlet was moving due and strong vertical gradients of PAA were present.

---

[33] https://www.atm.helsinki.fi/smear/smear-ii/, last access: 18th June 2025.

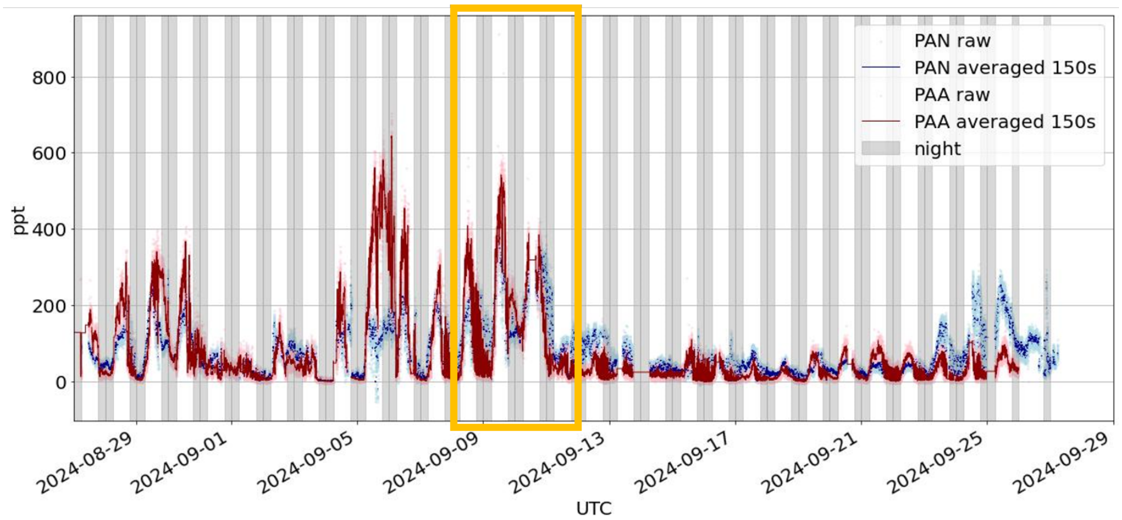

Figure 9.2.1: Time series of preliminary PAN and PAA measurements during the ground-based BAIRN-VIP campaign in Finland in autumn 2024. Phases of elevated PAN are marked by the yellow rectangle.

It is worth noting that no correction for humidity or for other possibly interfering species, such as HNO_3, has been applied yet to the data, and this remains an outstanding task.
Furthermore, the data has not been normalised to the primary ion signal, as it is still under investigation if the m145/m127 ratio during BAIRN-VIP holds as a measure of humidity.

Overview of preliminary data

Figure 9.2.1 presents the time series of preliminary PAN and PAA data during the BAIRN-VIP campaign. Maximum PAN was observed between 9-12th September 2024. The backward trajectories calculated with HYSPLIT during this phase indicate that air masses may have traveled in low altitudes with temperatures up to 300 K above big European cities such as Tallinn, Minsk, and Kiev within the previous 3 days, see Figure 9.2.2. This suggests that the observed high PAN levels during this phase may be related to the transport of anthropogenic pollution from these urban areas.

As an example of the diurnal cycle of PAN and PAA, the time series and vertical profile of PAN and PAA is depicted for 12th September 2024 in Figure 9.2.3. Due to a strong temperature inversion during the night between 12th and 13th, a clear decreasing gradient of PAN and PAA towards low altitudes was observed in both species during the night. In future analysis, the diurnal cycle of PAN and PAA may be analysed in more detail and also compared with other tracers such as ozone and NO_x in order to understand the interaction between biosphere and anthropogenic pollutants. Furthermore, the deposition rates of PAN and PAA from the vertical gradients may be retrieved after a detailed treatment of the data providing insights to the fate of these species in the boundary layer.

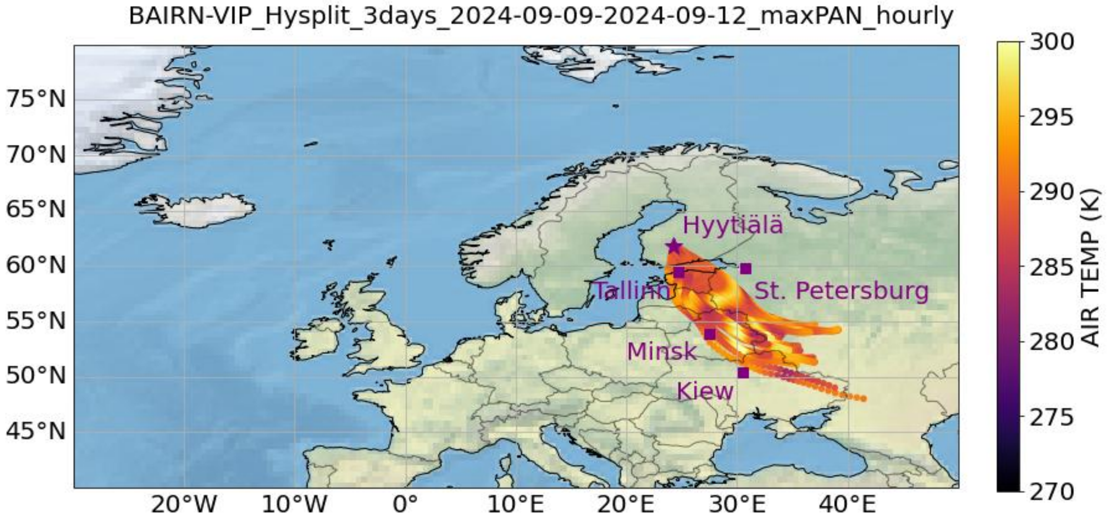

Figure 9.2.2: 3-days backward trajectories calculated with HYSPLIT for the phase of elevated PAN between 9-12th September 2024, as marked in Figure 9.2.2.

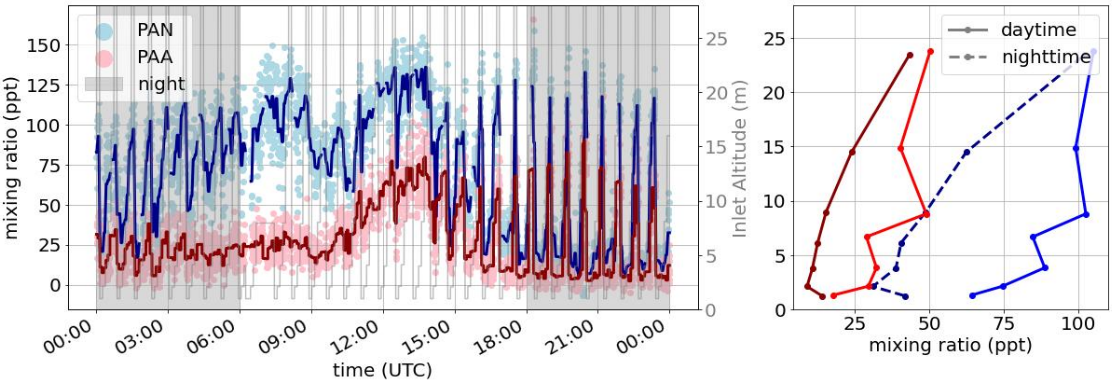

Figure 9.2.3: Left panel: time series of PAN (blue) and PAA (red) measured on 12th September 2024 during BAIRN-VIP. The lines indicate the 150 s averaged data. Nighttime is marked by the gray shaded areas. The sampling altitude is marked by the gray line in the background. Right panel: Daytime (solid line) and nighttime (dashed line) vertical profiles of PAN (blue) and PAA (red), derived from the data depicted in the left panel.

Part V

APPENDIX

A

SUPPLEMENTARY PLOTS

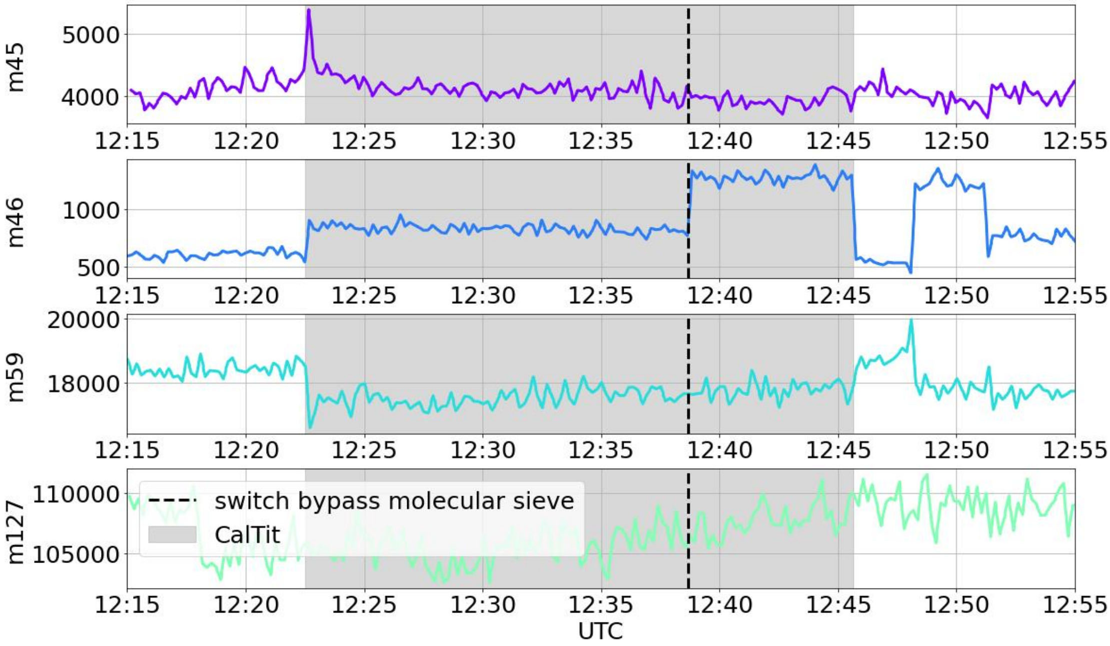

Figure A.0.1: Time series of a laboratory experiment on 26th September 2023 investigating the effect of a 0.3 nm molecular sieve inserted in the flow of titration NO. CIMS runs with synthetic air and the internal photo-chemical source is added. The gray shaded area marks the time when titration NO is added. The molecular sieve was inserted from the beginning of the experiment and bypassed after the black dashed marked time.

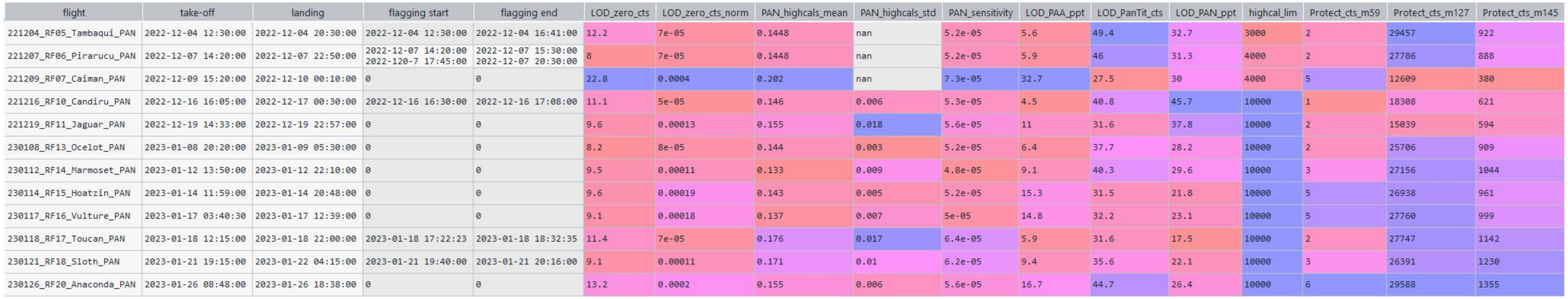

flight	take-off	landing	flagging start	flagging end	LOD_zero_cts	LOD_zero_cts_norm	PAN_highcals_mean	PAN_highcals_std	PAN_sensitivity	LOD_PAA_ppt	LOD_PanTit_cts	LOD_PAN_ppt	highcal_lim	Protect_cts_m59	Protect_cts_m127	Protect_cts_m145
221204_RF05_Tambaqui_PAN	2022-12-04 12:30:00	2022-12-04 20:30:00	2022-12-04 12:30:00	2022-12-04 16:41:00	12.2	7e-05	0.1448	nan	5.2e-05	5.6	49.4	32.7	3000	2	29457	922
221207_RF06_Pirarucu_PAN	2022-12-07 14:20:00	2022-12-07 22:50:00	2022-12-07 14:20:00 2022-120-7 17:45:00	2022-12-07 15:30:00 2022-12-07 20:30:00	8	7e-05	0.1448	nan	5.2e-05	5.9	46	31.3	4000	2	27786	888
221209_RF07_Caiman_PAN	2022-12-09 15:20:00	2022-12-10 00:10:00	0	0	22.8	0.0004	0.202	nan	7.3e-05	32.7	27.5	30	4000	5	12609	380
221216_RF10_Candiru_PAN	2022-12-16 16:05:00	2022-12-17 00:30:00	2022-12-16 16:30:00	2022-12-16 17:08:00	11.1	5e-05	0.146	0.006	5.3e-05	4.5	40.8	45.7	10000	1	18308	621
221219_RF11_Jaguar_PAN	2022-12-19 14:33:00	2022-12-19 22:57:00	0	0	9.6	0.00013	0.155	0.018	5.6e-05	11	31.6	37.8	10000	2	15039	594
230108_RF13_Ocelot_PAN	2023-01-08 20:20:00	2023-01-09 05:30:00	0	0	8.2	8e-05	0.144	0.003	5.2e-05	6.4	37.7	28.2	10000	2	25706	909
230112_RF14_Marmoset_PAN	2023-01-12 13:50:00	2023-01-12 22:10:00	0	0	9.5	0.00011	0.133	0.009	4.8e-05	9.1	40.3	29.6	10000	3	27156	1044
230114_RF15_Hoatzin_PAN	2023-01-14 11:59:00	2023-01-14 20:48:00	0	0	9.6	0.00019	0.143	0.005	5.2e-05	15.3	31.5	21.8	10000	5	26938	961
230117_RF16_Vulture_PAN	2023-01-17 03:40:30	2023-01-17 12:39:00	0	0	9.1	0.00018	0.137	0.007	5e-05	14.8	32.2	23.1	10000	5	27760	999
230118_RF17_Toucan_PAN	2023-01-18 12:15:00	2023-01-18 22:00:00	2023-01-18 17:22:23	2023-01-18 18:32:35	11.4	7e-05	0.176	0.017	6.4e-05	5.9	31.6	17.5	10000	2	27747	1142
230121_RF18_Sloth_PAN	2023-01-21 19:15:00	2023-01-22 04:15:00	2023-01-21 19:40:00	2023-01-21 20:16:00	9.1	0.00011	0.171	0.01	6.2e-05	9.4	35.6	22.1	10000	3	26391	1230
230126_RF20_Anaconda_PAN	2023-01-26 08:48:00	2023-01-26 18:38:00	0	0	13.2	0.0002	0.155	0.006	5.6e-05	16.7	44.7	26.4	10000	6	29588	1355

Figure A.0.2: Flight-specific analysis parameters for CAFE Brazil PAN and PAA measurement flights.

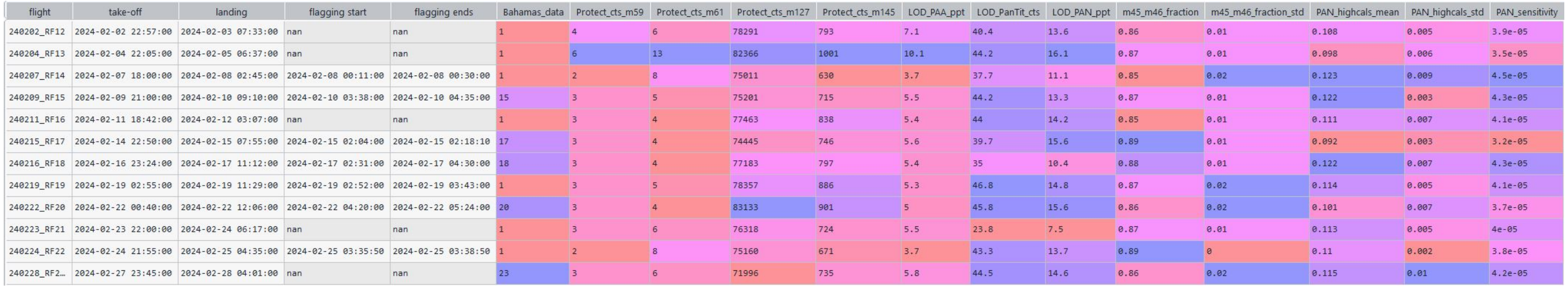

flight	take-off	landing	flagging start	flagging ends	Bahamas_data	Protect_cts_m59	Protect_cts_m61	Protect_cts_m127	Protect_cts_m145	LOD_PAA_ppt	LOD_PanTit_cts	LOD_PAN_ppt	m45_m46_fraction	m45_m46_fraction_std	PAN_highcals_mean	PAN_highcals_std	PAN_sensitivity
240202_RF12	2024-02-02 22:57:00	2024-02-03 07:33:00	nan	nan	1	4	6	78291	793	7.1	40.4	13.6	0.86	0.01	0.108	0.005	3.9e-05
240204_RF13	2024-02-04 22:05:00	2024-02-05 06:37:00	nan	nan	1	6	13	82366	1001	10.1	44.2	16.1	0.87	0.01	0.098	0.006	3.5e-05
240207_RF14	2024-02-07 18:00:00	2024-02-08 02:45:00	2024-02-08 00:11:00	2024-02-08 00:30:00	1	2	8	75011	630	3.7	37.7	11.1	0.85	0.02	0.123	0.009	4.5e-05
240209_RF15	2024-02-09 21:00:00	2024-02-10 09:10:00	2024-02-10 03:38:00	2024-02-10 04:35:00	15	3	5	75201	715	5.5	44.2	13.3	0.87	0.01	0.122	0.003	4.3e-05
240211_RF16	2024-02-11 18:42:00	2024-02-12 03:07:00	nan	nan	1	3	4	77463	838	5.4	44	14.2	0.85	0.01	0.111	0.007	4.1e-05
240215_RF17	2024-02-14 22:50:00	2024-02-15 07:55:00	2024-02-15 02:04:00	2024-02-15 02:18:10	17	3	4	74445	746	5.6	39.7	15.6	0.89	0.01	0.092	0.003	3.2e-05
240216_RF18	2024-02-16 23:24:00	2024-02-17 11:12:00	2024-02-17 02:31:00	2024-02-17 04:30:00	18	3	4	77183	797	5.4	35	10.4	0.88	0.01	0.122	0.007	4.3e-05
240219_RF19	2024-02-19 02:55:00	2024-02-19 11:29:00	2024-02-19 02:52:00	2024-02-19 03:43:00	1	3	5	78357	886	5.3	46.8	14.8	0.87	0.02	0.114	0.005	4.1e-05
240222_RF20	2024-02-22 00:40:00	2024-02-22 12:06:00	2024-02-22 04:20:00	2024-02-22 05:24:00	20	3	4	83133	901	5	45.8	15.6	0.86	0.02	0.101	0.007	3.7e-05
240223_RF21	2024-02-23 22:00:00	2024-02-24 06:17:00	nan	nan	1	3	6	76318	724	5.5	23.8	7.5	0.87	0.01	0.113	0.005	4e-05
240224_RF22	2024-02-24 21:55:00	2024-02-25 04:35:00	2024-02-25 03:35:50	2024-02-25 03:38:50	1	2	8	75160	671	3.7	43.3	13.7	0.89	0	0.11	0.002	3.8e-05
240228_RF2…	2024-02-27 23:45:00	2024-02-28 04:01:00	nan	nan	23	3	6	71996	735	5.8	44.5	14.6	0.86	0.02	0.115	0.01	4.2e-05

Figure A.0.3: Flight-specific analysis parameters for CAFE Pacific PAN and PAA measurement flights.

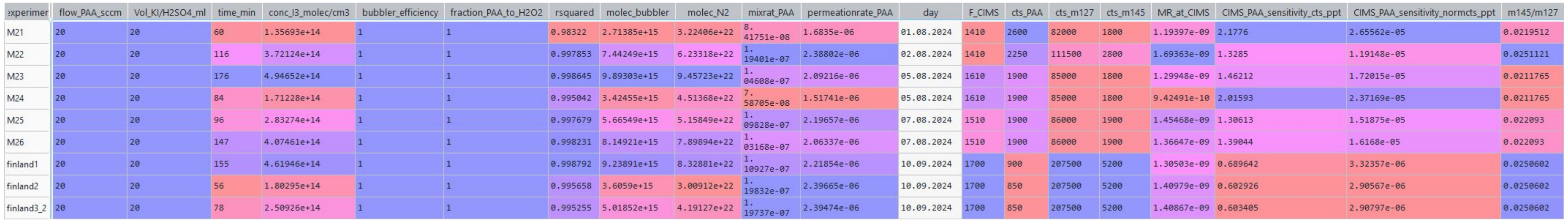

xperimer	flow_PAA_sccm	Vol_KI/H2SO4_ml	time_min	conc_I3_molec/cm3	bubbler_efficiency	fraction_PAA_to_H2O2	rsquared	molec_bubbler	molec_N2	mixrat_PAA	permeationrate_PAA	day	F_CIMS	cts_PAA	cts_m127	cts_m145	MR_at_CIMS	CIMS_PAA_sensitivity_cts_ppt	CIMS_PAA_sensitivity_normcts_ppt	m145/m127
M21	20	20	60	1.35693e+14	1	1	0.98322	2.71385e+15	3.22406e+22	8.41751e-08	1.6835e-06	01.08.2024	1410	2600	82000	1800	1.19397e-09	2.1776	2.65562e-05	0.0219512
M22	20	20	116	3.72124e+14	1	1	0.997853	7.44249e+15	6.23318e+22	1.19401e-07	2.38802e-06	02.08.2024	1410	2250	111500	2800	1.69363e-09	1.3285	1.19148e-05	0.0251121
M23	20	20	176	4.94652e+14	1	1	0.998645	9.89303e+15	9.45723e+22	1.04608e-07	2.09216e-06	05.08.2024	1610	1900	85000	1800	1.29948e-09	1.46212	1.72015e-05	0.0211765
M24	20	20	84	1.71228e+14	1	1	0.995042	3.42455e+15	4.51368e+22	7.58705e-08	1.51741e-06	05.08.2024	1610	1900	85000	1800	9.42491e-10	2.01593	2.37169e-05	0.0211765
M25	20	20	96	2.83274e+14	1	1	0.997679	5.66549e+15	5.15849e+22	1.09828e-07	2.19657e-06	07.08.2024	1510	1900	86000	1900	1.45468e-09	1.30613	1.51875e-05	0.022093
M26	20	20	147	4.07461e+14	1	1	0.998231	8.14921e+15	7.89894e+22	1.03168e-07	2.06337e-06	07.08.2024	1510	1900	86000	1900	1.36647e-09	1.39044	1.6168e-05	0.022093
finland1	20	20	155	4.61946e+14	1	1	0.998792	9.23891e+15	8.32881e+22	1.10927e-07	2.21854e-06	10.09.2024	1700	900	207500	5200	1.30503e-09	0.689642	3.32357e-06	0.0250602
finland2	20	20	56	1.80295e+14	1	1	0.995658	3.6059e+15	3.00912e+22	1.19832e-07	2.39665e-06	10.09.2024	1700	850	207500	5200	1.40979e-09	0.602926	2.90567e-06	0.0250602
finland3_2	20	20	78	2.50926e+14	1	1	0.995255	5.01852e+15	4.19127e+22	1.19737e-07	2.39474e-06	10.09.2024	1700	850	207500	5200	1.40867e-09	0.603405	2.90797e-06	0.0250602

Figure A.0.4: Overview of all performed KI-calibration experiments. Experiments M21-M26 were used to derive the PAA sensitivity for CAFE Pacific measurements after the campaign. Finland1-Finland3 were performed during the BAIRN-VIP campaign and used for the analysis of PAA measurements during this campaign.

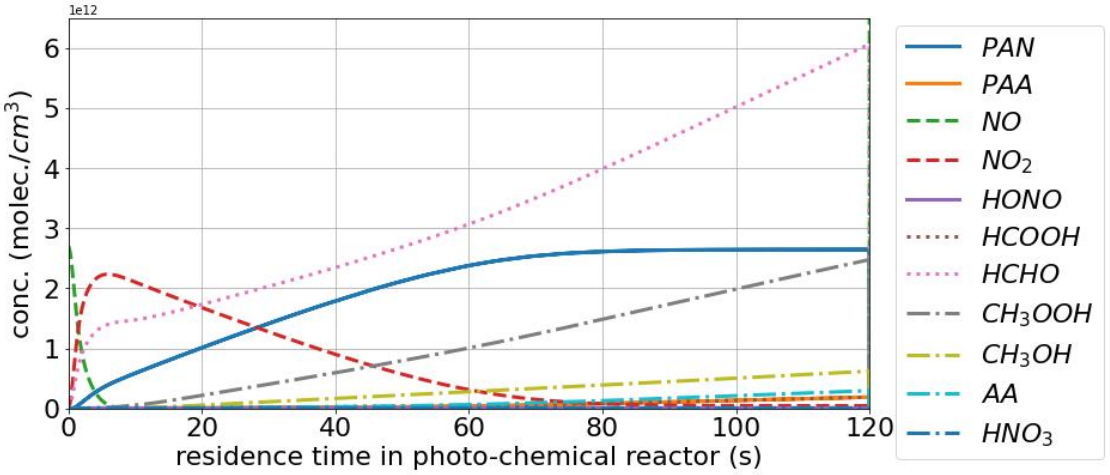

Figure A.0.5: Temporal evolution of species produced inside the CIMS internal photo-chemical source simulated in a FACSIMILE model by John Crowley.

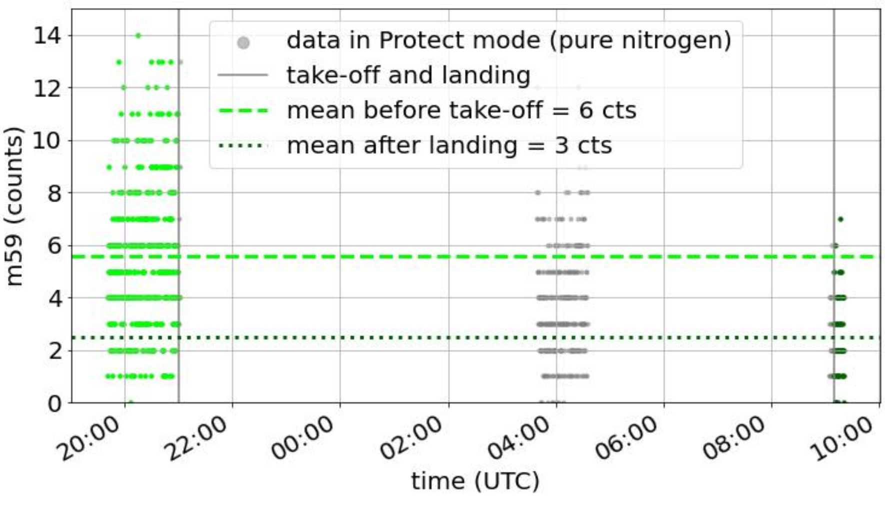

Figure A.0.6: Background on $\frac{m}{z} = 59$ captured in Protect mode before take-off (lime points), during a refueling stop (gray), and after landing (darkgreen), exemplarily shown for RF15 during CAFE Pacific. The horizontal lines indicate the average counts to the corresponding data points which are used as LOD rounded up to whole counts.

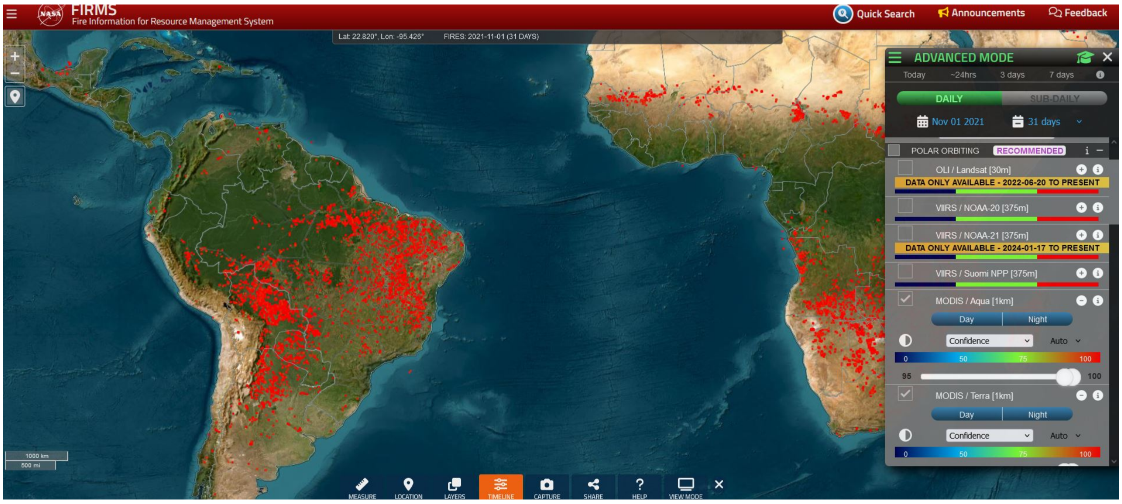

Figure A.0.7: Satellite observations of open fire events by the MODIS instrument with confidence above 95 % during November 2022, provided by FIRMS.

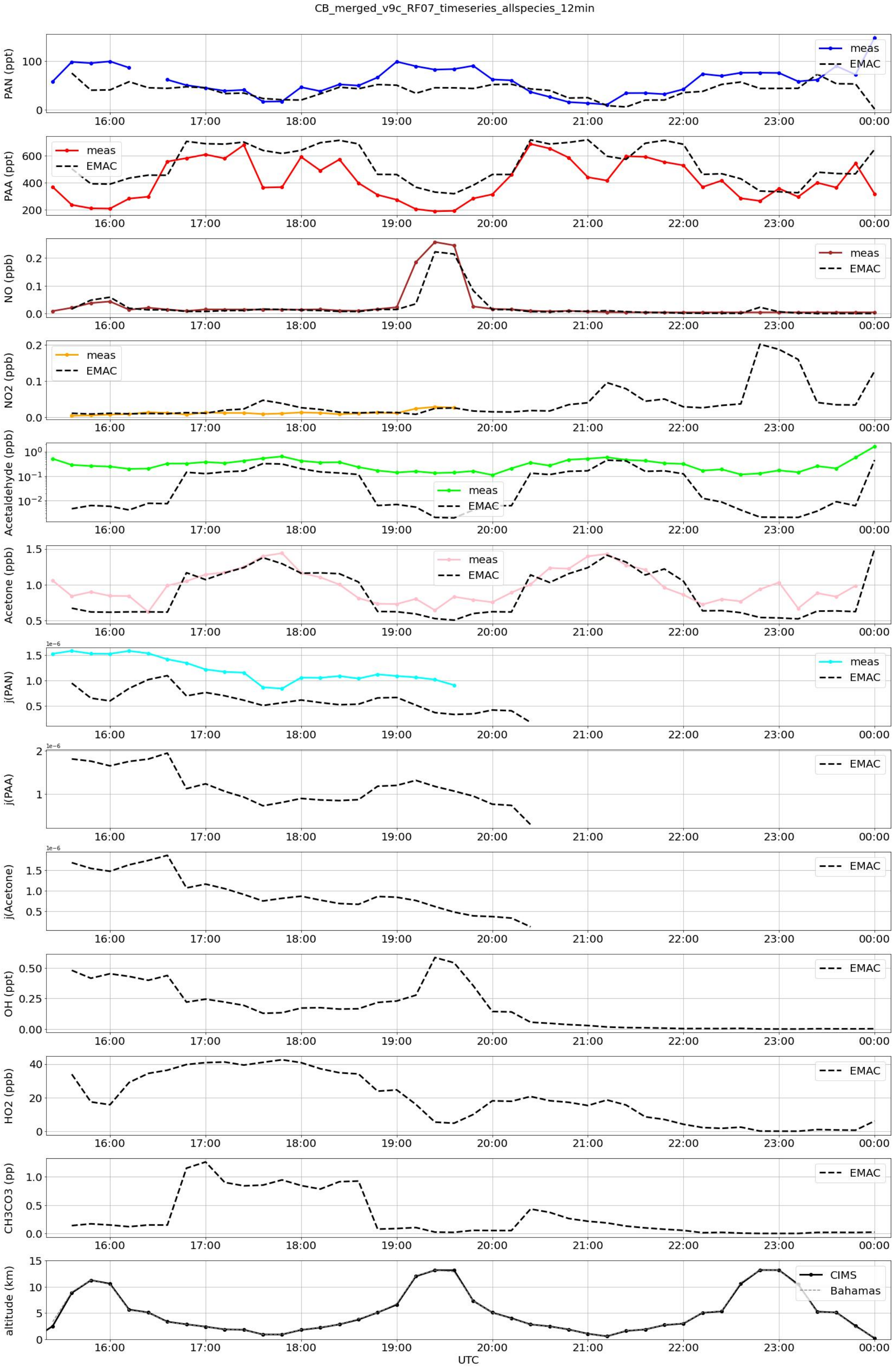

Figure A.0.8: Time series of resampled 12-min measured (HALO, solid lines) and modelled data (EMAC, dashed lines) of RF17 used for the steady state calculation. References to the data can be found in Table 1.

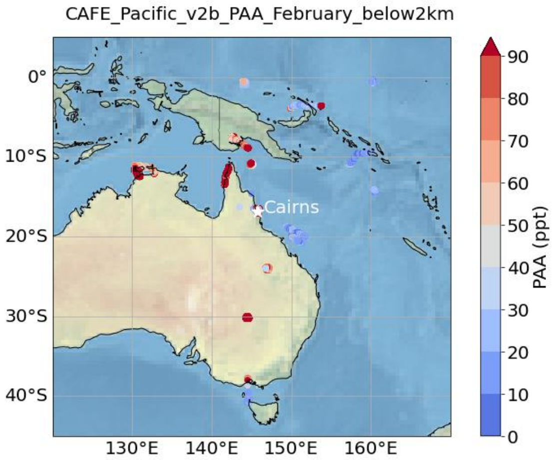

Figure A.0.9: Measured PAA with CIMS during CAFE Pacific at altitudes below 2 km.

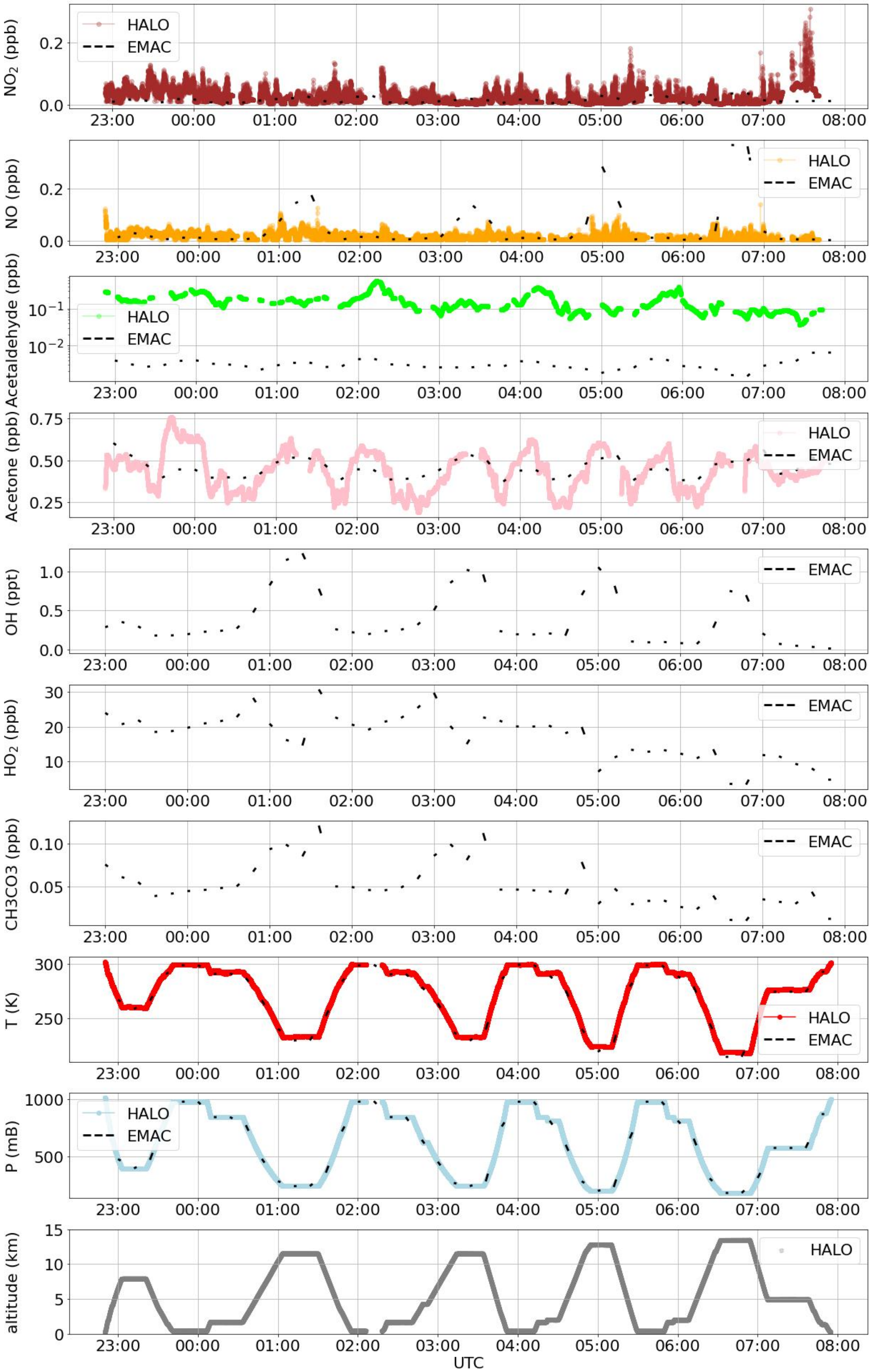

Figure A.0.10: Time series of measured (HALO, coloured lines) and modelled data (EMAC, dashed lines) of selected trace gases and meteorological parameters of RF17 used for the steady state calculation. References to the data can be found in Table 1.

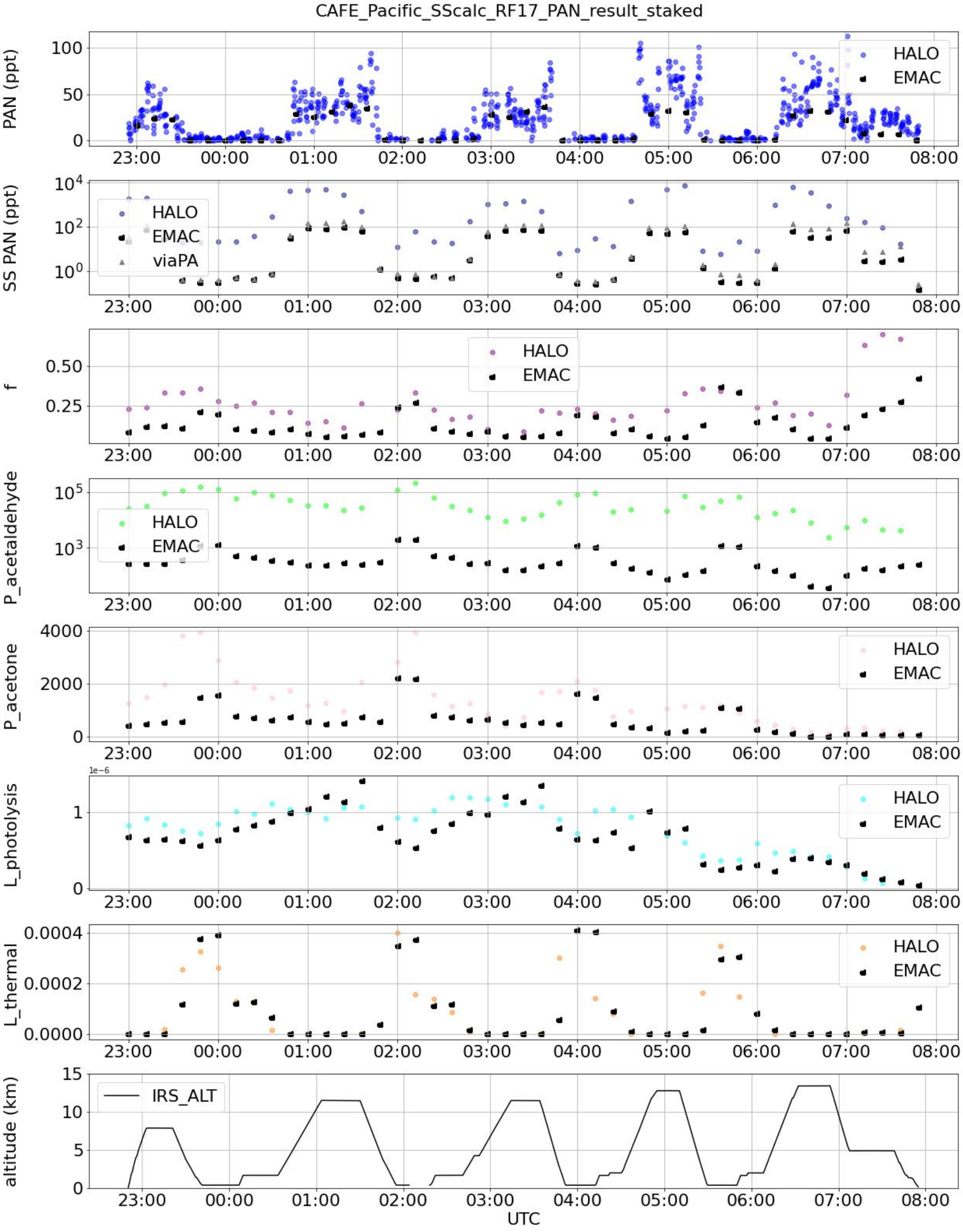

Figure A.0.11: Time series of the PAN steady state calculation output for RF17 during CAFE Pacific.

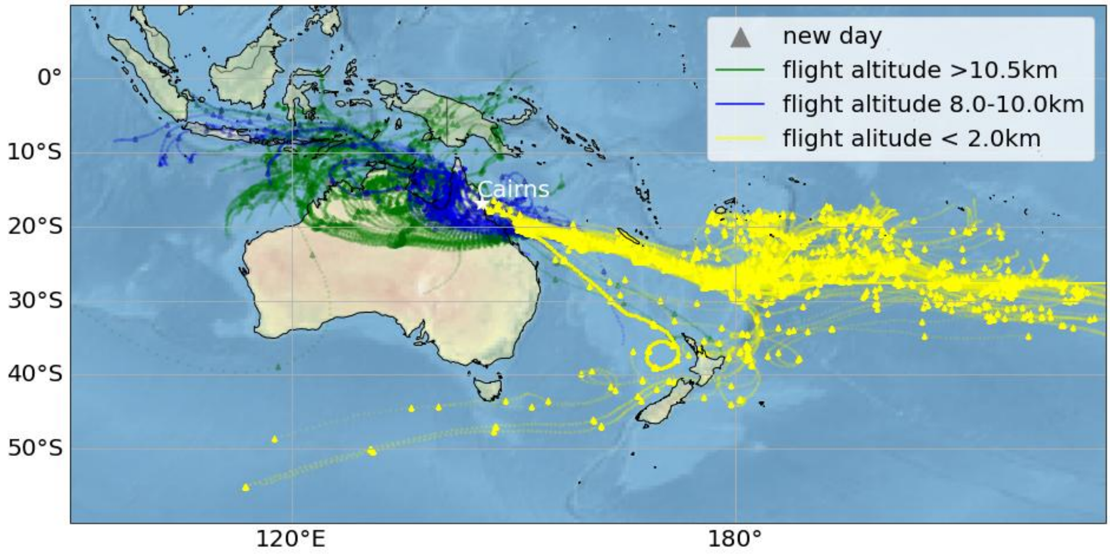

Figure A.0.12: 10-days back-trajectories calculated with HYSPLIT for RF17 during CAFE Pacific, colour-coded by measurement altitude ranges.

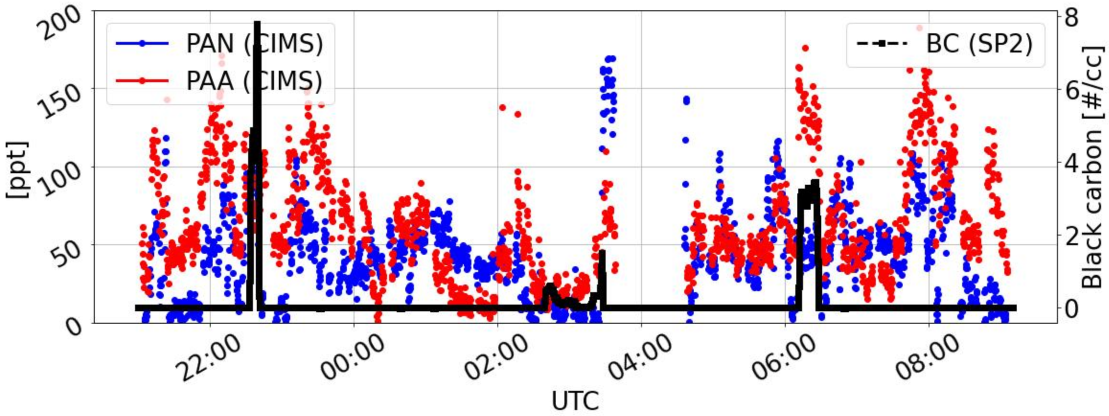

Figure A.0.13: Time series of PAN (blue), PAA (red), and black carbon (BC) (black) measurements in RF15 during CAFE Pacific. BC was measured with the SP2 instrument and is given in raw counts per cubic centimeter (#/cc).

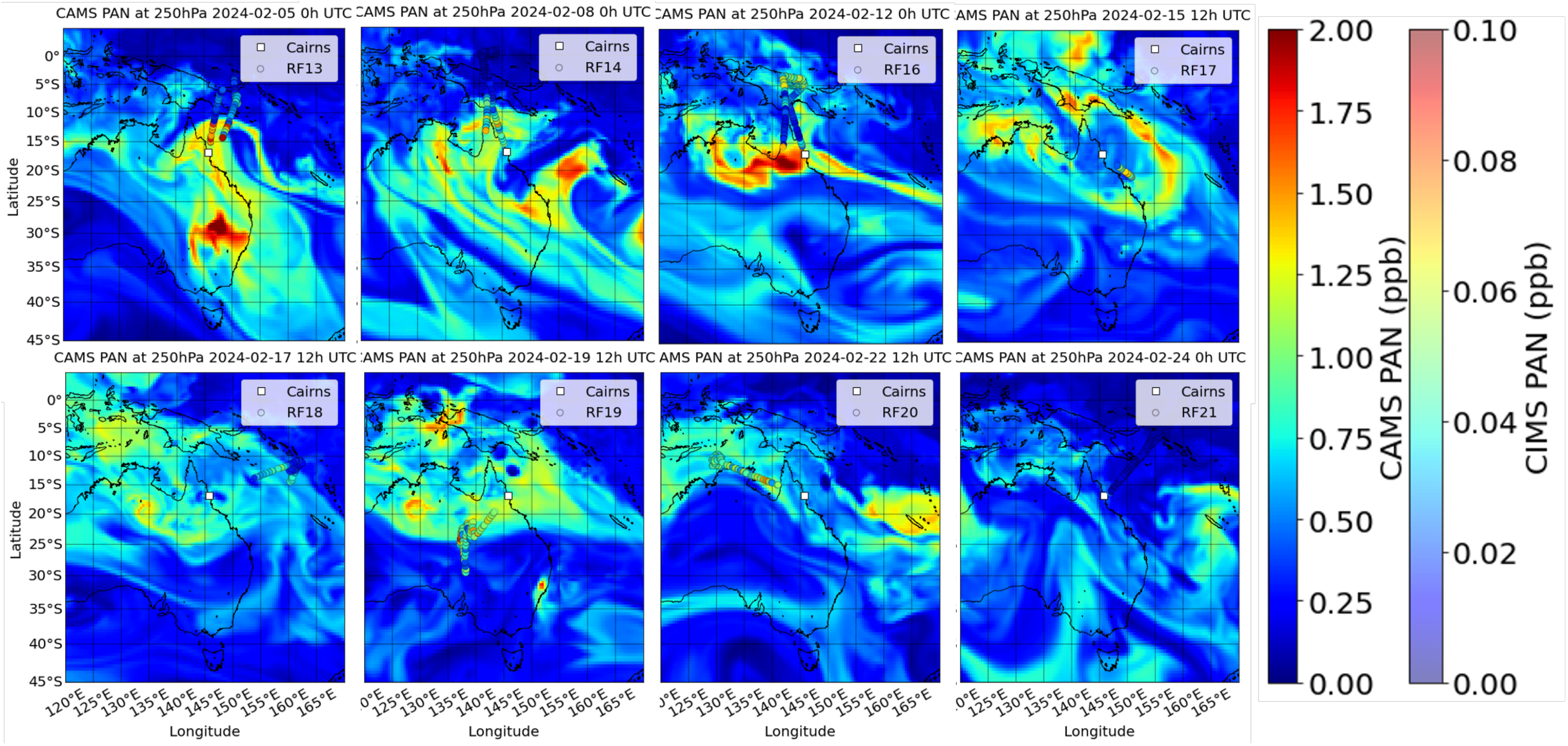

Figure A.0.14: Comparison of PAN measurements (coloured dots) with CAMS forecasts during CAFE Pacific for several research flights at 250 hPa. Note that the scale of the colour-codes differs by a factor of 20 for CAMS and CIMS levels. Generated using Copernicus Atmosphere Monitoring Service information (2024).

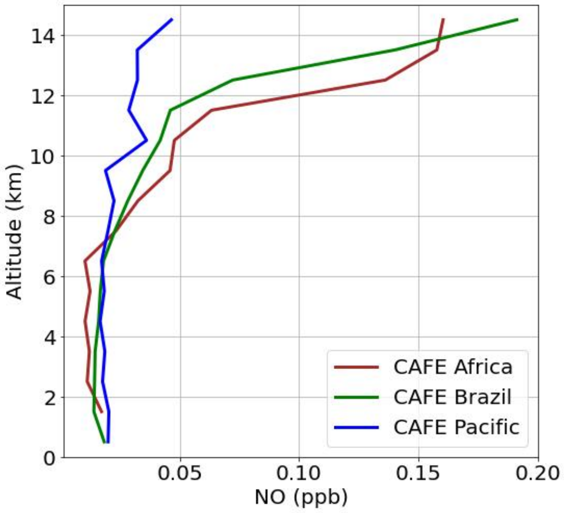

Figure A.0.15: Measured vertical median profiles of NO (left) and NO_2 (right panel) during all three CAFE campaigns. Only data above the instruments LOD is included. Note that NO_2 is calculated via photo stationary state assumptions from NO.

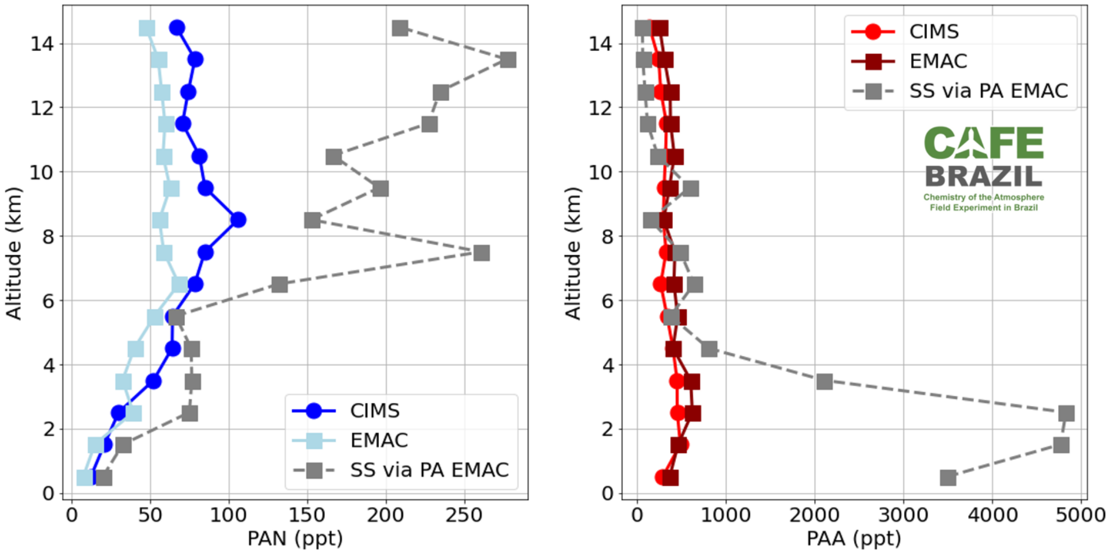

Figure A.0.16: Vertical profiles of steady state (SS) calculated PAN (left panel) and PAA (right panel) via EMAC PA (gray dashed line) for all flights during CAFE Brazil compared to observations (solid line with circles) and modelled results (solid line with squares).

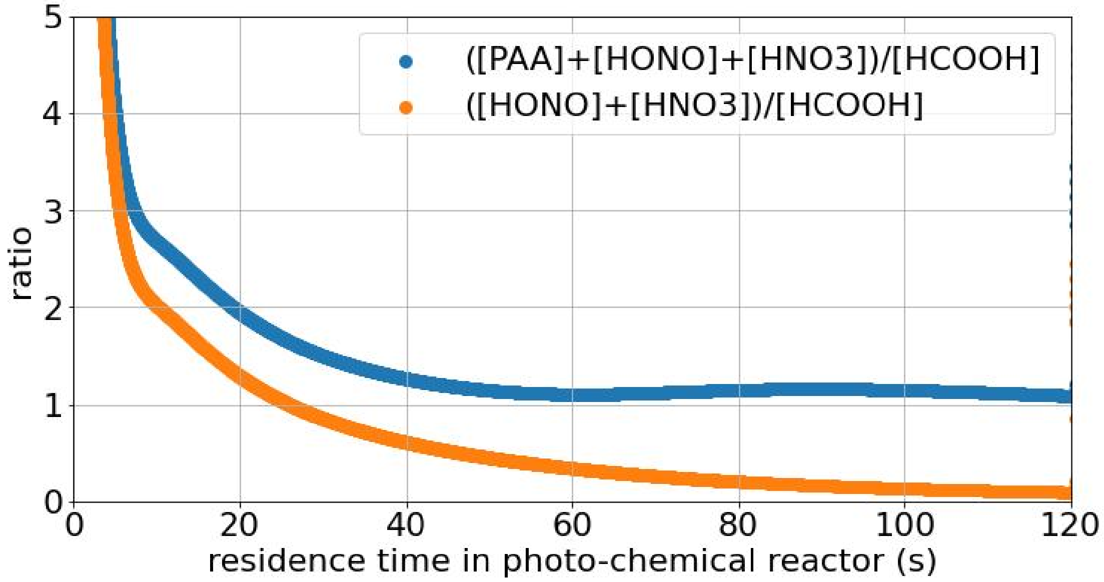

Figure A.0.17: Ratio of other detectable species with the acetate anion ($\frac{m}{z} = 59$) and formic acid in the photo-chemical source based on the FACSIMILE simulation in Figure A.0.5.

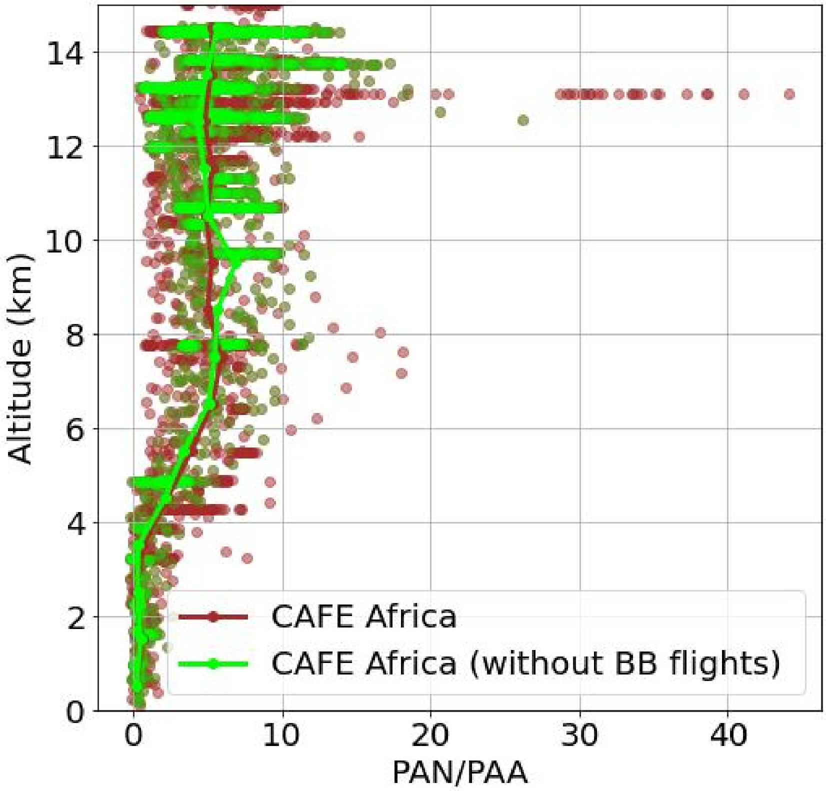

Figure A.0.18: Vertical profiles of the measured PAN-to-PAA ratio: One including all flights of CAFE Africa (brown) and the other excluding the biomass burning impacted flights RF04, RF10, RF12, and RF13 (lime). The lines represent the medians.

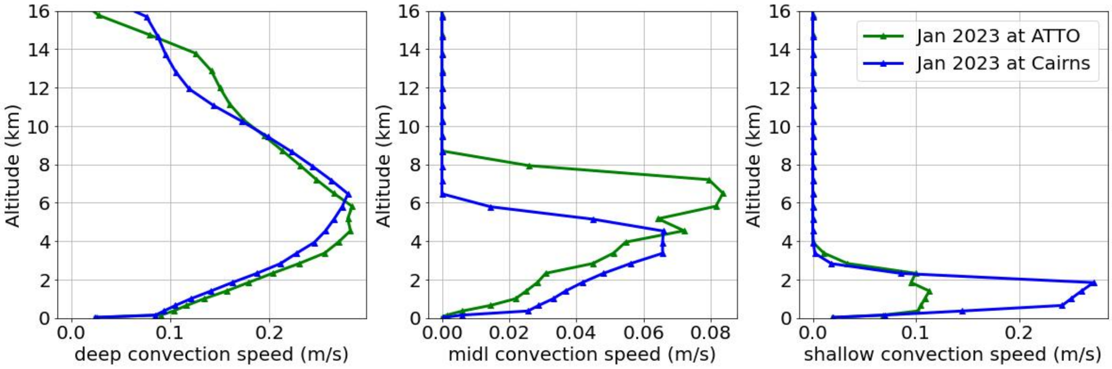

Figure A.0.19: Vertical profiles of daily maximal updraft speeds modelled for January 2023 above ATTO (green) and Cairns (blue), separated into deep, middle, and shallow convection (panels from left to right) from EMAC.

BIBLIOGRAPHY

Allen, H. M. et al. (2022). “H2O2 and CH3OOH (MHP) in the remote atmosphere: 1. Global distribution and regional influences.” In: *Journal of Geophysical Research: Atmospheres* 127.6, e2021JD035701. DOI: 10.1029/2021JD035701.

Alvarado, M. J. et al. (2010). “Nitrogen oxides and PAN in plumes from boreal fires during ARCTAS-B and their impact on ozone: an integrated analysis of aircraft and satellite observations.” In: *Atmospheric Chemistry and Physics* 10.20, pp. 9739–9760. DOI: 10.5194/acp-10-9739-2010.

Alvarado, M. J. et al. (2011). “Emission Ratios for Ammonia and Formic Acid and Observations of Peroxy Acetyl Nitrate (PAN) and Ethylene in Biomass Burning Smoke as Seen by the Tropospheric Emission Spectrometer (TES).” In: *Atmosphere (Basel)* 2.4, pp. 633–654. DOI: 10.3390/atmos2040633.

Andersen, S. T. et al. (2025). “Short-lived organic nitrates in a suburban temperate forest: an indication of efficient assimilation of reactive nitrogen by the biosphere?” In: *Atmospheric Chemistry and Physics* 25.11, pp. 5893–5909. DOI: 10.5194/acp-25-5893-2025.

Andreae, Meinrat O. (2019). “Emission of trace gases and aerosols from biomass burning – an updated assessment.” In: *Atmospheric Chemistry and Physics* 19.13, pp. 8523–8546. DOI: 10.5194/acp-19-8523-2019.

Andreae, Meinrat O. and Pedro Merlet (2001). “Emission of trace gases and aerosols from biomass burning.” In: *Global biogeochemical cycles* 15.4, pp. 955–966. DOI: 10.1029/2000GB001382.

Apel, E.C. et al. (2008). “Intercomparison of oxygenated volatile organic compound measurements at the SAPHIR atmosphere simulation chamber.” In: *Journal of Geophysical Research: Atmospheres* 113.D20. DOI: 10.1029/2008JD009865.

Arakawa, Akio (2004). “The cumulus parameterization problem: Past, present, and future.” In: *Journal of climate* 17.13, pp. 2493–2525.

Atkinson, R. et al. (2006). “Evaluated kinetic and photochemical data for atmospheric chemistry: Volume II - gas phase reactions of organic species.” In: *Atmospheric Chemistry and Physics* 6.11, pp. 3625–4055. DOI: 10.5194/acp-6-3625-2006.

Atkinson, Roger and Janet Arey (2003). “Atmospheric degradation of volatile organic compounds.” In: *Chemical reviews* 103.12, pp. 4605–4638. DOI: 10.1021/cr0206420.

Awad, Mohamed Ismail and Takeo Ohsaka (2003). “Potentiometric analysis of peroxyacetic acid in the presence of a large excess of hydrogen peroxide.” In: *Journal of Electroanalytical Chemistry* 544, pp. 35–40. DOI: 10.1016/S0022-0728(03)00057-3.

Awad, Mohamed Ismail et al. (2003). “Kinetic studies on the oxidation of iodide by peroxyacetic acid.” In: *Inorganica chimica acta* 344, pp. 253–256. DOI: 10.1016/S0020-1693(02)01337-3.

Awtrey, Alice D. and Robert E. Connick (1950). “The absorption spectra of I2-, I3-, I-, IO3-, S4O6 - and S2O3 . Heat of the reaction I3- = I2- + I-.” In: *Atmos Chem Phys*.

Baker, Alex R. et al. (2021). “Changing atmospheric acidity as a modulator of nutrient deposition and ocean biogeochemistry.” In: *Science Advances* 7.28, eabd8800. DOI: `10.1126/sciadv.abd8800`.

Bardakov, R. et al. (2022). “The Role of Convective Up- and Downdrafts in the Transport of Trace Gases in the Amazon.” In: *J Geophys Res Atmos* 127.18, e2022JD037265. DOI: `10.1029/2022JD037265`.

Barret, Brice et al. (2010). “Impact of West African Monsoon convective transport and lightning NOx production upon the upper tropospheric composition: a multi-model study.” In: *Atmospheric Chemistry and Physics* 10.12, pp. 5719–5738. DOI: `10.5194/acp-10-5719-2010`.

Bauer, Kristin (2012). *Bestimmung von Peressigsäure und Wasserstoffperoxid in der Atmosphäre*. Report. Max Planck Institute for Chemistry.

Beirle, S. et al. (2010). “Direct satellite observation of lightning-produced NO_x.” In: *Atmospheric Chemistry and Physics* 10.22, pp. 10965–10986. DOI: `10.5194/acp-10-10965-2010`.

Berasategui, Matias et al. (2020). “Reaction between CH3C(O)OOH (peracetic acid) and OH in the gas phase: a combined experimental and theoretical study of the kinetics and mechanism.” In: *Atmospheric Chemistry and Physics* 20.21, pp. 13541–13555. DOI: `10.5194/acp-20-13541-2020`.

Bichsel, Yves and Urs Von Gunten (1999). “Determination of iodide and iodate by ion chromatography with postcolumn reaction and UV/visible detection.” In: *Analytical chemistry* 71.1, pp. 34–38. DOI: `10.1021/ac980658j`.

Blanchard, P. et al. (1990). “A comparison of calibration and measruement tehcniques for gas chormatographic determination of atmospheric peroxyacetyl nitrate (PAN).” In: *Atmospheric Environment* 24A, pp. 2839–2846. DOI: `10.1016/0960-1686(90)90171-I`.

Bohn, Birger and Insa Lohse (2017). “Calibration and evaluation of CCD spectroradiometers for ground-based and airborne measurements of spectral actinic flux densities.” In: *Atmospheric measurement techniques* 10.9, pp. 3151–3174. DOI: `10.5194/amt-10-3151-2017`.

Bourtsoukidis, Efstratios et al. (2017). “An aircraft gas chromatograph–mass spectrometer System for Organic Fast Identification Analysis (SOFIA): design, performance and a case study of Asian monsoon pollution outflow.” In: *Atmospheric Measurement Techniques* 10.12, pp. 5089–5105. DOI: `10.5194/amt-10-5089-2017`.

Brauer, Heinz et al. (1989). “Peroxyacyl nitrates (PANS): Their physical and chemical properties.” In: *Air pollution*, pp. 1–38.

Brown, Steven S. and Jochen Stutz (2012). “Nighttime radical observations and chemistry.” In: *Chemical Society Reviews* 41.19, pp. 6405–6447. DOI: `10.1039/C2CS35181A`.

Chance, E. M. et al. (1977). “FACSIMILE: a computer program for flow and chemistry simulation, and general initial value problems.” In: *Report R* 8775.

Clarisse, Lieven et al. (2011). “Intercontinental transport of anthropogenic sulfur dioxide and other pollutants: An infrared remote sensing case study.” In: *Geophysical Research Letters* 38.19, n/a–n/a. DOI: `10.1029/2011gl048976`.

Coheur, P.-F. et al. (2007). “ACE-FTS observation of a young biomass burning plume: first reported measurements of C_2H_4, C_3H_6O, H_2CO and PAN by infrared occultation from space." In: *Atmospheric Chemistry and Physics* 7.20, pp. 5437–5446. DOI: 10.5194/acp-7-5437-2007.

Coheur, P.-F. et al. (2009). "IASI measurements of reactive trace species in biomass burning plumes." In: *Atmospheric Chemistry and Physics* 9.15, pp. 5655–5667. DOI: 10.5194/acp-9-5655-2009.

Crawford, James H. et al. (2021). "The Korea-United States air quality (KORUS-AQ) field study." In: *Elem Sci Anth* 9.1, p. 00163. DOI: 10.1525/elementa.2020.00163.

Crounse, J. D. et al. (2006). "Measurement of gas-phase hydroperoxides with CIMS." In: *Anal. chem.* 78. DOI: 10.1021/ac0604235.

Crowley, J. N. et al. (2018). "Insights into HOx and ROx chemistry in the boreal forest via measurement of peroxyacetic acid, peroxyacetic nitric anhydride (PAN) and hydrogen peroxide." In: *Atmospheric Chemistry and Physics* 18.18. ACP, pp. 13457–13479. DOI: 10.5194/acp-18-13457-2018.

Crowley, John N. et al. (2025). "Peroxy acetyl nitric anhydride (PAN) and peroxy acetic acid (PAA) over the Atlantic west of Africa during CAFE-Africa and the influence of biomass-burning." In: *Environmental Science: Atmospheres*. DOI: 10.1039/d5ea00006h.

Crutzen, Paul J. (2016). "The influence of nitrogen oxides on atmospheric ozone content." In: *Paul J. Crutzen: A Pioneer on Atmospheric Chemistry and Climate Change in the Anthropocene*, pp. 108–116. ISSN: 3319274597.

Crutzen, Paul J and Peter H Zimmermann (1991). "The changing photochemistry of the troposphere." In: *Tellus A: Dynamic Meteorology and Oceanography* 43.4, pp. 136–151. DOI: 10.3402/tellusa.v43i4.11943.

Curtius, Joachim et al. (2024). "Isoprene nitrates drive new particle formation in Amazon's upper troposphere." In: *Nature* 636.8041, pp. 124–130. DOI: 10.1038/s41586-024-08192-4.

De Deckker, Patrick (2016). "The Indo-Pacific Warm Pool: critical to world oceanography and world climate." In: *Geoscience Letters* 3.1, p. 20. DOI: 10.1186/s40562-016-0054-3.

De Gouw, J.A. et al. (2003). "Emission sources and ocean uptake of acetonitrile (CH3CN) in the atmosphere." In: *Journal of Geophysical Research: Atmospheres* 108.D11. DOI: 10.1029/2002JD002897.

Docherty, Kenneth S. et al. (2005). "Contributions of organic peroxides to secondary aerosol formed from reactions of monoterpenes with O3." In: *Environmental science & technology* 39.11, pp. 4049–4059. DOI: 10.1021/es050228s.

Doosthosseini, Ali et al. (2024). *Chat AI: A Seamless Slurm-Native Solution for HPC-Based Services*. arXiv: 2407.00110 [cs.DC]. URL: https://arxiv.org/abs/2407.00110.

Dörich, Raphael (2023). "Luft- und Bodengestützte Spurengasmessungen von Peroxyacylnitraten (PANs) und Peressigsäure (PAA) mittels Massenspektrometrie über chemische Ionisation mit Iodid Ionen." Thesis. Max Planck Institute for Chemistry, Mainz.

Dörich, Raphael et al. (2021). "Iodide CIMS and m/z 62: the detection of HNO3 as NO3- in the presence of PAN, peroxyacetic acid and ozone." In: *Atmospheric Measurement Techniques* 14.8, pp. 5319–5332. DOI: 10.5194/amt-14-5319-2021.

Eger, Philipp G. (2019). "A Chemical Ionisation Mass Spectrometer for Atmospheric Trace Gas Measurement: Characterisation and Deplyment in Field Studies." Thesis. Max Planck Institute for Chemistry, Mainz.

Eger, Philipp G. et al. (2019). "Chemical ionization quadrupole mass spectrometer with an electrical discharge ion source for atmospheric trace gas measurement." In: *Atmospheric Measurement Techniques* 12.3, pp. 1935–1954. DOI: `10.5194/amt-12-1935-2019`.

Eger, Philipp G. et al. (2020). "Pyruvic acid in the boreal forest: gas-phase mixing ratios and impact on radical chemistry." In: *Atmospheric Chemistry and Physics* 20.6, pp. 3697–3711. DOI: `10.5194/acp-20-3697-2020`.

Ehhalt, D. et al. (2001). "Atmospheric chemistry and greenhouse gases." In: *Climate change 2001: the scientific basis, Intergovernmental panel on climate change*. URL: `https://hal.science/hal-03333922`.

Elkins, J. W. et al. (2002). *Update: New Airborne Gas Chromatograph for NASA airborne platforms*. Conference Paper.

Engeln, Axel von and João Teixeira (2013). "A planetary boundary layer height climatology derived from ECMWF reanalysis data." In: *Journal of Climate* 26.17, pp. 6575–6590.

Ernle, Lisa et al. (2022). "Influence of ozone and humidity on PTR-MS and GC-MS VOC measurements with and without Na2S2O3 ozone scrubber." In: *Atmospheric Measurement Techniques Discussions* 2022, pp. 1–22. DOI: `10.5194/amt-16-1179-2023`.

Fahey, D. W. et al. (1986). "Reactive Nitrogen Species in the Troposphere: Measurements of NO, NO2, HNO3, Particulate Nitrate, Peroxyacetyl Nitrate (PAN), O3, and Total Reactive odd Nitrogen (NOy) at Niwot Ridge, Colorado." In: *Journal of Geophysical Research* 91, pp. 9781–9793. DOI: `10.1029/JD091iD09p09781`.

Fels, Michael and Wolfgang Junkermann (1994). "The occurrence of organic peroxides in air at a mountain site." In: *Geophysical research letters* 21.5, pp. 341–344.

Finlayson-Pitts, Barbara J. and James N. Pitts Jr. (1997). "Tropospheric air pollution: ozone, airborne toxics, polycyclic aromatic hydrocarbons, and particles." In: *Science* 276.5315, pp. 1045–1051. ISSN: 1095-9203.

Finlayson-Pitts, Barbara J. and James N. Pitts Jr. (2000). *Chemistry of the Upper and Lower Atmosphere Theory, Experiments, and Applications*. Academic Press.

Fischer, E. V. et al. (2014). "Atmospheric peroxyacetyl nitrate (PAN): a global budget and source attribution." In: *Atmospheric Chemistry and Physics* 14.5, pp. 2679–2698. DOI: `10.5194/acp-14-2679-2014`.

Fischer, E.V. et al. (2008). "Importing Ozone Precursors to the North American Free Troposphere: Spring 2008 Peroxyacetyl Nitrate (PAN) and NOx Observations from Mount Bachelor." In: *AGU Fall Meeting Abstracts*. Vol. 2008, A13F–01.

Fischer, E.V. et al. (2012). "The role of the ocean in the global atmospheric budget of acetone." In: *Geophysical Research Letters* 39.1.

Fischer, H. et al. (2008). "MIPAS: an instrument for atmospheric and climate research." In: *Atmospheric Chemistry and Physics* 8.8, pp. 2151–2188.

Fishman, Jack and Paul J. Crutzen (1978). "The origin of ozone in the troposphere." In: *Nature* 274.5674, pp. 855–858.

Fishman, Jack et al. (1996). "NASA GTE trace a experiment (September–October 1992): Overview." In: *Journal of Geophysical Research: Atmospheres* 101.D19, pp. 23865–23879.

Flemming, Johannes et al. (2017). "The CAMS interim Reanalysis of Carbon Monoxide, Ozone and Aerosol for 2003–2015." In: *Atmospheric Chemistry and Physics* 17.3, pp. 1945–1983. DOI: `10.5194/acp-17-1945-2017`.

Flocke, F. and A. J. Weinheimer (2003). *Measurement of peroxyacetyl nitrate (PAN), peroxypropionyl nitrate (PPN) and peroxymethacryloyl nitrate (MPAN) druing TRACE-P.* Report. National Center for Atmospheric Research Boulder, CO, United States.

Flocke, Frank M. et al. (2005). "On the Measurement of PANs by Gas Chromatography and Electron Capture Detection." In: *Journal of Atmospheric Chemistry* 52.1, pp. 19–43. DOI: `10.1007/s10874-005-6772-0`.

Friedrich, N. (2015). "Entwicklung und vergleichende Charakterisierung zweir Methoden zur nasschemischen Peressigsäure-Kalibration für die Chemische-Ionsiations-Massenspektrometrie." Thesis. MPIC.

Fu, Tzung-May et al. (2008). "Global budgets of atmospheric glyoxal and methylglyoxal, and implications for formation of secondary organic aerosols." In: *Journal of geophysical research: atmospheres* 113.D15.

Gaffney, Jeffrey S. and Nancy A. Marley (2021). "The impacts of peroxyacetyl nitrate in the atmosphere of megacities and large urban areas: A historical perspective." In: *ACS Earth and Space Chemistry* 5.8, pp. 1829–1841. ISSN: 2472-3452.

Galloway, James N. et al. (2004). "Nitrogen cycles: past, present, and future." In: *Biogeochemistry* 70, pp. 153–226.

Giez, A. et al. (2022). "Determination of the Measurement Errors for the HALO Basic Data System Bahamas by Means of Error Propagation." In: *Deutsches Zentrum für Luft- und Raumfahrt DLR*.

Giez, Andreas et al. (2021). *Calibration of a Nose Boom Mounted Airflow Sensor on an Atmospheric Research Aircraft by Inflight Maneuvers*. Tech. rep. Deutsches Zentrum für Luft- und Raumfahrt, Flugexperimente, Forschungsflugabteilung Oberpfaffenhofen. URL: `https://elib.dlr.de/145969/`.

Glatthor, N. et al. (2007). "Global peroxyacetyl nitrate (PAN) terieval in the upper troposphere from limb emission spectra of the Michelson Interferometer for Passive Atmospheric Sounding (MIPAS)." In: *Atmospheric Chemistry and Physics*.

Gomes Alves, E. et al. (2023). "Intra- and interannual changes in isoprene emission from central Amazonia." In: *Atmospheric Chemistry and Physics* 23.14. ACP, pp. 8149–8168. DOI: `10.5194/acp-23-8149-2023`.

Grewe, V. et al. (2001). "Origin and variability of upper tropospheric nitrogen oxides and ozone at northern mid-latitudes." In: *Atmospheric Environment* 35.20, pp. 3421–3433.

Grosjean, Daniel (1992). "Formic acid and acetic acid: emissions, atmospheric formation and dry deposition at two southern California locations." In: *Atmospheric Environment. Part A. General Topics* 26.18, pp. 3279–3286.

Guenther, Alex (2013). "Biological and chemical diversity of biogenic volatile organic emissions into the atmosphere." In: *International Scholarly Research Notices* 2013.1, p. 786290.

Haagen-Smit, A. J. (1952). "Chemistry and physiology of Los Angeles smog." In: *Industrial and engineering chemistry* 44.6, pp. 1342–1346.

Hamryszczak, Z. et al. (2023a). “HYPHOP: a tool for high-altitude, long-range monitoring of hydrogen peroxide and higher organic peroxides in the atmosphere.” In: *Atmospheric Measurement Techniques* 16.20. AMT, pp. 4741–4756. DOI: `10.5194/amt-16-4741-2023`.

Hamryszczak, Z. et al. (2023b). “Measurement report: Hydrogen peroxide in the upper tropical troposphere over the Atlantic Ocean and western Africa during the CAFE-Africa aircraft campaign.” In: *Atmospheric Chemistry and Physics* 23.10. ACP, pp. 5929–5943. DOI: `10.5194/acp-23-5929-2023`.

Hansel, Armin and Armin Wisthaler (2000). “A method for real-time detection of PAN, PPN and MPAN in ambient air.” In: *Geophysical Research Letters* 27.6, pp. 895–898. ISSN: 0094-8276.

Harris, Joyce M. et al. (2005). “Trajectory model sensitivity to differences in input data and vertical transport method.” In: *Journal of Geophysical Research: Atmospheres* 110.D14.

Hartmann, Antonia V. (2024). “Airborne NO2 measurements via photolysis-chemiluminescence in the upper tropical troposphere.” MA thesis. MPIC, Mainz. URL: `https://hdl.handle.net/21.11116/0000-000F-E5CD-8`.

Henneken, Hartmut et al. (2006). “Passive sampling of airborne peroxyacetic acid.” In: *Analytical chemistry* 78.18, pp. 6547–6555.

Hoell, J. M. et al. (1996). “Pacific Exploratory Mission-West A (PEM-West A): September–October 1991.” In: *Journal of Geophysical Research: Atmospheres* 101.D1, pp. 1641–1653.

Holanda, B. A. et al. (2020). “Influx of African biomass burning aerosol during the Amazonian dry season through layered transatlantic transport of black carbon-rich smoke.” In: *Atmospheric Chemistry and Physics* 20.8, pp. 4757–4785. DOI: `10.5194/acp-20-4757-2020`.

Holton, James R. et al. (1995). “Stratosphere-troposphere exchange.” In: *Reviews of geophysics* 33.4, pp. 403–439.

Holzinger, R. et al. (2005). “Oxygenated compounds in aged biomass burning plumes over the Eastern Mediterranean: evidence for strong secondary production of methanol and acetone.” In: *Atmospheric Chemistry and Physics* 5.1, pp. 39–46. DOI: `10.5194/acp-5-39-2005`.

Huey, L. Gregory (1995). “Reactions of SF6- and I- with AtmosphericTrace Gases.” In: *J. Phys. Chem* 99, pp. 5001–5008.

Huey, L. Gregory (2007). “Measurement of trace atmospheric species by chemical ionization mass spectrometry: Speciation of reactive nitrogen and future directions.” In: *Mass spectrometry reviews* 26.2, pp. 166–184. ISSN: 0277-7037.

Ichoku, Charles (July 2020). *African Biomass Burning and Its Atmospheric Impacts*. DOI: `10.1093/acrefore/9780190228620.013.523`.

Iyer, Siddharth et al. (2016). “Modeling the detection of organic and inorganic compounds using iodide-based chemical ionization.” In: *The Journal of Physical Chemistry A* 120.4, pp. 576–587.

Jacob, Daniel James et al. (2010). “The Arctic Research of the Composition of the Troposphere from Aircraft and Satellites (ARCTAS) mission: design, execution, and first results.” In: *Atmospheric Chemistry and Physics* 10.11, pp. 5191–5212.

Ji, Yi et al. (2020). "A vacuum ultraviolet ion source (VUV-IS) for iodide–chemical ionization mass spectrometry: a substitute for radioactive ion sources." In: *Atmospheric Measurement Techniques* 13.7, pp. 3683–3696. ISSN: 1867-1381.

Jiang, Zhe et al. (2016). "Ozone export from East Asia: The role of PAN." In: *Journal of Geophysical Research: Atmospheres* 121.11, pp. 6555–6563. DOI: `10.1002/2016jd024952`.

Jöckel, P. et al. (2010). "Development cycle 2 of the Modular Earth Submodel System (MESSy2)." In: *Geoscientific Model Development* 3.2, pp. 717–752. DOI: `10.5194/gmd-3-717-2010`.

Jöckel, Patrick et al. (2006). "The atmospheric chemistry general circulation model ECHAM5/MESSy1: consistent simulation of ozone from the surface to the mesosphere." In: *Atmospheric Chemistry and Physics* 6.12, pp. 5067–5104.

Jost, C. et al. (2003). "Atmospheric pressure chemical ionization mass spectrometry for the detection of tropospheric trace gases: the influence of clustering on sensitivity and precision." In: *International Journal of Mass Spectrometry* 223, pp. 771–782.

Jung, Sang-hyuk et al. (2014). "Determination of triiodide ion concentration using UV-visible spectrophotometry." In: *Asian Journal of Chemistry* 26.13, p. 4084.

Kames, Jost and Ulrich Schurath (1995). "Henry's law and hydrolysis-rate constants for peroxyacyl nitrates (PANs) using a homogeneous gas-phase source." In: *Journal of Atmospheric Chemistry* 21, pp. 151–164.

Keim, C. et al. (2008). "Vertical profile of peroxyacetyl nitrate (PAN) from MIPAS-STR measurements over Brazil in February 2005 and its contribution to tropical UT NOy partitioning." In: *Atmospheric Chemistry and Physics* 8.16. ACP, pp. 4891–4902. DOI: `10.5194/acp-8-4891-2008`.

Khan, M. A. H. et al. (2015). "The global budgets of organic hydroperoxides for present and pre-industrial scenarios." In: *Atmospheric Environment* 110, pp. 65–74.

Kurz, Christian and Volker Grewe (2002). "Lightning and thunderstorms, Part I: Observational data and model results." In: *Meteorologische Zeitschrift* 11.6, pp. 379–394.

LaFranchi, B.W. et al. (2009). "Closing the peroxy acetyl nitrate budget: observations of acyl peroxy nitrates (PAN, PPN, and MPAN) during BEARPEX 2007." In: *Atmospheric Chemistry and Physics* 9.19, pp. 7623–7641. DOI: `10.5194/acp-9-7623-2009`.

Laborde, M. et al. (2013). "Black carbon physical properties and mixing state in the European megacity Paris." In: *Atmospheric Chemistry and Physics* 13.11, pp. 5831–5856. DOI: `10.5194/acp-13-5831-2013`.

Lamarque, J.-F. et al. (1996). "Three-dimensional study of the relative contributions of the different nitrogen sources in the troposphere." In: *Journal of Geophysical Research: Atmospheres* 101.D17, pp. 22955–22968.

Leather, K. E. et al. (2012). "Acid-yield measurements of the gas-phase ozonolysis of ethene as a function of humidity using Chemical Ionisation Mass Spectrometry (CIMS)." In: *Atmospheric Chemistry and Physics* 12.1, pp. 469–479. DOI: `10.5194/acp-12-469-2012`.

Lee, Ben H. et al. (2014). "An iodide-adduct high-resolution time-of-flight chemical-ionization mass spectrometer: Application to atmospheric inorganic and organic compounds." In: *Environmental science & technology* 48.11, pp. 6309–6317.

Leighton, Philip (2012). *Photochemistry of air pollution*. Elsevier.

Lelieveld, Jos and Paul J. Crutzen (1994). "Role of deep cloud convection in the ozone budget of the troposphere." In: *Science* 264.5166, pp. 1759–1761.

Lelieveld, Jos and Frank J. Dentener (2000). “What controls tropospheric ozone?” In: *Journal of Geophysical Research: Atmospheres* 105.D3, pp. 3531–3551. DOI: `10.1029/1999jd901011`.

Lelieveld, Jos et al. (2016). “Global tropospheric hydroxyl distribution, budget and reactivity.” In: *Atmospheric Chemistry and Physics* 16.19, pp. 12477–12493.

Lind, John A. et al. (1987). “Aqueous phase oxidation of sulfur (IV) by hydrogen peroxide, methylhydroperoxide, and peroxyacetic acid.” In: *Journal of Geophysical Research: Atmospheres* 92.D4, pp. 4171–4177.

Lovelock, James E. (1977). “PAN in the natural environment; its possible significance in the epidemiology of skin cancer.” In: *Ambio*, pp. 131–133.

Malhi, Yadvinder and Oliver Phillips (2005). *Tropical forests and global atmospheric change*. OUP Oxford.

Mielke, Levi H. and Hans D. Osthoff (2012). “On quantitative measurements of peroxycarboxylic nitric anhydride mixing ratios by thermal dissociation chemical ionization mass spectrometry.” In: *International Journal of Mass Spectrometry* 310, pp. 1–9. DOI: `10.1016/j.ijms.2011.10.005`.

Millet, Dylan B. et al. (2010). “Global atmospheric budget of acetaldehyde: 3-D model analysis and constraints from in-situ and satellite observations.” In: *Atmospheric Chemistry and Physics* 10.7, pp. 3405–3425. DOI: `10.5194/acp-10-3405-2010`.

Moore, D. P. and J. J. Remedios (2010). “Seasonality of Peroxyacetyl nitrate (PAN) in the upper troposphere and lower stratosphere using the MIPAS-E instrument.” In: *Atmospheric Chemistry and Physics* 10.13, pp. 6117–6128. DOI: `10.5194/acp-10-6117-2010`.

Moxim, W.J. et al. (1996). “Simulated global tropospheric PAN: Its transport and impact on NO x.” In: *Journal of Geophysical Research: Atmospheres* 101.D7, pp. 12621–12638. ISSN: 0148-0227.

Northway, M.J. et al. (2004). “Evaluation of the role of heterogeneous oxidation of alkenes in the detection of atmospheric acetaldehyde.” In: *Atmospheric Environment* 38.35, pp. 6017–6028.

Nussbaumer, C. M. et al. (2021). “Modification of a conventional photolytic converter for improving aircraft measurements of NO2 via chemiluminescence.” In: *Atmospheric Measurement Techniques* 14.10, pp. 6759–6776. DOI: `10.5194/amt-14-6759-2021`.

Nussbaumer, Clara M. et al. (2024). “Ozone Formation Sensitivity to Precursors and Lightning in the Tropical Troposphere Based on Airborne Observations.” In: *Journal of Geophysical Research: Atmospheres* 129.14. DOI: `10.1029/2024jd041168`.

Nussbaumer, Clara M. et al. (2025). “Low tropospheric ozone over the Indo-Pacific warm pool related to non-electrified convection.” In: *Geophysical Research Letters* 52.5, e2024GL112788.

Ort, L. et al. (2024). “In-flight characterization of a compact airborne quantum cascade laser absorption spectrometer.” In: *Atmospheric Measurement Techniques* 17.11, pp. 3553–3565. DOI: `10.5194/amt-17-3553-2024`.

Ouwersloot, H. G. et al. (2015). “Revision of the convective transport module CVTRANS 2.4 in the EMAC atmospheric chemistry–climate model.” In: *Geoscientific Model Development* 8.8, pp. 2435–2445. DOI: `10.5194/gmd-8-2435-2015`.

Palmer, Donald A et al. (1984). “Triiodide ion formation equilibrium and activity coefficients in aqueous solution.” In: *Journal of solution chemistry* 13, pp. 673–683.

Pätz, H.W. et al. (2002). “Validation of a new method for the calibration of peroxy acetyl nitrate (PAN)-analyzers.” In: *GEFAHRSTOFFE REINHALTUNG DER LUFT-GERMAN EDITION-*, pp. 215–220.

Paulson, Suzanne E. and John H Seinfeld (1992). “Development and evaluation of a photooxidation mechanism for isoprene.” In: *Journal of Geophysical Research: Atmospheres* 97.D18, pp. 20703–20715.

Payne, Vivienne H. et al. (2017). “Spatial variability in tropospheric peroxyacetyl nitrate in the tropics from infrared satellite observations in 2005 and 2006.” In: *Atmospheric Chemistry and Physics* 17.10, pp. 6341–6351.

Phillips, G. J. et al. (2013). “Peroxyacetyl nitrate (PAN) and peroxyacetic acid (PAA) measurements by iodide chemical ionisation mass spectrometry: first analysis of results in the boreal forest and implications for the measurement of PAN fluxes.” In: *Atmospheric Chemistry and Physics* 13.3, pp. 1129–1139. DOI: `10.5194/acp-13-1129-2013`.

Pozzer, A. et al. (2022). “Simulation of organics in the atmosphere: evaluation of EMAC v2.54 with the Mainz Organic Mechanism (MOM) coupled to the ORACLE (v1.0) submodel.” In: *Geoscientific Model Development* 15.6, pp. 2673–2710. DOI: `10.5194/gmd-15-2673-2022`.

Price, Colin and David Rind (1992). “A simple lightning parameterization for calculating global lightning distributions.” In: *Journal of Geophysical Research: Atmospheres* 97.D9, pp. 9919–9933.

Remedios, J.J. et al. (2007). “Detection of organic compound signatures in infra-red, limb emission spectra observed by the MIPAS-B2 balloon instrument.” In: *Atmospheric Chemistry and Physics* 7.6, pp. 1599–1613.

Rex, M. et al. (2014). “A tropical West Pacific OH minimum and implications for stratospheric composition.” In: *Atmospheric Chemistry and Physics* 14.9, pp. 4827–4841. DOI: `10.5194/acp-14-4827-2014`.

Ringsdorf, A. et al. (2024). “Investigating carbonyl compounds above the Amazon rainforest using a proton-transfer-reaction time-of-flight mass spectrometer (PTR-ToF-MS) with NO+ chemical ionization.” In: *Atmospheric Chemistry and Physics* 24.20, pp. 11883–11910. DOI: `10.5194/acp-24-11883-2024`.

Roberts, James M. (1990). “The atmospheric chemistry of organic nitrates.” In: *Atmospheric Environment. Part A. General Topics* 24.2, pp. 243–287. URL: `https://www.sciencedirect.com/science/article/pii/096016869090108Y?via%3Dihub`.

Roberts, James M. (2007). “PAN and related compounds.” In: *Volatile organic compounds in the atmosphere*, pp. 221–268.

Roberts, James M. et al. (1995). “Relationships between PAN and ozone at sites in eastern North America.” In: *Journal of Geophysical Research: Atmospheres* 100.D11, pp. 22821–22830.

Roberts, James M. et al. (2001). “Application of a sequential reaction model to PANs and aldehyde measurements in two urban areas.” In: *Geophysical research letters* 28.24, pp. 4583–4586.

Roberts, James M. et al. (2002). “Ground-based measurements of peroxycarboxylic nitric anhydrides (PANs) during the 1999 Southern Oxidants Study Nashville Intensive." In: *Journal of Geophysical Research: Atmospheres* 107.D21. DOI: 10.1029/2001jd000947.

Roberts, James M. et al. (2004). "Measurement of peroxycarboxylic nitric anhydrides (PANs) during the ITCT 2K2 aircraft intensive experiment." In: *Journal of Geophysical Research: Atmospheres* 109.D23. DOI: 10.1029/2004jd004960.

Röder, Lenard L. et al. (2024). "Quantitative analysis of temporal stability and instrument performance during field experiments of an airborne QCLAS via Allan–Werle-plots." In: *Applied Physics B* 130.7, p. 118. DOI: 10.1007/s00340-024-08254-5.

Roiger, A. et al. (2011). "An aircraft-borne chemical ionization – ion trap mass spectrometer (CI-ITMS) for fast PAN and PPN measurements." In: *Atmospheric Measurement Techniques* 4.2, pp. 173–188. DOI: 10.5194/amt-4-173-2011.

Russo, R. S. et al. (2003). "Chemical composition of Asian continental outflow over the western Pacific: Results from Transport and Chemical Evolution over the Pacific (TRACE-P)." In: *Journal of Geophysical Research: Atmospheres* 108.D20. DOI: 10.1029/2002jd003184.

Sander, R. et al. (2019). "The community atmospheric chemistry box model CAABA / MECCA-4.0." In: *Geoscientific Model Development* 12.4, pp. 1365–1385. DOI: 10.5194/gmd-12-1365-2019.

Sander, Rolf (1999). *Compilation of Henry's law constants for inorganic and organic species of potential importance in environmental chemistry.*

Schlager, Hans et al. (2012). "Chemical composition of the atmosphere." In: *Atmospheric Physics: Background–Methods–Trends*. Springer, pp. 17–35.

Schultz, Martin G. et al. (1999). "On the origin of tropospheric ozone and NOx over the tropical South Pacific." In: *Journal of Geophysical Research: Atmospheres* 104.D5, pp. 5829–5843.

Schumann, U. and H. Huntrieser (2007). "The global lightning-induced nitrogen oxides source." In: *Atmospheric Chemistry and Physics* 7.14, pp. 3823–3907. DOI: 10.5194/acp-7-3823-2007.

Seinfeld, John H. and Spyros N. Pandis (1998). *Atmospheric chemistry and physics: from air pollution to climate change*. John Wiley and Sons. ISBN: 1118947401.

Shogrin, Madison J. et al. (2024). "Changes to Peroxyacyl Nitrates (PANs) Over Megacities in Response to COVID-19 Tropospheric NO2 Reductions Observed by the Cross-Track Infrared Sounder (CrIS)." In: *Geophysical Research Letters* 51.6. DOI: 10.1029/2023gl104854.

Singh, H. B. (1981a). "PAN in the unpolluted atmosphere: an important reservoir species." In: *AGU*.

Singh, H. B. and L. J. Salas (1983). "Peroxyacetyl nitrate in the free troposphere." In: *Nature* 302.5906, pp. 326–328. ISSN: 0028-0836. URL: https://www.nature.com/articles/302326a0.pdf.

Singh, H. B. et al. (1990). "Peroxyacetyl Nitrate Measurements Over the Brazilian Amazon Basin During the Wet Season: Relationships With Nitrogen Oxides and Ozone." In: *Journal of Geophysical Research* 95, p. 16.

Singh, H. B. et al. (1996a). "Impact of biomass burning emissions on the composition of the South Atlantic troposphere: Reactive nitrogen and ozone." In: *Journal of Geophysical Research: Atmospheres* 101.D19, pp. 24203–24219. DOI: 10.1029/96jd01018.

Singh, H. B. et al. (1996b). “Reactive nitrogen and ozone over the western Pacific: Distribution, partitioning, and sources.” In: *Journal of Geophysical Research: Atmospheres* 101.D1, pp. 1793–1808. DOI: 10.1029/95jd01029.

Singh, H. B. et al. (1999). “SONEX airborne mission and coordinated POLINAT-2 activity: Overview and accomplishments.” In: *Geophysical Research Letters* 26.20, pp. 3053–3056.

Singh, H. B. et al. (2000a). “Biomass burning influences on the composition of the remote South Pacific troposphere: analysis based on observations from PEM-Tropics-A.” In: *Atmospheric Environment* 34.4, pp. 635–644.

Singh, H. B. et al. (2000b). “Distribution and fate of selected oxygenated organic species in the troposphere and lower stratosphere over the Atlantic.” In: *Journal of Geophysical Research: Atmospheres* 105.D3, pp. 3795–3805.

Singh, H. B. et al. (2001). “Evidence from the Pacific troposphere for large global sources of oxygenated organic compounds.” In: *Nature* 410.6832, pp. 1078–1081.

Singh, H. B. et al. (2004). “Analysis of the atmospheric distribution, sources, and sinks of oxygenated volatile organic chemicals based on measurements over the Pacific during TRACE-P.” In: *Journal of Geophysical Research: Atmospheres* 109.D15.

Singh, H. B. et al. (2006). “Overview of the summer 2004 Intercontinental Chemical Transport Experiment–North America (INTEX-A).” In: *Journal of Geophysical Research: Atmospheres* 111.D24. DOI: 10.1029/2006jd007905.

Singh, H. B. et al. (2007). “Reactive nitrogen distribution and partitioning in the North American troposphere and lowermost stratosphere.” In: *Journal of Geophysical Research: Atmospheres* 112.D12.

Singh, H. B. et al. (2009). “Chemistry and transport of pollution over the Gulf of Mexico and the Pacific: spring 2006 INTEX-B campaign overview and first results.” In: *Atmospheric Chemistry and Physics* 9.7, pp. 2301–2318. DOI: 10.5194/acp-9-2301-2009.

Singh, Hanwant B. (1987). “Reactive nitrogen in the troposphere.” In: *Environmental science & technology* 21.4, pp. 320–327.

Singh H. B.; Hanst, P. L. (1981b). “Peroxyacetyl nitrate PAN in the unpolluted atmosphere An important reservoir for nitrogen oxides.” In: *Geophysical Research Letters* 8, pp. 941–944.

Slusher, Darlene L. (2004). “A thermal dissociation–chemical ionization mass spectrometry (TD-CIMS) technique for the simultaneous measurement of peroxyacyl nitrates and dinitrogen pentoxide.” In: *Journal of Geophysical Research* 109.D19. DOI: 10.1029/2004jd004670.

Sparks, J. P. et al. (2003). “The uptake of gaseous organic nitrogen by leaves: A significant global nitrogen transfer process.” In: *Geophysical Research Letters* 30.23. DOI: 10.1029/2003gl018578.

Stavrakou, Trissevgeni et al. (2021). “Atmospheric impacts of COVID-19 on NOx and VOC levels over China based on TROPOMI and IASI satellite data and modeling.” In: *Atmosphere* 12.8, p. 946.

Stein, Ariel F. et al. (2015). “NOAA’s HYSPLIT atmospheric transport and dispersion modeling system.” In: *Bulletin of the American Meteorological Society* 96.12, pp. 2059–2077.

Stephens, Edgar R. (1969). “The formation, reactions and properties of peroxyacyl nitrates (PANs) in photochemical air pollution.” In: *Advances in environmental sciences* 1.

Stephens, Edgar R. (1987). “Smog studies of the 1950s.” In: *Eos, Transactions American Geophysical Union* 68.7, pp. 89–93.

Tadic, Ivan et al. (2021). “Central role of nitric oxide in ozone production in the upper tropical troposphere over the Atlantic Ocean and western Africa.” In: *Atmospheric chemistry and physics* 21.10, pp. 8195–8211.

Talbot, R. W. et al. (1999). “Reactive nitrogen budget during the NASA SONEX Mission.” In: *Geophysical Research Letters* 26.20, pp. 3057–3060. DOI: `10.1029/1999gl-900589`.

Talukdar, Ranajit K. et al. (1995). “Investigation of the loss processes for peroxyacetyl nitrate in the atmosphere: UV photolysis and reaction with OH.” In: *Journal of Geophysical Research: Atmospheres* 100.D7, pp. 14163–14173.

Tanimoto, Hiroshi et al. (1999). “A new measurement technique of peroxyacetyl nitrate at parts per trillion by volume levels: Gas chromatography/negative ion chemical ionization mass spectrometry.” In: *Journal of Geophysical Research: Atmospheres* 104.D17, pp. 21343–21354.

Taylor, O. Clifton (1969). “Importance of peroxyacetyl nitrate (PAN) as a phytotoxic air pollutant.” In: *Journal of the Air Pollution Control Association* 19.5, pp. 347–351.

Tereszchuk, K. A. et al. (2013). “Observations of peroxyacetyl nitrate (PAN) in the upper troposphere by the Atmospheric Chemistry Experiment-Fourier Transform Spectrometer (ACE-FTS).” In: *Atmospheric Chemistry and Physics* 13.11, pp. 5601–5613. DOI: `10.5194/acp-13-5601-2013`.

Thompson, Chelsea R et al. (2022). “The NASA Atmospheric Tomography (ATom) mission: Imaging the chemistry of the global atmosphere.” In: *Bulletin of the American Meteorological Society* 103.3, E761–E790.

Thornton, Donald C. et al. (2002). “Fast airborne sulfur dioxide measurements by atmospheric pressure ionization mass spectrometry (APIMS).” In: *Journal of Geophysical Research: Atmospheres* 107.D22, ACH 13–1–ACH 13–10. ISSN: 0148-0227.

Toon, Owen B. et al. (2016). “Planning, implementation, and scientific goals of the Studies of Emissions and Atmospheric Composition, Clouds and Climate Coupling by Regional Surveys (SEAC4RS) field mission.” In: *Journal of Geophysical Research: Atmospheres* 121.9, pp. 4967–5009.

Tost, Holger et al. (2007). “Lightning and convection parameterisations - uncertainties in global modelling.” In: *Atmospheric Chemistry and Physics* 7.17, pp. 4553–4568. DOI: `10.5194/acp-7-4553-2007`.

Tost, Holger et al. (2010). “Uncertainties in atmospheric chemistry modelling due to convection parameterisations and subsequent scavenging.” In: *Atmospheric Chemistry and Physics* 10.4, pp. 1931–1951.

Travis, K. R. et al. (2020). “Constraining remote oxidation capacity with ATom observations.” In: *Atmospheric Chemistry and Physics* 20.13, pp. 7753–7781. DOI: `10.5194/acp-20-7753-2020`.

Travis, K. R. et al. (2024). “Impact of improved representation of volatile organic compound emissions and production of NOx reservoirs on modeled urban ozone production." In: *Atmospheric Chemistry and Physics* 24.16, pp. 9555–9572. DOI: 10.5194/acp-24-9555-2024.

Treadaway, V. et al. (2018). "Measurement of formic acid, acetic acid and hydroxyacetaldehyde, hydrogen peroxide, and methyl peroxide in air by chemical ionization mass spectrometry: airborne method development." In: *Atmospheric Measurement Techniques* 11.4, pp. 1901–1920. DOI: 10.5194/amt-11-1901-2018.

Tripathi, Nidhi et al. (2025). "Impacts of convection, chemistry, and forest clearing on biogenic volatile organic compounds over the Amazon." In: *Nature Communications* 16.1, pp. 1–10.

Troy, Robert C et al. (1991). "Non-metal redox kinetics: Iodine monobromide reaction with iodide ion and the hydrolysis of IBr." In: *Inorganic Chemistry* 30.25, pp. 4838–4845.

Tuazon, Ernesto C. et al. (1981). "Trace pollutant concentrations in a multiday smog episode in the California South Coast Air Basin by long path length Fourier transform infrared spectroscopy." In: *Environmental science and technology* 15.10, pp. 1232–1237. ISSN: 0013-936X.

Turnipseed, A. A. et al. (2006). "Eddy covariance fluxes of peroxyacetyl nitrates (PANs) and NOy to a coniferous forest." In: *Journal of Geophysical Research: Atmospheres* 111.D9.

Tyndall, Geoffrey S. et al. (1995). "Rate coefficients for the reactions of OH radicals with methylglyoxal and acetaldehyde." In: *International journal of chemical kinetics* 27.10, pp. 1009–1020.

Tyndall, Geoffrey S. et al. (2001). "Atmospheric chemistry of small organic peroxy radicals." In: *Journal of Geophysical Research: Atmospheres* 106.D11, pp. 12157–12182.

Veres, P. et al. (2008). "Development of negative-ion proton-transfer chemical-ionization mass spectrometry (NI-PT-CIMS) for the measurement of gas-phase organic acids in the atmosphere." In: *International Journal of Mass Spectrometry* 274.1-3, pp. 48–55. DOI: 10.1016/j.ijms.2008.04.032.

Voigt, Christiane et al. (2022). "Cleaner skies during the COVID-19 lockdown." In: *Bulletin of the American Meteorological Society* 103.8, E1796–E1827.

Volz-Thomas, A. et al. (2002). "Automatic gas chromatograph and calibration system for ambient measurements of PAN and PPN." In: *Environmental science and pollution research* 9.PreJuSER-34322, pp. 72–76.

Wang, Hao et al. (2024). "Regional to global distributions, trends, and drivers of biogenic volatile organic compound emission from 2001 to 2020." In: *Atmospheric Chemistry and Physics* 24.5, pp. 3309–3328.

Wang, S. et al. (2019). "Atmospheric Acetaldehyde: Importance of Air-Sea Exchange and a Missing Source in the Remote Troposphere." In: *Geophys Res Lett* 46.10, pp. 5601–5613. DOI: 10.1029/2019GL082034.

Wang, Xue-Bin et al. (2006). "Ddetermination of the electron affinity of the acetyloxyl radical-(CH3COO) by low temperature anion." In: *J. Phys. Chem* 110, pp. 5047–5050.

Wang, Yin et al. (2016). "Observation of atmospheric peroxides during Wangdu Campaign 2014 at a rural site in the North China Plain." In: *Atmospheric Chemistry and Physics* 16.17, pp. 10985–11000.

Warneck, Peter and Thomas Zerbach (1992). “Synthesis of peroxyacetyl nitrate in air by acetone photolysis.” In: *Environmental science and technology* 26.1, pp. 74–79. ISSN: 0013-936X.

Wei, Nana et al. (2024). “characterization of reactive nitrogen in the global upper troposphere using reent and historic commercial and research aircraft campaigns and GEOS-Chem.” In: *EGUsphere*. DOI: 10.5194/egusphere-2024-3388.

Wendisch, Manfred et al. (2016). “ACRIDICON–CHUVA campaign: Studying tropical deep convective clouds and precipitation over Amazonia using the new German research aircraft HALO.” In: *Bulletin of the American Meteorological Society* 97.10, pp. 1885–1908.

Wennberg, P. O. et al. (1998). “Hydrogen radicals, nitrogen radicals, and the production of O3 in the upper troposphere.” In: *science* 279.5347, pp. 49–53.

Wiegele, A et al. (2012). “Global distributions of C 2 H 6, C 2 H 2, HCN, and PAN retrieved from MIPAS reduced spectral resolution measurements.” In: *Atmospheric Measurement Techniques* 5.4, pp. 723–734.

Wienhold, FG et al. (1998). “TRISTAR-A tracer in-situ TDLAS for atmospheric research.” In: *Applied Physics B* 67, pp. 411–417. DOI: 10.1007/s003400050524.

Williams, Jonathan and Ralf Koppmann (2007). “Volatile organic compounds in the atmosphere: an overview.” In: *Volatile organic compounds in the atmosphere* 1.

Wofsy, Steven C. (2011). “HIAPER Pole-to-Pole Observations (HIPPO): fine-grained, global-scale measurements of climatically important atmospheric gases and aerosols.” In: *Philosophical Transactions of the Royal Society A: Mathematical, Physical and Engineering Sciences* 369.1943, pp. 2073–2086. DOI: 10.1098/rsta.2010.0313.

Wolfe, G. M. et al. (2007). “Influence of trans-Pacific pollution transport on acyl peroxy nitrate abundances and speciation at Mount Bachelor Observatory during INTEX-B.” In: *Atmospheric Chemistry and Physics* 7.20, pp. 5309–5325. URL: https://acp.copernicus.org/articles/7/5309/2007/acp-7-5309-2007.pdf.

Wolfe, G. M. et al. (2009). “Eddy covariance fluxes of acyl peroxy nitrates (PAN, PPN and MPAN) above a Ponderosa pine forest.” In: *Atmospheric Chemistry and Physics* 9.2, pp. 615–634. DOI: 10.5194/acp-9-615-2009.

Wolfe, G. M. et al. (2021). “Photochemical evolution of the 2013 California Rim Fire: synergistic impacts of reactive hydrocarbons and enhanced oxidants.” In: *Atmospheric Chemistry and Physics Discussions* 2021, pp. 1–35.

Wüst, Laura et al. (2024). “Influence of ambient NO and NO2 on the quantification of total peroxy nitrates (ΣPNs) and total alkyl nitrates (ΣANs) by thermal dissociation cavity ring-down spectroscopy (TD-CRDS).” In: *EGUsphere* 2024, pp. 1–26.

Xiao, Junyang et al. (2019). “Simultaneous spectrophotometric determination of peracetic acid and the coexistent hydrogen peroxide using potassium iodide as the indicator.” In: *Analytical methods* 11.14, pp. 1930–1938.

Xu, W. et al. (2023). “O3 and PAN in southern Tibetan Plateau determined by distinct physical and chemical processes.” In: *Atmospheric Chemistry and Physics* 23.13, pp. 7635–7652. DOI: 10.5194/acp-23-7635-2023.

Yokelson, Robert J. et al. (2009). “Emissions from biomass burning in the Yucatan.” In: *Atmospheric Chemistry and Physics* 9.15, pp. 5785–5812.

Zahn, A. et al. (2012). “A fast and precise chemiluminescence ozone detector for eddy flux and airborne application.” In: *Atmospheric Measurement Techniques* 5.2, pp. 363–375.

Zhang, X. et al. (2010). “Peroxyacetic acid in urban and rural atmosphere: concentration, feedback on PAN-NOx cycle and implication on radical chemistry.” In: *Atmospheric Chemistry and Physics* 10.2, pp. 737–748. DOI: `10.5194/acp-10-737-2010`.

Zheng, W. et al. (2011). “Characterization of a thermal decomposition chemical ionization mass spectrometer for the measurement of peroxy acyl nitrates (PANs) in the atmosphere.” In: *Atmospheric Chemistry and Physics* 11.13, pp. 6529–6547. DOI: `10.5194/acp-11-6529-2011`.

Zhu, Liye et al. (2015). “TES observations of the interannual variability of PAN over Northern Eurasia and the relationship to springtime fires.” In: *Geophysical Research Letters* 42.17, pp. 7230–7237. DOI: `10.1002/2015gl065328`.

LIST OF FIGURES

LIST OF TABLES

ACRONYMS

AA	acetic acid
ATTO	Amazon Tall Tower Observatory
BAIRN-VIP	Biosphere-Atmosphere Interactions and the Reactive Nitrogen Budget: VertIcal Profiles of Key Species
ATom	Atmospheric Tomography mission
BAHAMAS	Basic HALO Measurement and Sensor System
BB	biomass burning
BC	black carbon
CAMS	Copernicus Atmospheric Monitoring Service
CIMS	Chemical Ionisation Mass Spectrometry
CAFE	Chemistry of the Atmosphere Field Experiments
CDC	collision dissociation chamber
DLR	German Aerospace Center
ECD	electron capture detector
EMAC	ECHAM/MESSy Atmospheric Chemistry
ECHAM	European Centre HAMburg general circulation
ECMWF	European Centre for Medium-Range Weather Forecasts
FACSIMILE	Flow and chemistry simulator
FAIRO	Fast accurate airborne ozone instrument
fPAN	trifluoroacetyl nitrate
FIRMS	Fire Information for Resource Management System
FJZ	Forschungszentrum Jülich
GC	gas chromatography
GC-ECD	electron capture gas chromatograph
GC-MS	gas chromatography-mass spectrometry
HALO	High Altitude and Long Range Research aircraft
HO_x	$OH + HO_2$

HYPHOP	HYdrogen Peroxide and Higher Organic Peroxides monitor
HYSPLIT	HYbrid Single-Particle Lagrangian Integrated Trajectory
IBAIRN	Influence of Biosphere-Atmosphere Interactions on the Reactive Nitrogen budget
IMR	Ion molecule reactor
ITCZ	Intertropical Convergence Zone
IUPAC	International union of pure and applied chemistry
IPWP	Indo-Pacific Warm Pool
KIT	Karlsruhe Institute of Technology
LOD	limit of detection
MACR	methacrolein
MVK	methylvinyl ketone
MGLY	methyl glyoxal
MHP	methyl hydroperoxide
MPIC	Max Planck Institute for Chemistry, Mainz
MPN	methyl peroxy nitrate
MPAN	peroxymethacrylic nitric anhydride
MOM	Mainz Organic Mechanism
MODIS	Moderate Resolution Imaging Spectroradiometer
MIPAS	Michelson Interferometer for Passive Atmospheric Sounding
m/z	mass to charge ratio
NASA	National Aeronautics and Space Administration
NMVOC	non-methane volatile organic compound
NO_x	$NO + NO_2$
NO_y	$NO_x + HONO + N_2O_5 + PAN + RONO_2 + ROONO_2 + NO_3 + HNO_4 + \ldots$
NOAA	National Oceanic and Atmospheric Administration
NOAH	Nitrogen Oxides Analyzer for HALO
NPF	new particle formation
PA	peroxyacetyl

PAA	peracetic acid
PAN	peroxyacetyl nitrate
ppb	parts per billion
ppm	part per million
ppt	parts per trillion
PFA	perfluoroalkoxyalkane
PSS	photostationary state
KI	potassium iodide
PiBN	peroxyisobutyryl nitrate
PPN	peroxy propionyl nitrate
ProcState	process state
PTR-MS	proton-transfer reaction mass spectrometry
RF	research flight
RH	relative humidity
SOA	secondary organic aerosol
SP2	soot photometer
SR	spectroradiometer
sccm	standard cubic centimeter
slm	standard liter per minute
TD	thermal dissociation
TDR	thermal dissociation region
TGI	trace gas inlet
TMU	total measurement uncertainty
ToF	time-of-flight
TROPOS	Leibniz Institute for Tropospheric Research
TUV	Tropospheric Ultraviolet and Visible Radiation Model
UT	upper troposphere
UTLS	upper troposphere, lower stratosphere
UTC	coordinated universal time

UV	ultra violet
UV/VIS	ultra violet/visible
VOC	volatile organic compounds
V-UV	vacuum ultra violet

B

ACKNOWLEDGEMENTS

Removed for data protection reasons.

DECLARATION

I hereby declare that I wrote the dissertation submitted without any unauthorized external assistance and used only sources acknowledged in the work. All textual passages which are appropriated verbatim or para- phrased from published and unpublished texts as well as all information obtained from oral sources are duly indicated and listed in accordance with bibliographical rules. In carrying out this research, I complied with the rules of standard scientific practice as formulated in the statutes of Johannes Gutenberg-University Mainz to insure standard scientific practice.

Mainz, Published under CC-BY-SA-4.0

Anna Carolina Nelson

In certain sections of this work, I utilized the stand alone large language model web service ChatAI[34] provided by the Gesellschaft für wissenschaftliche Datenverarbeitung mbH Göttingen (GWDG) (Doosthosseini et al., 2024) for language assistance. I employed the mentioned AI tool solely for linguistic improvements, paraphrasing, and editing purposes, and not for generating ideas or original content, in accordance with the principles of good scientific practice.

---

[34] `https://chat-ai.academiccloud.de/chat`, last access: 14th June 2025.